VRIJE
UNIVERSITEIT
BRUSSEL

Research Foundation
Flanders
Opening new horizons

Thesis submitted in fulfilment of the requirements for the award of the degree of
Doctor of Sciences

THE STOCHASTIC GRAVITATIONAL-WAVE BACKGROUND

From Models to Observations

Kevin Turbang

July 2024

Promotor:	Prof. Dr. Alberto Mariotti Prof. Dr. Alexander Sevrin Prof. Dr. Nick van Remortel
Jury:	Prof. Dr. Michael Tytgat, chairman Prof. Dr. Sara Bals, secretary Prof. Dr. Irina Dvorkin Prof. Dr. Nelson Christensen

Faculty of Sciences and Bio-Engineering Sciences
Department of Physics

The Stochastic Gravitational-Wave Background: from Models to Observations

Kevin Turbang

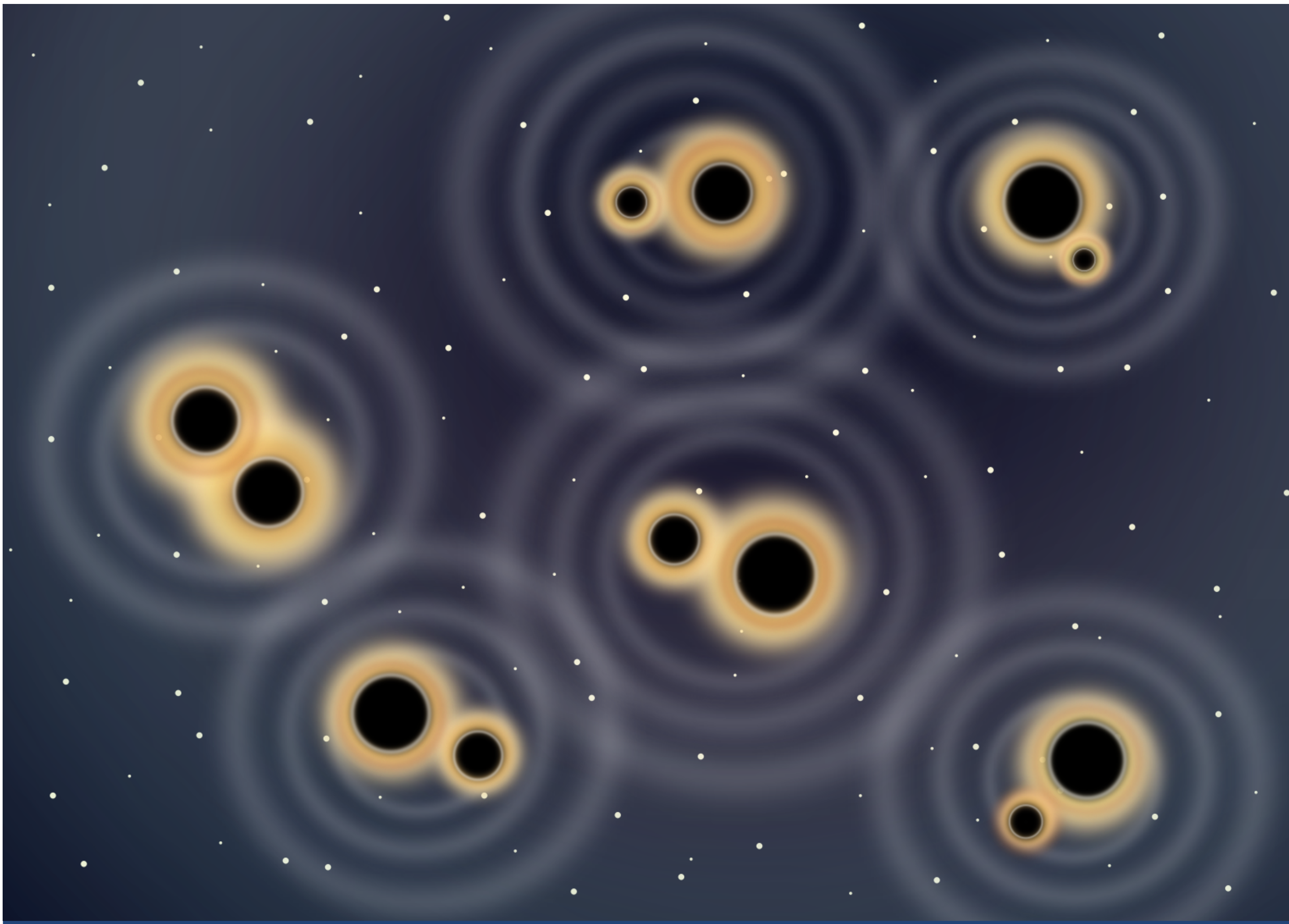

Supervisors: Alberto Mariotti | Alexander Sevrin | Nick van Remortel

Thesis submitted for the degree of Doctor in Sciences: Physics
Faculty of Sciences | Department of Physics | Antwerp 2024

Universiteit Antwerpen

Research Foundation Flanders
Opening new horizons

CONTENTS

ABSTRACT IN ENGLISH

In 1915, Albert Einstein formulated his theory of general relativity and then predicted the existence of ripples of space-time: gravitational waves (GWs). The first detection of GWs by the LIGO-Virgo-KAGRA (LVK) collaborations happened almost a century later, and started a new era: GW astronomy. In addition to the ninety GW detections in the third LVK observing run, a large amount of weaker sources are expected to contribute to an overall gravitational-wave background (GWB). Depending on the source, astrophysical or cosmological contributions can be distinguished. The former receives contributions such as the merger of binary black holes (BBHs) or supernova explosions, whereas the latter would come from cosmological processes that happened during the history of our Universe. Due to the many sources contributing to the background, its detection would reveal a wealth of information and represents the holy grail of GW astronomy. Furthermore, the cosmological background forms a unique way to probe the high energy scales involved in these processes, usually unattainable by detectors on Earth. This thesis considers both contributions to the GWB, both from a data analysis and modelling perspective, with emphasis on bridging the two.

For the astrophysical background, the development of a new data analysis technique to reduce the time until the detection of such a background forms an important part of this work. The GWB from BBHs can be distinguished from other contributions in the LVK detectors through its intermittent nature. As the duration of the signals is shorter than the time in between signals, this background appears popcorn-like. A new data analysis method that targets this intermittency is developed and the improvements in time-to-detection compared to other searches are illustrated. In addition, the implications of the detection of this background for the formation and evolution of BBHs are explored, by using data from the LVK detectors.

Within the possible cosmological sources, attention is paid to first order phase transitions. As the temperature of the Universe decreases, these phase transitions can take place and generate a GWB. The study of these phase transitions and the resulting GWB forms the target of the last part of this work. The goal is to understand the detectability of such signals and to set constraints on models given available GW data from the LVK detectors. This illustrates how particle physics and GW physics can go together to unlock the information contained in the background and elucidate the mysteries of our Universe.

ABSTRACT IN HET NEDERLANDS

In 1915 formuleerde Albert Einstein zijn algemene relativiteitstheorie en voorspelde hij daarna het bestaan van golven van de ruimtetijd: zwaartekrachtgolven (ZG). De eerste waarneming van ZG door de LIGO-Virgo-KAGRA (LVK) samenwerking vond bijna een eeuw later plaats en zo begon een nieuw tijdperk: ZG-astronomie. Naast de negentig ZG-detecties tegen het einde van de derde LVK-observatierun, wordt verwacht dat een groot aantal zwakkere bronnen zal bijdragen tot een algemene zwaartekrachtgolfachtergrond (ZGA). Afhankelijk van de bron die bijdraagt aan de achtergrond, kunnen astrofysische of kosmologische bijdragen worden onderscheiden. De eerste ontvangt bijdragen zoals de samensmelting van binaire zwarte gaten (BZG) of supernova-explosies, terwijl de tweede afkomstig zou zijn van kosmologische processen die tijdens de geschiedenis van ons heelal hebben plaatsgevonden. Door de vele bronnen die bijdragen aan de achtergrond, zou de detectie ervan informatie onthullen over het heelal en vormt het de heilige graal van de ZG-astronomie. Bovendien vormt de kosmologische achtergrond een unieke manier om de hoge energieschalen te onderzoeken die betrokken zijn bij deze processen, die gewoonlijk onbereikbaar zijn voor detectoren op aarde. Deze thesis beschouwt beide bijdragen aan de ZGA, zowel vanuit het perspectief van data-analyse als van modellering, met de nadruk op het verbinden van de twee.

Binnen de context van de astrofysische achtergrond vormt de ontwikkeling van een nieuwe data-analysetechniek om de tijd tot detectie van zo'n achtergrond te verkorten een belangrijk onderdeel van dit werk. De ZGA van BZG kan worden onderscheiden van andere bijdragen in de LVK detectoren door zijn intermitterende aard. Omdat de duur van de signalen korter is dan de tijd tussen de signalen, lijkt deze achtergrond namelijk popcornachtig. Er wordt een nieuwe data-analysemethode ontwikkeld die zich richt op deze intermitterende aard en de verbeteringen in detectietijd in vergelijking met andere methoden worden geïllustreerd. Daarnaast worden de implicaties van de detectie van de astrofysische achtergrond voor de vorming en evolutie van systemen bestaande uit BZG onderzocht door gegevens van de LVK detectoren te gebruiken.

Binnen de mogelijke kosmologische bronnen wordt aandacht besteed aan eerste orde faseovergangen. Naarmate het heelal afkoelt, kunnen deze faseovergangen plaatsvinden en een ZGA genereren. De studie van deze faseovergangen en hun resulterende ZGA vormt het

doel van het laatste deel van dit werk. De bedoeling is om de detecteerbaarheid van zulke signalen te begrijpen en om beperkingen op te leggen aan modellen, gegeven de ZG-data van de LVK detectoren. Dit onderzoek illustreert hoe deeltjesfysica en ZG-fysica samen kunnen gaan om informatie in de achtergrond te onthullen en zo de mysteries van ons Universum op te helderen.

Acronyms

AION Atom Interferometer Observatory and Network

ASD amplitude spectral density

BBH binary black hole

BBN Big Bang Nucleosynthesis

BNS binary neutron star

BPL broken power law

BSM beyond the Standard Model

CBC compact binary coalescence

CE Cosmic Explorer

CMB Cosmic Microwave Background

CSD cross-spectral density

DECIGO DECi-hertz Interferometer Gravitational wave Observatory

DSI deterministic search for intermittent backgrounds

ELGAR European Laboratory for Gravitation and Atom-interferometric Research

EPTA European Pulsar Timing Array

ET Einstein Telescope

FAR false-alarm rate

FOPT first order phase transition

GMM Gaussian mixture-model

GR general relativity

GW gravitational wave

GWB gravitational-wave background

InPTA Indian Pulsar Timing Array

IPTA International Pulsar Timing Array

KS Kolmogorov-Smirnov

LIGO Laser Interferometer Gravitational-Wave Observatory

LISA Laser Interferometer Space Antenna

LVK LIGO-Virgo-KAGRA

MAGIS-100 Matter-wave Atomic Gradiometer Interferometric Sensor

MIGA Matter wave-laser based Interferometer Gravitation Antenna

NANOGrav North American Nanohertz Observatory of Gravitational Waves

NSBH neutron star black hole

ORF overlap reduction function

PI power-law integrated

PPTA Parkes Pulsar Timing Array

PSD power spectral density

PTA pulsar timing array

QCD quantum chromodynamics

SFR star formation rate

SM Standard Model

SMBBH super-massive binary black hole

SNR signal-to-noise ratio

SOPT second order phase transition

SSC standard cross-correlation search for a continuous-Gaussian background

SSI stochastic search for intermittent backgrounds

TT transverse-traceless

UIV uniform-in-volume

VEV	vacuum expectation value
ZAIGA	Zhaoshan long-baseline Atom Interferometer Gravitation Antenna

AUTHOR'S CONTRIBUTIONS

Publications

This thesis does not contain material from the publications denoted with an asterisk (*).

1. *Iason Baldes *et al.* "Baryogenesis via relativistic bubble expansion". In: *Physical Review D* 104.11 (Dec. 2021). DOI: 10.1103/physrevd.104.115029. URL: https://doi.org/10.1103%2Fphysrevd.104.115029

   Contribution: Study of the first order phase transition and resulting gravitational-wave background signal in our model. Detectability assessment with current and future gravitational-wave interferometers.

2. Nick van Remortel, Kamiel Janssens, and Kevin Turbang. "Stochastic gravitational wave background: Methods and implications". In: *Progress in Particle and Nuclear Physics* 128 (Jan. 2023), p. 104003. DOI: 10.1016/j.ppnp.2022.104003. URL: https://doi.org/10.1016%2Fj.ppnp.2022.104003

   Contribution: Reviewed detection methods other than interferometry, alternatives to the standard cross-correlation search for gravitational-wave backgrounds, and the astrophysical and cosmological implications given current constraints on the gravitational-wave background.

3. Charles Badger *et al.* "Probing early Universe supercooled phase transitions with gravitational wave data". In: *Physical Review D* 107.2 (Jan. 2023). DOI: 10.1103/physrevd.107.023511. URL: https://doi.org/10.1103%2Fphysrevd.107.023511

   Contribution: Study of two concrete particle physics models and the predicted gravitational-wave background from first order phase transitions in each of these. Using current gravitational-wave data to place constraints on the parameter space of these models.

4. *Simone Blasi *et al.* "Friction on ALP domain walls and gravitational waves". In: *Journal of Cosmology and Astroparticle Physics* 2023.04 (Apr. 2023), p. 008. DOI: 10.1088/1475-

7516/2023/04/008. URL: https://doi.org/10.1088%2F1475-7516%2F2023%2F04%2F008

Contribution: Study of domain wall gravitational-wave signatures and their detectability with current and future gravitational-wave detectors.

5. Jessica Lawrence *et al.* "A stochastic search for intermittent gravitational-wave backgrounds". In: *Physical Review D* 107.10 (May 2023). DOI: 10.1103/physrevd.107.103026. URL: https://doi.org/10.1103%2Fphysrevd.107.103026

   Contribution: Together with Jessica Lawrence, we were in charge of the full analysis on toy models and production of results as displayed in the paper.

6. Arianna I. Renzini *et al.* "pygwb: A Python-based Library for Gravitational-wave Background Searches". In: *Astrophys. J.* 952.1 (2023), p. 25. DOI: 10.3847/1538-4357/acd775. arXiv: 2303.15696 [gr-qc]

   Contribution: In charge of (or contributed a lot to) the following `pygwb` modules (both from a coding point of view, as well as paper writing): `simulator`, `pe`, `network`, and `statistical checks`.

7. Kevin Turbang *et al.* "The Metallicity Dependence and Evolutionary Times of Merging Binary Black Holes: Combined Constraints from Individual Gravitational-wave Detections and the Stochastic Background". In: *Astrophys. J.* 967.2 (2024), p. 142. DOI: 10.3847/1538-4357/ad3d5c. arXiv: 2310.17625 [astro-ph.HE]

   Contribution: Fully in charge of the whole analysis and paper writing.

8. Arianna I. Renzini *et al.* "pygwb: a Python-based library for gravitational-wave background searches". In: *Journal of Open Source Software* 9.94 (2024), p. 5454. DOI: 10.21105/joss.05454. URL: https://doi.org/10.21105/joss.05454

   Contribution: Updated all the code documentation, was in direct correspondence with the reviewer for the code and the documentation improvements, and am still maintaining the code regularly.

Presentations

- Virgo week, online, April 19, 2021
  –Speaker on *'Updating the Virgo non-discrimination policy.'*

- LVK meeting - Stochastic F2F, online, September 7, 2021
  – Speaker on *'Updates about the stochastic search for intermittent backgrounds.'*

- Belgian Gravitational-wave Meeting, Brussels, November 3, 2021
  – Speaker on *'A search for intermittent gravitational wave backgrounds.'*

- Beyond the standard model summer school, Cargèse, France, August 3, 2022
  – Speaker on *'Gravitational-wave backgrounds from first order phase transitions.'*

- Gravitational-wave orchestra, Louvain-La-Neuve, September 9th, 2022
  – Poster presentation on *'Stochastic search for intermittent backgrounds.'*

- LVK meeting - Stochastic F2F, Evanston (IL), USA, March 14, 2023
  – Speaker on *'Stochastic search for intermittent backgrounds.'*

- LVK meeting, Evanston (IL), USA, March 14, 2023
  – Poster presentation on *'Inferring the time-delay distribution and metallicity dependence of binary black holes.'*

- Caltech, Pasadena (CA), USA, March 30, 2023
  – Speaker on *'Gravitational-wave background: searches and implications.'*

- Theory at Sea, Oostende, June 8, 2023
  – Speaker (gong show) on *'Probing early Universe first order phase transitions with gravitational-wave data.'*

- Gravitational-wave populations: whats next?, Milan, Italy, June 11, 2023
  – Speaker (gong show) on *'Inferring the time-delay distribution and metallicity dependence of binary black holes.'*

- Belgian-Dutch Gravitational Wave Meeting, Maastricht, NL, October 23-23, 2023
  – Speaker on *'Inferring the time-delay distribution and metallicity dependence of binary black holes.'*

ACKNOWLEDGEMENT

This PhD has been a fantastic journey with an uncountable amount of amazing people. Below, I would like to take the time to thank some of them explicitly.

I would like to thank my supervisors at the Vrije Universiteit Brussel Prof. Alexander Sevrin and Prof. Alberto Mariotti without whom this adventure could not have been possible. Throughout the years, you inspired me and contributed to shaping me into the physicist I am today. Whether for an informal chat, guidance, or specific physics questions, your door was always open for me. During more difficult times, you were able to find the right words to motivate me again.

At the Universiteit Antwerpen, I would like to thank my supervisor Prof. Nick van Remortel. I am glad we decided to make my PhD a joint one with the Universiteit Antwerpen. Your position within the LVK stochastic group was key to get me involved in several projects of this PhD, something I am very thankful for.

Additionally, I would also like to extend my gratitude towards the other members of my PhD jury: Prof. Sara Bals, Prof. Irina Dvorkin, Prof. Michael Tytgat, and Prof. Nelson Christensen. I am extremely thankful that you took the time to go through my thesis and ask interesting questions during the private defence. Although before the defence I could not have imagined I would have said this, I can now say that I truly enjoyed the defence and answering your questions. Your personal research expertise resulted in varied questions and an exciting moment to share my acquired knowledge and brainstorm about future research avenues.

Office mates come and go, but I am grateful for each one of them whom I got to meet along the way: Aäron, Max, Kamiel, Hannah, Alba, Simone, Miguel, Xander, and Sam. There is nothing better than a coffee break with people who understand you and the possible struggles you might be experiencing. Seeing some of these work acquaintances evolve into long-lasting friendships was one of the unexpected aspects of my PhD, for which I am extremely grateful. In particular, I would like to thank Kamiel who helped me out at the start of my PhD and made sure

to always be there when I had questions. Your positivity and ability to maintain a nice work-life balance while still achieving great academic work were inspiring.

Although she is not technically an office mate, it sure felt like it given the large amount of time we spent together on calls to work on common projects. Jessica, knowing I had someone to work with side by side in several projects made this experience so much more enjoyable. I will cherish the memories of our chats -whether work-related or not- and our productive work together.

Additionally, I would like to give a shout-out to Nina. Although we were not on the same floor, we would occasionally run into each other at the coffee machine. Thank you for always taking such good care of all administrative tasks related to my PhD. Your excellent work has definitely made that side of my PhD as smooth as possible.

A special thank you goes out to Joe, whom I learned a lot from and had the chance to work with for most of my PhD. I remember starting my PhD and reading many of your publications, being impressed by your work and knowledge. Little did I know that I would end up working with you. I am very happy that we got to collaborate; a part of my PhD I will not easily forget.

I would also like to thank Arianna and Tom. A large portion of my PhD was dedicated to projects we worked on together. I truly enjoyed our collaboration and the occasional visits. Working with you both inspired me and gave me a perspective on what kind of scientist I wanted to strive to be. I look up to you both enormously, and wish you all the best in your future (academic) careers.

My physics journey started almost nine years ago at the Vrije Universiteit Brussel. I am beyond happy that the friends I made along this adventure are still here for me today: Alison, Djunes, Robin, Louise, Saar, Lennart, Joeri, and Yens. Game nights, good food, and lots of laughter were always a great recipe to forget about physics for a little while and just enjoy being together. An additional thanks to Margot and Leonie, who have been around since high school and have supported me throughout the years; I am so glad you are both still part of my life.

Most importantly, thank you to my family, Papa, Loïc, Mamy, Papilou, Bonne Maman, Bon Papa, Kelly, Bill, Austin, and Gianna for supporting me and my aspirations. Over the course of my PhD, it was heart-warming to see your continuous interest in how my career as a PhD student was going. There is something truly magical about seeing the people you care most about in life being proud of you.

I would also like to thank my partner, Tom. At the start of this adventure, we did not *know each other. However, a few months after meeting you, it was already clear that your capability to put things into perspective, to cheer me up when needed and to find the right words to motivate me would be key to the successful completion of this PhD. I am thankful for your support and would not have wanted to do this without you by my side.*

Finally, a special thought goes out to Ian who would probably have taken a quick look at this manuscript and laughed at me saying "Nerd!" in the most loving and brotherly way possible.

Funding and resources
The first year of this PhD was supported by a one year grant of the Vrije Universiteit Brussel Research Council. The rest of this PhD was supported by FWO-Vlaanderen through grant number 1179522N. Part of this research has made use of data, software and/or web tools obtained from the Gravitational Wave Open Science Center (https://www.gw-openscience.org), a service of LIGO Laboratory, the LIGO Scientific Collaboration and the Virgo Collaboration. Virgo is funded by the French Centre National de Recherche Scientifique (CNRS), the Italian Istituto Nazionale della Fisica Nucleare (INFN) and the Dutch Nikhef, with contributions by Polish and Hungarian institutes. This material is based upon work supported by NSFs LIGO Laboratory which is a major facility fully funded by the National Science Foundation. We are grateful for computational resources provided by the LIGO Laboratory and supported by NSF Grants PHY-0757058 and PHY-0823459.

INTRODUCTION

Describing and understanding nature through the laws of physics are almost a tale as old as time. Throughout the years, people have been fascinated by the world surrounding us, both on the smallest and largest scales. Some are intrigued by the tiny building blocks that make life around us what it is, whereas others are puzzled by the processes happening on the largest distances within the vast extent of our Universe. These curiosities have fuelled scientists' imagination, culminating into two of the building blocks of modern physics: quantum physics and general relativity. Whereas the former describes the physical interactions on the smallest scales, the latter concerns the interaction of matter and gravity throughout the Universe. Although each of these could be thought of as the almost perfect theory in their own realm, the two theories seem to be irreconcilable. In times where we naively think we understand the majority of the world that surrounds us, this illusion appears to be just that... an illusion. Many mysteries, such as the nature of dark matter, dark energy, the Big Bang, and the reconciliation of the quantum world and gravity still trouble contemporary physicists, leaving scientists to long for a theory of everything.

Over the course of the last few centuries, experiments of increasing complexity have been put forward to shed light on these question marks. Whether the design for a new particle collider was proposed, or a more powerful telescope, or even a laser interferometer, humankind found a way to engineer it and turn these into state-of-the-art experiments. All of these are purposefully designed to answer some of the open questions physicists still deal with today and unlock the mysteries of the Universe. Among these experiments are the Large Hadron Collider at CERN, the Hubble Telescope, and IceCube – to only name a few.

An additional experiment, which will be at the center of this thesis, is the Laser Interferometer Gravitational-wave Observatory (LIGO). It distinguishes itself from other detectors by detecting tiny ripples in the fabric of our Universe, called gravitational waves (GWs), as a way to further our understanding of the Universe, the physical objects within it, and the processes that happened in its very early stages. The first direct detection of GWs in 2015 by the LIGO-Virgo collaborations kickstarted the field of GW astronomy and opened a new window to the Universe. Indeed, contrarily to other cosmological probes such as the Cosmic Microwave Background, our ability to perceive GWs originating from the early stages of the Universe is not limited to times after recombination when photons and matter decoupled. Gravitational waves therefore offer a completely novel way to observe the first few instants of the Universe and attempt to answer some of the long-standing questions in the field.

A specific GW signature will be sought for in this thesis: the stochastic gravitational-wave background (GWB). Coming from the superposition of many weak, unresolvable events throughout the Universe, it can be thought of as the soft, melodic symphony of the Universe. While we cannot distinguish the individual instruments making up the orchestra, experiencing the orchestra as an entity can provide information about the symphony being played melodiously. Similarly, although the individual contributors to the GWB cannot be distinguished due to their inherently weak nature, measuring the background as a whole could elucidate some of the mysteries of the Universe. It is important to note that depending on the type of contributor to the background, two categories can usually be distinguished: the astrophysical and cosmological background. The former pertains to astrophysical contributors, such as binary black holes or binary neutron stars, whereas the latter refers to the plethora of cosmological processes that could have generated GWs during the history of the Universe. The goal of this thesis is to explore both categories of contributors to the GWB, and to do so both through a data analysis and modelling perspective, while focusing on the potential implications that can be derived.

The main part of this work is structured into three distinct parts. The first part introduces the necessary concepts and reviews the framework used in the remainder of the thesis. More specifically, Chapter 1 introduces general relativity and GWs, as well as several detection methods, both current and future. The GWB is introduced in Chapter 2, and covers a theoretical introduction to the background and reviews the search method currently in place to look for such a GWB. This concludes the first part of this work, allowing us to move on to the second part of the thesis, which focusses on the astrophysical background. First, a new data analysis method is introduced in Chapter 3: the stochastic search for intermittent backgrounds. By properly modelling the intermittent nature of the astrophysical binary black hole background, we show that the time-to-detection of this background can significantly be reduced compared to traditional search methods, such as the one introduced in Chapter 2. In the following chapter, Chapter 4, we seek to apply current GWB upper limits to derive constraints on the formation of binary black holes and more concretely, the metallicity dependence and evolutionary times of merging binary black holes. This is done in a framework where both individually detected binary black holes and the upper limits on the binary black hole background are used simultaneously. In the last part of the thesis, we switch gears slightly and concentrate on the cosmological background. Within the vast amount of possible cosmological candidates to have contributed to this background, we focus on first order phase transitions. Similarly to water boiling from water to gas, the Universe could have undergone a series of phase transitions, generating a cosmological GWB in the process. Current data from the LIGO-Virgo-KAGRA detectors are used to set constraints on the resulting background from first order phase transitions, as well as on specific particle physics models in which these phase transitions arise.

As the title of this thesis suggests, both observations and modelling are at the center of this work. By dedicating a chapter to each aspect, i.e., data analysis techniques, as well as astrophysical and cosmological implications, we hope to give a glimpse into the fascinating world of GWB analyses and its implications. Each of these chapters forms a testament to the abundance of possible applications using GWB data. In addition to the results presented in this thesis, promising results and implications from other experiments in the context of GWBs, such as pulsar timing arrays, showcase the wealth of science cases possible with a GWB measurement and steadily pave the way to unlocking the mysteries of the Universe. Although still in its infancy compared to other fields in physics, GW physics, and more particularly GWB physics, has an enormous potential of illuminating the first few instances of our Universe that have remained in the darkness until this day.

4

Part I

Gravitational Waves and Gravitational-Wave Backgrounds

The first part of this work forms a review of the material needed for the other chapters in this thesis. General concepts and equations pertaining to gravitational waves and data analysis thereof are introduced. This is by no means a complete review on the topic, but highlights important aspects relevant to this thesis. In the absence of detailed discussions, references will be provided.

Chapter 1 - Gravitational Waves

Gravitational waves were predicted as a consequence of Einstein's theory of general relativity. In this chapter, we start by reviewing how gravitational waves arise as solutions to the Einstein equations. We then proceed by discussing different detection methods, giving an overview of current and future gravitational-wave experiments. We conclude by discussing the various sources of gravitational waves, with particular emphasis on the ones potentially detectable by current gravitational-wave interferometers.

Chapter 2 - Gravitational-Wave Background

In addition to resolvable compact binary coalescence events, such as the ones currently detected by the LIGO-Virgo-KAGRA collaborations, a background from the superposition of faint gravitational waves is expected: the gravitational-wave background. This chapter introduces the formalism used to describe and search for such a background. In addition, several indispensable tools for gravitational-wave background data analysis are also given. An overview of the current constraints on the gravitational-wave background using different detection methods concludes this chapter.

1 GRAVITATIONAL WAVES

> Space-time tells matter how to move;
> matter tells space-time how to curve.
>
> John Archibald Wheeler

Not long after Albert Einstein published his theory of general relativity (GR) in 1915, he also predicted the existence of ripples in space-time as a consequence of his theory: gravitational waves (GWs) [114–117]. Although long predicted to exist, the first indirect detection was only made in 1974 by Hulse and Taylor [160, 248], with an additional forty-one years until the direct detection of GWs by the Laser Interferometer Gravitational-Wave Observatory (LIGO)-Virgo collaborations in 2015 [6].

The first chapter of this work is meant as an introduction to Einstein's theory and lays the foundation for the rest of the thesis. We start by reviewing some aspects of Einstein's theory of GR to get to the GW solution of the Einstein equations in Section 1.1. We then discuss several detections methods, with an emphasis on laser interferometry and the LIGO-Virgo-KAGRA (LVK) instruments in Section 1.2. Proposed next-generation detectors and their main characteristics are also touched upon. We conclude this chapter in Section 1.3 with an overview of the different GW sources and comment on the current GW population catalogue as observed by the LVK collaborations.

1.1 General Relativity and Gravitational Waves

In this section, we review various aspects of GR in order to describe GWs. The necessary concepts are defined to formulate the Einstein equations, after which we consider these in the context of the linearised theory. We will see that adopting a specific gauge will reveal the GW solution to the Einstein equations. We conclude by discussing the main properties of these GW solutions. This section is largely based on [190].

1.1.1 The Einstein Equations

At the center of the GR formalism lies the idea that gravity is encoded in the fabric of space-time. The geometry of space-time is then represented by a two-dimensional, symmetric tensor: the metric $g_{\mu\nu}$[1]. For flat space-times, this metric is called the Minkowski metric $\eta_{\mu\nu}$, for which we adopt the convention $\eta_{\mu\nu} = \mathrm{diag}(-,+,+,+)$.

In GR, space-time is described by the Einstein-Hilbert action:

$$S_E = \frac{c^3}{16\pi G} \int d^4x \sqrt{-g} R, \tag{1.1}$$

where g denotes the determinant of the curved space-time metric $g_{\mu\nu}$, and the Ricci scalar is given by:

$$R = g^{\mu\nu} R_{\mu\nu}. \tag{1.2}$$

The Ricci tensor $R_{\mu\nu}$ can be obtained from the Riemann tensor by contracting the first and third indices as follows:

$$R_{\mu\nu} = R^{\alpha}{}_{\mu\alpha\nu}, \tag{1.3}$$

where the Riemann tensor takes the form:

$$R^{\mu}{}_{\nu\rho\sigma} = \partial_\rho \Gamma^{\mu}_{\nu\sigma} - \partial_\sigma \Gamma^{\mu}_{\nu\rho} + \Gamma^{\mu}_{\alpha\rho}\Gamma^{\alpha}_{\nu\sigma} - \Gamma^{\mu}_{\alpha\sigma}\Gamma^{\alpha}_{\nu\rho}. \tag{1.4}$$

In the above expressions, the geometry of the space-time manifold is encoded in the Christoffel symbols:

$$\Gamma^{\rho}_{\mu\nu} = \frac{1}{2} g^{\rho\sigma} \left(\partial_\mu g_{\sigma\nu} + \partial_\nu g_{\sigma\mu} - \partial_\sigma g_{\mu\nu} \right). \tag{1.5}$$

In addition to the Einstein-Hilbert action, the gravitational action receives a contribution from the matter content of the Universe. The variation of the matter action S_M under a metric transformation $g_{\mu\nu} \to g_{\mu\nu} + \delta g_{\mu\nu}$ takes the form:

$$\delta S_M = \frac{1}{2c} \int d^4x \sqrt{-g}\, T^{\mu\nu} \delta g_{\mu\nu}. \tag{1.6}$$

Varying the total action with respect to the metric $g_{\mu\nu}$ gives rise to the so-called Einstein equations:

$$R_{\mu\nu} - \frac{1}{2} g_{\mu\nu} R = \frac{8\pi G}{c^4} T_{\mu\nu}. \tag{1.7}$$

These equations dictate how matter, as encoded in the energy-momentum tensor $T_{\mu\nu}$, interacts

---

[1] Note that the Greek indices denote all four dimensions 0, ..., 3 (including the time component given by 0), whereas Latin indices represent the spatial dimensions 1, 2, 3.

with space-time, as represented by the various quantities containing the metric $g_{\mu\nu}$ on the left-hand side of the equation. To study these equations in more detail, we will work within the context of linearised GR theory. This will allow us to bring these equations into a clearer form, revealing the GW solution to these equations.

1.1.2 Linearised Theory

In linearised GR theory, the metric $g_{\mu\nu}$ is expanded around the flat-space Minkowski metric $\eta_{\mu\nu}$:

$$g_{\mu\nu} = \eta_{\mu\nu} + h_{\mu\nu}, \qquad (|h_{\mu\nu}| \ll 1), \tag{1.8}$$

where $h_{\mu\nu}$ denotes a small perturbation away from the Minkowski metric. Assuming this expansion, the Riemann tensor, given by Eq. (1.4), then takes the form

$$R_{\mu\nu\rho\sigma} = \frac{1}{2}\left(\partial_\nu\partial_\rho h_{\mu\sigma} + \partial_\mu\partial_\sigma h_{\nu\rho} - \partial_\mu\partial_\rho h_{\nu\sigma} - \partial_\nu\partial_\sigma h_{\mu\rho}\right). \tag{1.9}$$

We now write the trace of the metric perturbation as

$$h = \eta^{\mu\nu} h_{\mu\nu}, \tag{1.10}$$

and introduce the following shorthand notation:

$$\bar{h}_{\mu\nu} = h_{\mu\nu} - \frac{1}{2}\eta_{\mu\nu} h, \tag{1.11}$$

or equivalently:

$$h_{\mu\nu} = \bar{h}_{\mu\nu} - \frac{1}{2}\eta_{\mu\nu} \bar{h}, \tag{1.12}$$

which allows us to write the Einstein equations more compactly. These are now given by:

$$\Box\bar{h}_{\mu\nu} + \eta_{\mu\nu}\partial^\rho\partial^\sigma\bar{h}_{\rho\sigma} - \partial^\rho\partial_\nu\bar{h}_{\mu\rho} - \partial^\rho\partial_\mu\bar{h}_{\nu\rho} = -\frac{16\pi G}{c^4} T_{\mu\nu}. \tag{1.13}$$

To continue investigating the above set of equations, we note that GR is invariant under a large symmetry group. Indeed, it is invariant under any diffeomorphism $x'^\mu(x)$, i.e., a differentiable and invertible function, and having a differentiable inverse:

$$x^\mu \to x'^\mu(x). \tag{1.14}$$

Under such a coordinate transformation, the metric transforms as

$$g_{\mu\nu}(x) \to g'_{\mu\nu}(x') = \frac{\partial x^\rho}{\partial x'^\mu}\frac{\partial x^\sigma}{\partial x'^\nu} g_{\rho\sigma}(x). \tag{1.15}$$

We now consider the following coordinate transformation

$$x^\mu \to x'^\mu = x^\mu + \xi^\mu(x). \tag{1.16}$$

One can show, given Eq.(1.15), that, under the above transformation, the metric perturbation transforms as

$$h_{\mu\nu}(x) \to h'_{\mu\nu}(x') = h_{\mu\nu}(x) - \left(\partial_\mu \xi_\nu + \partial_\nu \xi_\mu\right), \tag{1.17}$$

assuming $|\partial_\mu \xi_\nu|$ are of the same order of magnitude as $|h_{\mu\nu}|$, and the condition $|h_{\mu\nu}| \ll 1$ is therefore preserved. In addition, one can also consider Lorentz transformations:

$$x^\mu \to \Lambda^\mu{}_\nu x^\nu. \tag{1.18}$$

Noting that for Lorentz transformations the following relation holds:

$$\Lambda_\mu{}^\rho \Lambda_\nu{}^\sigma \eta_{\rho\sigma} = \eta_{\mu\nu}, \tag{1.19}$$

one can show that the metric transforms as

$$g_{\mu\nu}(x) \to g'_{\mu\nu}(x') = \eta_{\mu\nu} + \Lambda_\mu{}^\rho \Lambda_\nu{}^\sigma h_{\rho\sigma}(x), \tag{1.20}$$

or that the perturbation transforms as

$$h'_{\mu\nu}(x') = \Lambda_\mu{}^\rho \Lambda_\nu{}^\sigma h_{\rho\sigma}(x). \tag{1.21}$$

From Eq. (1.15), it is clear that the metric is also invariant under translations $x_\mu \to x_\mu + \alpha_\mu$, such that the linearised theory is invariant under the finite Poincaré group formed by translations and Lorentz transformations.

The above discussion motivates us to choose a specific gauge in which to consider the Einstein equations. Given the gauge freedom in Eq. (1.17), we decide to work in the so-called Lorenz gauge[2]:

$$\partial^\nu \bar{h}_{\mu\nu} = 0, \tag{1.22}$$

where $\bar{h}_{\mu\nu}$ was introduced in Eq. (1.11). Indeed, using the transformation in Eq. (1.17), one

---

[2] This is also called the harmonic or de Donder gauge.

can show that

$$\bar{h}_{\mu\nu} \rightarrow \bar{h}'_{\mu\nu} = \bar{h}_{\mu\nu} - \left(\partial_\mu \xi_\nu + \partial_\nu \xi_\mu - \eta_{\mu\nu}\partial_\rho \xi^\rho\right), \tag{1.23}$$

and therefore,

$$\partial^\nu \bar{h}_{\mu\nu} \rightarrow (\partial^\nu \bar{h}_{\mu\nu})' = \partial^\nu \bar{h}_{\mu\nu} - \Box \xi_\mu, \tag{1.24}$$

where $\Box$ denotes the d'Alembertian in Minkowski space. Now, say that $\partial^\nu \bar{h}_{\mu\nu} = f_\mu(x)$. Then, using Eq. (1.24), one can ensure that the Lorenz gauge in Eq. (1.22) is satisfied by performing a coordinate transformation with

$$\Box \xi_\mu = f_\mu(x). \tag{1.25}$$

Since the d'Alembertian operator is invertible, one can use a Green's function to solve the above equation, namely:

$$\xi_\mu(x) = \int d^4x G(x-y) f_\mu(y), \tag{1.26}$$

with

$$\Box_x G(x-y) = \delta^4(x-y). \tag{1.27}$$

Using the above Lorenz gauge, the Einstein equations given in Eq. (1.13) take a much simpler form:

$$\Box \bar{h}_{\mu\nu} = -\frac{16\pi G}{c^4} T_{\mu\nu}, \tag{1.28}$$

and reveal a simple wave equation. In addition, the Lorenz gauge in Eq. (1.22) and the above wave equation imply conservation of momentum: $\partial^\nu T_{\mu\nu} = 0$.

At the start of this section, we considered the Einstein equations in the full theory. However, by working in the linearised theory, and assuming the Lorenz gauge, this intricate set of equations reduces to a simple wave equation. We now proceed with an additional gauge choice, the so-called transverse-traceless gauge, to study the GW solution in more detail.

1.1.3 The Transverse-Traceless Gauge

To study the properties of GWs, we are interested in understanding the wave equation outside the source, where $T_{\mu\nu} = 0$. In that case, Eq. (1.28) now takes the form

$$\Box \bar{h}_{\mu\nu} = 0. \tag{1.29}$$

As a reminder, we note that $\Box = -(1/c^2)\partial_0^2 + \nabla^2$, from which it follows that GWs travel at the speed of light c. Furthermore, we note that, although the Lorenz gauge was chosen, this does not completely fix the gauge. In fact, the Lorenz gauge condition $\partial^\nu \bar{h}_{\mu\nu} = 0$ is not spoiled by an additional coordinate transformation $x^\mu \to x^\mu + \xi^\mu$, as long as

$$\Box \xi_\mu = 0, \tag{1.30}$$

since $\partial^\nu \bar{h}_{\mu\nu}$ transforms as in Eq. (1.24) under such a coordinate transformation. As partial derivatives commute with the d'Alembertian operator, it is also true that $\Box \xi_{\mu\nu} = 0$, where

$$\xi_{\mu\nu} = \partial_\mu \xi_\nu + \partial_\nu \xi_\mu - \eta_{\mu\nu} \partial_\rho \xi^\rho. \tag{1.31}$$

Therefore, one can subtract the functions $\xi_{\mu\nu}$, which satisfy $\Box \xi_{\mu\nu} = 0$, from the six independent components of $\bar{h}_{\mu\nu}$, which also obey $\Box \bar{h}_{\mu\nu} = 0$. The four functions ξ_μ can thus be chosen to impose four conditions on the metric perturbation $h_{\mu\nu}$, reducing the number of degrees of freedom to two. Concretely, the trace $\bar{h}$ can be made to vanish by an appropriate choice of ξ^0. If $\bar{h} = 0$, then $\bar{h}_{\mu\nu} = h_{\mu\nu}$, such that the Lorenz condition in Eq. (1.22) for $\mu = 0$ reads

$$\partial^0 h_{00} + \partial^i h_{0i} = 0. \tag{1.32}$$

Choosing the additional three functions ξ^i such that $h^{0i} = 0$, the above equation reduces to

$$\partial^0 h_{00} = 0, \tag{1.33}$$

such that h_{00} is constant in time. However, such a time-independent term corresponds to the static Newtonian potential generated by the source, whereas the GW solution would be captured by a time-dependent term. Therefore, since we are interested in the GW solutions, the condition $\partial^0 h_{00} = 0$ implies $h_{00} = 0$. This sets all four components $h^{0\mu}$ to zero, leaving only the spatial components h^{ij} to be non-zero. The Lorenz gauge for these components reads $\partial^j h_{ij} = 0$, and the condition on the tracelessness of the metric now takes the form $h^i{}_i = 0$. To summarise, we took

$$h^{0\mu} = 0, \qquad h^i{}_i = 0, \qquad \partial^j h_{ij} = 0. \tag{1.34}$$

The above gauge choice defines the transverse-traceless (TT) gauge. We recall that we originally started from a symmetric metric perturbation $h_{\mu\nu}$, which had ten degrees of freedom. The choice of Lorenz gauge reduced the degrees of freedom to six, with an additional residual gauge captured by the four ξ_μ functions bringing the overall number of degrees of freedom to two.

The wave equation in Eq. (1.29) has plane-wave solutions given by $h_{ij}^{TT}(x) = e_{ij}(\mathbf{k}) e^{ikx}$, where $k^\mu = (\omega/c, \mathbf{k})$ and $\omega/c = |\mathbf{k}|$, and $e_{ij}(\mathbf{k})$ is the so-called polarisation tensor. Using Eq. (1.34), one can see that for a single plane wave, the only non-zero components are the ones perpendicular to the direction of propagation $\mathbf{k}$, as $\partial^j h_{ij} = 0$ implies $k^j h_{ij} = 0$. For concreteness, if one chooses a wave travelling along the z axis, and assuming the metric h_{ij} is symmetric and traceless, one finds

$$h_{ab}(t,z) = \begin{pmatrix} h_+ & h_\times \\ h_\times & -h_+ \end{pmatrix}_{ab} \cos\left(\omega\left(t - \frac{z}{c}\right)\right), \tag{1.35}$$

where h_+ and $h_\times$ denote the amplitude of the + and × polarisation waves, and the indices $a, b \in \{1,2\}$ denote the (x,y) plane. The effect of the above metric perturbation will be to stretch space-time. In particular, an example of the effect of a "+"-polarised GW is given in Figure 1.1.

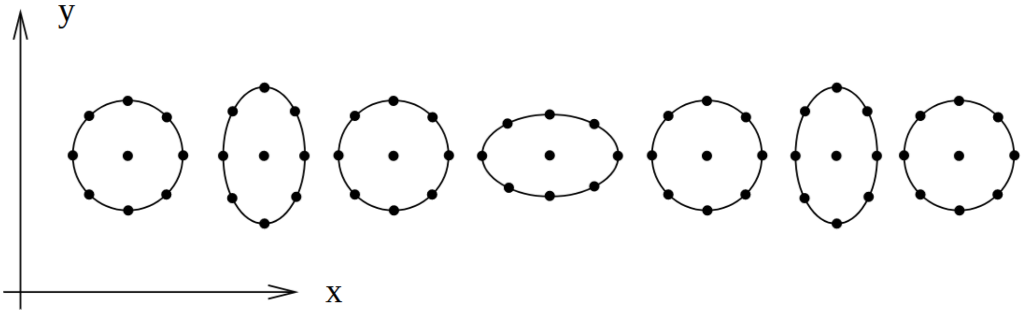

Figure 1.1. Effect of a "+"-polarised GW on a set of test masses. A "×"-polarised GW would stretch the test masses diagonally, instead of vertically and horizontally. Figure taken from [76].

We conclude this section with an example to better illustrate the effect of a GW. Still working under the assumption of a GW travelling along the z axis, one can consider two events at coordinates $(t, x_1, 0, 0)$ and $(t, x_2, 0, 0)$, with coordinate distance $x_2 - x_1 = L$. In the TT gauge, this distance remains constant, whereas the proper distance is given by[3]:

$$s = (x_2 - x_1)(1 + h_+ \cos(\omega t))^{1/2} \simeq L\left(1 + \frac{1}{2}h_+ \cos(\omega t)\right). \tag{1.36}$$

This illustrates that the GW induces a periodic change in the proper distance. In other words, GWs cause a relative change in length, also called strain, which takes the form:

$$h = \frac{\Delta L}{L} = \frac{1}{2}h_+ \cos(\omega t), \tag{1.37}$$

where, as will be illustrated below, typical values for the strain are of the order of $h \sim 10^{-21}$. Although this is a tiny effect, this readily provides a way to experimentally detect GWs by measuring these length changes. Before introducing the engineering marvels that can detect such tiny distortions of space-time, we comment on the generation of GWs in the next section.

---

[3] Up to linear order in h_+.

1.1.4 Generating Gravitational Waves

To conclude this section on GR, we comment on the generation of GWs. We continue to work within the approximation of linearised theory, meaning that we assume that space-time is sufficiently flat[4]. Recall that in linearised GR theory, the Einstein equations reduce to the form given in Eq. (1.28). Now that we are interested in the generation of GWs, we cannot set $T_{\mu\nu} = 0$ as we did in the previous section where we were interested in the propagation of GWs outside the source. Nevertheless, Eq. (1.28) can be solved using Green's function method. The exact derivation is not provided here, but we discuss the main result thereof. We refer the reader to [190] for detailed calculations and additional information.

Working in the TT gauge, it can be shown that, when working in the small velocity expansion[5], the first non-vanishing term in a multipole expansion of the solution to Eq. (1.28) is given by the mass quadrupole, where the mass quadrupole takes the form:

$$Q_{ij} = \int d^3x \rho(t, \mathbf{x}) \left(x_i x_j - \frac{1}{3} r^2 \delta_{ij} \right), \tag{1.38}$$

and r denotes the distance between the observer and the GW source. The first non-vanishing term in the expansion then takes the form:

$$h_{ij}^{\mathrm{TT}}(t, \mathbf{x}) \Big|_{\mathrm{quad}} = \frac{1}{r} \frac{2G}{c^4} \ddot{Q}_{ij}^{\mathrm{TT}}(t - r/c). \tag{1.39}$$

Under this quadrupole approximation, the radiated power by the source is:

$$P_{\mathrm{quad}} = \frac{G}{5c^5} \left\langle \dddot{Q}_{ij} \dddot{Q}_{ij} \right\rangle, \tag{1.40}$$

where this quantity is evaluated at $t - r/c$, the so-called retarded time corresponding to the time of emission at the source. The above equations illustrate that GWs can only be emitted by non-spherically symmetric massive objects, with a time-dependent density. In Section 1.3, we will give a few examples of such objects and discuss several GW sources in the frequency band of the LVK detectors.

The first section of this chapter reviewed the basic principles of Einstein's theory of GR in its linearised form, with GWs as one of its important predictions. In the remainder of this chapter, we review various detection methods for GWs, and conclude by going over several classes of GW sources, focussing on the ones in the frequency range of the LVK detectors.

---

[4] Note that, for most GW sources, this is only an approximation and so-called post-Newtonian physics needs to be taken into account.

[5] This assumes that the velocity of the source is much smaller than the speed of light, i.e., $v \ll c$.

1.2 Detection Methods

Einstein's GR theory and GWs as a consequence represent one of the major physics accomplishments of the twentieth century. Although predicted over a century ago, GWs were not directly observed until almost a century later by the LIGO-Virgo collaborations in 2015 [6]. In this section, we give an overview of some of the basic principles behind several GW detection methods. Particular attention is dedicated to laser interferometers in Section 1.2.1, including current and future GW experiments. Nevertheless, other detection methods are also discussed in Section 1.2.2.

1.2.1 Laser Interferometry

Current Laser Interferometers

We start by reviewing the basic principles of current laser interferometers, focussing on the case of the Advanced LIGO interferometer, and discuss some of its main noise sources. The discussion remains at the introductory, qualitative level, but we refer the reader to [88, 182, 190, 238] for more detailed explanations. Furthermore, for the reader interested in the characteristics of the Italian Virgo detector, we suggest having a look to [21].

A brief introduction to Advanced LIGO

Currently, two Advanced LIGO interferometers are operating in the United Stated of America (Hanford (Washington) and Livingston (Louisiana))[190], although a third LIGO detector is expected to be built in India [161, 234]. Both American LIGO detectors are depicted in Figure 1.2.

Figure 1.2. Aerial view of the two L-shaped LIGO interferometers: Hanford (left) and Livingston (right). Credit: LIGO Laboratory.

Through their impressive 4 km arm length[6] and multitude of engineering marvels, the LIGO detectors are able to measure changes in relative arm length due to the passage of GWs – or strain, as previously introduced in Eq. (1.37) – as tiny as 10^{-21}. The LIGO interferometer is based on the principle of a Michelson interferometer, although several additions make it into the state-of-the-art instrument it is today. Schematically, laser light is emitted, and split by a beam splitter, which sends the laser ray down each arm of the interferometer. After being reflected on the mirrors[7], so-called test masses, the two laser beams are recombined and read out by a photodiode output reader. The interference pattern, and hence, the associated power of the recombined laser, contains information about the relative phase of the laser light accumulated due to the GW interferometer arm distortion from the passage of GWs. This setup is illustrated in Figure 1.3.

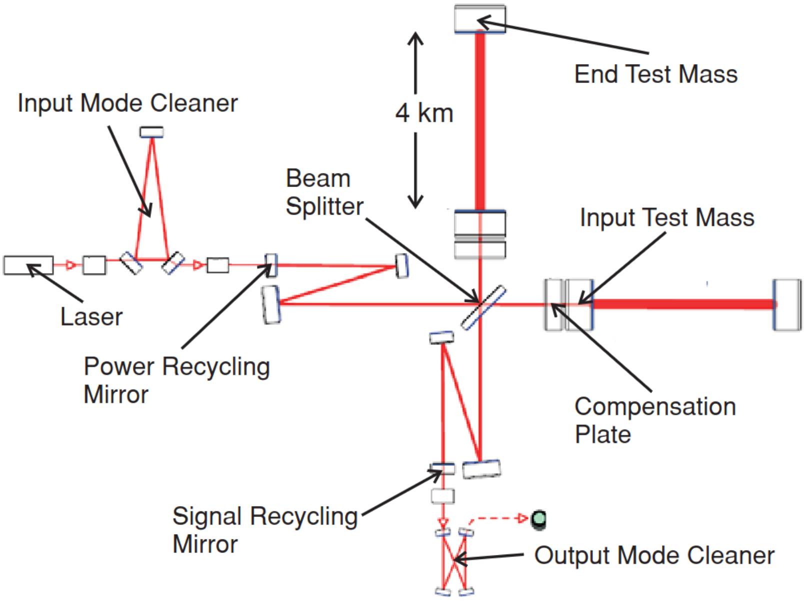

Figure 1.3. Schematic overview of the Advanced LIGO detector. We refer to the main text for an explanation of the various components of this setup. Figure taken from [182].

Although designed to detect GWs, a plethora of noise sources form a major challenge for these interferometers. We briefly comment on the noise sources for the LIGO detectors, before discussing next-generation detectors.

Noise sources for Earth-based interferometers

In reality, actual GWs only form a small fraction of the data observed by GW interferometers, which are largely dominated by detector noise. The amount of noise is captured by the noise

---

[6] Note that the Virgo interferometer in Italy has slightly smaller arms of 3 km [21].

[7] Each of the mirrors is suspended through four pendulums to mechanically isolate the mirrors and mimic free-falling objects.

power spectral density (PSD) $P(f)$, defined as

$$\left\langle \tilde{n}(f)\tilde{n}^*(f')\right\rangle = \frac{1}{2}\delta(f-f')P(f), \tag{1.41}$$

where $\tilde{n}(f)$ denotes the Fourier transform of the time-domain noise data $n(t)$, and $\tilde{n}^*(f)$ denotes the complex conjugate of $\tilde{n}(f)$. In practice, however, the noise dominates in the detector strain data, which is why the noise PSD is usually well-approximated by

$$\left\langle \tilde{s}(f)\tilde{s}^*(f')\right\rangle \approx \frac{1}{2}\delta(f-f')P(f), \tag{1.42}$$

where $\tilde{s}(f)$ is the Fourier transform of the detector strain data. For future reference, we also introduce the amplitude spectral density (ASD), which is related to the PSD through:

$$A(f) = \sqrt{P(f)}. \tag{1.43}$$

Alternatively, one can also define the characteristic strain as a sensitivity measure:

$$h_c(f) = \sqrt{f P(f)}. \tag{1.44}$$

In Figure 1.4, we show the target sensitivity of the Advanced LIGO instruments at design sensitivity [88]. Many individual noise contributions are shown, including environmental and instrumental noise. The former includes seismic movement of the Earth itself, or even tiny variations in the gravitational field around the detector. Other noise sources are instrumental, i.e., intrinsic to the detector itself. A few examples of these noise sources include the excess gas in the vacuum tubes containing the optical systems, the thermal noise in the mirror suspensions and the mirror coatings. Additionally, quantum noise, i.e., where the characteristics of individual photons in the laser become apparent, also limits the sensitivity of the detectors. In particular, the sensitivity at low frequencies is lessened due to radiation from the individual photons hitting the mirrors, whereas at high frequencies, Poissonian fluctuations in photon counting, so-called shot noise, limits the sensitivity. The latter can be limited through the increase in laser power, which in practice is achieved by applying a mirror coating which traps the light in the arms, or installing a power recycling mirror which sends a portion of the laser light back to the input laser and into the instrument. In addition, the laser power can be increased through the usage of so-called Fabry-Pérot cavities. These are added in the arms of the interferometer, trapping the light for several round trips in the cavity, effectively increasing the arm length of the detectors and the power contained in each cavity. Furthermore, with the addition of a signal recycling mirror, the interferometer can be tuned to a specific source, or increase the bandwidth of the detector. More details can be found in [190].

The curves reported in Figure 1.4, however, are theoretical curves produced from predic-

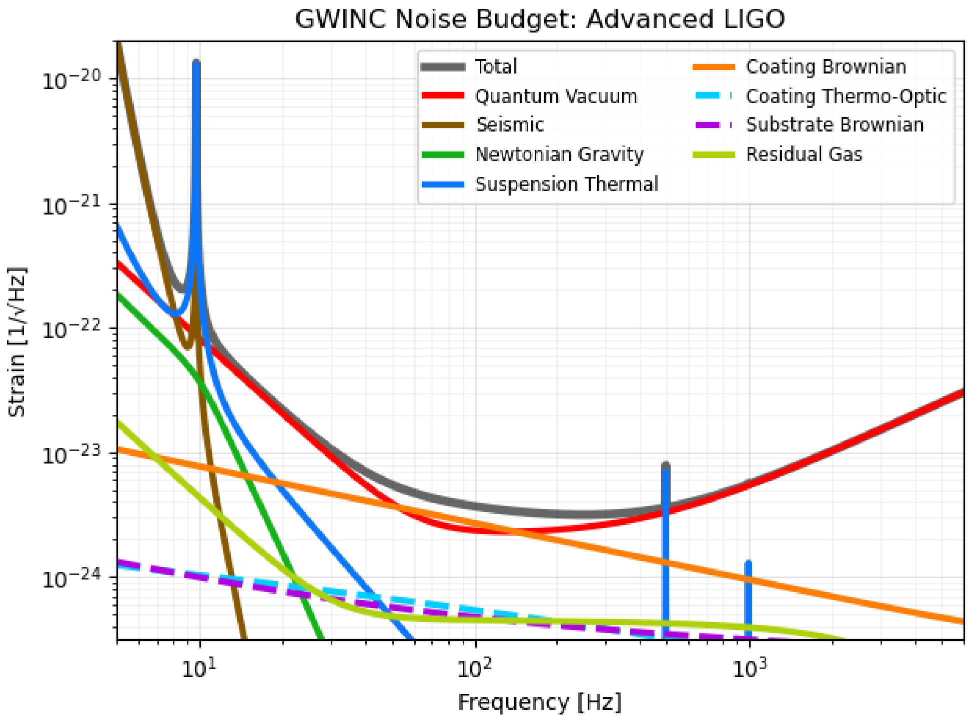

Figure 1.4. The characteristic strain noise curve for the Advanced LIGO detector at design sensitivity. Individual contributions to the total noise are shown as well. Additional information about the Advanced LIGO detector and its principal noise sources can be found in [88]. This figure was produced using the open source code `pyGWINC` [229] and can also be found in [221] with additional information.

tions for the noise budget of the detectors. Real detector data will follow a similar curve, but will look noisier, as illustrated in Figure 1.5. There, the PSDs of a two hour data segment (from March 1,2020 12:00:00-14:00:00 UTC) from the LIGO Hanford and LIGO Livingston detectors are shown. A major difference between the PSD shown in this figure and the characteristic strain[8] shown in Figure 1.4, is the presence of (very) narrow spectral features, called noise lines. The origin of such lines can broadly be defined into three categories [1]:

- **Calibration lines:** A set of lines that are purposely injected into the detector to control and calibrate the detector. For example, in Figure 1.5, the LIGO Hanford interferometer has a calibration line around 332 Hz.

- **Mechanical resonances:** Detector components have intrinsic resonances and their spectral artefacts are therefore an intrinsic part of detector design and cannot be completely removed. An example of this are so-called violin modes around 300 Hz coming from the suspensions that hang the beam splitter.

---

[8] Note that the PSD can be converted to characteristic strain using Eq. (1.44).

- **Instrumental lines:** Other lines originate from operating instruments (e.g., air conditioning, vacuum equipment, ...). Often these operate at a certain frequency, inducing spectral lines corresponding to that frequency. The coupling mechanism (e.g., vibrational, magnetic, ...) depends on the type of noise and equipment. An example of such a line is the noise line associated with the power mains in the USA at 60 Hz.

It is important to assess the nature and impact of these noise artefacts, as they can potentially bias GW analyses. To avoid any contamination, most of these lines are typically excluded from the analyses. Additional information can be found in [221], with more concrete examples of lines for the LIGO detectors in [100] and for the Virgo detector in [1, 23].

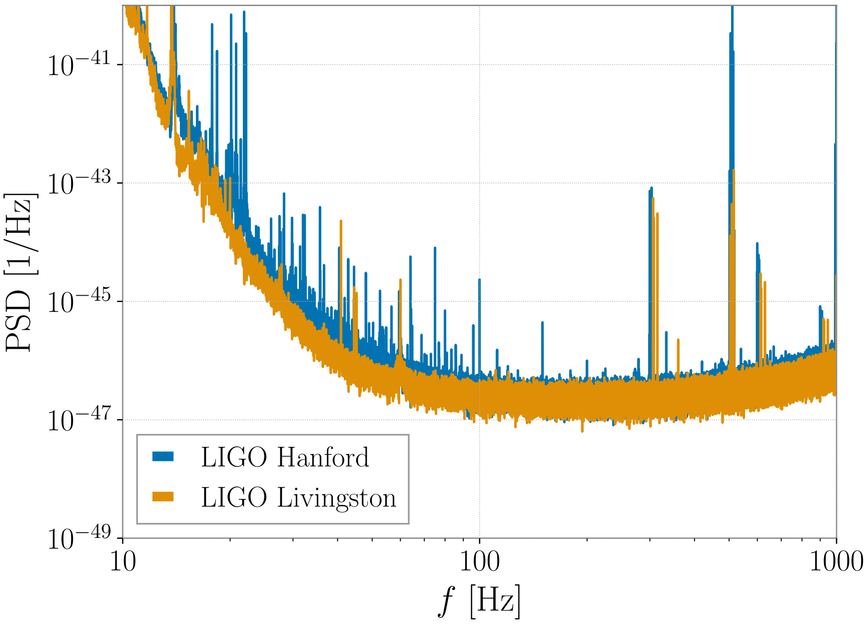

Figure 1.5. Example of the PSDs of two-hour LIGO data segments from March 1, 2020, 12:00:00-14:00:00 UTC during the second half of the third LVK observing run (O3b). Data were obtained through GWOSC [16].

After each observing run, the LVK detectors undergo a series of upgrades which increases their sensitivity. In particular, after the ongoing fourth observing run, the LIGO detectors will be upgraded to their Advanced LIGO A+ sensitivity with upgrades including improved mirror coatings and reduced quantum vacuum noise via frequency dependent squeezing [57]. These great improvements, however, are still not enough to overcome some of the challenges current-generation detectors face. Thankfully, several proposals for next-generation detectors, both Earth-based and space-based, are being considered. These are briefly introduced in the next section.

Next-Generation Laser Interferometers

With the future upgrades of current-generation GW interferometers, these detectors are slowly approaching their design limitations, and therefore their sensitivity limitations as well. Fortunately, concrete plans for next-generation detectors are currently being developed. The better sensitivity of these detectors will allow to probe larger regions of the Universe and the GW sources therein. Below, we give some examples of both Earth-based and space-based next generation detectors.

Earth-based next-generation detectors

One of the proposed third generation interferometers is the Einstein Telescope (ET) [192]. With its 10 km arms embedded in a triangular[9] design operating at cryogenic temperatures, ET sensitivity will be improved by an order of magnitude compared to the Advanced LIGO A+ design and will be sensitive to lower frequencies, reaching below the current 10 Hz LIGO frequency limit [192]. Two main sites have been put forward as possible locations for the new interferometer: the Sos Enattos site in Sardinia, or the Meuse-Rhine Euregion at the three-country point between Belgium, the Netherlands and Germany [192]. As we await the decision on the site of the future ET detector, planned to be made in 2025-2026, design and planning for the interferometer are currently ongoing, with the ETpathfinder in Maastricht, the Netherlands, as a prime example of the facilities currently developing and testing the new technologies involved in this experiment [123].

Another proposal is that of Cosmic Explorer (CE) planned to be constructed in the United States of America [220]. This interferometer is projected to become a large-scale copy of the LIGO A+ detectors. With its 40 km long arms, it will be able to access lower frequency ranges than the current Earth-based interferometers. In a second stage, the detector optics are planned to be improved by using cryogenic technologies and better mirror substrates, with the goal of reaching even better sensitivities [220].

For comparison purposes, the predicted sensitivity of ET and CE are shown in terms of the characteristic strain noise, introduced in Eq. (1.44), in Figure 1.6. Other than the overall better sensitivity of the detectors, we note the larger frequency range of the next-generation detectors compared to the future sensitivity of the LIGO instruments (LIGO A+).

Space-based next-generation detectors

To circumvent some of the limitations associated to terrestrial interferometers, such as the Newtonian noise at low frequencies, or the interferometer arm length limitations, several space-based interferometers were put forward. These include the Laser Interferometer Space Antenna

---

[9] Although the triangular design was originally proposed, this could be revisited in the future. See e.g., [63, 162] which looks into the different designs of ET.

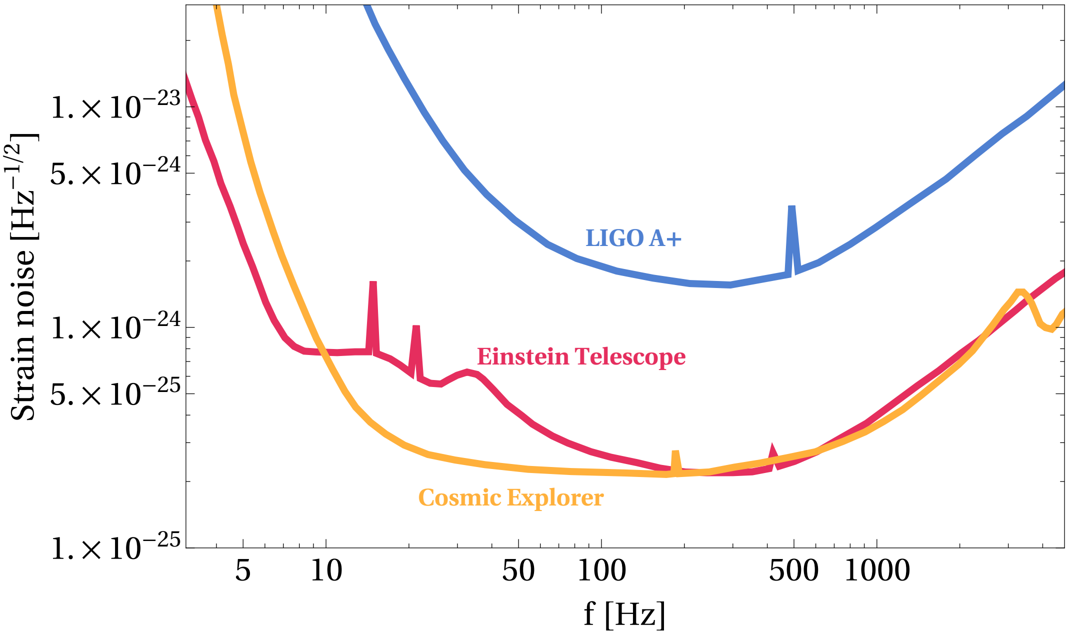

Figure 1.6. Next-generation detector sensitivity in terms of the characteristic strain noise for the Einstein Telescope (red), Cosmic Explorer (yellow), and for comparison, LIGO A+ (blue). Noise lines in these curves come from the suspension thermal noise of the interferometers. Figure adapted from [124].

(LISA) [37, 99], TianQin [187, 201], and the DECi-hertz Interferometer Gravitational wave Observatory (DECIGO) [169] detectors.

LISA is designed to detect GWs in the mHz frequency band. This is achieved through a triangular configuration with 2.5 million km long arms in space, which will follow Earth's orbit around the Sun [37, 99]. The proposed TianQin interferometer, planned for 2035, will be sensitive to the same frequencies as LISA. Also in the 2030s, the launch of another space-based interferometer, B-DECIGO, is planned [169]. B-DECIGO is the scientific pathfinder for DECIGO, which will already collect scientific data at a lesser sensitivity compared to DECIGO. B-DECIGO and DECIGO will be observing GWs in the frequency band from 0.1 Hz to 10 Hz, bridging the gap between LISA and the frequency band of Earth-based detectors. Typical examples of GW sources targeted by space-based interferometers include the inspirals of galactic white dwarf binaries, binary coalescences of massive black holes and the pre-merger phase of the compact binary coalescence (CBC) events observed by Earth-based interferometers [37, 226, 237].

With around ninety detections by the LVK collaborations by the end of their third observing run [15], current laser interferometers have shown to be powerful detection methods, with expected further improvements with next-generation detectors. Nevertheless, many other detection methods exist, which we discuss below.

1.2.2 Other Detection Methods

In the remainder of this section, we discuss some of the alternative GW detection methods. This section should be regarded as a general discussion to give a sense of what these methods are about, rather than an in-depth description of the methods. This section is partially based on an original review paper [221]. Additional references will be provided for the interested reader.

Atom Interferometry

Within the realm of the quantum-mechanical world, a particle-wave duality is predicted. Not only does this means that what is traditionally thought of as a wave e.g., light, can be described in terms of particles, i.e., photons, but that what is usually thought of as particles, e.g., atoms, have an associated wave-like nature as well. This lies at the core of atom interferometry, where the wave-like nature of atoms is exploited for various physical measurements. Atom interferometry can be used to measure several physical constants, e.g., the gravitational or fine-structure constant, to test the equivalence principle [106, 233], or even detect GWs [131, 252].

Much like a laser interferometer, atom interferometers rely on splitting a wave and investigating the interference pattern obtained after recombination. However, instead of looking at the interference pattern of recombined laser light, it is the recombined atomic waveform that is investigated.

After cooling a cloud of atoms, the atoms are manipulated using laser beams or magnetic fields to create a series of coherent atomic matter waves. The cloud is split into two separate wave packets, similar to the way a beam splitter divides a beam of light in traditional laser interferometers. These distinct wave packets each follow different paths, controlled using additional laser pulses or magnetic fields. These manipulations impart a phase shift to the atomic waves. After travelling along distinct paths, the two wave packets interfere, resulting in an interference pattern due to the relative phase shift acquired during their separate travels. This interference is similar to the interference of light waves in laser interferometers [73]. A visual representation of atom interferometers manipulated by laser light is shown in Figure 1.7.

Atom interferometers provide a new window to a previously unexplored frequency range, as traditional laser interferometers fail to bridge the gap between the ∼mHz and ∼Hz range between the LISA and LVK instruments. Examples of current and proposed atom interferometers include the Matter wave-laser based Interferometer Gravitation Antenna (MIGA) [73], the Matter-wave Atomic Gradiometer Interferometric Sensor (MAGIS-100) [20], the Atom Interferometer Observatory and Network (AION) [51], the Zhaoshan long-baseline Atom Interferometer Gravitation Antenna (ZAIGA) [266], and the European Laboratory for Gravitation and Atom-interferometric Research (ELGAR) [72]. We refer the interested reader to the references above for a more detailed discussion of the specifications and scientific applications of each of the detectors.

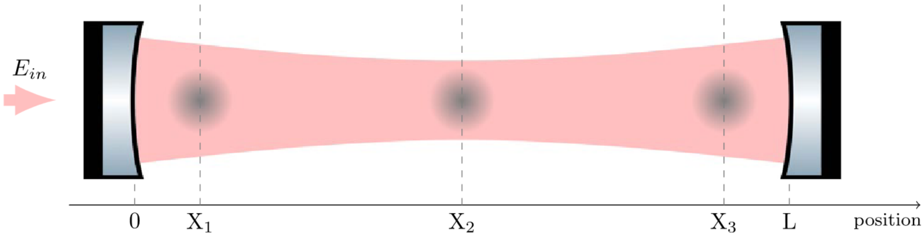

Figure 1.7. Representation of three atom interferometers manipulated coherently by a laser in an optical cavity. Figure taken from [73].

Planetary Bodies as Resonant Detectors

The idea of using resonant objects as GW detectors was first proposed by Weber in 1960 [260]. The principle is based on the observation that as a GW passes through a massive object, it will cause the object to resonate, provided the frequency of the GW is the same as the natural frequency of the object. Several resonant bar detectors with increasing sensitivity have been proposed since the conception of Weber's idea, although no detection of a GW signal has been claimed [45–47]. In the remainder of this paragraph, however, we focus on applying the concept of GW resonance to planetary bodies.

As GWs are expected to interact with elastic bodies they will do so with planetary bodies as well, e.g., Earth itself. Therefore, GWs can excite Earth's free oscillations, called normal modes. Using a network of gravimeters and seismometers, it is possible to monitor Earth's normal modes and excitations thereof by the passage of a GW [89]. By comparing this to the precise prediction for the Earth's response to the passage of a GW and the cross-correlation across various gravimeters and seismometers, one can look for GWs.

More recently, the idea to use the Moon as a GW experiment was also put forward [147]. At the core of this idea lies the same principle as the one used for the Earth's normal mode measurements described above. The Lunar Gravitational-Wave Antenna experiment entails the deployment of seismometers on the Moon to measure its normal modes and measure or constrain GWs. This experiment would be sensitive to the normal modes of the Moon within the 1 mHz - 1 Hz frequency band excited by GWs. An advantage compared to using the Earth as a GW observatory is the lower seismic activity of the Moon. Indeed, the absence of oceans and lower tidal activity increases the sensitivity of seismometers on the Moon to detect GWs.

The main seismic noise sources on the Moon include Moonquakes and meteoroid impacts. The latter has been shown to be below the targeted sensitivity of the experiment [147], while the annual rate of seismic energy release has been shown to be up to 8 orders of magnitude smaller than on Earth [170].

Pulsar Timing Arrays

An alternative method to detect GWs consists of using an array of pulsars. Pulsars are rapidly rotating neutron stars, whose rotation and magnetic axes are misaligned [185]. Because of this misalignment, one observes regular radio pulses on Earth coinciding with the moment that the magnetic axis of the rotating pulsar is aligned with the Earth. Due to the regularity of these pulses, pulsars can be thought of as astrophysical clocks. In fact, deviations in the time of arrival of these pulses is what is sought for in pulsar timing arrays (PTAs), as the passage of a GW would cause the times of arrival of pulses to deviate from their expected value.

Although conceptually simple, the PTA detection method does come with several real-life complications. A first difficulty in the analysis stems from the uncertainty in modelling the time of arrival of the pulses emitted by the pulsars. Typically, these timing models are captured by fits to data obtained from the pulsars themselves, e.g., rotational period and time evolution thereof. Since a fit that is completely independent of the pulsars is not possible, such model fits could unknowingly already contain a GW signal contribution [185].

In addition, PTA data are noisy, containing both white and red[10] noise. However, red common process spectra could mimic the presence of a GW signal. Nevertheless, all is not lost as an additional feature distinguishes the GW signal from other processes: the spatial correlation. In order to claim the detection of a GW signal, it is essential to observe a spatial correlation across the various pulsars caused by the passage of GWs. This spatial correlation is known as the Hellings and Downs correlation[11] [149] and is given by:

$$\Gamma(\xi_{ab}) = \frac{3}{2}\left(\frac{1-\cos\xi_{ab}}{2}\ln\frac{1-\cos\xi_{ab}}{2} - \frac{1}{6}\frac{1-\cos\xi_{ab}}{2} + \frac{1}{3}\right), \tag{1.45}$$

where ξ_{ab} denotes the angle in the sky between pulsar pairs. Long sought for in data obtained by PTA experiments, evidence for this correlation is finally emerging from the data. This will be discussed in more detail in Section 2.3.

Given the $\mathcal{O}(1)$ week duration between pulses, the datasets used by PTA experiments can get quite lengthy [185]. With total dataset durations of around ten years, PTAs are most sensitive in the 1-10 nHz frequency band[12]. Among the detectable sources in that frequency range

---

[10] Meaning coloured, i.e., with a non-trivial frequency dependence.

[11] This correlation will be illustrated in Figure 2.10 in Section 2.3.

[12] The corresponding frequencies can be obtained as the inverse of the dataset duration.

are super-massive binary black hole (SMBBH) mergers whose component masses are larger than 10^8 $M_\odot$. These would emit a continuous signal in the PTA frequency band over several thousands of years [185]. In addition, a gravitational-wave background (GWB)[13] sourced by cosmic strings or primordial GWs could also be detectable at the frequencies accessible by PTAs. More details about the possible signals at PTA experiments can be found in Section 2.3 of Chapter 2 and references therein.

A few examples of PTA collaborations are the North American Nanohertz Observatory of Gravitational Waves (NANOGrav) [198], the European Pulsar Timing Array (EPTA) [179], the Parkes Pulsar Timing Array (PPTA) [154], the Indian Pulsar Timing Array (InPTA) [209], the MeerTime Pulsar Timing Array [246], and the Chinese Pulsar Timing Array [177]. Several of these experiments join efforts in the detection of GWs in the International Pulsar Timing Array (IPTA) consortium [155]. Recently, strong evidence for a GWB[13] was reported by several of these collaborations. This will be discussed in more detail in Chapter 2.

1.3 Sources of Gravitational Waves

We end this chapter by giving an overview of several broad categories of GW sources, with an emphasis on the ones expected in the LVK frequency band: compact binary coalescences, bursts, continuous waves, and gravitational-wave backgrounds.

1.3.1 Compact Binary Coalescences

As seen in Section 1.1.4, a system with a non-vanishing time-varying quadrupole will emit GWs. A prime example of such systems is that of CBCs, in which two bodies orbit around each other. Examples include binary black holes (BBHs), binary neutron stars (BNSs), and neutron star black hole (NSBH) systems. As the two compact objects orbit around each other, the system will emit GWs. While GWs are emitted, the orbit reduces, bringing the two objects closer to each other (inspiral), until eventually, the two objects merge (merger). As the newly combined object settles (ringdown), GWs continue to be emitted. This is illustrated in Figure 1.8.

First Gravitational-Wave Detection

Although predicted over a century ago, the first evidence of the existence of GWs was first put forward in 1974 by Hulse and Taylor [160, 248]. Through the observation of the double neutron star system PSR B1913+16, they showed that the orbiting frequency of the system

---

[13] To be introduced later in Chapter 2.

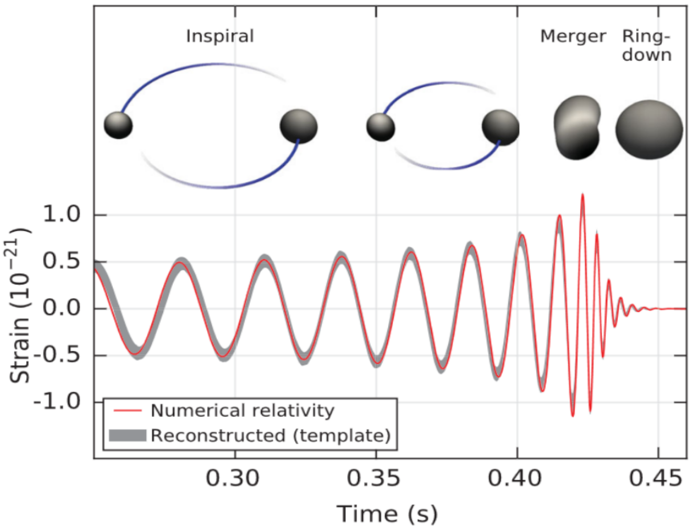

Figure 1.8. Representation of the different phases of a CBC event: inspiral, merger, and ringdown. The strain is the estimated GW strain amplitude from the first GW detection, GW150914, in the LIGO Hanford detector. Figure taken from [6].

increased over time, and that the two stars were spiralling towards each other. The orbit reduction corresponded exactly to the energy lost in GWs, as predicted by Einstein's theory of GR. This discovery marked the first indirect detection of GWs and was awarded the Nobel Prize in 1993 [213].

The direct detection of GWs emitted by a BBH system was only claimed four decades later, almost a century after originally predicted by Einstein. On September 14, 2015, the LIGO detectors observed a transient signal coming from the merger of two black holes at redshift $z = 0.09^{+0.03}_{-0.04}$ with masses $36^{+5}_{-4} M_\odot$ and $29^{+4}_{-4} M_\odot$, resulting in a black hole of mass $62^{+4}_{-4} M_\odot$[14] [6]. The event is illustrated in Figure 1.9. This first direct detection marked the start of GW astronomy, a new window to the Universe, with many more detections to follow.

The Population of Binary Black Holes Thus Far

The first direct detection of GWs was only the first of many, with a total number of ninety CBCs detected by the end of the third LVK observing run [15]. With the ongoing fourth LVK observing run, this number increases steadily, allowing for the study of the population of binaries throughout the Universe with increasing accuracy. In particular, the mass, redshift and spin distributions form the target of population studies such as the ones performed after the third observing run of the LVK collaborations [17]. For example, these results reveal a primary mass distribution that decreases with increasing primary mass, together with peaks at chirp masses[15]

---

[14] Uncertainties denote 90% credible intervals.

[15] The chirp mass is defined as $\mathcal{M} = \frac{(m_1 m_2)^{3/5}}{(m_1+m_2)^{1/5}}$, where m_i denotes the mass of the individual BBH.

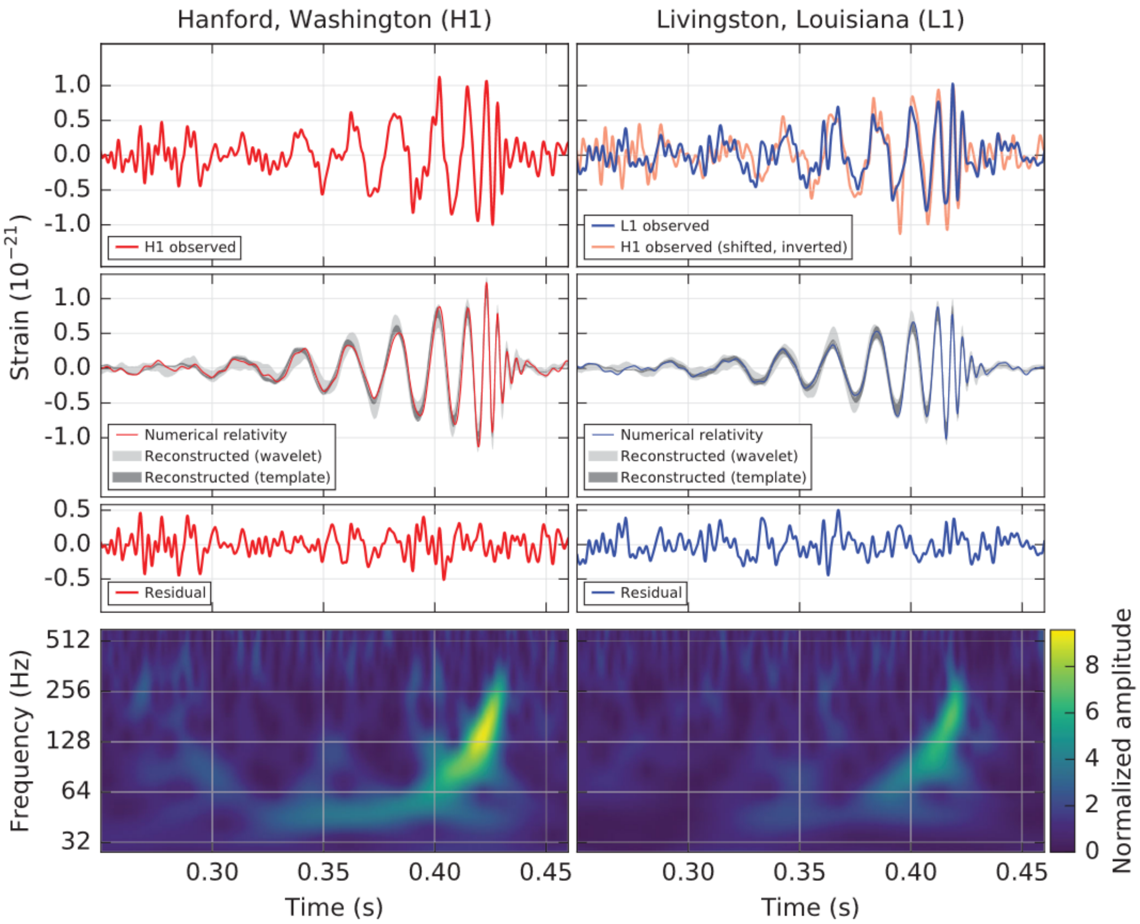

Figure 1.9. The first GW event GW150914 observed by the LIGO Hanford (H1, left column panels) and Livingston (L1, right column panels) detectors. Times are shown relative to September 14, 2015 at 09:50:45 UTC. **Top row, left**: H1 strain. **Top row, right**: L1 strain. GW150914 arrived first at L1 and $6.9^{+0.5}_{-0.4}$ ms later at H1; for a visual comparison, the H1 data are also shown, shifted in time by this amount and inverted (to account for the detectors' relative orientations). **Second row**: Gravitational-wave strain projected onto each detector in the 35-350 Hz band. Solid lines show a numerical relativity waveform for a system with parameters consistent with those recovered from GW150914. Shaded areas show 90% credible regions for two independent waveform reconstructions. **Third row**: Residuals after subtracting the filtered numerical relativity waveform from the filtered detector time series. **Bottom row**: A time-frequency representation of the strain data, showing the signal frequency increasing over time. Caption and figure taken from [6].

$8.3^{+0.3}_{-0.5}M_\odot$ and $27.9^{+1.9}_{-1.8}M_\odot$ emerging above the power-law behaviour of the mass distribution. In addition, the BBH merger rate is found to be between 17.9 Gpc^{3}yr^{-1} and 44 Gpc^{3}yr^{-1} at a redshift $z = 0.2$. In fact, the BBH merger rate increases with redshift at $z \lesssim 1$ as $(1+z)^\kappa$, with $\kappa = 2.9^{+1.7}_{-1.8}$, consistent with the Madau-Dickinson star formation rate at low redshifts[16] [188]. In addition, BBH spin measurements form an interesting quantity to measure as they

---

[16] Note that this is not expected across all redshifts due to the time delay between star formation and binary merger. For more details about the time delay, see Chapter 4.

might provide hints about the formation and evolution of merging binaries [125, 136, 228]. Observed spin magnitudes are small, with evidence for negatively aligned spins and misalignment of spins relative to the orbital angular momentum of the binary. Furthermore, correlation between the mass ratio and the spin is found in the data, where more unequal mass ratios give rise to larger spin magnitudes.

As the number of detected CBC events increases, the properties of the binary population will be measured more accurately, uncovering the features hidden in the various distributions. Furthermore, detectors with better sensitivities will allow for an exploration deeper into the Universe, resolving an even larger part of the CBC population[17].

1.3.2 Bursts

Another category of signals searched for by the LVK collaborations are bursts of GWs, which are transient GW signals with a typical duration of less than a second [190]. Usually associated with the sudden release of a large amount of GW energy, these signals do not obey a clean waveform as the CBCs introduced above. Examples of bursts include cosmic strings across the whole frequency range[18] [12, 98] or supernova explosions in the Hz-kHz range [190]. Although GW bursts have escaped detection until this day, the efforts by the LVK collaborations to detect such bursts over the years are discussed in [7–9, 11].

1.3.3 Continuous Waves

Sources of continuous waves emit GWs almost mono-chromatically, and do so for a long period of time. Astrophysical objects displaying some spherical asymmetry are one of the main contributors to this category, with neutron stars as a concrete example. The long GW emission times permit long observing times of the sources, which allows to integrate the signal over time, thereby increasing the sensitivity to weak signals. Despite ongoing efforts within the LVK collaborations, this type of signal remains to be detected. More details on the topic can be found in [190], with an overview of searches performed by the LVK collaborations in [202].

---

[17] As we await the better sensitivity of next-generation detectors, we discuss a method to probe some of the population properties at larger redshifts in Chapter 4, and more specifically, the BBH merger rate.

[18] The frequency of GWs emitted by cosmic strings can be related to the energy scale of the symmetry breaking when strings are formed [75]. A similar phenomenon will be discussed in Chapter 5 in the context of first order phase transitions.

1.3.4 Gravitational-Wave Backgrounds

An additional category can be distinguished: the gravitational-wave background [230]. Coming from the superposition of many faint, unresolved GWs, this background is expected to contain a wealth of information about the sources that generated it. Among these sources are several astrophysical ones such as weak GWs from CBCs, core collapse supernovae, but many cosmological processes could have contributed to the background as well: inflation, first order phase transitions, cosmic strings, domain walls, ...[19] The former contribution is referred to as the astrophysical GWB, whereas the latter as the cosmological GWB. Both contributions to the GWB are at the center of this work and will be discussed in the remainder of this thesis. The next chapter is dedicated to the GWB, and will review the most important aspects governing the theory of GWBs.

---

[19] See Ref. [68, 75] for a complete overview of possible cosmological sources.

2 GRAVITATIONAL-WAVE BACKGROUND

> The subconscious is ceaselessly murmuring, and it is by listening to these murmurs that one hears the truth.
>
> Gaston Bachelard

In addition to individually detectable GW events as currently detected by the LVK collaborations, a GWB is expected to arise from the superposition of many unresolvable GW events. Many astrophysical sources, such as faint BBH and BNS mergers, contribute to an astrophysical GWB. Furthermore, a plethora of early Universe events could have contributed to a cosmological GWB, including first order phase transitions[1], domain walls[2], inflation and cosmic strings[3]. Both contributions therefore contain invaluable information about the population of GW sources in the Universe and the processes happening in its very early stages. Hence, the detection of a GWB will provide a wealth of information and truly represents the holy grail of GW physics.

In this chapter we review the formalism used to describe the GWB. We introduce the concept of a cross-correlation statistic in order to extract the GWB signal from noisy detector data, and discuss the generalisations needed to account for the non-trivial geometry of the detectors. Additionally, we provide a review of helpful tools for the enthusiastic GWB data analyst, covering power-law integrated sensitivity curves, Bayesian inference, and an open source GWB analysis code, `pygwb` [222, 223]. We end this chapter with a review of the current constraints on the GWB.

This chapter is partially based on a review paper in collaboration with Kamiel Janssens, and Nick van Remortel [221]. Furthermore, aspects of work in collaboration with Arianna Renzini, Alba Romero-Rodriguez, Colm Talbot, Max Lalleman, Shivaraj Kandhasamy, et al. are also used in this chapter [222, 223].

---

[1] This forms the topic of Chapter 5.

[2] Domain walls are not part of this thesis, but were studied during the timeline of the PhD in [61].

[3] See Ref. [68, 75] for a complete overview of possible cosmological sources.

2.1 Theoretical Introduction

In this first section, we review the formalism and techniques used to describe the GWB. Starting with a general introduction to the GWB, we then elaborate on this to introduce various concepts related to the GWB and the effect of detector geometry on a GWB search. We end this section by introducing a so-called optimal estimator for the GWB signal, as used by the LVK collaborations [19]. This section is based on [230].

2.1.1 Introduction

Coming from the superposition of many unresolvable signals, the GWB is, by definition, a very weak signal that cannot be distinguished from noise in the data stream of a single detector. However, as the GWB permeates the Universe, the GWB will be present in multiple detectors, offering a possibility to distinguish it from detector noise through cross-correlation of data across detectors. Schematically, one can represent the data from two GW interferometers as:

$$s_1 = n_1 + h \tag{2.1}$$

$$s_2 = n_2 + h, \tag{2.2}$$

where the data s_I are composed of noise n_I and a GW signal h. Conceptually, looking at the cross-correlation of the two data streams, one obtains:

$$\begin{aligned} C &\sim \langle s_1 s_2 \rangle \\ &\sim \langle (n_1 + h)(n_2 + h) \rangle \\ &\sim \left\langle h^2 \right\rangle + \langle n_1 h \rangle + \langle n_2 h \rangle + \langle n_1 n_2 \rangle \\ &\sim \left\langle h^2 \right\rangle . \end{aligned} \tag{2.3}$$

The second and third terms vanish as the GW signal is not correlated with the noise in each of the detectors, whereas the last term vanishes under the assumption of uncorrelated noise between the detectors[4]. The above cross-correlation computation schematically illustrates how data from multiple detectors can be used to extract the GWB, despite its inherently weak nature. This simple, yet effective, idea will be at the core of the techniques discussed in the remainder of this section. Before formalising this concept, we comment on a few additional properties of the background.

---

[4] At current detector sensitivity, this is a valid assumption. However, with the increasing sensitivity of the interferometers, so-called Schumann resonances might form a non-negligible source of correlated noise, as discussed in [162, 163].

Properties and assumptions

Although some of these assumptions can be relaxed, the remainder of this chapter will assume that the GWB is: isotropic, unpolarised, stationary, and Gaussian.

As the background comes from the superposition of faint sources throughout the Universe, the assumption of isotropy will hold to a first approximation. Analogously, also the Cosmic Microwave Background (CMB) is isotropic to a first approximation, only revealing anisotropies on very small scales [24]. We note that dedicated searches for anisotropies exist within the LVK collaborations, as reviewed in [221, 230], for which results are presented in [18]. However, this type of search goes beyond the scope of this work and will therefore not be touched upon.

In addition, we will assume that the GWB is unpolarised, meaning that both + and × polarisations, as first introduced in Eq. (1.35), are statistically equally probable. However, the standard GWB search can easily be generalised to search for deviations from this assumption, as done by [195], for example.

Furthermore the background is assumed to be stationary, meaning the statistical quantities are only dependent on time differences, rather than on the choice of origin time. As the age of the Universe is much larger than the typical wave periods detectable by the LVK detectors, this is a realistic assumption.

Since the GWB comes from the superposition of many independent sources, the central limit theorem can be invoked to motivate the assumption of Gaussianity: the superposition of many statistically independent random variables is a Gaussian variable. As will be shown below, the GWB is completely characterised by a mean $\langle h_I(t)\rangle$ and a second-order moment $\langle h_I(t)h_J(t)\rangle$, where $h_I(t)$ denotes the strain in detector I.

As mentioned before, some of the above assumptions can be relaxed. However, we will assume here that all these hold true. For more information about these assumptions, we refer the reader to [230]. Keeping these in mind, we now proceed with the definition of the formalism to describe an isotropic, unpolarised, stationary, and Gaussian GWB.

2.1.2 Gravitational-Wave Background Formalism

We now formalise the general cross-correlation idea introduced in the previous section by first considering the metric perturbation defined in the previous chapter. Recall that GWs are the solution to the wave equation defined in Eq. (1.29), and can therefore be expressed as the superposition of plane waves:

$$h_{ab}(t,\vec{x}) = \int_{-\infty}^{\infty} df \int d^2\Omega_{\hat{n}} h_{ab}(f,\hat{n}) e^{2\pi i f(t+\hat{n}\cdot\vec{x}/c)}, \tag{2.4}$$

where f denotes the frequency, and $\hat{n}$ the direction on the sky, with associated solid angle $\Omega_{\hat{n}}$. Note that with the latter choice, the propagation direction of the GW is $\hat{k} = -\hat{n}$. The + and × polarisation tensors, as first introduced around Eq. (1.35), can be used to expand the coefficients $h_{ab}(f, \hat{n})$:

$$h_{ab}(f,\hat{n}) = h_{+}(f,\hat{n})e^{+}_{ab}(\hat{n}) + h_{\times}(f,\hat{n})e^{\times}_{ab}(\hat{n}), \tag{2.5}$$

where

$$e^{+}_{ab}(\hat{n}) = \hat{l}_a\hat{l}_b - \hat{m}_a\hat{m}_b, \tag{2.6}$$

$$e^{\times}_{ab}(\hat{n}) = \hat{l}_a\hat{m}_b + \hat{m}_a\hat{l}_b. \tag{2.7}$$

The vectors $\hat{n}$, $\hat{l}$, and $\hat{m}$ represent the spherical unit vectors, as depicted in Figure 2.1:

$$\hat{n} = \sin\theta\cos\phi\,\hat{x} + \sin\theta\sin\phi\,\hat{y} + \cos\theta\,\hat{z} = \hat{r}, \tag{2.8}$$

$$\hat{l} = \cos\theta\cos\phi\,\hat{x} + \cos\theta\sin\phi\,\hat{y} = \hat{\theta}, \tag{2.9}$$

$$\hat{m} = -\sin\phi\,\hat{x} + \cos\phi\,\hat{y} = \hat{\phi}. \tag{2.10}$$

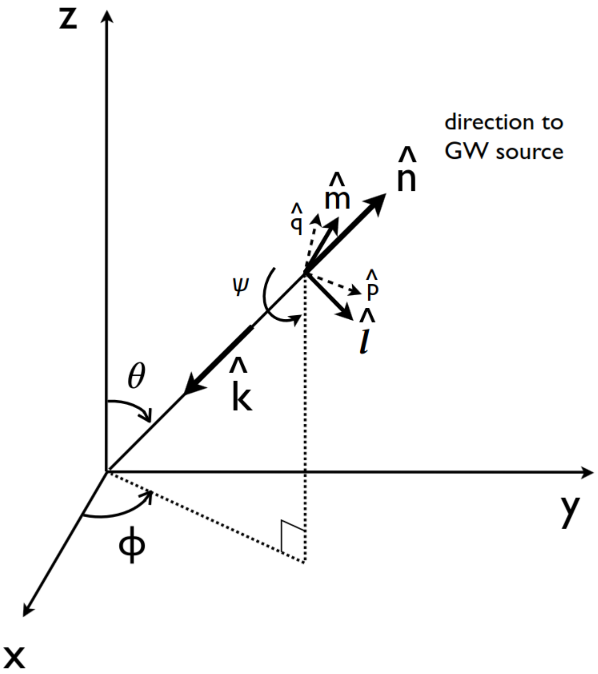

Figure 2.1. Illustration of the unit vectors $\hat{n}$, $\hat{l}$, and $\hat{m}$ that appear in the expressions for the polarisation basis tensors. The GW propagation direction is given by $\hat{k} = -\hat{n}$, where $\hat{n}$ points to the GW source. The vectors $\hat{l}$ and $\hat{m}$ lie in a plane perpendicular to the unit vector $\hat{n}$. Figure taken from [230].

One of the assumptions about the properties of the GWB was that of Gaussianity. One recalls this means that the GWB can be completely characterised through its first two moments. Without loss of generality, the background can be assumed to have zero mean [230]:

$$\langle h_{ab}(t,\vec{x})\rangle = 0 \iff \langle h_A(f,\hat{n})\rangle = 0, \tag{2.11}$$

where $A = \{+,\times\}$ denotes the polarisation.

Keeping in mind all other assumptions as well, the quadratic expectation values for such a background, the so-called second-order moment, can then be written as:

$$\left\langle h_A(f,\vec{n})h^*_{A'}(f',\vec{n}')\right\rangle = \frac{1}{16\pi}S_h(f)\delta\left(f-f'\right)\delta_{AA'}\delta^2(\hat{n},\hat{n}'), \tag{2.12}$$

where the $\delta^2(\hat{n},\hat{n}')$ enforces isotropy, $\delta_{AA'}$ reflects the fact that polarisation modes are statistically independent of each other and equally probable, and finally, the $\delta(f-f')$ results from the stationarity assumption. The function $S_h(f)$ is the one-sided strain PSD, as previously introduced in the context of the detector noise PSD in Eq. (1.41). Note that the above equation formalises the general cross-correlation idea first introduced at the beginning of this chapter, and more particularly in Eq. (2.3).

Instead of being represented in terms of the strain PSD, the GWB is usually reported in terms of the dimensionless energy density ratio:

$$\Omega_{\text{GW}}(f) = \frac{1}{\rho_c}\frac{d\rho_{\text{GW}}}{d\ln f}(f), \tag{2.13}$$

where the critical energy density of the Universe is given by $\rho_c = 3H_0^2c^2/(8\pi G)$, with $H_0 = 67.9$ km s^{-1} Mpc^{-1} the value of the Hubble parameter [212], c the speed of light, and G Newton's constant. The quantity $d\rho_{\text{GW}}$ is the GW energy density contained in the frequency interval $f + df$. To facilitate comparison with other content of the Universe, this can be integrated over the desired frequency range, resulting in:

$$\Omega_{\text{GW}} = \int_{f_{\min}}^{f_{\max}} d(\ln f)\Omega_{\text{GW}}(f), \tag{2.14}$$

where $f_{\min}$ ($f_{\max}$) denotes some minimum (maximum) frequency cut-off. Examples of this quantity for other contents in the Universe are $\Omega_B \simeq 4.4\%$ for baryons and $\Omega_{\text{DM}} = 22\%$ for dark matter [60]. Note that the dimensionless energy density ratio can be related to the previously introduced strain PSD through:

$$S_h(f) = \frac{3H_0^2}{2\pi^2}\frac{\Omega_{\text{GW}}(f)}{f^3}. \tag{2.15}$$

The above defined the formalism in which GWBs can be formulated and highlights $\Omega_{\mathrm{GW}}(f)$ as the quantity of interest in GWB searches. We now go a step further by considering the detector geometry and its response to the GW signal, and modify the expression for the cross-correlation accordingly.

2.1.3 Detector Response and Overlap Reduction Function

The strain measured by the interferometer will be influenced by how the instrument "sees" the metric perturbation induced by GWs. For a realistic detector configuration, the strain of the detector can be written as the convolution of the detector impulse response $R^{ab}(t,\vec{x})$ and the metric perturbations $h_{ab}(t,\vec{x})$:

$$h(t) = (\mathbf{R} * \mathbf{h})(t,\vec{x}) = \int_{-\infty}^{\infty} d\tau \int d^3y R^{ab}(\tau,\vec{y}) h_{ab}(t-\tau,\vec{x}-\vec{y}), \tag{2.16}$$

where $\vec{x}$ denotes the measurement location at time t. Substituting the plane-wave expansion previously introduced in Eq. (2.4), one obtains

$$h(t) = \int_{-\infty}^{\infty} df \int d^2\Omega_{\hat{n}} R^{ab}(f,\hat{n}) h_{ab}(f,\hat{n}) e^{2\pi i f t}, \tag{2.17}$$

which, once Fourier-transformed, takes the form:

$$\tilde{h}(f) = \int d^2\Omega_{\hat{n}} R^{ab}(f,\hat{n}) h_{ab}(f,\hat{n}). \tag{2.18}$$

The Fourier-transformed impulse response of the detector $R^{ab}(f,\hat{n})$ in the expression above is given by:

$$R^{ab}(f,\hat{n}) = e^{2\pi i f \hat{n}\cdot\vec{x}/c} \int_{-\infty}^{\infty} d\tau \int d^3y R^{ab}(\tau,\vec{y}) e^{-2\pi i f(\tau+\hat{n}\cdot\vec{y}/c)}. \tag{2.19}$$

Considering the polarisation basis with coefficients $h_+(f,\hat{n})$ and $h_\times(f,\hat{n})$ defined in Eq. (2.5), Eq. (2.18) can be rewritten as

$$\tilde{h}(f) = \int d^2\Omega_{\hat{n}} \sum_A R^A(f,\hat{n}) h_A(f,\hat{n}), \tag{2.20}$$

where

$$R^A(f,\hat{n}) = R^{ab}(f,\hat{n}) e^A_{ab}(\hat{n}). \tag{2.21}$$

We recall that the quantity of interest in GWB data analysis is the cross-correlation of strain data between two detectors. Considering the above discussion allows us to revise the expression for the cross-correlation of the data from an interferometer baseline IJ, as previously defined in Eq. (2.12). This is now modified as follows:

$$\left\langle h_I(t)h_J(t')\right\rangle = \frac{1}{2}\int_{-\infty}^{\infty} df\, e^{2\pi i f(t-t')}\Gamma_{IJ}(f)S_h(f), \tag{2.22}$$

where Γ_{IJ} encodes the geometry of the detector baseline IJ:

$$\Gamma_{IJ}(f) = \frac{1}{8\pi}\int d^2\Omega_{\hat{n}} \sum_A R_I^A(f,\hat{n})R_J^{A*}(f,\hat{n}). \tag{2.23}$$

Often, a normalised overlap reduction function (ORF) is defined, such that $\gamma_{IJ}(0) = 1$ for co-aligned and co-located detectors:

$$\gamma_{IJ}(f) = \frac{5}{\sin^2\beta}\Gamma_{IJ}(f), \tag{2.24}$$

where β denotes the opening angle between the two arms of an equal-arm Michelson interferometer (e.g., $\pi/2$ for LIGO). This function is illustrated in Figure 2.2 for different detector baselines.

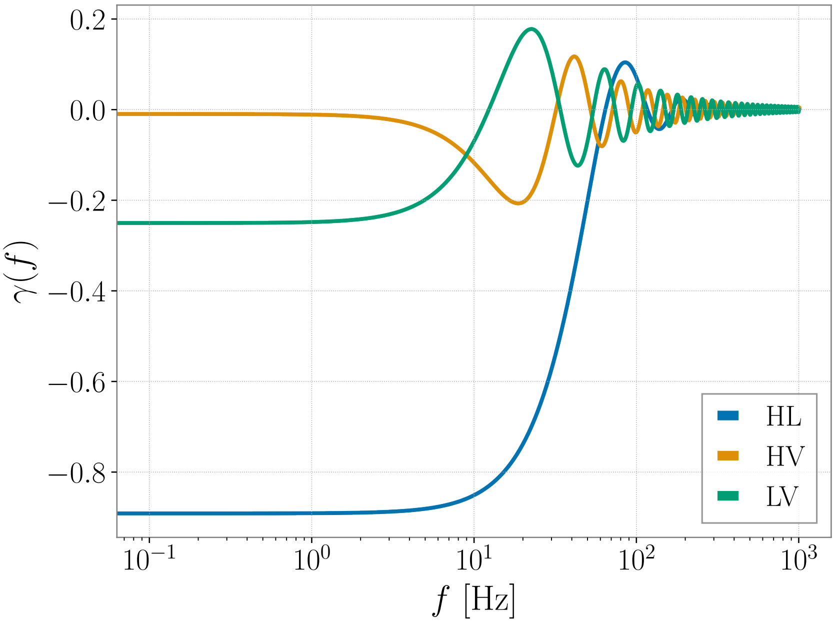

Figure 2.2. Overlap reduction function $\gamma(f)$ for the LIGO Hanford and LIGO Livingston detector baseline (HL, blue), LIGO Hanford and Virgo baseline (HV, orange), and the LIGO Livingston and Virgo baseline (LV, green).

Alternatively, Eq. (2.22), can be written in the Fourier domain as:

$$\left\langle \tilde{h}_I(f)\tilde{h}_J^*(f')\right\rangle = \frac{1}{2}\delta(f-f')\Gamma_{IJ}(f)S_h(f), \tag{2.25}$$

clearly revealing the $\Gamma_{IJ}(f)$ factor in the cross-correlation expression previously introduced in Eq. (2.12).

Starting from the concept of cross-correlation of data from two detectors, we refined this idea to account for the geometry of the detector through the introduction of the ORF. The above expression forms the starting point for the next section, in which we define a cross-correlation estimator for the GWB.

2.1.4 Cross-Correlation Estimator and Optimal Filtering

We now want to apply the concepts introduced in the previous sections to extract an estimate of the GWB, described by an $\Omega_{\rm GW}(f)$ spectrum, from real detector data. To this end, we define a cross-correlation estimator as follows:

$$\hat{C}_{IJ}(f) = \frac{2}{T}\frac{\mathrm{Re}\left[\tilde{s}_I^\star(f)\tilde{s}_J(f)\right]}{\gamma_{IJ}(f)S_0(f)}, \tag{2.26}$$

where $\tilde{s}_I(f)$ denotes the Fourier-transformed data in detector I, T is the observation time[5], $\gamma_{IJ}(f)$ is the normalised ORF for the detector pair IJ as defined in Eq. (2.24), and $S_0(f) = 3H_0^2/(10\pi^2 f^3)$ allows to go from PSD to $\Omega_{\rm GW}$ units. Assuming there is no correlated noise between the detectors, this estimator is such that $\left\langle \hat{C}_{IJ}(f)\right\rangle = \Omega_{\rm GW}(f)$. The associated variance is given by

$$\sigma_{IJ}^2(f) \approx \frac{1}{2T\Delta f}\frac{P_I(f)P_J(f)}{\gamma_{IJ}^2(f)S_0^2(f)}, \tag{2.27}$$

where the small signal-to-noise ratio (SNR) limit was assumed. The frequency resolution is denoted by Δf, and $P_I(f)$ denotes the one-sided PSD of detector I.

From the above quantities, one can construct an optimal[6] estimator given any spectral shape of the GWB spectrum. This is done by combining the various spectra and applying some form of appropriate weighting given by some function $w(f)$:

$$\hat{C}_{IJ} = \frac{\sum_k w(f_k)\hat{C}_{IJ}(f_k)\sigma_{IJ}^{-2}(f_k)}{\sum_k w(f_k)^2\sigma_{IJ}^{-2}(f_k)}, \tag{2.28}$$

---

[5] In practice, the data are split into smaller analysis segments and recombined using the same inverse noise weighting approach as shown in Eq. (2.32) for combining the different baselines [19, 230].

[6] "Optimal" in the sense that it maximises the SNR. More information regarding the optimal filtering can be found in [35, 230].

and

$$\sigma_{IJ}^{-2} = \sum_k w(f_k)^2 \sigma_{IJ}^{-2}(f_k), \tag{2.29}$$

where the sum runs over the frequency bins f_k. The weights[7] $w(f)$ are defined as follows:

$$w(f) = \frac{\Omega_{\mathrm{GW}}(f)}{\Omega_{\mathrm{GW}}(f_{\mathrm{ref}})}, \tag{2.30}$$

where $\Omega_{\mathrm{GW}}(f)$ is the assumed spectral shape to obtain the optimal estimator, and the reference frequency f_{ref} is usually taken to be 25 Hz in LVK GWB searches, although this is an arbitrary choice[8].

Note that many GWBs are predicted to follow a power law in the frequency band of the LVK instruments[9]. For example, the background from unresolved CBCs is expected to follow a 2/3 power law, the spectrum from core collapse supernovae will display a spectrum with a spectral index $\alpha = 3$, and cosmic strings are predicted to have a flat spectrum in the LVK frequency range [19]. A common choice for the optimal weights therefore assumes a power-law spectrum:

$$\Omega_{\mathrm{GW}}(f) = \Omega_{\mathrm{ref}} \left(\frac{f}{f_{\mathrm{ref}}} \right)^{\alpha}, \tag{2.31}$$

where Ω_{ref} is the value of the $\Omega_{\mathrm{GW}}(f)$ spectrum at a reference frequency f_{ref}, and α is the spectral index.

Finally, one can construct an overall, optimally weighted point estimate and variance for the whole network of interferometers by summing over detector baselines IJ:

$$\hat{C} = \frac{\sum_{IJ} \hat{C}_{IJ} \sigma_{IJ}^{-2}}{\sum_{IJ} \sigma_{IJ}^{-2}}, \qquad \sigma^{-2} = \sum_{IJ} \sigma_{IJ}^{-2}. \tag{2.32}$$

The previous section established the necessary theoretical background to be able to perform a GWB analysis. Starting from the simple idea of cross-correlation, we constructed an optimal cross-correlation estimator for the GWB. This cross-correlation estimator forms the target quantity to compute in LVK GWB searches. We now slightly switch gears and review a few tools that are useful within the context of GWB data analysis.

---

[7] In practice, the weights can be obtained by maximising the SNR, after which a dependence on the assumed underlying $\Omega_{\mathrm{GW}}(f)$ spectrum itself would become apparent [35, 230].

[8] This choice approximately corresponds to the start of frequency region where the isotropic search with LVK instruments is most sensitive [19].

[9] An example of different GWB spectra following a broken power law will be introduced in Chapter 5 in the context of first order phase transitions.

2.2 A Gravitational-Wave Background Analysis Toolbox

This section provides a few helpful tools for GWB data analysis. We review the concept of power-law integrated (PI) sensitivity curves, explain the basics of Bayesian inference and provide some additional information about an open source GWB analysis package: `pygwb`.

2.2.1 Power-Law Integrated Sensitivity Curves

The PI sensitivity curves address the need for a quick, graphical tool that predicts whether a GWB spectrum is potentially detectable by a given set of detectors. As this formalism is widely used within the community, as well as within this thesis, the method to construct such curves is outlined below. The review of the method closely follows [250], where the formalism was first proposed.

To construct a PI curve, one starts with the noise PSDs of the detectors, $P_{nI}(f)$ and $P_{nJ}(f)$, as defined in Eq. (1.41), as well as the ORF $\Gamma_{IJ}(f)$, which encodes the geometry of the detector baseline, as previously introduced in Eq. (2.23). These serve as ingredients to compute the effective strain PSD $S_{\rm eff}(f)$ for M detectors:

$$S_{\rm eff}(f) = \left(\sum_{I=1}^{M} \sum_{J>I}^{M} \frac{\Gamma_{IJ}^2(f)}{P_{nI}(f) P_{nJ}(f)} \right)^{-1/2}, \tag{2.33}$$

which can be converted into an effective dimensionless energy density $\Omega_{\rm eff}(f)$ using Eq. (2.15). Containing both the ORF and the noise PSDs, the effective strain PSD captures the sensitivity of the whole detector network. The SNR of the network can be constructed as follows:

$$\rho = \sqrt{2T} \left(\int_{f_{\rm min}}^{f_{\rm max}} df \, \frac{S_h^2(f)}{S_{\rm eff}^2(f)} \right)^{1/2}, \tag{2.34}$$

where the GW strain power $S_h(f)$ was introduced in Eq. (2.25) and can once again be translated in terms of Ω units using Eq. (2.15). Assuming an observing time T and a reference frequency $f_{\rm ref}$[10], one can compute the value of the amplitude Ω_β of a power-law GWB with spectral index β such that the integrated SNR reaches some fixed threshold value $\rho^{\rm thr}$:

$$\Omega_\beta = \frac{\rho^{\rm thr}}{\sqrt{2T}} \left(\int_{f_{\rm min}}^{f_{\rm max}} df \, \frac{(f/f_{\rm ref})^{2\beta}}{\Omega_{\rm eff}^2(f)} \right)^{-1/2}. \tag{2.35}$$

---

[10] The choice of $f_{\rm ref}$ is arbitrary and does not affect the PI sensitivity curve.

This is repeated for a series of power-law spectral indices, e.g., $\beta \in \{-10, \ldots, 10\}$, after which each of the $\Omega_{\rm GW}(f) = \Omega_\beta (f/f_{\rm ref})^\beta$ can be plotted. The envelope[11] of the curves forms the PI sensitivity curve for a correlation measurement between the detectors. Mathematically, one can express this envelope as:

$$\Omega_{\rm PI}(f) = \max_\beta \left(\Omega_\beta \left(\frac{f}{f_{\rm ref}} \right)^\beta \right). \tag{2.36}$$

Graphically, the PI sensitivity curve can be used to make statements about the detectability of any power-law $\Omega_{\rm GW}(f)$. A spectrum tangent to the PI curve has an integrated SNR that corresponds to the threshold used during the construction of the PI curve. Any line above the PI curve has a SNR larger than the threshold, while the opposite is true for lines below the PI curve.

These PI curves are particularly useful when determining the detectability of a signal using future sensitivities of current or next-generation detectors. A few examples of PI curves are given in Figure 2.3 for the current and future sensitivities of the LVK detectors.

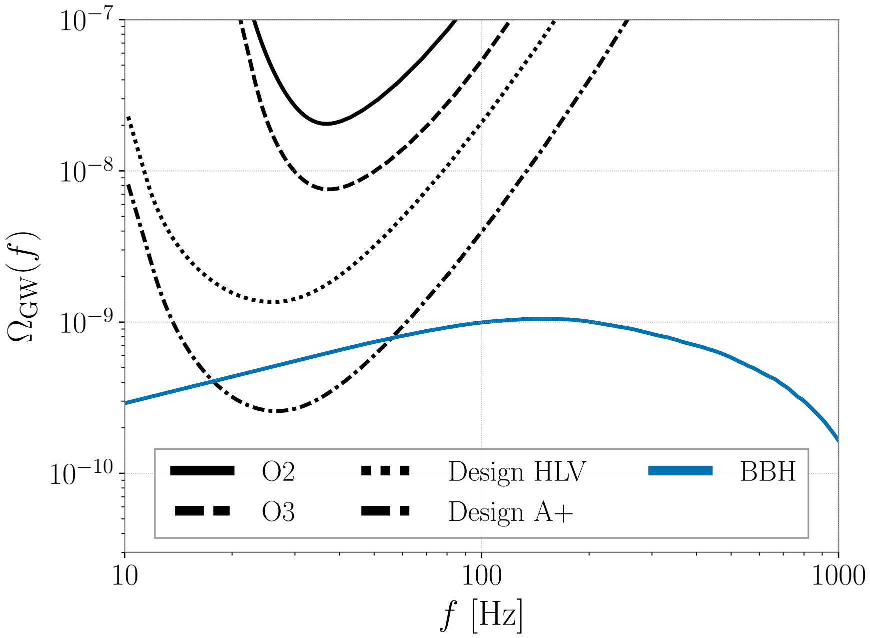

Figure 2.3. A few examples of 2σ PI curves at O2 (full) and O3 (dashed) sensitivities, as well as projections at design (dotted) and design A+ (dot-dashed) sensitivities of the LIGO-Virgo detectors assuming a one year observing time. In addition, the predicted BBH background is shown in blue. As it intersects with the Design A+ PI curve, the BBH should have a SNR above the detectability threshold at that sensitivity. Figure adapted from [19].

---

[11] See [250] for a visual representation of this.

2.2.2 Bayesian Inference

We now move to another useful framework when performing GWB analyses, and specifically when trying to infer the value of certain model parameters: Bayesian inference[12] [230, 251]. At the center of the method lies Bayes' theorem:

$$p(\boldsymbol{\Theta}|d) = \frac{\mathcal{L}(d|\boldsymbol{\Theta})p(\boldsymbol{\Theta})}{p(d)}, \tag{2.37}$$

where $\boldsymbol{\Theta}$ represents the parameters of the model, and d the GW data, e.g., the cross-correlation statistic introduced in Eq. (2.26). This theorem allows us to go from the likelihood of observing data d given a set of parameters $\boldsymbol{\Theta}$, to the probability distribution on these parameters given the observed data, which is ultimately what we are interested in.

The likelihood of observing data d, given a set of parameters $\boldsymbol{\Theta}$ is given by the likelihood function $\mathcal{L}(d|\boldsymbol{\Theta})$. For GWB searches, the likelihood is approximately Gaussian, and takes the form

$$\mathcal{L}\left(\hat{C}_{IJ}|\boldsymbol{\Theta}\right) \propto \exp\left(-\frac{1}{2}\sum_{IJ}\sum_{k}\left(\frac{\hat{C}_{IJ}(f_k)-\Omega_M(f_k|\boldsymbol{\Theta})}{\sigma_{IJ}(f_k)}\right)^2\right), \tag{2.38}$$

where $\hat{C}_{IJ}(f_k)$ is the cross-correlation estimator evaluated at frequency bin f_k, with associated variance $\sigma^2_{IJ}(f_k)$, introduced in Eqs. (2.26) and (2.27), respectively. The sums in the above expression run over frequency bins f_k and baselines IJ. The function $\Omega_M(f_k|\boldsymbol{\Theta})$ is the model for $\Omega_{\rm GW}(f)$ one is interested in, given some model parameters $\boldsymbol{\Theta}$. A concrete model choice is that of the previously mentioned power-law $\Omega_{\rm GW}(f)$ spectrum, although more complicated models can be used as well, as will be shown in the remaining chapters of the thesis.

In addition, one needs to specify the prior $p(\boldsymbol{\Theta})$, which parameterizes the prior knowledge about the parameters. For example, in LVK GWB searches, it is common to assume a uniform or log-uniform prior on the amplitude of the power-law GWB spectrum $\Omega_{\rm ref}$ as defined in Eq. (2.31) [19].

The quantity $p(d)$ is called the model evidence, and is usually regarded as an overall normalisation factor:

$$p(d) = \int \mathcal{L}(d|\boldsymbol{\Theta})p(\boldsymbol{\Theta})d\boldsymbol{\Theta}. \tag{2.39}$$

Finally, the full posterior $p(\boldsymbol{\Theta}|d)$ can be obtained through Bayes' theorem given in Eq. (2.37). However, in practice, one could be interested in the posterior for a specific parame-

---

[12] Throughout this work, "Bayesian inference" and "parameter estimation" will be used interchangeably to denote the same concept.

ter Θ_i, in which case one can marginalise over the other parameters:

$$p(\Theta_i|d) = \int d\mathbf{\Theta}\ p(\Theta_i, \mathbf{\Theta}|d) = \int d\mathbf{\Theta}\ p(\Theta_i|\mathbf{\Theta}, d)p(\mathbf{\Theta}). \tag{2.40}$$

This is often the case in so-called posterior corner plots, where each plot denotes the posterior on two parameters at a time, or marginalised over all but one parameter, as will be seen in later sections.

In practice, the above Bayesian inference framework is implemented in codes using Markov-Chain Monte-Carlo algorithms. Examples of such codes are `bilby` [43] with its `dynesty` sampler [245], as well as `numpyro` [210], although many alternatives exist. For additional information on Bayesian inference, especially in the context of GW data analysis, we refer the reader to the comprehensive review in [251].

Credible intervals and upper limits

Bayesian inference can be used to determine credible intervals and credible upper limits, which allow to make statements about the values and associated uncertainties on the inferred parameters.

Credible intervals are usually determined when a parameter can sufficiently be constrained. Formally, the $X\%$ credible interval can be defined as[13]:

$$\text{Prob}(a_{\text{mode}} - \Delta < a < a_{\text{mode}} + \Delta|d) = X\%. \tag{2.41}$$

For example, on the left-hand side of Figure 2.4, we show the 95% credible interval of parameter a.

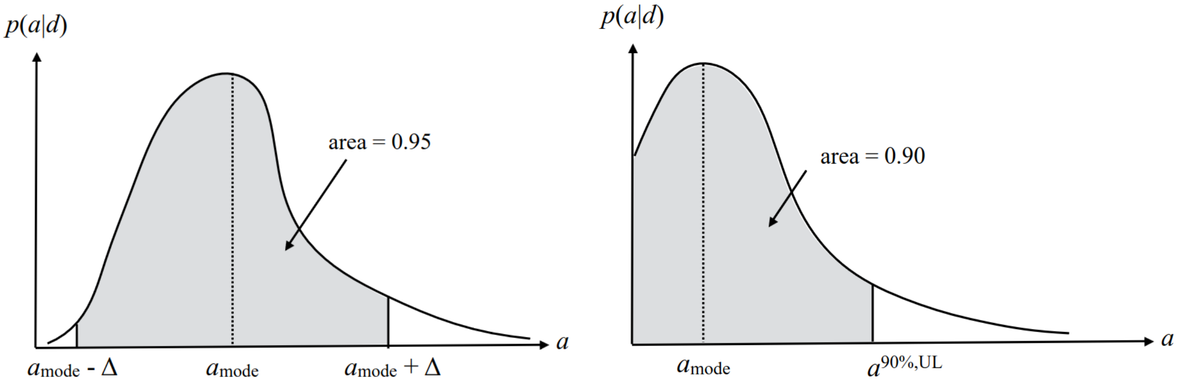

Figure 2.4. **Left**: Illustration of a Bayesian credible interval. The example features a symmetric 95% credible interval around the mode of the distribution. **Right**: Example of a 90% credible upper limit for a parameter a. Both figures are taken from [230].

---

[13] For a random variable, the mode of the distribution a_{mode} is the value of the parameter a that appears most often.

Credible upper limits on the other hand, are usually constructed when a parameter cannot be constrained away from its minimum value. Nevertheless, one can make statements about the $X\%$ upper limit, constructed as follows:

$$\text{Prob}(0 < a < a^{X\%,\text{UL}}|d) = X\%. \tag{2.42}$$

A visual representation of a credible upper limit is depicted in the right-hand side of Figure 2.4. Within the context of GWB searches for example, upper limits can be placed on the amplitude Ω_{ref} of the GWB spectrum in the absence of a detection, as will be illustrated in Section 2.3.

Model selection using Bayesian inference

A useful application of Bayesian inference is the ability to perform model selection using the Bayes factor:

$$\mathcal{B}_{\alpha\beta}(d) = \frac{p(d|\mathscr{M}_\alpha)}{p(d|\mathscr{M}_\beta)}, \tag{2.43}$$

where $p(d|\mathscr{M}_i)$ denotes the evidence, under the assumption that model $\mathscr{M}_i$ describes the data. Depending on the value of the Bayes factor, one can make statements about the evidence for model $\mathscr{M}_\alpha$ relative to model $\mathscr{M}_\beta$, as illustrated in Table 2.1 [230]. For example, one could consider $\mathscr{M}_\alpha$ to model a GWB signal and noise, versus $\mathscr{M}_\beta$ assuming only noise in the data. The Bayes factor associated to these models would then represent the evidence for having a signal and noise present in the data, rather than noise only.

Interpretation of Bayes factors	
$\mathcal{B}_{\alpha_\beta}(d)$	Evidence for model $\mathscr{M}_\alpha$ relative to $\mathscr{M}_\beta$
< 1	Negative (supports model $\mathscr{M}_\beta$)
$1 - 3$	Not worth more than a bare mention
$3 - 20$	Positive
$20 - 150$	Strong
> 150	Very strong

Table 2.1. Interpretation of Bayes factors as evidence for a model relative to another one. Table adapted from [230].

2.2.3 `pygwb`: a Python-Based Library for Gravitational-Wave Background Searches

The implementation of the analysis described in Section 2.1.4 can get quite involved from a programming point of view, with many intricacies along the computation. The `pygwb`[14] code addresses the need for a user-friendly GWB data analysis package [222, 223]. We briefly discuss some aspects of the package below, basing ourselves on original work [222, 223].

A Brief Overview

The `pygwb` package consists of several modules, each in charge of a specific task. A few examples of these tasks include the preprocessing of detector data, performing data quality cuts, the computation of PSDs and cross-spectral densities (CSDs), and computing the cross-correlation estimator and its variance, as defined in Eqs. (2.26) and (2.27). In addition, the code features a parameter estimation module, which can be used to perform Bayesian inference, as described in Section 2.2.2, with a series of pre-implemented GWB models at hand. Furthermore, it also allows model-builders to implement their favourite models and run parameter estimation on the output of a `pygwb` run. The package includes a simulator code, which gives the user the opportunity to simulate their own GWB signal, after which it can be readily analysed with the remainder of the `pygwb` code. Additionally, the package comes with a series of statistical checks which are used to determine the data quality of an analysis run. An overview of all the modules and their dependencies is given in Figure 2.5.

Before discussing the `parameter estimation` and `statistical checks` modules in a bit more detail in the next two subsections, we show some results of the `pygwb` package. Because of the modularity of the code, the different modules can be assembled into a pipeline that addresses the needs of the LVK collaborations – or any other user. As an example, we run `pygwb` on data from the third observing run of the LVK collaborations and reproduce the results of [19]. These are reported in Figure 2.6. In particular, we note agreement with the results presented in [19].

In addition, we employ the `simulator` module of `pygwb` to generate a GWB signal with a fixed PSD. This allows us to simultaneously test that module and the analysis pipeline as a whole. The injected GWB is scale-invariant, i.e., $\Omega_{\rm GW}(f)$ is constant over frequencies:

$$\Omega_{\rm inj}(f) = 1.06 \times 10^{-7}\,. \tag{2.44}$$

---

[14] A large amount of time during this PhD was dedicated to the development of the code and the documentation, as well as the maintenance of the `pygwb` package. More information about the package can be found in the online documentation: `https://pygwb.docs.ligo.org/pygwb/`.

Additional noise is injected on top of the GWB signal, which is taken to be Gaussian, coloured using the the Advanced LIGO noise PSD [88]. One hundred days of consecutive data are simulated. Each of the one hundred days is analysed separately, and we recover a distribution of $\hat{C}$ point estimates, previously defined in Eq. (2.28), using a power law for the optimal weights with $\alpha = 0$ and $f_{\mathrm{ref}} = 25$ Hz in the pipeline. These are shown in Figure 2.7 (left). Analysing one hundred days separately allows us to construct a distribution of recovered point estimates, which is useful to assess the ability of the `simulator` module to inject a GWB signal correctly. We perform parameter estimation on the combined one hundred days, presented in Figure 2.7 (right). We assume a log-uniform prior from 10^{-11} to 10^{-6} for Ω_{ref} and a Gaussian prior with mean 0 and standard deviation 1.5 for α. This shows a recovery within 1σ for Ω_{ref} and within 2σ for the spectral index α.

The tests above illustrate that the `simulator` module is able to successfully inject a GWB signal and that the `pygwb` pipeline is able to recover this injection.

Parameter Estimation

As parameter estimation and Bayesian inference were already extensively discussed in Section 2.2.2, we remain brief in the description of the module.

Parameter estimation in the `pygwb` package is based on the `bilby` Bayesian inference package [43] , and relies on the `dynesty` package [245] for the sampling. Therefore, it inherits all the functionalities of these packages, for which we refer the interested reader to the original documentation. Furthermore, it forms an integral part of the code, which naturally follows the computation of the optimal estimator of the GWB. This is a notable improvement compared to previous LVK analyses, where data products and parameter estimation were handled independently by packages in different programming languages [222, 223].

An example of the typical output of the `parameter estimation` module is presented in the right-hand side of Figure 2.7 for the one hundred day dataset described above. This shows the two-dimensional posterior distribution on the parameters Ω_{ref} and α, with the marginalised posteriors shown as histograms for each of the parameters. For more information on these concepts, we refer the reader to the discussion on parameter estimation in Section 2.2.2.

In addition, we want to highlight a particularly useful feature of the module: it allows to combine two models and infer the parameters of both models jointly. A concrete application of this could be the joint inference of a cosmological GWB in the presence of an astrophysical GWB, where $\Omega_M(f) = \Omega_{\mathrm{CBC}}(f) + \Omega_{\mathrm{COS}}(f)$ in Eq. (2.38). This joint inference could also be useful to estimate the GWB in the presence of correlated magnetic noise, where $\Omega_M(f) = \Omega_{\mathrm{CBC}}(f) + \Omega_{\mathrm{MAG}}(f)$ in Eq. (2.38). More information on the analysis of magnetic noise in the LVK GWB search during the third observing run can be found in [19].

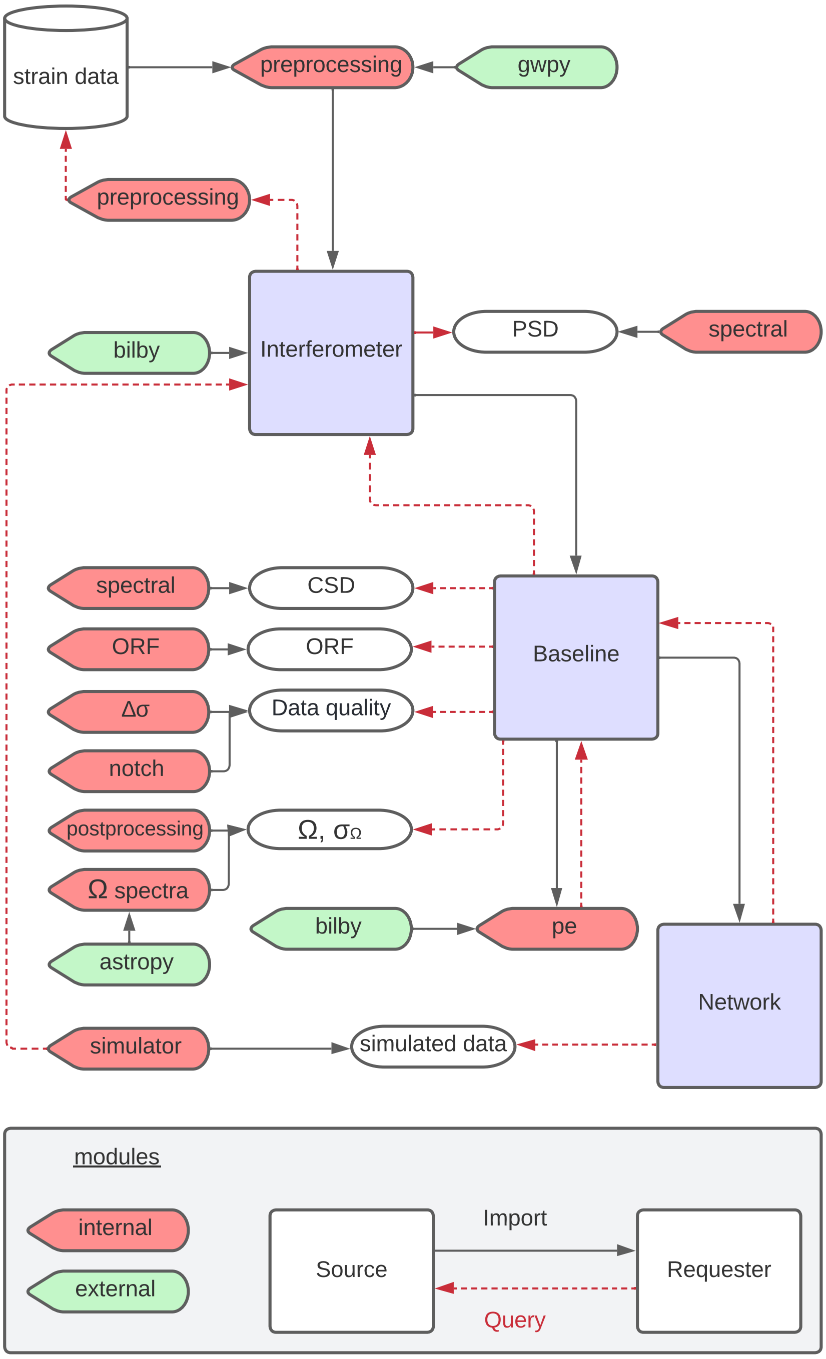

Figure 2.5. Schematic overview of the `pygwb` analysis flow. In blue squares, we show the manager objects of the code that handle the analysis internally. These manager objects query (red arrows) different modules for specific objects, calculations, or quantities (rounded bubbles), imported (grey arrows) by either internal (i.e., within `pygwb`) or external modules (i.e., outside of `pygwb`). Internal modules are indicated in red, while external modules are indicated in green. Figure and caption taken from [222, 223].

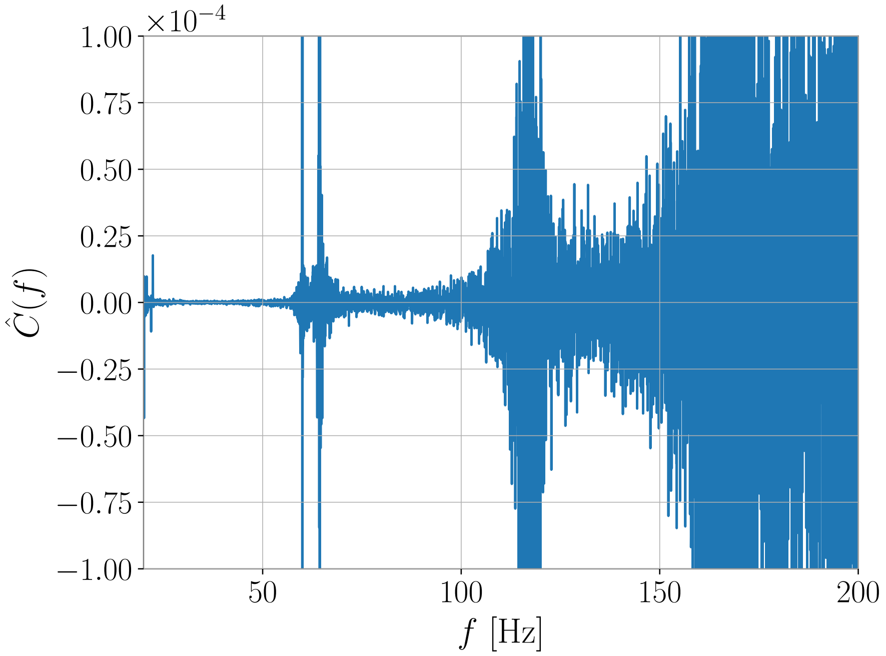

Figure 2.6. Estimated cross-correlation measurement of $\Omega_{\rm GW}(f)$ for the LIGO Hanford and LIGO Livingston baseline using data from the third LVK observing run (for details, see [222, 223]). Figure adapted from [222, 223].

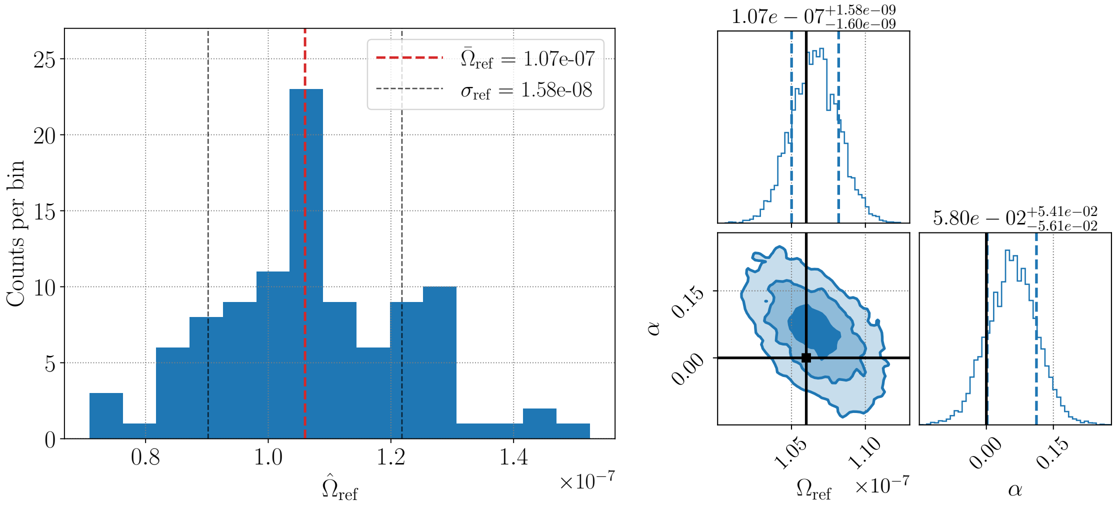

Figure 2.7. **Left**: Distribution of the recovered point estimate for each day in the dataset. The injected value is denoted by the red line. $\overline{\Omega}_{\rm ref}$ and $\sigma_{\rm ref}$ denote the mean and the standard deviation of the one hundred point estimates. **Right**: Parameter estimation performed on the combined one hundred days, obtained assuming a log-uniform prior from 10^{-11} to 10^{-6} for $\Omega_{\rm ref}$ and a Gaussian prior with mean 0 and standard deviation 1.5 for α. The injected values are denoted by the black lines, while the contours represent the 1σ, 2σ, and 3σ contours. The vertical dashed lines represent the 1σ confidence interval. Figure and caption taken from [222, 223].

Statistical Checks

With the `statistical checks` module, the package provides a tool to perform initial statistical analyses of a `pygwb` run result set, and visualise them in pre-formatted plots. In fact, this module is actively used for initial monitoring of the data quality of the ongoing fourth LVK observing run. Several categories of statistical checks can be distinguished:

- An important quantity for GWB searches is the SNR. In particular, one can look at the SNR as a function of frequency to gauge where most of the sensitivity of the search is coming from. The SNR spectrum is defined as

  $$\mathrm{SNR}(f) = \frac{\hat{C}(f)}{\sigma(f)}, \tag{2.45}$$

  where $\hat{C}(f)$ and $\sigma(f)$ are defined in Eqs. (2.26) and (2.27), respectively. An example of these plots can be found in [222, 223]. These plots are a faithful representation of the "noisiness" of each frequency bin and how much each bin contributes to the analysis.
- A visual representation of quantities as a function of time, while the amount of analysed data increases, is very interesting to consider. For example the point estimate defined in Eq. (2.28) or the variance in Eq. (2.29) can be visually represented as a function of time. The visualisation of running quantities is extremely useful to identify trends in the data, and ultimately will flag a possible detection. An example of these plots is given in Figure 2.8.

- The effect of the $\Delta\sigma$ data quality cut on the analysis run is investigated as well. This cut is designed to flag any non-stationarities in the data by comparing the noise in neighbouring analysis segments, as captured by the σ in Eq. (2.29). Schematically, an analysis segment will be flagged as "bad" when

  $$\frac{|\sigma_i - \sigma_{i+1}| + |\sigma_i - \sigma_{i-1}|}{2\sigma_i} > \text{threshold} \tag{2.46}$$

  where the subscript i denotes the i-th analysis segment. The threshold has previously been chosen to be 0.2 for LVK GWB searches [19]. The `statistical checks` module displays several quantities before and after the cut to asses the impact of the non-stationarity cut: segment-wise point estimate, standard deviation, and the deviations in SNR, as defined by:

  $$\Delta\mathrm{SNR}_i = \frac{\hat{C}_i - \langle \hat{C}_i \rangle}{\sigma_i}. \tag{2.47}$$

  Some representative plots are shown in Figure 2.9.

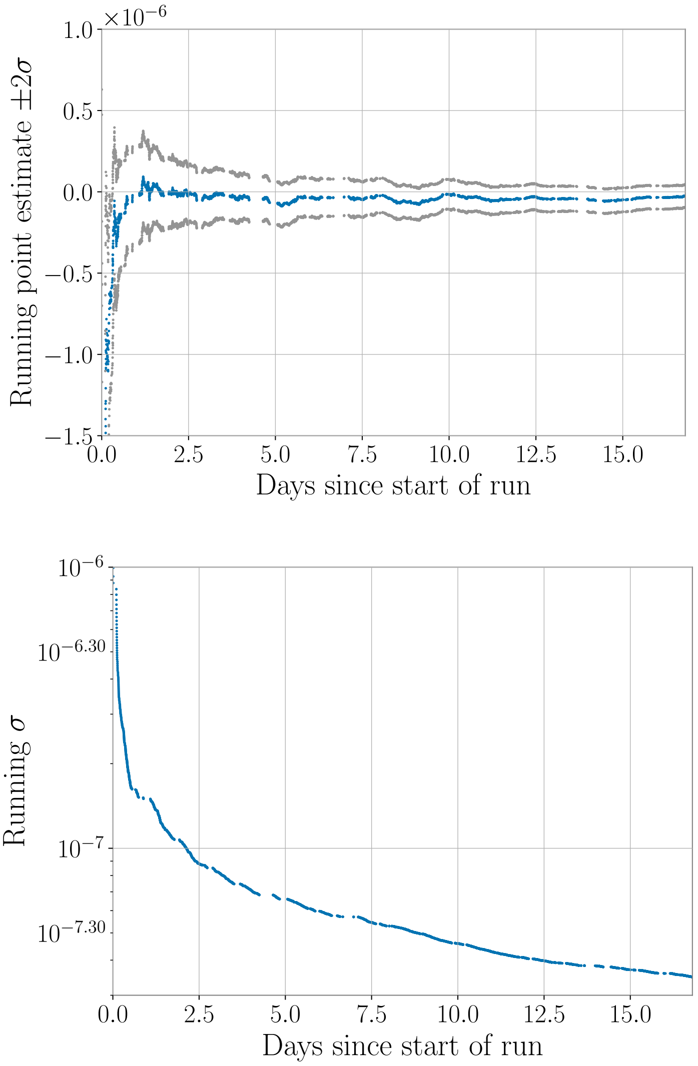

Figure 2.8. **Top**: Running point estimate values as more data is analysed. The grey lines denote the 2σ uncertainty band. **Bottom**: The running σ values as more data is analysed. In particular, we note the $1/\sqrt{T}$ behaviour, as predicted by Eq. (2.27). Both results were found using public LVK data from March 10, 2020 21:39:05 UTC to Mar 27, 2020 01:16:52 UTC obtained through GWOSC [16], and analysed using `pygwb`.

- The last set of checks concerns a Kolmogorov-Smirnov (KS) test that is used to verify that the $\Delta\mathrm{SNR}_i$ are consistent with a Gaussian distribution. The KS test implementation of this module returns the KS test statistic, which is the maximal deviation from the Gaussian cumulative distribution function, as well as the p-value. These values can then be used to make statements about the Gaussianity of the data [107].

The above categories introduced some aspects of the `statistical checks` module of the `pygwb` package and highlighted some of its most important features. For additional information on this module, or the `pygwb` package in general, we refer the interested reader to [222, 223] or the online documentation here.

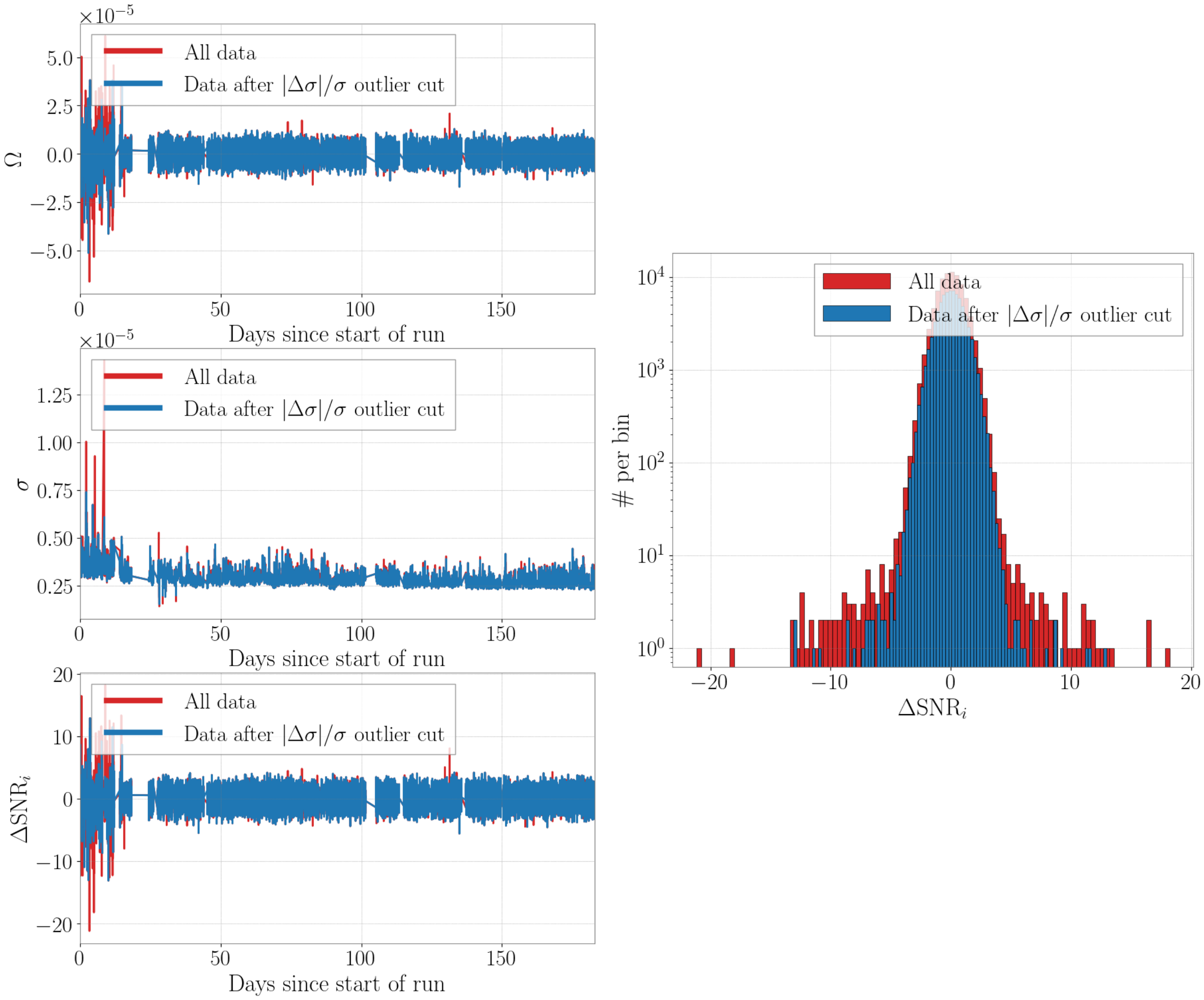

Figure 2.9. **Left**: Point estimate (Eq. (2.28)), sigma (Eq. (2.29)) and deviates $\Delta\mathrm{SNR}_i$ (Eq. (2.47)) for each analysis segment before the $\Delta\sigma$ cut (red) and after the cut (blue). **Right**: Distribution of the deviates $\Delta\mathrm{SNR}_i$, as defined in Eq. (2.47), before the $\Delta\sigma$ cut (red) and after the cut (blue). Figures taken from [222, 223].

This concludes the section in which we provided an overview of helpful tools pertaining to the analysis of GWB data. Power-law integrated sensitivity curves, Bayesian inference, and the `pygwb` analysis package were introduced, and will be referred to throughout this thesis. We now conclude this chapter by reviewing the current constraints on the GWB using various detection methods.

2.3 Constraints on the Gravitational-Wave Background

In the last section of this chapter, we review existing constraints on the GWB across the whole frequency band. Special attention is devoted to the results obtained by the LVK collaborations using data from their third observing run, as well as the recent strong evidence reported by several PTA experiments. Constraints from other detection methods are briefly touched upon as well.

The LIGO-Virgo-KAGRA Interferometers

The past three observing runs of the LVK collaborations have allowed to put stringent constraints on the dimensionless energy density ratio of GWs [19]. After computing the cross-correlation estimator, as defined in Eq. (2.26), this estimator can be used to perform parameter estimation, as introduced in Section 2.2.2. In [19], a power-law model is assumed for $\Omega_M(f)$ in Eq. (2.38), allowing to put constraints on both the spectral index α and the GWB amplitude $\Omega_{\rm ref}$. Upper limits are reported in Table 2.2 for different fixed values of the spectral index α, as well as for the case α is marginalised[15] over.

Upper limits on $\Omega_{\rm ref}^{95\%}$		
α	Uniform prior	Log-Uniform prior
0	1.7×10^{-8}	5.8×10^{-9}
2/3	1.2×10^{-8}	3.4×10^{-9}
3	1.3×10^{-9}	3.9×10^{-10}
Marg.	2.7×10^{-8}	6.6×10^{-9}

Table 2.2. 95% upper limits on the $\Omega_{\rm ref}$ parameter of a power-law GWB model at a reference frequency $f_{\rm ref} = 25$ Hz. Several spectral indices α are considered, corresponding to a GWB from CBCs ($\alpha = 2/3$), from core collapse supernovae ($\alpha = 3$), or from cosmic strings ($\alpha = 0$), as well as a result marginalised over all possible spectral indices. The results are quoted for two sets of priors used during the Bayesian inference analysis: a uniform and a log-uniform prior on the $\Omega_{\rm ref}$ parameter. This table is adapted from [19].

Constraining a power-law spectrum is not the only application of the LVK cross-correlation estimator and parameter estimation. In fact, a multitude of models can be constrained using the cross-correlation estimator: BBH merger rate evolution with redshift[16][19], beyond GR polarisations [19], parity violation [195], first order phase transitions[17] [231], primordial black

---

[15] See Eq. (2.40) for a definition of marginalisation.

[16] Original work on constraining the merger rate of BBHs will be presented in Chapter 4.

[17] Original work on constraining first order phase transitions will be presented in Chapter 5.

holes [232], and cosmic strings [12]. We do not discuss the constraints obtained on each of these models, but refer the interested reader to the relevant references or a comprehensive review in [221]. The abundance of applications from a GWB measurement illustrate the invaluable amount of information contained in such a measurement and the wealth it represents from a physics point of view.

Pulsar Timing Arrays

Until recently, the GWB had escaped detection despite the many efforts across different frequency ranges. However, in 2023, several PTA collaborations independently reported evidence for a GWB in the nano-Hertz frequency band [31, 41, 87, 218]. We recall that the PTA detection method was previously introduced in Section 1.2.2 of Chapter 1, and refrain from reviewing the method here. We summarise the constraints on the GWB from PTAs below.

Concretely, constraints are placed on a common coloured, i.e., frequency-dependent, spectrum with the following shape:

$$S_{ab}(f) = \Gamma(\xi_{ab}) \frac{A^2_{\mathrm{GWB}}}{12\pi^2} \frac{1}{T} \left(\frac{f}{f_{\mathrm{ref}}} \right)^{-\gamma_{\mathrm{GWB}}} f_{\mathrm{ref}}^{-3}, \tag{2.48}$$

where $\Gamma(\xi_{ab})$ denotes the Hellings and Downs curve, as introduced in Eq. (1.45). Using Bayesian inference, which was introduced in Section 2.2.2, results displayed in Figure 2.10 (top) are obtained by the NANOGrav collaboration[18] [31]. This shows the posterior probability distribution on the parameters γ_{GWB} and A_{GWB} of Eq. (2.48), with clear constraints on both parameters.

Furthermore, evidence for the Hellings and Downs spatial correlation is reported by the NANOGrav collaboration[18], as shown in Figure 2.10 (bottom). The results are quoted for a fixed spectral index of $\gamma_{\mathrm{GWB}} = 13/3$, corresponding to the expected main contributor to the background in that frequency band: the GWB of SMBBHs [31]. We remind the reader that, as mentioned in Section 1.2.2, measuring the Hellings and Downs spatial correlation is of the utmost important to claim evidence for a GWB, since other coloured noise processes could mimic the presence of a background, but do not display this particular correlation [185].

In addition to the more conventionally expected SMBBH background, an abundance of possible alternatives was also explored by each of the PTA collaborations, including GWBs of cosmological origin. We refer the reader to the relevant papers for more details: for NANOGrav, see [25, 28–30, 32, 33], for EPTA, see [38–40, 42, 240], and for PPTA, see [218, 268].

---

[18] Note that similar results were obtained by other PTA collaborations in [41, 87, 218].

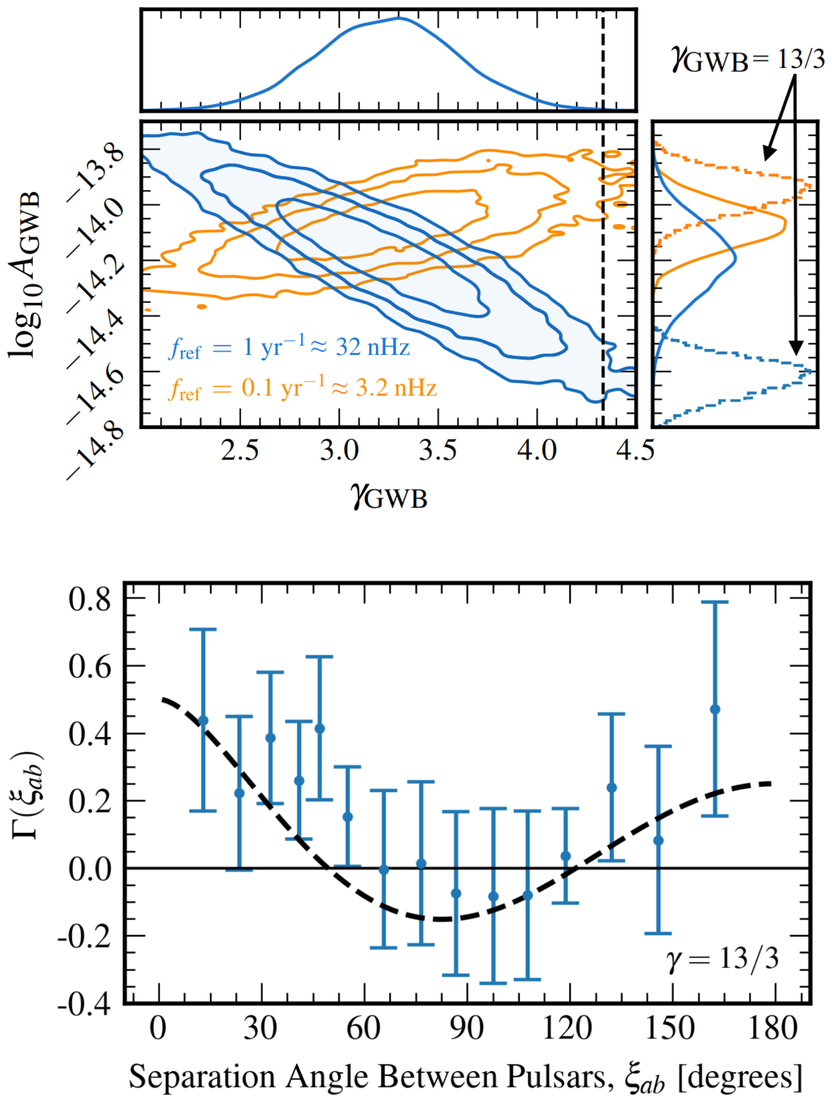

Figure 2.10. **Top**: Posterior probability distribution of the GWB amplitude A_{GWB} and the spectral index γ_{GWB} in a Hellings-Downs power-law model, showing 1σ-2σ-3σ credible regions. The value $\gamma_{\mathrm{GWB}} = 13/3$ (dashed black line) is included in the 99% credible region. The amplitude is referenced to $f_{\mathrm{ref}} = 1\ \mathrm{yr}^{-1}$ (blue) and $0.1\ \mathrm{yr}^{-1}$ (orange). The dashed blue and orange curves in the $\log_{10} A_{\mathrm{GWB}}$ sub-panel shows its marginal posterior density for a $\gamma = 13/3$ model, with $f_{\mathrm{ref}} = 1\ \mathrm{yr}^{-1}$ and $f_{\mathrm{ref}} = 0.1\ \mathrm{yr}^{-1}$, respectively. **Bottom**: Angular-separation-binned inter-pulsar correlations, measured from 2211 distinct pairings in NANOGrav's 67-pulsar array, assuming a $\gamma = 13/3$ common-process amplitude from a Bayesian inference analysis. The dashed black lines represents the Hellings-Downs curve, as introduced in Eq. (1.45). Figures are taken from [31], with adapted captions.

Other Constraints

To end this section, we provide a few additional constraints on the amplitude of the GWB. These come from the Earth normal modes, the CMB, and Big Bang Nucleosynthesis (BBN).

As mentioned in Section 1.2.2, the Earth itself can be used as a giant resonant cavity to measure GWs. A GWB would create standing waves, which could be detected using seismometers and gravimeters. However, the constraints derived from this method are quite faint: $h^2\Omega_{\rm GW} < 0.035 - 0.15$ in the 0.3 mHz to 5 mHz region [89].

Additionally, due to its near isotropy, CMB measurements can be used to constrain the energy density contained in GWs, which could have generated a quadrupole anisotropy or fluctuations on smaller angular scales were they too abundant [113, 208]. The constraints in Figure 2.11 are such that a larger amount of GW energy density would have altered the current CMB measurements.

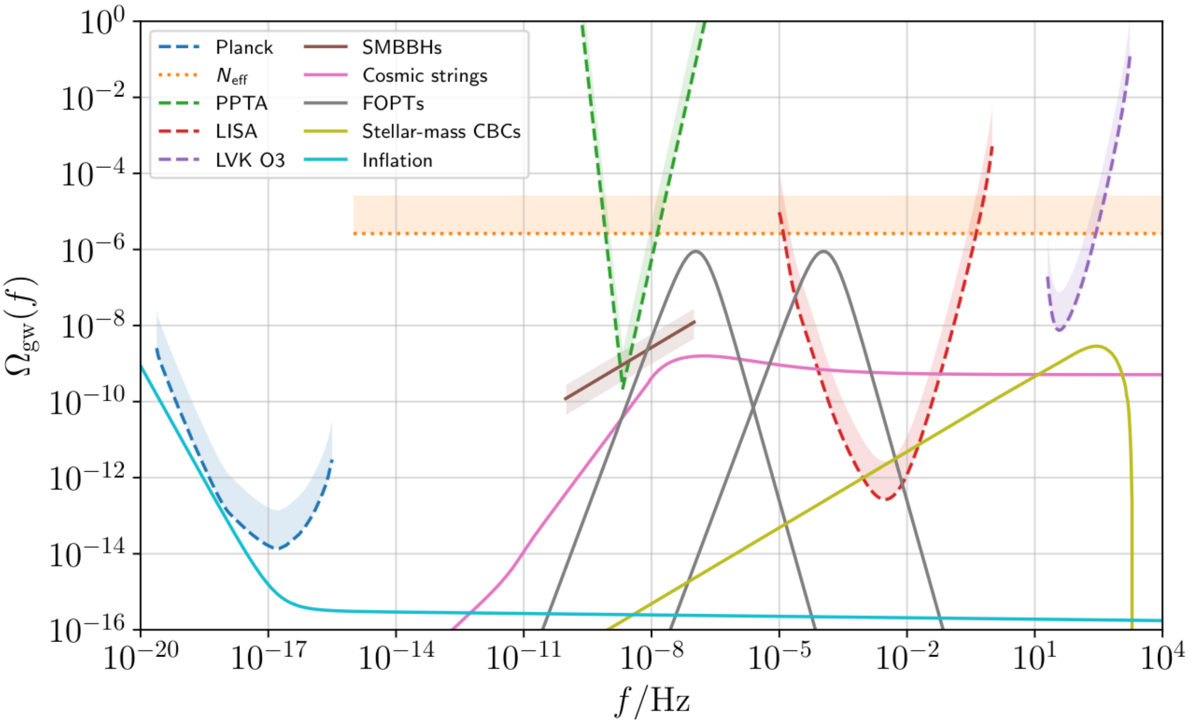

Figure 2.11. Example of potential GWB signals across the whole frequency range, including a signal from inflation, cosmic strings, SMBBHs, first order phase transitions, and stellar-mass CBCs (for more details about the signals, see [224]). Constraints from Planck, the third observing run of the LVK collaborations, PTA experiments, and indirect limits coming from BBN (here $N_{\rm eff}$) are shown as well. Note that the PTA constraints represented here are the ones before evidence for the Hellings and Downs correlation was observed, as described in [175]. Figure taken from [224].

Similarly, additional indirect limits can be obtained from the abundance of deuterium, helium, and lithium. During BBN, their production would have been altered by the presence of a larger GW abundance, as this would have caused the expansion rate of the Universe to increase, and thus, lower the amount of helium produced from deuterium [171, 208]. Indeed, extra relativistic degrees of freedom that would have altered BBN can be related to the effective number of GWs degrees of freedom $N_{\rm eff}$, introduced in Eq. (2.14), therefore providing a constraint on the dimensionless energy density $\Omega_{\mathrm{GW}}(f)$ itself [208, 242]. These constraints are illustrated by the orange, dotted line in Figure 2.11.

To conclude, we give an overview of the expected sensitivity of several future GW detectors, together with the sensitivity of current detectors. Various PI sensitivity curves, as introduced in Section 2.2.1, are reported in Figure 2.11, together with examples of possible signals across different frequency bands. The sensitivity improvements of current and future GW experiments, together with the development of detectors in previously unexplored frequency ranges are opening a gateway to the vast landscape of GWBs across frequencies, ensuring a bright GWB future.

Part II

The Astrophysical Gravitational-Wave Background

The first part of the original work conducted in this thesis is centred around the astrophysical GWB, and more specifically, the background coming from BBH mergers. Throughout these chapters, particular attention will be paid to applying the concepts outlined in the previous chapters as tools to understand the BBH population.

Chapter 3 - Stochastic Search for Intermittent Backgrounds

The current implementation of the search for a GWB assumes that the background is continuous in time. However, the GWB from unresolved BBHs is expected to be intermittent. Indeed, the short signal durations compared to the time in between events cause the signal to be popcorn-like in the LVK instruments. We address this discrepancy by proposing a novel method: the stochastic search for intermittent backgrounds. The method targets the intermittent nature of the BBH background by introducing a new parameter, the duty cycle, which allows the signal to be on or off, thus capturing the popcorn-like feature of this background. On a series of toy models of increasing complexity we show that the method performs better than the standard search for a continuous GWB.

Chapter 4 - The Metallicity Dependence and Evolutionary Times of Merging BBHs

Gravitational-wave events detected by current-generation interferometers happen at low to moderate redshifts, limiting our ability to probe the high redshift evolution of the compact binary population in the Universe. As the GWB comes from the superposition of all compact binary mergers across the Universe, [71] demonstrated that it can be used to infer properties of the BBH distribution at larger redshifts. In this chapter, we use this formalism to infer the metallicity dependence and evolutionary times of BBH mergers. We perform our analysis using data from the first three observing runs of the LVK collaborations, and consider the future Advanced LIGO A+ sensitivity as well.

3 STOCHASTIC SEARCH FOR INTERMITTENT GRAVITATIONAL-WAVE BACKGROUNDS

> I would like some sugar on that popcorn.
>
> ---
>
> No one. Ever.

A likely source of a GWB in the frequency band of the LVK detectors is the population of stellar-mass BBH mergers throughout the Universe. Rate estimates calculated from the BBH signals detected to date predict a BBH merger in the observable Universe every $\sim$ 5-10 minutes on average [3, 17]. Since the duration of a BBH merger in the LVK band is of the order of a second, the duty cycle ξ of such events (defined as the time in band for one merger signal divided by the average time between successive mergers) is of order 10^{-3}. Thus, the expected GWB signal is "popcorn-like" or *intermittent*, with the signal being "on" only a small fraction of the total observation time.

The total expected BBH GWB signal is potentially detectable with the Advanced LVK detectors when observing at design sensitivity [4, 17]. Although the SNRs for the individual BBH events are small, the combined SNR of the correlated data summed over all events grows like the square-root of the observation time, reaching a detectable level of 3σ (corresponding to a false alarm probability of approximately 10^{-3}) after $\sim$40 months of observation [4]. This estimate of the time-to-detection is based on the standard cross-correlation search, as described in the previous chapter [35]. Recall that this search looks for evidence of excess cross-correlated signal power, assuming that the amplitude of the GW signal component is drawn from a continuous-Gaussian distribution. This search assumes that the signal is "on" all the time, in conflict with the intermittent nature of the stellar-mass BBH background, which is expected to be the dominant signal. Thus, although the standard cross-correlation search is able to detect the time-averaged signal from an intermittent GWB [199], this search is sub-optimal in the sense that the time-to-detection will be longer than that for a search which properly takes into account the intermittent nature of the background.

Therefore, the purpose of this chapter is to introduce a new stochastic-signal-based search that specifically targets intermittent GWBs, and hence can potentially reduce the time-to-detection of the BBH background signal. This new search is built on the seminal work of Drasco and Flanagan, who proposed a Gaussian mixture-model (GMM) likelihood function for analysing intermittent GWBs (as will be reviewed in Section 3.1.2) [111]. Based on this idea, our proposed search for intermittent GWBs looks for excess cross-correlated power in short stretches of data. Conversely, a deterministic-signal-based search for the intermittent BBH background was proposed by Smith and Thrane, which involves marginalising over the signal parameters for deterministic BBH chirp waveforms in short (~ 4 s) stretches of data (as will be discussed in Section 3.1.3) [241]. By construction, our proposed search is adaptable to a generic intermittent GWB since it looks only for excess cross-correlated power. We also expect our proposed search to be computationally more efficient in detecting a signal than the deterministic-signal-based approach of Smith and Thrane, since our search ignores the deterministic form of the GW signal waveforms and hence the need to marginalise over all the associated signal parameters.

A brief outline of this chapter is as follows: first, we give an overview of the current searches for intermittent GWBs in Section 3.1. We then proceed by introducing our proposed stochastic search for intermittent GWBs in Section 3.2. To compare the performance of the various search methods mentioned above, we analyse a series of datasets which are tailored to highlight the merits and shortcomings of each style of search. We start in Section 3.3.1 by considering stationary-Gaussian white noise in two co-located and co-aligned detectors, and inject an intermittent GWB made up of white GW bursts with Gaussian signal amplitudes scaled by distances to the sources drawn from a uniform-in-volume (UIV) distribution. We then consider a background made up of coloured, i.e., frequency-dependent, GW bursts[1] in Section 3.3.2, which follow the expected spectral shape of BBH mergers. Finally, we analyse a set of deterministic BBH chirp waveforms in Section 3.3.3, where the chirp parameters are fixed except for the distance to the source, which is also drawn from a UIV distribution. In Section 3.4, we discuss some generalisations to the method since the publication of our original methods paper in [176]. We conclude in Section 3.5 by discussing further extensions of our method and additional necessary tests before applying it to real GW data.

This chapter is based on work in collaboration with Jessica Lawrence, Arianna Renzini, Andrew Matas, Joseph Romano, and Nick van Remortel, as published in [176].

---

[1] The term "burst" will be used throughout this chapter as it is the most general, irrespective of the type of signal. In the context of compact binary mergers, these bursts of GWs are often referred to as "transients".

3.1 An Overview of Proposed Searches for Intermittent GWBs

Before introducing our search for intermittent backgrounds, we review the current proposed searches for such backgrounds. We first comment on the standard continuous search in Section 3.1.1, then introduce a GMM approach to detecting intermittent GWBs in Section 3.1.2, as first proposed in [111]. We conclude by introducing a deterministic search for intermittent backgrounds in Section 3.1.3, which was first proposed in [241].

3.1.1 Standard Continuous Cross-correlation Search

One recalls from Chapter 2 that the standard continuous cross-correlation search aims to measure the fractional energy density of a GWB $\Omega_{\rm GW}(f)$, as previously defined in Eq. (2.13) [35]. For the target signal of a BBH GWB, it is well known that the fractional energy density spectrum is $\Omega_{\rm GW}(f) \sim f^{2/3}$ to good approximation, in the frequency ranges probed by the LVK interferometers [219]. This knowledge can be incorporated into the search, reducing it to the measurement of a single quantity $\Omega_{\rm GW}(f_{\rm ref})$, where $f_{\rm ref}$ is a reference frequency chosen where the sensitivity of the LVK detectors is best (typically 25 Hz) [19]. For the remainder of the chapter, we will refer to $\Omega_{\rm GW}(f_{\rm ref})$ simply as $\Omega_{\rm GW}$ for brevity. For a set of data containing enough events to be statistically significant, $\Omega_{\rm GW}$ is the amplitude of the time and population-averaged energy density. We will refer to this stochastic search as the standard cross-correlation search for a continuous-Gaussian background (SSC). A short overview of this search and how it compares to other searches is provided in Figure 3.1.

Since this search assumes a continuous-in-time signal in the data, it does not properly model an important feature of the BBH GWB signal – the intermittency. To remedy this improper modelling, several searches targeting intermittent GWBs specifically have been proposed. We start by giving a high-level overview of these different analysis methods. However, we refrain from giving details about the actual form of the likelihoods and refer to Appendix A for more information.

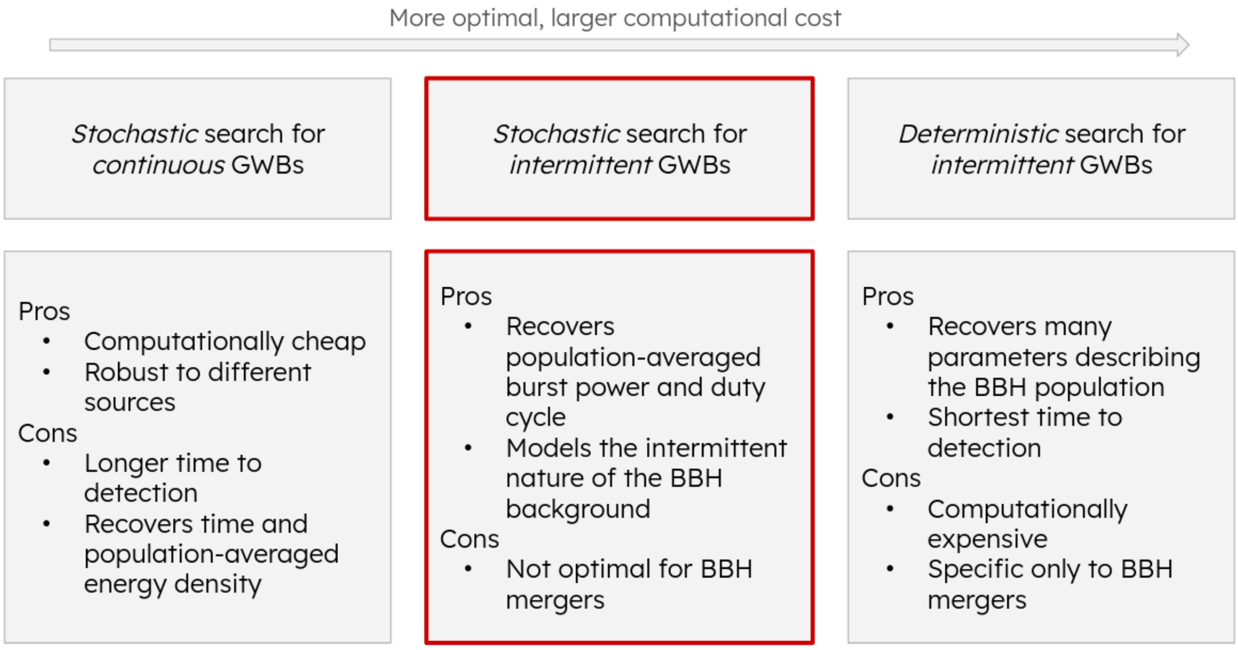

Figure 3.1. Overview of different search methods, listing their advantages and disadvantages. Note that the optimality increases from left to right, however at an increased computational cost as well.

3.1.2 Gaussian Mixture-model Likelihood Function for Intermittent GWBs

Method

In 2003, Drasco and Flanagan proposed a search for an intermittent GWB that makes use of a GMM likelihood function of the form

$$\mathcal{L}_{\rm tot} = \prod_{I}^{N_{\rm seg}} \left[\xi \mathcal{L}_{s,I} + (1-\xi)\mathcal{L}_{n,I} \right] , \tag{3.1}$$

where ξ is the probability that a particular segment contains a GW signal, i.e., the duty cycle [111]. The quantities $\mathcal{L}_{s,I}$ and $\mathcal{L}_{n,I}$ are the likelihood functions for segment I in the presence and absence of a GW signal, namely the signal and noise likelihoods. For the simple toy model considered in their paper (i.e., single-sample[2] GW "bursts", occurring with probability ξ drawn from a fixed Gaussian distribution with variance σ_b^2, and injected into uncorrelated white noise in two co-located and co-aligned detectors[3]), the signal and noise parameters that enter the likelihood functions $\mathcal{L}_{s,I}$ and $\mathcal{L}_{n,I}$ are the variances $\mathbf{\Theta}_s = (\sigma_b^2, \sigma_{n_1}^2, \sigma_{n_2}^2)$ and $\mathbf{\Theta}_n = (\sigma_{n_1}^2, \sigma_{n_2}^2)$,

---

[2] Single-sample bursts are bursts whose duration is less than the sample period Δt.

[3] This means that the ORF, as introduced in Section 2.1.3, does not need to be taken into account.

respectively. By maximising $\mathcal{L}_{\rm tot}$ with respect to all four parameters $(\xi, \sigma_b^2, \sigma_{n_1}^2, \sigma_{n_2}^2)$, Drasco and Flanagan obtained a detection statistic (the maximum-likelihood statistic), which they could use to search for intermittent GWBs. Note that in the case $\xi = 1$, i.e., assuming the signal is always present, one recovers the SSC introduced above.

Although Drasco and Flanagan tested their proposed method with a test statistic within a frequentist framework, we have decided to work within a Bayesian framework in this chapter[4]. We define several concepts of importance within this framework before moving on to the discussion of the results by Drasco and Flanagan.

Most concepts related to Bayesian inference were already introduced in Section 2.2.2. Nevertheless, we review some of these expressions explicitly within the context of this chapter. For example, given a likelihood function $\mathcal{L}_{\rm tot}$ and priors π, the joint posterior distribution for the duty cycle and the signal+noise parameters can be computed using Bayes' theorem:

$$p(\xi, \sigma_b^2, \sigma_{n_1}^2, \sigma_{n_2}^2 | d) = \frac{\mathcal{L}_{\rm tot}(d|\xi, \sigma_b^2, \sigma_{n_1}^2, \sigma_{n_2}^2)\pi(\xi)\pi(\sigma_b^2)\pi(\sigma_{n_1}^2)\pi(\sigma_{n_2}^2)}{\mathcal{Z}(d)}, \tag{3.2}$$

where

$$\mathcal{Z}(d) \equiv \int \mathrm{d}\xi \int \mathrm{d}\sigma_b^2 \int \mathrm{d}\sigma_{n_1}^2 \int \mathrm{d}\sigma_{n_2}^2\, \mathcal{L}_{\rm tot}(d|\xi, \sigma_b^2, \sigma_{n_1}^2, \sigma_{n_2}^2)\pi(\xi)\pi(\sigma_b^2)\pi(\sigma_{n_1}^2)\pi(\sigma_{n_2}^2) \tag{3.3}$$

is the model evidence. Marginalised posterior distributions (for each parameter separately) are obtained by integrating the joint posterior distribution over all the other parameters, e.g.,

$$p(\xi) = \int \mathrm{d}\sigma_b^2 \int \mathrm{d}\sigma_{n_1}^2 \int \mathrm{d}\sigma_{n_2}^2\, p(\xi, \sigma_b^2, \sigma_{n_1}^2, \sigma_{n_2}^2). \tag{3.4}$$

Of course, likelihood functions, priors, etc., are all calculated in the context of a particular choice of analysis model $\mathcal{M}_\alpha$ (e.g., a GMM likelihood search for intermittent GWBs or the SSC), which we have not indicated in the above expressions. If we explicitly denote the dependence of the above distributions on the choice of analysis model, we can define the Bayes factor between models $\mathcal{M}_\alpha$ and $\mathcal{M}_\beta$, as done in Eq. (2.43). Recall from Section 2.2.2 that the Bayes factor tells us how much more the data favours model $\mathcal{M}_\alpha$ relative to $\mathcal{M}_\beta$[5]. Throughout this chapter, we will make plots of the natural logarithm of the Bayes factor as a function of the duty cycle to compare the various search methods.

---

[4] For a discussion and comparison on frequentist versus Bayesian statistics, see [230].

[5] More information on the Bayes factor and its interpretation can be found in Section 2.2.2 and [230, 251].

Results

With these concepts in mind, we now move to the discussion of the results of the proposed GMM likelihood. Drasco and Flanagan showed that their detection statistic for intermittent GWBs performs better than the standard cross-correlation statistic for continuous-Gaussian backgrounds when the duty cycle ξ is sufficiently small. To illustrate this, we implement their proposed GMM likelihood in a Bayesian framework[6]. Instead of using their proposed frequentist detection statistic, we use the Bayes factor as a measure of efficiency[7]. To be able to study its behaviour as a function of the duty cycle, we combine 100 data realisations for each ξ value. Each data realisation consists of 40,000 segments, where a fraction of them contains single-sample bursts drawn from a Gaussian distribution with variance $\sigma_b^2 = 1$.

We keep the total continuous-Gaussian SNR fixed to 3, computed using Eqs. (3.5) and (3.7), by adjusting the noise variances for each value of the duty cycle, rather than adjusting the signal parameters. So, as ξ decreases, the segment SNRs must increase, which means that the noise variances must decrease. This is illustrated in Figure 3.2, where both the continuous-in-time, i.e., $\xi = 1$ in Eq. (3.1), and the intermittent GMM likelihood analysis methods are used. Each plotted point corresponds to the mean of the ln Bayes factor over 100 realisations of data, while the error bars correspond to the standard deviation of the ln Bayes factor.

While the continuous search performs equally well for all duty cycles, since it assumes $\xi = 1$, the Bayes factor for the GMM likelihood increases as ξ decreases, exceeding the continuous stochastic likelihood Bayes factor. This illustrates that the GMM likelihood performs better than the continuous likelihood for smaller values of ξ. Equivalently, the relative performance of the Bayes factors shown in Figure 3.2 can be expressed in terms of the expected SNR in an individual segment assuming the presence of a GW signal with burst variance σ_b^2:

$$\rho_{\rm seg} \equiv \frac{\sigma_b^2}{\sigma_{n_1}\sigma_{n_2}} \,. \tag{3.5}$$

In terms of $\rho_{\rm seg}$, the condition for the GMM likelihood to perform better than the continuous likelihood is

$$\rho_{\rm seg} \sim 1 \,. \tag{3.6}$$

In the limit where $\rho_{\rm seg} \ll 1$, the GW signals in an individual segment are sufficiently weak that the GMM likelihood does not perform any better than the standard stochastic continuous likelihood. Conversely, when $\rho_{\rm seg} \gg 1$, the GW signals in the individual segments are so strong that they are individually resolvable, with segment SNRs exceeding the threshold needed for

---

[6] For more details on this implementation and the likelihoods, we refer the reader to Appendix A.1.

[7] For the Bayes factor, in Eq. (2.43), we consider the model $\mathscr{M}_\alpha$ to contain a signal and noise, whereas $\mathscr{M}_\beta$ represents the noise only model.

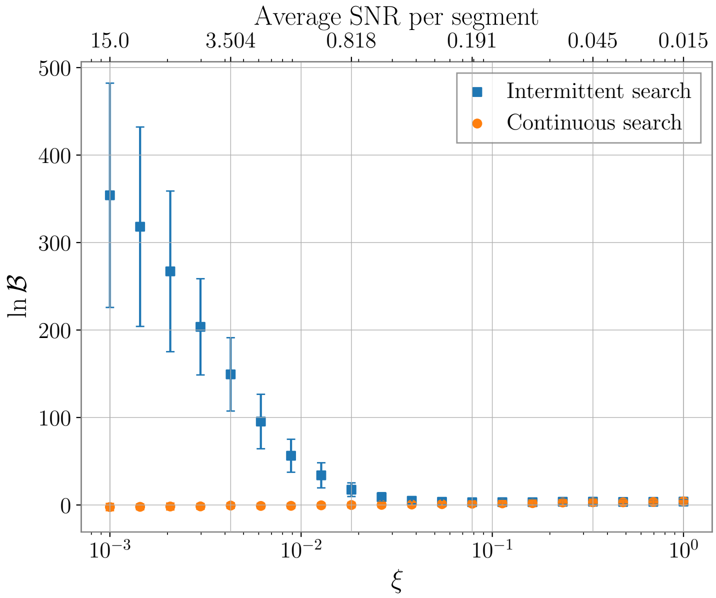

Figure 3.2. ln Bayes factors of the signal+noise model to the noise-only model as a function of the duty cycle ξ for the intermittent search (blue) and the continuous search (orange) where the signal consists of single sample bursts drawn from a Gaussian distribution of variance σ_b^2. The GMM likelihood outperforms the SSC method for small duty cycles.

detection with a single-detector burst statistic. In other words, a search for an intermittent GWB is the most sensitive search when the GW signals in the individual segments are marginally subthreshold ($\rho_{\text{seg}} \sim 1$).

Furthermore, we can determine an approximate value of ρ_{seg} for the LVK detectors, for the population of stellar-mass BBH mergers throughout the Universe. As mentioned previously, it should take ~ 40 months of observation using the SSC cross-correlation statistic to observe the BBH background with a total SNR $\rho_{\text{tot}} = 3$ [4]. Since the segment duration[8] proposed by Smith and Thrane for an intermittent search is of order $T_{\text{seg}} \sim 4$ s [241], 40 months of observation corresponds to $N_{\text{seg}} \sim 2.5 \times 10^7$ segments. The final input that we need to do the calculation is the expected duty cycle of the signal, which for stellar-mass BBH mergers throughout the Universe is $\xi \sim 10^{-3}$. These values imply

$$\rho_{\text{seg}} = \frac{\rho_{\text{tot}}}{\xi \sqrt{N_{\text{seg}}}} \sim 0.6 \,, \tag{3.7}$$

which is in the regime where a search for an intermittent GWB should start to perform better than the SSC cross-correlation search. The value of ρ_{seg} at which the intermittent search begins to outperform the continuous search in Figure 3.2 matches this result.

The proper modelling of the intermittent BBH background will be at the core of our method

---

[8] See Section 3.1.3 for more details.

as well, similarly to the GMM likelihood by Drasco and Flanagan [111]. Before illustrating how our method builds on the work of Drasco and Flanagan, we briefly review the deterministic search proposed by Smith and Thrane.

3.1.3 Deterministic-signal-based Search for Intermittent GWBs

In 2018, Smith and Thrane extended the work of Drasco and Flanagan by proposing an optimal fully-Bayesian deterministic-signal-based search for the intermittent GWB produced by the population of stellar-mass BBH mergers throughout the Universe: the Bayesian Search [241]. As in [111], Smith and Thrane assumed a mixture model for the intermittent GW signals. They chose a segment duration ~ 4 s, which is long enough to include a typical BBH chirp signal, yet short enough that the probability of two such signals occurring in a single segment is negligibly small ($\sim 10^{-4}$). However, instead of considering single-sample GW bursts drawn from a fixed Gaussian distribution, they considered finite-duration deterministic BBH chirp waveforms $h = h_{\rm chirp}(t;\theta)$, where θ are the chirp parameters (e.g., the component masses and spins of the two black holes, the inclination angle of the orbital plane relative to the line of sight, etc). Smith and Thrane then marginalised (instead of maximised) over the signal parameters for each segment of data, assuming prior probability distributions for these parameters, while replacing the noise parameters by measured estimates of these quantities. If the signal priors are conditioned on segment-independent population parameters $\theta_{\rm pop}$, which parameterize the distributions from which the individual masses, spins, etc., are drawn, then the final (marginalised) likelihood function $\mathcal{L}_{\rm tot} \equiv \mathcal{L}_{\rm tot}(d|\xi, \theta_{\rm pop})$ depends only on the duty cycle ξ and the population parameters $\theta_{\rm pop}$. Finally, doing Bayesian inference calculations given $\mathcal{L}_{\rm tot}$ and a prior for ξ and $\theta_{\rm pop}$, Smith and Thrane were able to construct joint posterior distributions for ξ and $\theta_{\rm pop}$ as well as Bayes factors comparing the evidence for this intermittent signal model and e.g., that for the standard cross-correlation search for a continuous-Gaussian GWB.

The deterministic-signal-based search of Smith and Thrane is expected to decrease the time-to-detection of the intermittent GWB produced by stellar-mass BBH mergers by a factor of ~ 1000 relative to the SSC by taking into account both the intermittent nature of the signal as well as knowledge of the form of the individual waveforms, whose parameters are marginalised over [241]. For this factor of ~ 1000 determination, they did not consider any population parameters, so the only parameter that they needed to infer from the data was the duty cycle ξ. A posterior distribution for ξ sufficiently bounded away from zero would be evidence of a confident detection of an intermittent GWB signal. The gain in time-to-detection comes at the computational cost of having to perform Bayesian marginalisation over all the BBH chirp signal parameters for every 4 s segment of data. This search is currently in the testing phase, in preparation for running on real LVK data in the near future. A brief summary of the pros and cons of this search is given in Figure 3.1.

Within this chapter, for comparative purposes, we will implement a much simpler version of this deterministic-signal-based search. We will label this deterministic-signal-based search the deterministic search for intermittent backgrounds (DSI) throughout this work.

3.2 SSI: Stochastic Search for Intermittent GWBs

Building off the work of Drasco and Flanagan [111], we propose a new search based on a stochastic-signal model consisting of intermittent "bursts" of correlated stochastic GWs with unknown duty cycle ξ, in otherwise uncorrelated noise in two detectors. We call this search SSI, for s̲tochastic s̲earch for i̲ntermittent GWBs, referencing both the signal model the analysis assumes, as well as the type of background for which it is designed. To make the connection with BBH mergers, we assume that these bursts of GWs last on the order of a few seconds so the data are split into short, 4 second stretches as in Smith and Thrane, and that the PSD in the LVK detectors goes like $f^{-7/3}$, appropriate for binary inspiral[9]. This corresponds to a fractional energy density spectrum $\Omega_{\rm GW}(f) \sim f^{2/3}$, as converted by using Eq. (2.15).

Rather than marginalise over the parameters of deterministic BBH chirp waveforms as in the deterministic-signal-based approach, our search looks for excess cross-correlated power when the signal is assumed to be present, using a mixture-model likelihood function. Thus, we trade off optimality for computational efficiency and flexibility relative to the deterministic-signal-based approach, while still accounting for the intermittent nature of the BBH background, which is missing from the SSC.

We begin by dividing up the data into short segments such that the probability of a segment containing more than one signal is small. The total likelihood is given by a product over segments of the GMM likelihood function:

$$\mathcal{L}_{\rm tot}(d|\xi, \theta_{s,{\rm pop}}, \theta_n) = \prod_I \left[\xi \mathcal{L}_s(d_I|\theta_{s,{\rm pop}}, \theta_n) + (1-\xi)\mathcal{L}_n(d_I|\theta_n)\right], \tag{3.8}$$

where θ_n represents the noise parameters, $\theta_{s,{\rm pop}}$ represents the signal population parameters, and d_I represents the data in segment I.

For our stochastic-signal-based search, the segment-dependent signal likelihood takes the form

$$\mathcal{L}_s(d_I|\theta_{s,{\rm pop}}, \theta_n) \equiv \int {\rm d}\theta_{s,I}\, \mathcal{L}_s(d_I|\theta_{s,I}, \theta_n)\pi(\theta_{s,I}|\theta_{s,{\rm pop}}), \tag{3.9}$$

where the segment-dependent signal parameters $\theta_{s,I}$ are marginalised over. Marginalising over

---

[9] Note that this could easily be generalised to different values of the spectral index.

the correct segment prior is an important and necessary step in order to recover correct and unbiased results.

We choose to write the likelihood for a specific set of parameters, $\theta_{s,\mathrm{pop}} = \langle\Omega_b\rangle$, $\theta_{s,I} = \Omega_{b,I}$, and $\theta_n = \{\sigma^2_{n_1}, \sigma^2_{n_2}\}$, where $\langle\Omega_b\rangle$ is the population-averaged energy density amplitude of bursts of GW power and $\Omega_{b,I}$ is the energy density amplitude in data segment I. The population parameter $\langle\Omega_b\rangle$ is related to Ω_{GW} (what the SSC estimates), introduced at the beginning of Section 3.1.1, by:

$$\Omega_{\mathrm{GW}} = \xi\langle\Omega_b\rangle, \tag{3.10}$$

where ξ is the duty cycle, as appearing in Eq. (3.8).

For the analyses included in this chapter, we simulate stationary, white-Gaussian noise. This means that the noise PSD is independent of frequency and has the value

$$P_{n_\mu} = \frac{\sigma^2_{n_\mu}}{f_{\mathrm{high}} - f_{\mathrm{low}}}, \tag{3.11}$$

where $\mu = 1, 2$ is the detector index and f_{low} and f_{high} are the low- and high-frequency cut-offs for our search. We will take f_{high} to equal the Nyquist critical frequency $f_{\mathrm{nyq}} \equiv 1/(2\Delta t)$, where Δt is the sample period. Each segment of time-domain data of duration T is Fourier transformed and coarse-grained to frequencies f_k having frequency resolution M/T. We then take our noise parameters to be the variance of the noise in each detector, $\sigma^2_{n_\mu}$. Under these assumptions, the segment-dependent signal likelihood in Eq. (3.9) becomes

$$\begin{aligned}\mathcal{L}_s(d_I|\langle\Omega_b\rangle, \sigma^2_{n_1}, \sigma^2_{n_2}) = \int d\Omega_{b,I}\,\pi(\Omega_{b,I}|\langle\Omega_b\rangle) \prod_k \frac{1}{(\pi T/2)^{2M}(P_{1,I}(f_k)P_{2,I}(f_k) - P^2_{b,I}(f_k))^M} \\ \times \exp\left\{-\frac{M}{(P_{1,I}(f_k)P_{2,I}(f_k) - P^2_{b,I}(f_k))}\left[\hat{P}_{1,Ik}P_{2,I}(f_k) + \hat{P}_{2,Ik}P_{1,I}(f_k) - 2\hat{P}_{b,Ik}P_{b,I}(f_k)\right]\right\},\end{aligned} \tag{3.12}$$

where

$$P_{1,I}(f) \equiv \frac{\sigma^2_{n_1}}{f_{\mathrm{high}} - f_{\mathrm{low}}} + P_{b,I}(f), \qquad P_{2,I}(f) \equiv \frac{\sigma^2_{n_2}}{f_{\mathrm{high}} - f_{\mathrm{low}}} + P_{b,I}(f), \qquad P_{b,I}(f) \equiv \Omega_{b,I}H(f), \tag{3.13}$$

are the total auto-correlated power spectra in each detector and the PSD for a GW burst in segment I, and k runs over the coarse-grained frequencies f_k. The spectral shape $H(f)$ is of the form

$$H(f) \equiv \frac{3H_0^2}{10\pi^2}\frac{1}{f^3_{\mathrm{ref}}}\left(\frac{f}{f_{\mathrm{ref}}}\right)^{-7/3}, \tag{3.14}$$

and allows to go from the dimensionless energy density fraction $\Omega_b(f)$ to PSD $P_b(f)$, as also previously seen in Eq. (2.15). The Fourier transformed data $\tilde{d}_{\mu,Ik}$ enter the evidence via the following quadratic combinations:

$$
\begin{aligned}
\hat{P}_{1,Ik} &\equiv \frac{2}{T}\frac{1}{M}\sum_{k'=k-M/2T}^{k+M/2T-1} |\tilde{d}_{1,Ik'}|^2\,,\\
\hat{P}_{2,Ik} &\equiv \frac{2}{T}\frac{1}{M}\sum_{k'=k-M/2T}^{k+M/2T-1} |\tilde{d}_{2,Ik'}|^2\,,\\
\hat{P}_{b,Ik} &\equiv \frac{2}{T}\frac{1}{M}\sum_{k'=k-M/2T}^{k+M/2T-1} \mathrm{Re}\left(\tilde{d}^*_{1,Ik'}\tilde{d}_{2,Ik'}\right)\,,
\end{aligned}
\tag{3.15}
$$

which are coarse-grained estimators (i.e., averaged over fine-grained frequencies labelled by k') of the total auto-correlated and cross-correlated power spectra in the two detectors.

The segment-dependent noise likelihood can similarly be written as

$$
\mathcal{L}_n(d_I|\sigma^2_{n_1},\sigma^2_{n_2}) = \prod_k \frac{1}{(\pi T/2)^{2M}\left(P_{n_1}(f_k)P_{n_2}(f_k)\right)^M}\exp\left\{-M\left[\frac{\hat{P}_{1,Ik}}{P_{n_1}}+\frac{\hat{P}_{2,Ik}}{P_{n_2}}\right]\right\}\,. \tag{3.16}
$$

Reduced form of the likelihood

In principle, the noise parameters $\theta_n = \{\sigma^2_{n_1},\sigma^2_{n_2}\}$ in the likelihood functions above should be inferred together with the signal population parameters $\theta_{s,\text{pop}} = \langle\Omega_b\rangle$ as part of the Bayesian inference procedure. Doing so defines the so-called *full* version of the analyses. However, as the noise in the LVK detectors is stationary to good approximation, it is typically sufficient to use measured estimates of the noise parameters (denoted by $\bar{\sigma}^2_{n_1}$ and $\bar{\sigma}^2_{n_2}$ and computed using Eq. (A.16) in Appendix A) in the likelihood function, thereby avoiding having to infer them in this analysis. We refer to this approach as the *reduced* form of the analyses, which is computationally cheaper than the full form. The reduced version of the likelihood requires that the cross-correlation estimators be approximately Gaussian, which holds only if the number of samples per segment N is sufficiently large. For additional information, we refer the reader to [197], where a detailed comparison between full and reduced likelihoods was performed.

The reduced segment-dependent signal likelihood is given by [197]:

$$
\mathcal{L}_s(d_I|\langle\Omega_b\rangle,\bar{\sigma}^2_{n_1},\bar{\sigma}^2_{n_2}) = \int d\Omega_{b,I}\,\pi(\Omega_{b,I}|\langle\Omega_b\rangle)\frac{1}{\sqrt{2\pi\,\mathrm{var}(\bar{\Omega}_{b,I})}}\exp\left[-\frac{(\hat{\Omega}_{b,I}-\Omega_{b,I})^2}{2\,\mathrm{var}(\bar{\Omega}_{b,I})}\right]\,, \tag{3.17}
$$

where

$$
\hat{\Omega}_{b,I} \equiv \frac{\sum_k Q_I(f_k)\hat{P}_{b,Ik}}{\sum_{k'} Q_I(f_{k'})H(f_{k'})}\,,\qquad \mathrm{var}(\bar{\Omega}_{b,I}) \equiv \left(2M\sum_k Q_I(f_k)H(f_k)\right)^{-1}\,. \tag{3.18}
$$

These are the optimally-filtered cross-correlation estimators and corresponding variances, which are constructed from coarse-grained estimates of the cross-correlated power $\hat{P}_{b,Ik}$, given by Eq. (3.15), and the segment-dependent optimal filter function

$$Q_I(f) \equiv \frac{H(f)}{\bar{P}_{1,I}(f)\bar{P}_{2,I}(f)} \,. \tag{3.19}$$

In the above expression,

$$\bar{P}_{1,I}(f) \equiv \frac{\bar{\sigma}^2_{n_1}}{f_{\text{high}} - f_{\text{low}}} + \Omega_{b,I} H(f) \,, \qquad \bar{P}_{2,I}(f) \equiv \frac{\bar{\sigma}^2_{n_2}}{f_{\text{high}} - f_{\text{low}}} + \Omega_{b,I} H(f) \,, \tag{3.20}$$

where $H(f)$ was previously defined in Eq. (3.14). Note that $Q_I(f)$ is a generalisation of the standard optimal filter[10] for an $f^{-7/3}$ PSD, extended to include the segment-dependent burst contribution, i.e., dependent on the likelihood parameter $\Omega_{b,I}$, to the total auto-correlated power estimates $\bar{P}_{1,I}(f)$ and $\bar{P}_{2,I}(f)$.

The reduced segment-dependent noise likelihood $\mathcal{L}_n(d_I|\bar{\sigma}^2_{n_1}, \bar{\sigma}^2_{n_2})$ is given by

$$\mathcal{L}_n(d_I|\bar{\sigma}^2_{n_1}, \bar{\sigma}^2_{n_2}) = \frac{1}{\sqrt{2\pi \, \text{var}(\bar{\Omega}_b)}} \exp\left[-\frac{(\hat{\Omega}_{b,I})^2}{2\,\text{var}(\bar{\Omega}_b)} \right] , \tag{3.21}$$

where $\hat{\Omega}_{b,I}$ and $\text{var}(\bar{\Omega}_b)$ are the same as for the segment-dependent signal likelihood, but with a segment-*independent*, noise-only optimal filter function

$$Q(f) \equiv \frac{H(f)}{\bar{P}_{n_1} \bar{P}_{n_2}} \,. \tag{3.22}$$

The above expressions establish the methodology behind SSI. We now proceed to testing its implementation on several datasets of increasing complexity, and compare its performance with other search methods.

3.3 Analyses

In this section, we describe in detail a set of analyses, which we use to illustrate various aspects of the search methods described above. The tests that these analyses allow us to perform should be thought of as providing a "proof-of-principle" demonstration of our proposed SSI method. A more rigorous test of this search on actual LVK noise and realistic injected BBH chirp signals is a topic for future investigation[11]. A schematic overview of the different analyses we

---

[10] More information on optimal filtering can be found in Section 2.1.4 and in [35, 230].

[11] For additional information on possible generalisations of the method, see Sections 3.4 and 3.5.

consider in this chapter is provided in Figure 3.3.

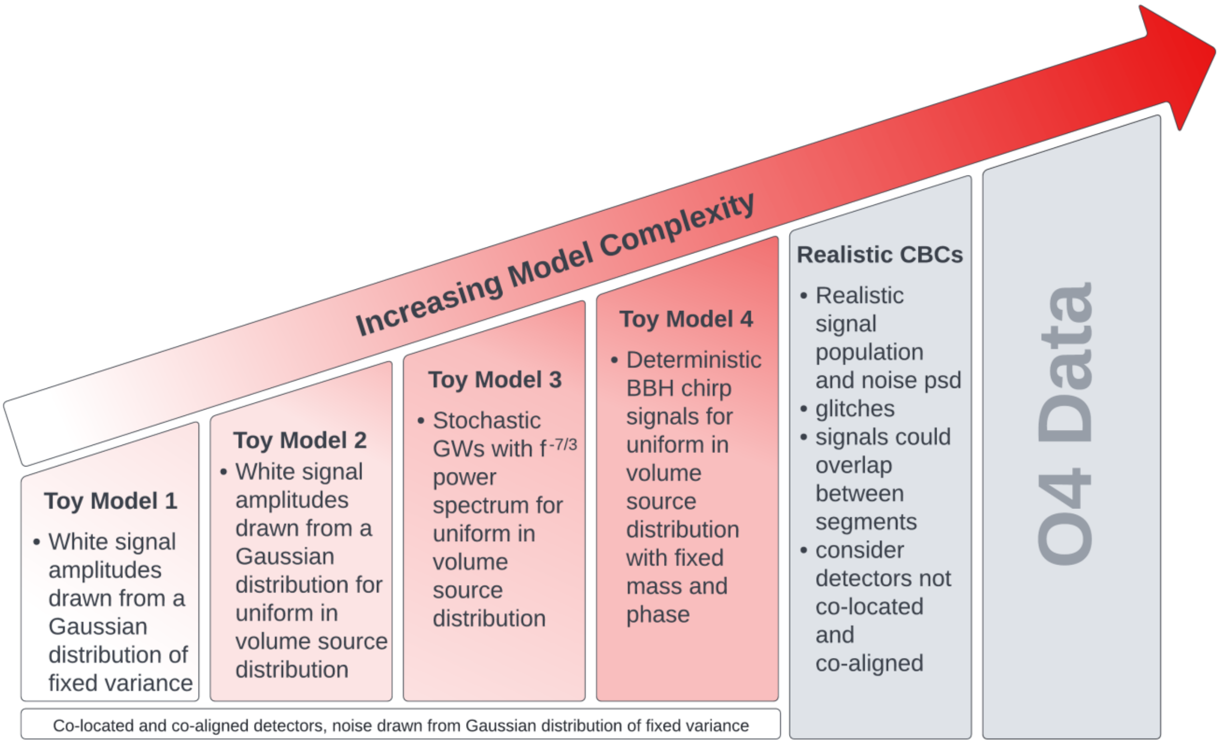

Figure 3.3. Schematic overview of the different stages of the development of SSI. Various toy models are given with a short description, illustrating the increasing complexity of the considered models.

For all the analyses we consider, we assume white, stationary-Gaussian noise in two co-located and co-aligned detectors with variances $\sigma_{n_1}^2$ and $\sigma_{n_2}^2$, respectively. The assumption of co-located and co-aligned detectors means that we can ignore the ORF, which, as one recalls, encodes the reduction in cross-correlated power that comes from correlating two physically separated and possibly misaligned detectors, as introduced in Section 2.1.3 [79, 130]. To calculate the total SNR for each set of data, we use the average SNR per segment computed using formulas specified below for each dataset and rearrange Eq. (3.7) to solve for ρ_{tot}. We note that this ρ_{tot} is the total SNR of the continuous-in-time cross-correlation search, which assumes the signal is present in every segment of data. For our intermittent analyses, we use this definition of total SNR to quantify the strength of the GW signal.

3.3.1 Extension of Previous Work

Recall that in Section 3.1.2, the results of Drasco and Flanagan [111] were reproduced within a Bayesian framework, as illustrated in Figure 3.2. We remind the reader that the signals considered there are single-sample GW "bursts" drawn from a fixed Gaussian distribution with variance σ_b^2. We now build on this and proceed with the generalisation of the proposed GMM likelihood to allow for more realistic signals.

Model description

As a first step, we now allow multi-sample ($N \gg 1$) bursts of white stochastic GWs having duty cycle ξ, with signal samples drawn from a probability distribution that depends on the distance r to an individual source. For a source at arbitrary reference distance r_{ref}, we draw the signal samples from a Gaussian distribution with fixed variance σ_{ref}^2. For a source at a general distance r, we first draw the signal samples from a Gaussian distribution with variance σ_{ref}^2 as explained above, and then rescale the samples by a factor of r_{ref}/r, since GW signal amplitudes fall off as $1/r$ [190]. Thus,

$$\sigma_b^2(r) \equiv \sigma_{\mathrm{ref}}^2 \frac{r_{\mathrm{ref}}^2}{r^2} \tag{3.23}$$

is the burst variance for a source at distance r.

For the population model, we will assume that the source distances are drawn from a UIV probability distribution

$$p(r|r_{\mathrm{max}}) \equiv \frac{3r^2}{r_{\mathrm{max}}^3 - r_{\mathrm{min}}^3}\,, \tag{3.24}$$

where r_{max} is the maximum distance out to which the sources are formed (i.e., an unknown population parameter that will eventually be inferred from the data). The parameter r_{min} is taken to be a fixed, known parameter, for simplicity. Note that choosing $r_{\mathrm{min}} \neq 0$ in the simulation process limits the number of GW bursts that are so loud that they are individually detectable in a single segment of data. We also note that this choice of population model is a simplification as it does not take into account cosmology.

It follows from Eqs. (3.23) and (3.24) that

$$p(\sigma_b^2(r)|r_{\mathrm{max}}) = \frac{3r_{\mathrm{ref}}^3}{2(r_{\mathrm{max}}^3 - r_{\mathrm{min}}^3)} (\sigma_{\mathrm{ref}}^2)^{3/2} (\sigma_b^2(r))^{-5/2} \tag{3.25}$$

is the probability distribution for the signal variance $\sigma_b^2(r)$ associated with a source at distance r. We also define the population-averaged burst variance:

$$\langle \sigma_b^2 \rangle \equiv \int_{r_{\mathrm{min}}}^{r_{\mathrm{max}}} \mathrm{d}r\, p(r|r_{\mathrm{max}}) \sigma_b^2(r) = 3\sigma_{\mathrm{ref}}^2 \frac{r_{\mathrm{ref}}^2 (r_{\mathrm{max}} - r_{\mathrm{min}})}{r_{\mathrm{max}}^3 - r_{\mathrm{min}}^3}\,, \tag{3.26}$$

which is obtained by averaging $\sigma_b^2(r)$ over the UIV-distributed source distances r. We define $\sigma_{\mathrm{GW}}^2 \equiv \xi \langle \sigma_b^2 \rangle$, which has the interpretation of being the time and population-averaged variance of the signals. This quantity is what the SSC estimates.

Since the probability distribution for $\sigma_b^2(r)$ depends on just one free parameter, i.e., $r_{\max}$ in Eq. (3.25), we can equally well use the population-averaged variance $\langle\sigma_b^2\rangle$ as the population parameter for the probability distribution. Solving Eq. (3.26) for $r_{\max}$ in terms of $\langle\sigma_b^2\rangle$, we find

$$\begin{aligned} r_{\max} &= r_{\min}\left(\sqrt{-\frac{3}{4}+3\frac{\sigma^2_{b,\max}}{\langle\sigma_b^2\rangle}}-\frac{1}{2}\right), \\ \sigma^2_{b,\max} &\equiv \sigma_b^2(r_{\min}) = \sigma^2_{\text{ref}}\frac{r^2_{\text{ref}}}{r^2_{\min}}, \end{aligned} \tag{3.27}$$

leading to

$$p(\sigma_b^2(r)|\langle\sigma_b^2\rangle) = \frac{\langle\sigma_b^2\rangle(\sigma^2_{b,\max})^{1/2}}{\sqrt{-3+12\sigma^2_{b,\max}/\langle\sigma_b^2\rangle}-3}(\sigma_b^2(r))^{-5/2}. \tag{3.28}$$

The above expression is somewhat messy, but it will be useful when we perform Bayesian inference on $\langle\sigma_b^2\rangle$. Building on the above, we define the average segment SNR of the distribution in a similar manner as Eq. (3.26):

$$\langle\rho_{\text{seg}}\rangle = \int_{r_{\min}}^{r_{\max}} \mathrm{d}r\, p(r|r_{\max})\rho_{\text{seg}}(r), \tag{3.29}$$

where $\rho_{\text{seg}}(r)$ for these signals is given by Eq. (3.5) with σ_b^2 replaced by $\sigma_b^2(r)$.

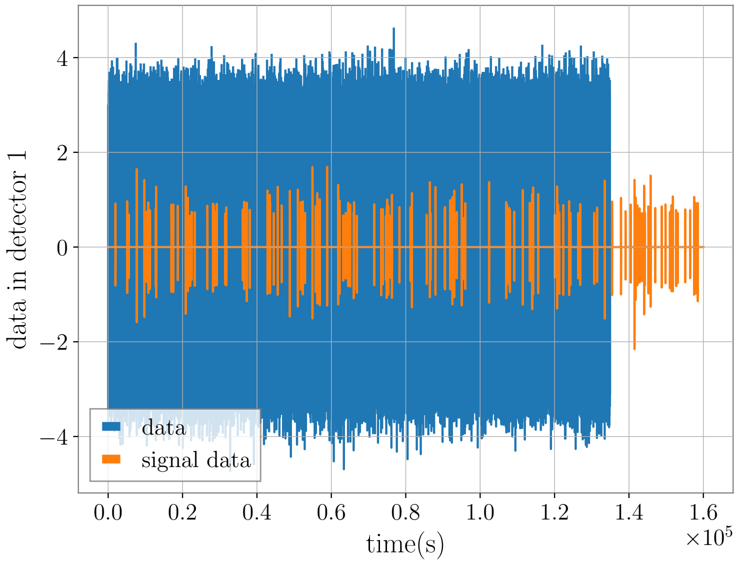

Figure 3.4. Example of simulated data with amplitudes drawn from a UIV distribution. The parameters used for this injection are given in the ‘Extension of previous work’ section of Table 3.1.

Extension of previous work										
$N_{\rm seg}$	N	ξ	$r_{\rm min}$	$r_{\rm max}$	$r_{\rm ref}$	$\sigma^2_{\rm ref}$	$\langle\sigma^2_b\rangle$	σ^2_n	$\langle\rho_{\rm seg}\rangle$	$\rho_{\rm tot}$
4×10^4	2048	2.98×10^{-3}	2	5	1	1	0.0769	0.691	5.04	3

Stochastic bursts												
$N_{\rm seg}$	N	T	ξ	$r_{\rm min}$	$r_{\rm max}$	$r_{\rm ref}$	$\Omega_{\rm ref}$	$\langle\Omega_b\rangle$	$f_{\rm low}$	$f_{\rm high}$	$\langle\rho_{\rm seg,stoch}\rangle$	$\rho_{\rm tot,stoch}$
4×10^4	2048	4 s	2.98×10^{-3}	2 Mpc	5 Mpc	2 Mpc	2.61	0.803	20 Hz	256 Hz	5.04	3

Deterministic chirps													
$N_{\rm seg}$	N	T	$r_{\rm min}$	$r_{\rm max}$	$f_{\rm low}$	$f_{\rm high}$	m	$\langle\Omega_b\rangle$	ξ	$\langle\rho_{\rm seg,stoch}\rangle$	$\rho_{\rm tot,stoch}$	$\langle\rho_{\rm seg,det}\rangle$	$\rho_{\rm tot,det}$
4×10^4	2048	4 s	2 Mpc	5 Mpc	20 Hz	256 Hz	30 $M_\odot$	0.803	2.98×10^{-3}	5.04	3	13.2	7.86

Table 3.1. Parameters used for the different analyses in Section 3.3. Parameters listed in ‘Extension of previous work’ and ‘Stochastic bursts’ were used in the production of Figure 3.6 and Figure 3.7, respectively. The first 9 columns in ‘Deterministic chirps’ were used in the production of Figure 3.9, while the last 5 columns specified the additional parameters used for Figures 3.10 and 3.11.

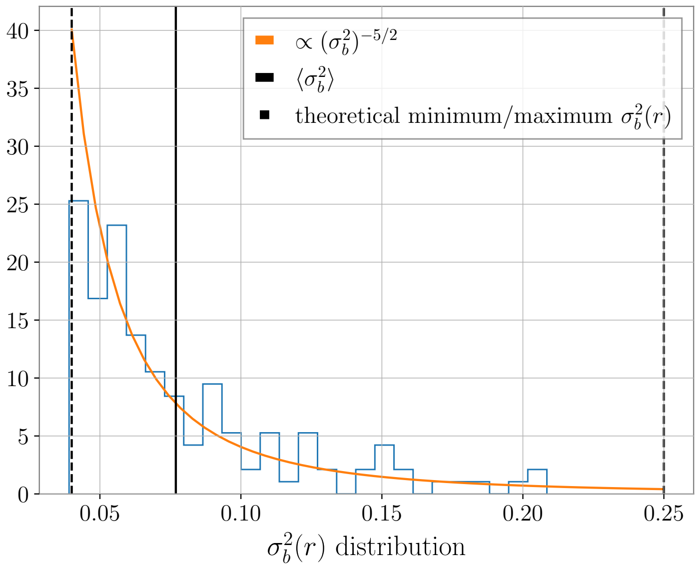

Figure 3.5. Distribution of the burst variances drawn from a UIV distribution, with theoretical minimum and maximum burst variance evaluated at r_{max} and r_{min}, respectively, and average burst variance $\langle\sigma_b^2\rangle$ computed according to Eq. (3.26).

Results

We now generate multi-sample ($N = 2048$) bursts of white stochastic GWs having duty cycle $\xi = 2.98 \times 10^{-3}$, with signal samples drawn from a probability distribution that depends on the distance r to an individual source, as described above. With the chosen parameters (listed explicitly in Table 3.1) the population-averaged variance is $\langle\sigma_b^2\rangle = 0.0769$ and the noise variances are $\sigma_{n_1}^2 = \sigma_{n_2}^2 = 0.691$. An example of the simulated data is shown in Figure 3.4, together with the distribution of the burst variances $\sigma_b^2(r)$ in Figure 3.5.

We analyse the data with SSC and SSI, using the full version of the likelihoods, i.e., inferring the noise parameters as well as the population parameters. We will not consider DSI for this particular data. The concrete expressions for the likelihoods can be found in Appendix A.1. In Figure 3.6, we display the recovery of our SSI search, illustrating that the generalisations made in this section compared to Section 3.1.2 still allow for a successful recovery of the population and noise parameters.

We note that given the large number of samples per segment ($N = 2048$) used for this analysis, one could have resorted to the reduced version of the likelihoods, where the estimates of the noise parameters are used, as provided in Appendix A.1.4. We refrain from entering into a detailed comparison between full and reduced implementations of the likelihoods, as this was the topic of work by Matas and Romano [197]. However, throughout the remainder of this chapter, we will work with a large number of samples per segment and will employ the reduced version of the likelihoods.

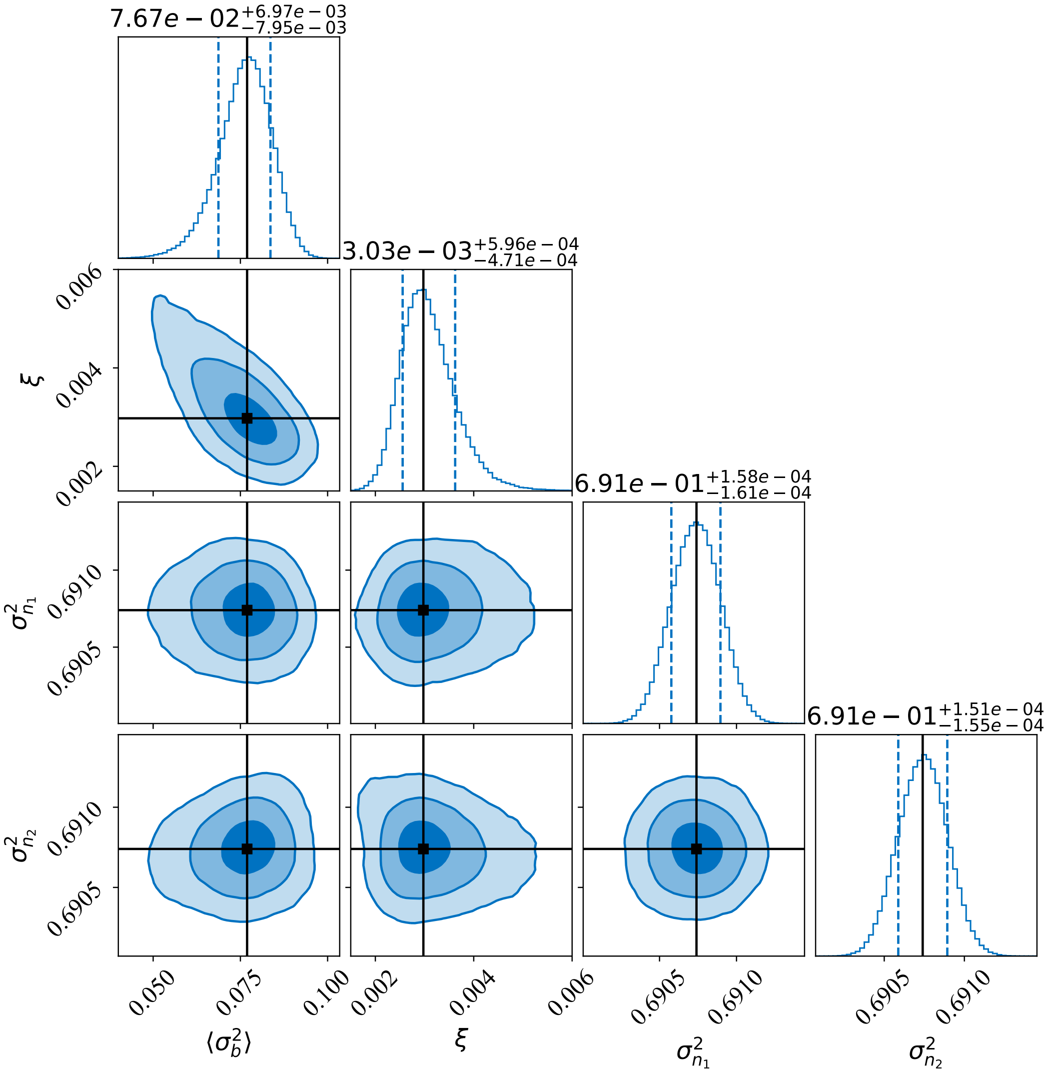

Figure 3.6. Corner plot for the full version of the SSI analysis, combining the posteriors of 100 realisations of the data. The black lines show the injected values of the parameters used for the simulated data, and the three shaded regions for the 2D joint posteriors correspond to 1σ, 2σ, and 3σ uncertainty levels. All parameters are recovered within a 1σ credible interval.

3.3.2 Stochastic Bursts

We extend the analysis described in the previous section to include frequency dependence. We analyse data defined by multi-sample ($N \gg 1$) bursts of stochastic GWs having duty cycle ξ and an $f^{-7/3}$ PSD[12], for a UIV distribution of source distances between $r_{\rm min}$ to $r_{\rm max}$, as in Section

---

[12] Note that we only generalise the signal PSD to a frequency-dependent spectrum. The injected noise remains white and Gaussian.

3.3.1. The choice of spectral index $\alpha = -7/3$ is appropriate for compact binary inspiral. We first simulate data for a source at reference distance $r_{\rm ref}$ so that it has the following PSD[13]:

$$P_{\rm ref}(f) = A_{\rm ref}\left(\frac{f}{f_{\rm ref}}\right)^{-7/3}, \tag{3.30}$$

where $A_{\rm ref}$ is some fixed amplitude, and $f_{\rm ref}$ is a reference frequency, usually taken to be 25 Hz in line with LVK searches [19]. For a source at a general distance r, we do the same as above, and then rescale the amplitude of the simulated signal by a factor of $r_{\rm ref}/r$, which is equivalent to having

$$A_b(r) \equiv A_{\rm ref}\frac{r_{\rm ref}^2}{r^2} \tag{3.31}$$

as the amplitude of the PSD for a GW burst at source distance r. The PSD of a burst is therefore

$$P_b(r;f) = A_{\rm ref}\frac{r_{\rm ref}^2}{r^2}\left(\frac{f}{f_{\rm ref}}\right)^{-7/3}. \tag{3.32}$$

Note that by using Eq. (2.15), we can also write the above expression in terms of the fractional energy density spectrum $\Omega_b(r;f)$. Then by taking $f = f_{\rm ref}$, we can define the amplitude of the energy density at reference frequency $f_{\rm ref}$ of a burst at distance r:

$$\Omega_b(r) \equiv \frac{10\pi^2}{3H_0^2} f_{\rm ref}^3 P_b(r; f_{\rm ref}) = \Omega_{\rm ref}\frac{r_{\rm ref}^2}{r^2}, \qquad \Omega_{\rm ref} \equiv \frac{10\pi^2}{3H_0^2} f_{\rm ref}^3 A_{\rm ref}. \tag{3.33}$$

By following the same derivation as the one given in Eq. (3.26), the population-averaged energy density amplitude for sources distributed uniformly-in-volume between $r_{\rm min}$ and $r_{\rm max}$ is

$$\langle\Omega_b\rangle = 3\Omega_{\rm ref}\frac{r_{\rm ref}^2(r_{\rm max} - r_{\rm min})}{r_{\rm max}^3 - r_{\rm min}^3}. \tag{3.34}$$

The probability distribution of the amplitude of the energy density of the bursts $\Omega_b(r)$ has the same form as Eq. (3.28):

$$p(\Omega_b(r)|\langle\Omega_b\rangle) = \frac{\langle\Omega_b\rangle\Omega_{b,\rm max}^{1/2}}{\sqrt{-3 + 12\Omega_{b,\rm max}/\langle\Omega_b\rangle} - 3}\,\Omega_b^{-5/2}(r), \qquad \Omega_{\rm b,max} \equiv \Omega_b(r_{\rm min}). \tag{3.35}$$

Thus, the signal segment likelihood used for SSI is given by Eqs. (3.12) (full) and (3.17) (reduced) with prior given by Eq. (3.35) (i.e., $\pi(\Omega_{b,I}|\langle\Omega_b\rangle) = p(\Omega_b(r_I)|\langle\Omega_b\rangle)$). The integration bounds are then $\Omega_{\rm b,min}(\langle\Omega_b\rangle)$ and $\Omega_{\rm b,max}$ where $\Omega_{\rm b,min} = \Omega_b(r_{\rm max})$ and $r_{\rm max}$ is written in terms of

---

[13] In practice, we first simulate the data in the frequency domain with an amplitude spectral density $\sqrt{P_{\rm ref}(f)}$ and random phases, and then inverse-Fourier-transform the data back to the time domain.

the population parameter $\langle\Omega_b\rangle$, in the same manner as in Eq. (3.27).

For reference, we note that the expected value of the stochastic (optimally-filtered) SNR for a segment that contains a GWB burst is

$$\rho_{\rm seg,stoch} = \sqrt{2T}\left[\int_{f_{\rm low}}^{f_{\rm high}} df\, \frac{P_b^2(f)}{P_{n_1}P_{n_2}}\right]^{1/2}, \tag{3.36}$$

where P_{n_1} and P_{n_2} are the noise PSDs in each detector. Note that, if the two detectors were not co-located and co-aligned, we would need to include a factor of the ORF squared in the numerator of the integrand in the above equation, as was the case in Eq. (2.34) [79, 130]. The above expression for $\rho_{\rm seg,stoch}$ is a *power* SNR, defined as the expected value of the optimally-filtered cross-correlation statistic divided by its standard deviation, see e.g., [230].

Results

As mentioned before, our stochastic-signal-based search looks for a GWB consistent with a PSD with spectral index $\alpha = -7/3$, as expected for BBH mergers. In contrast, the deterministic-signal-based search described in Section 3.1.3 (which we call DSI) looks for deterministic BBH chirp waveforms, where the signal parameters of the individual chirps must be marginalised over. We inject intermittent, stochastic bursts with an $f^{-7/3}$ PSD and duty cycle $\xi = 2.98\times10^{-3}$. The parameters used for the injection are displayed in Table 3.1. We arbitrarily choose the reference distance $r_{\rm ref} = r_{\rm min}$. The value of $\Omega_{\rm ref}$ is chosen to be 2.61 (to be consistent with the parameters chosen in Section 3.3.3). With these parameters, the population-averaged energy density amplitude of the bursts is $\langle\Omega_b\rangle = 0.803$. The noise is then set such that the average SNR per segment, as computed with Eq. (3.36), is 5.04 to give a total SNR of $\rho_{\rm tot} = 3$, as obtained by using Eq. (3.7).

We analyse our data with the reduced likelihood forms which estimate the noise parameters of SSI and DSI. The exact form of the likelihood is given in Eq. (3.17) (with coarse-graining factor $M = 16$) and Eq. (A.2.4), respectively. The population parameter recovered by SSI is $\langle\Omega_b\rangle$ while the population parameter recovered by DSI is $r_{\rm max}$. However, we note that these are related by Eq. (3.34) and can easily be mapped into each other. In Figure 3.7, we demonstrate that DSI cannot recover the signal in the data, since no chirp waveform exists. While this result is in a sense obvious, it highlights the challenges that a deterministic-signal-based search faces. Incorrectly modelling the waveforms of the chirps could lead the search to overlook a signal which is present. Conversely, SSI recovers both stochastic bursts of GW power as well as deterministic waveforms, as we will see in the next section.

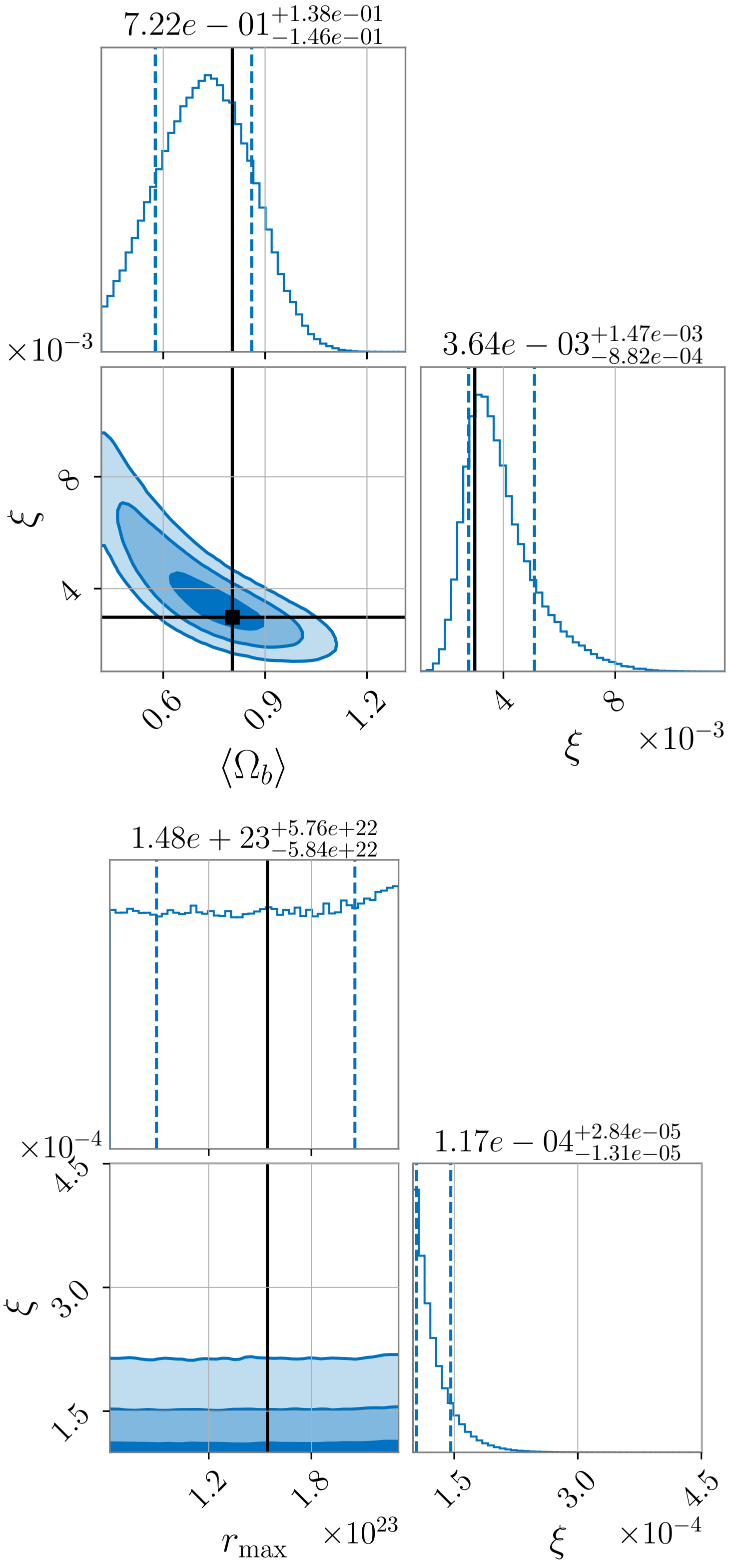

Figure 3.7. For intermittent, stochastic bursts with an $f^{-7/3}$ PSD, we demonstrate recovery of our search (top) and compare it to that of a deterministic-signal-based search (bottom). Our search recovers the injected signal parameters within a 1σ credible interval, while DSI recovers the uniform prior on $r_{\rm max}$ and the lower boundary of the prior imposed on the duty cycle ($\xi = 10^{-4}$). Thus, the DSI analysis finds no signal in the data.

3.3.3 Deterministic Chirps

Finally, we consider multi-sample bursts of GWs produced by deterministic BBH chirp signals, for a UIV distribution of sources as in Eq. (3.24). The corresponding PSD will necessarily have an approximate $f^{-7/3}$ frequency dependence. By using deterministic BBH chirp signals, this analysis is more in line with the assumptions made by the deterministic-signal-based search DSI.

Model description

We assume that all parameters defining the chirp waveforms except for the distances to the sources (e.g., the chirp mass $\mathcal{M}_c \equiv (m_1 m_2)^{3/5}/(m_1+m_2)^{1/5}$, the inclination angle ι, the coalescence time $t_{\rm col}$, and the phase of coalescence within a segment) have fixed values and are known a priori by the DSI search. For simplicity, we choose the two component masses to be equal (i.e., $m_1 = m_2 \equiv m$); the inclination angle $\iota = \pi/2$ so that the source is linearly polarised (i.e., $h(t) = h_+(t)$, $h_\times(t) = 0$); the phase at coalescence Φ_0 to be zero; and the coalescence time $t_{\rm col}$ to occur at the end of a segment, so $t_{\rm col} = T$, the segment duration. Fixing the value of almost all waveform parameters allows us to simplify our implementation of DSI without having to resource to marginalisation over all these parameters. Nevertheless, our implementation of the DSI method retains two important aspects of the DSI search: the deterministic waveforms and the intermittent nature of the signal.

For a source drawn from the population with distance r, the explicit form for the simulated deterministic chirp signal is given in the time domain by [190]:

$$h_{\rm chirp}(t;r) = \frac{1}{2r}\left(\frac{G\mathcal{M}_c}{c^2}\right)^{5/4}\left(\frac{5}{c\tau}\right)^{1/4}\cos\left[\Phi(\tau)\right]\,, \qquad \tau \equiv t_{\rm col} - t\,. \tag{3.37}$$

The quantity

$$\Phi(\tau) \equiv -2\left(\frac{5G\mathcal{M}_c}{c^3}\right)^{-5/8}\tau^{5/8} + \Phi_0 \tag{3.38}$$

encodes the frequency evolution of the chirp:

$$f(t) \equiv -\frac{1}{2\pi}\frac{\mathrm{d}}{\mathrm{d}\tau}\Phi(\tau) = \frac{1}{\pi}\left(\frac{G\mathcal{M}_c}{c^3}\right)^{-5/8}\left(\frac{5}{256}\frac{1}{\tau}\right)^{3/8}. \tag{3.39}$$

The corresponding BBH chirp PSD is

$$P_{\rm chirp}(r;f) = \frac{2}{T}\left|\tilde{h}_{\rm chirp}(r;f)\right|^2 \equiv A_{\rm chirp}(r)\left(\frac{f}{f_{\rm ref}}\right)^{-7/3}, \tag{3.40}$$

where $\tilde{h}_{\rm chirp}$ is the Fourier transform of the chirp waveform and

$$A_{\rm chirp}(r) = A_{\rm ref}\frac{r_{\rm ref}^2}{r^2}\,, \qquad A_{\rm ref} \equiv \frac{2}{T}\frac{c^2}{4r_{\rm ref}^2}\left(\frac{5\pi}{24}\right)\left(\frac{G\mathscr{M}_c}{c^3}\right)^{5/3}(\pi f_{\rm ref})^{-7/3}\,. \tag{3.41}$$

Note one can express the chirp PSD $P_{\rm chirp}$ in terms of the fractional energy density of the chirps $\Omega_{\rm chirp}$ by using Eq. (2.15). Figure 3.8 shows a plot of a representative BBH chirp signal in the time domain (top panel) and an average over an ensemble of BBH chirp signals in the frequency domain (bottom panel).

For reference, we note that the expected value of the deterministic (matched-filter) SNR for a segment which contains a BBH chirp signal is [230]:

$$\rho_{\rm seg,det} = \left[4\sum_{\mu=1}^{2}\int_{f_{\rm low}}^{f_{\rm high}} {\rm d}f\;\frac{|\tilde{h}_{\rm chirp}(f)|^2}{P_{n_\mu}}\right]^{1/2} = \sqrt{2T}\left[\sum_{\mu=1}^{2}\int_{f_{\rm low}}^{f_{\rm high}} {\rm d}f\;\frac{P_{\rm chirp}(f)}{P_{n_\mu}}\right]^{1/2}\,, \tag{3.42}$$

where P_{n_μ} is the noise PSD in detector $\mu = 1, 2$, as defined in Eq. (3.11). The above expression for $\rho_{\rm seg,det}$ is an *amplitude* SNR, defined as the expected value of the matched-filter statistic divided by its standard deviation. The quadrature sum takes into account the contribution from using both detectors to do the analysis.

As mentioned in Section 3.1.2, the detection statistic in our Bayesian framework is the Bayes factor where the models in Eq. (2.43) are the signal+noise model and the noise only model for a particular search. While SSC and SSI contain the same noise model, the noise model in DSI does not take the same form. Hence, the Bayes factors for the different searches are not computed with respect to the same noise model and one cannot compare these methods with one another in terms of the Bayes factor. Instead, we evaluate how the intermittent nature of the signal impacts each search method's effectiveness in recovering the signal by plotting the ln Bayes factor as a function of the duty cycle. In other words, we wish to answer two questions:

1. How well does SSI do in recovering the signal at different duty cycles for a constant total stochastic SNR?

2. How well does DSI do in recovering the signal at different duty cycles for a constant total deterministic SNR?

The answers to the questions are independent of one another and cannot be used as a way to assess if one search is "better" than the other. However, since SSC and SSI contain the same noise model, these searches can be compared to one another using the Bayes factor.

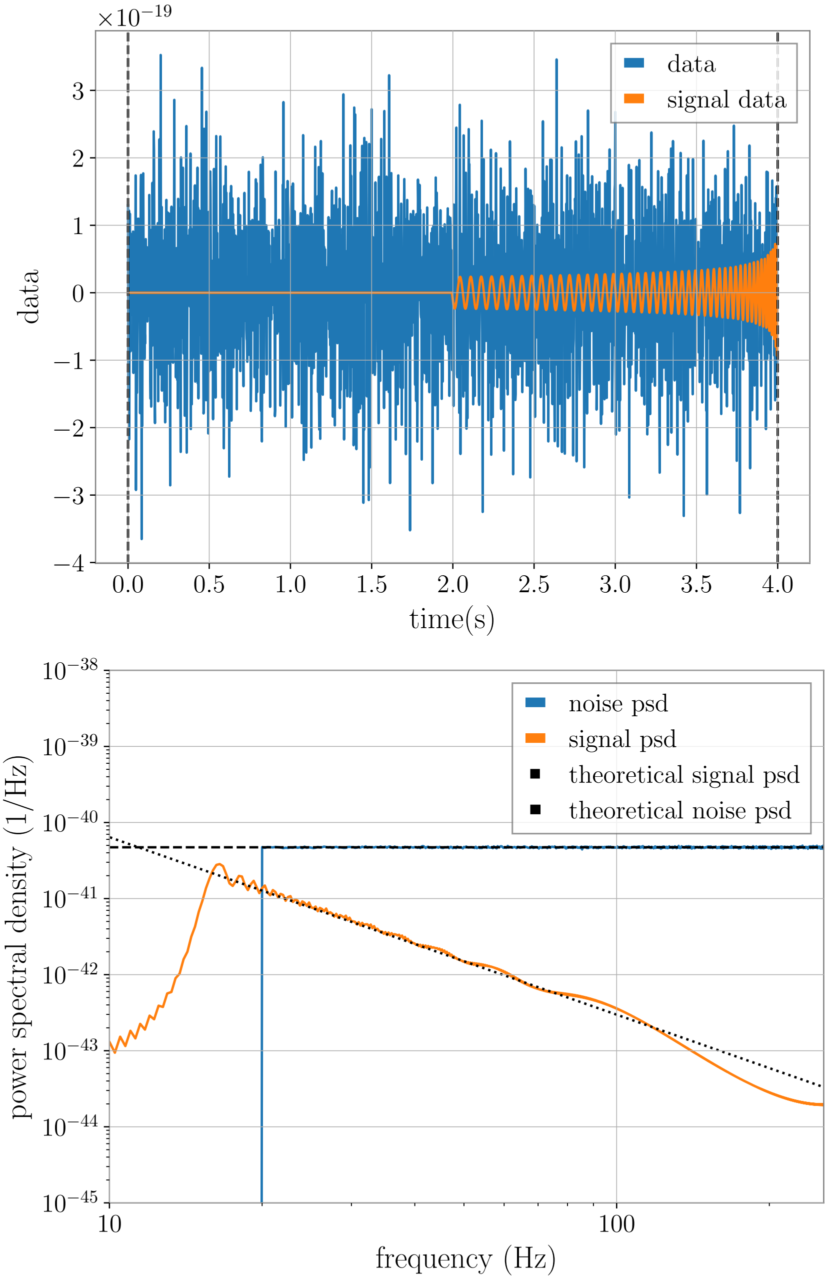

Figure 3.8. **Top:** Example BBH chirp signal in the time domain as given by Eq. (3.37). **Bottom:** Averaged PSD of an ensemble of BBH chirp signals as a function of frequency for the noise and signal separately, together with their theoretical predictions according to the injected values.

Results

In order to assess the efficiency of the methods with respect to their respective noise-only models, we simulate 40,000 segments of data with each segment being 4 seconds long. We choose values of $r_{\text{min}} = 2$ Mpc, $r_{\text{max}} = 5$ Mpc and the BBH component masses to each be $30 M_\odot$. These parameters give a value of $\langle \Omega_b \rangle = 0.803$. The parameters used for this analysis are tabulated in the first 9 columns of the 'Deterministic chirps' section in Table 3.1. Thus, the signal has the same strength as in Section 3.3.2, but it is now composed of deterministic chirps, instead of stochastic bursts. The same coarse-graining factor and low- and high-frequency cut-offs that were used in Section 3.3.2 are used for this case as well when analysing the data.

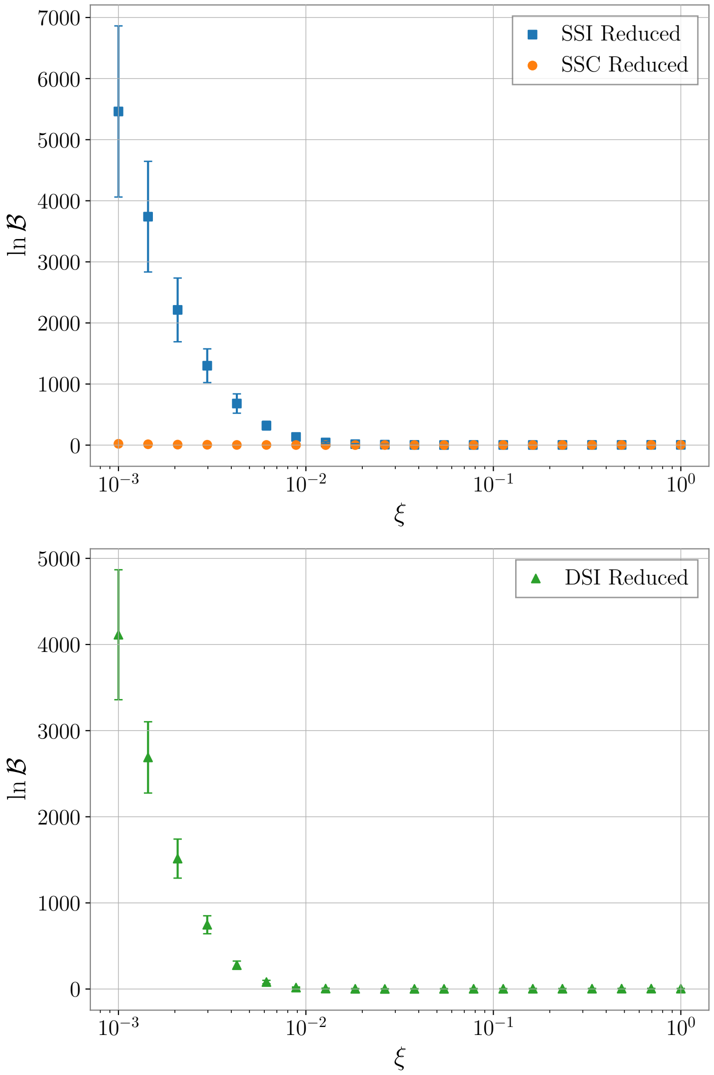

Figure 3.9. Plots of the ln Bayes factor averaged over 100 data realisations for SSC and SSI (top) and DSI (bottom) for deterministic chirp signals occurring with various values of the duty cycle ξ. Both intermittent searches are well-suited for detecting signals with a low duty cycle.

Figure 3.9 shows the ln Bayes factors for the stochastic-signal-based searches (top panel) and for the deterministic-signal-based search (bottom panel) as a function of the duty cycle. Analogously to what was done in Section 3.1.2, the total SNR is kept constant by adjusting the noise levels. For the stochastic searches, we keep the total power SNR constant, computed using Eq. (3.36), while for the deterministic search we keep the total amplitude SNR constant, obtained using Eq. (3.42). We see that both intermittent searches (SSI and DSI) perform well at low duty cycles, with values of the ln Bayes factors reaching over 1000 for some of the smallest values of the duty cycle considered.

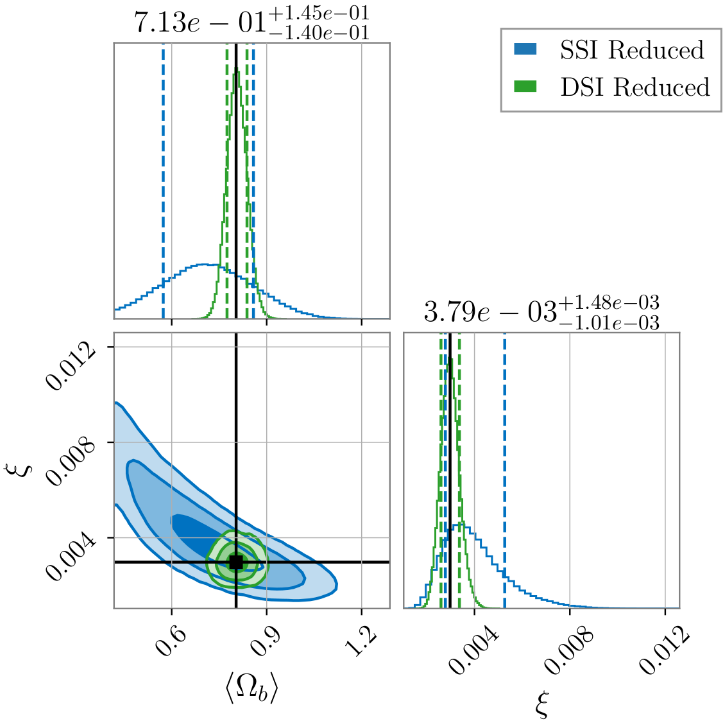

Figure 3.10. Posterior corner plot combined over 100 data realisations analysed with SSI Reduced (blue) and DSI Reduced (green). Both searches recover the injected signal parameters ($\xi = 2.98 \times 10^{-3}$ and $\langle\Omega_b\rangle = 0.803$) within a 1σ confidence interval. The reported recovered values and uncertainties are those recovered by the SSI Reduced search.

In order to directly compare SSI with DSI, we now run both analyses on the same dataset. The data is generated such that the duty cycle is $\xi = 2.98 \times 10^{-3}$. The signal is the same as described above and the noise variance is chosen such that the average stochastic SNR per segment, computed using Eq. (3.36), is equal to 5.04 and the total stochastic SNR is equal to 3. Note for these values, the average deterministic SNR per segment, computed using Eq. (3.42), is 13.20 with the total deterministic SNR being 7.86, which is considerably larger than the total stochastic SNR. Note that these parameters are displayed in the remaining columns of the 'Deterministic chirps' section of Table 3.1. A comparison of the recovered corner plots is shown in Figure 3.10. We see that for this data, both searches recover the signal within a 1σ credible interval, with the error bars for DSI much smaller than SSI, due to the deterministic approach appropriately modelling the chirp waveform of the signal. We also show a comparison of 1D posterior plots[14] of Ω_{GW} in Figure 3.11. Similarly to the corner plot, the posterior width is smaller for DSI than SSI, although SSI still performs better than SSC.

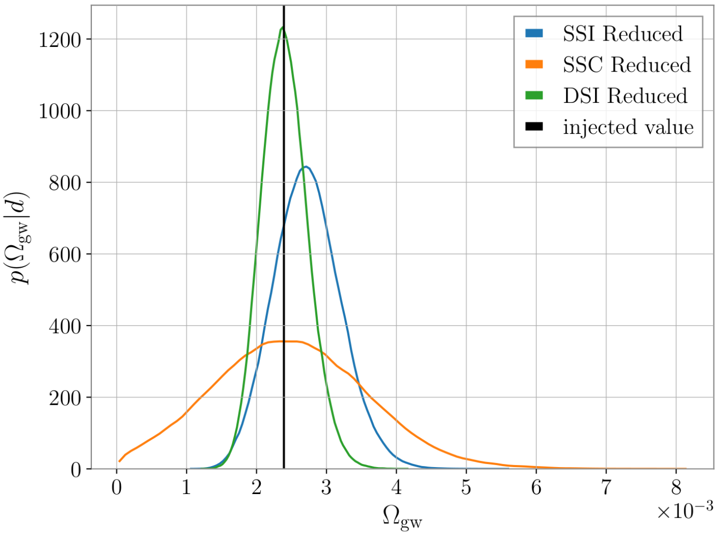

Figure 3.11. 1D posterior plot of Ω_{GW} samples from SSI Reduced (blue), SSC Reduced (orange) and DSI Reduced (green) constructed by combining posterior samples for ξ and $\langle\Omega_b\rangle$ using Eq. (3.10). Note that the inference done with the DSI likelihood gives posterior samples for the parameters ξ and r_{max} and the values of r_{max} are then converted to samples in $\langle\Omega_b\rangle$ by Eq. (3.34), since the other variables in Eq. (3.34) are fixed and known.

One notes a small bias in the recovery of Ω_{GW} for SSI in Figure 3.11. In Figure 3.12 we show the relative difference of the injected value and recovered value of Ω_{GW} as a function of ξ for the three searches, together with the 1σ uncertainty band, after combining the posterior over 100 realisations of data. We note that the biased recovery is not always towards higher values of Ω_{GW}. We also note that the width of the uncertainty for the DSI analysis improves as ξ increases because the total deterministic SNR is not held constant and increases.

To conclude, we give an estimate of the improvement in time-to-detection of a GWB with our search. Note that this estimate is computed under the assumptions adopted in this chapter and will therefore most likely differ for a realistic detector configuration, with realistic detector noise. We also note that the strength of the signal may affect these values. Nevertheless, to obtain such an estimate, we simulate a GWB consisting of deterministic chirps with parameters $\langle\rho_{\text{seg,stoch}}\rangle = 2$ (corresponding to $\langle\rho_{\text{seg,det}}\rangle = 8.3$) and $\xi = 2.98\times10^{-3}$. We then vary the number

---

[14] For both SSI and DSI, the posterior plot on Ω_{GW} is obtained by multiplying the posterior on ξ with the posterior on $\langle\Omega_b\rangle$ according to Eq. (3.10).

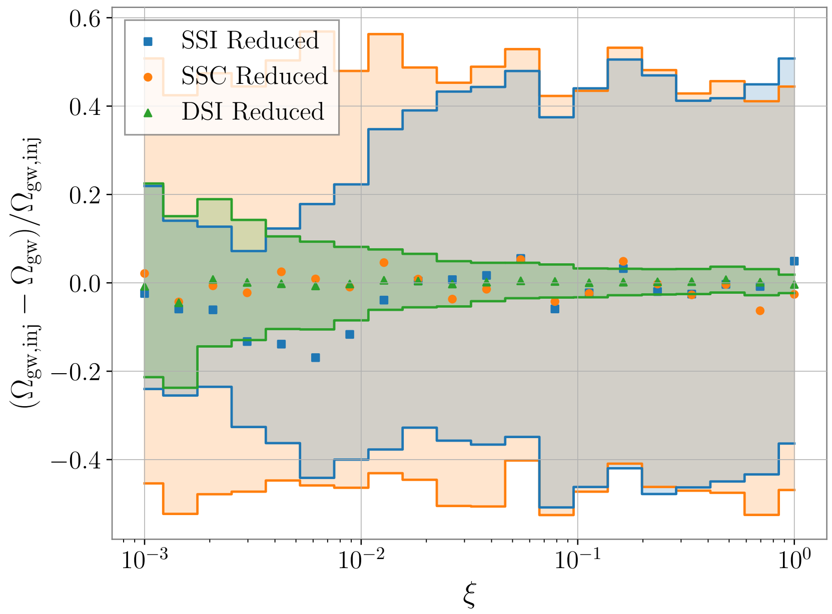

Figure 3.12. Comparison of recovered values to injected value of $\Omega_{\rm GW}$ for SSI Reduced (blue), SSC Reduced (orange) and DSI Reduced (green) for different values of the duty cycle. All injected parameters are equivalent to the parameters used in the top panel of Figure 3.9 and the recovered values are those after combining 100 realisations of data. The shaded regions represent the 1σ credible interval of the combined 100 realisations of data.

of data segments and assess how many 4 second segments are needed to reach a threshold value of the ln Bayes factor which is large enough to claim a detection. We define this threshold to be of value 12.5, corresponding to a detection with SNR equal to 5. This is shown in Figure 3.13 for SSI and SSC. Due to the large difference in deterministic and stochastic SNR, the ln Bayes factor for DSI already reaches $\sim$ 160 at the first value of $N_{\rm seg}$ considered. We therefore do not include DSI on this plot to avoid scaling issues. We estimate that SSC would cross this threshold after 650,000 segments of data, whereas SSI already reaches this threshold after 12,000 segments. This corresponds to a factor of $\sim$ 54 improvement in time-to-detection for SSI versus SSC for these parameters and assumptions.

The above sections established the methodology behind SSI and illustrated its performance relative to other search methods for a series of toy models of increasing complexity. Although these results are a testament to the promising capabilities of the method, several alterations need to be implemented before being able to run on real detector data. Some of these are discussed in the next section.

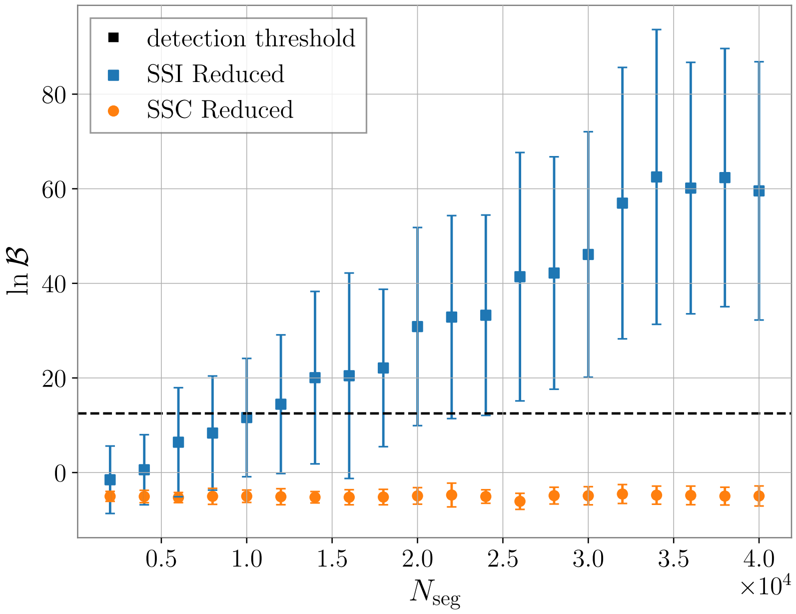

Figure 3.13. ln Bayes factor vs $N_{\rm seg}$ for data with $\langle \rho_{\rm seg,stoch} \rangle = 2$ and $\xi = 2.98 \times 10^{-3}$. We define a detection threshold of $\ln \mathcal{B} = 12.5$. SSI crosses this threshold after $\sim 12{,}000$ segments of data, while SSC crosses this threshold after $\sim 650{,}000$ segments of data, corresponding to a factor of improvement in detecting the signal of roughly 54 for SSI relative to SSC.

3.4 Towards More Realistic Signals

Our work [176] ended with a series of possible generalisations towards more realistic signals to allow us to run our method on real detector data. This section contains unpublished results to illustrate the steps undertaken in an attempt to make our SSI method work on more realistic data. This section is meant to give a broad overview of the current generalisations and showcase the improvements since the publication of [176], rather than an in depth discussion of each aspect. Concretely, the following points are addressed:

- Integration of SSI within the `pygwb` package
- Non co-located, non co-aligned detector configurations
- Coloured noise PSDs

Each of these points is briefly touched upon below, with some preliminary, unpublished results to illustrate each of the generalisations.

3.4.1 Integration of SSI within `pygwb`

After the publication of our work [176], the SSI code was slightly rewritten to be able to make extensive use of the capabilities of the `pygwb` package, which was introduced in Section 2.2.3 [222, 223]. Not only does this allow us to streamline the data generation and analysis thereof, but it also allows us to speed up the computation significantly. We highlight the most important changes related to this below. Additionally, this illustrates the synergy between the different parts of the thesis, connecting `pygwb` to other projects carried out during the timeline of this PhD.

Computation of CSDs and PSDs

Recall that in our SSI method, the strain data are used in the computation of the PSDs and CSDs on a segment per segment basis, making use of Eq. (3.15). These then entered the likelihood in e.g., Eqs. (3.18) and (3.20). Although previously computed with our own code implementation, the SSI likelihood now relies on `pygwb` to compute PSDs and CSDs. Outsourcing this computation to the `pygwb` package allows us to speed up the computation of these quantities, as `pygwb` is naturally equipped to run these computations in parallel. Additionally, the PSD and CSD computations now benefit from all the features present in the `pygwb` code, such as windowing, downsampling, etc. Although we did not have to rely on these techniques for our toy model data in [176], having access to these data processing methods is extremely useful as we move towards the analysis of real detector data.

Data simulation

On top of the vast simulation capabilities already present in the `simulator` module of the `pygwb` package, the module underwent several modifications to accommodate the needs of the SSI search. Concretely, all features present in our version of the SSI code were ported over to the `pygwb` package, allowing us to simulate intermittent stochastic bursts within the `pygwb` framework. Furthermore, CBC waveforms can easily be generated and injected in the simulated data, thanks to the interaction of `pygwb` with the `bilby` package [43]. These waveforms are generated using a pre-defined population of CBCs with specific mass and distance distributions, as well as sky-localisation and spin distributions. In addition, most waveform approximants include the full waveform, i.e., inspiral, merger and ringdown[15]. This allows us to steadily move towards more and more realistic signals and populations, relaxing some of the assumptions made in our methods paper [176]. For example, one could study the impact of modifying the mass distribution to results obtained by the LVK collaborations in their third observing run,

---

[15] Note that in our chirp toy model discussed in Section 3.3.3, only the $f^{-7/3}$ inspiral phase was considered in the simplified waveform.

instead of fixing the mass to an arbitrary value, as done in our work for simplicity (described in Section 3.3.3).

Additionally, as will be expanded upon below, one of the generalisations needed towards the analysis of real data is the ability to run our method on spatially separated detectors. Recall that in our work, we assumed the detectors to be co-located and co-aligned. However, the `simulator` module naturally accommodates non co-located and non co-aligned detectors, as will be discussed below.

Merging our method with the existing capabilities of the `pygwb` package and building upon these offers us a considerable head start in the generalisation of the method, both from the point of view of data analysis and data generation. Below, we discuss some additional modifications to the method, which all heavily rely on the interaction with the core functionalities of the `pygwb` package described previously.

3.4.2 Non Co-located and Non Co-aligned Detectors

For each of our toy models described in Section 3.3, the detectors were assumed to be co-located and co-aligned, for simplicity [176]. As discussed in Section 2.1.3, a non-trivial detector baseline geometry introduces the need for the ORF, which encapsulates the reduction in sensitivity due to the physical separation and relative orientation of the detectors. Here, we generalise the SSI method to allow for such non co-located and non co-aligned detector setups and introduce the ORF in the likelihood to properly take this into account. In practice, the expressions in Eqs. (3.18) and (3.19) of the SSI likelihood are modified as follows:

$$\hat{\Omega}_{b,I} \equiv \frac{\sum_k Q_I(f_k)\hat{P}_{b,Ik}}{\sum_{k'} Q_I(f_{k'})H(f_{k'})\gamma(f_k)}, \qquad \mathrm{var}(\bar{\Omega}_{b,I}) \equiv \left(2M\sum_k Q_I(f_k)H(f_k)\gamma(f_k)\right)^{-1} \tag{3.43}$$

and

$$Q_I(f) \equiv \frac{H(f)\gamma(f_k)}{\bar{P}_{1,I}(f)\bar{P}_{2,I}(f)}, \tag{3.44}$$

where $\gamma(f)$ denotes the baseline ORF in both expressions, as introduced in Section 2.1.3. The remainder of the likelihood is left unchanged. This simple alteration allows the SSI analysis to run on data obtained from non co-located and non co-aligned detectors. Additionally, from the point of view of data generation and the computation of PSDs and CSDs, we still entirely rely on the `pygwb` package. As pointed out in the previous section, data can easily be generated for non co-located and non co-aligned detectors in `pygwb` [222, 223]. We now move to the discussion of more realistic noise PSDs.

3.4.3 Coloured Noise PSD

Recall that the simulated noise in the various toy models presented in Section 3.3 was assumed to be white and Gaussian, i.e., without a frequency-dependent spectrum:

$$P_n(f) = \frac{\sigma_n^2}{f_{\text{high}} - f_{\text{low}}}, \tag{3.45}$$

where σ_n^2 denoted the noise variance, and f_{low} and f_{high} the low- and high-frequency cut-offs for our search. However, realistic noise curves from the LVK detectors are far from flat across the frequency range of interest. This was illustrated in e.g., Figure 1.5 of Section 1.2.1 where the noise PSD of the two LIGO detectors was displayed for a chunk of data in the third LVK observing run. We therefore generalise our investigation from the previous sections to non-trivial noise PSDs, both at the level of the signal simulation and the analysis, and allow for coloured, i.e., frequency-dependent, noise PSDs[16]. Concretely, the expression in Eq. (3.20) is altered such that the estimated noise PSDs are now given by:

$$\bar{P}_{1,I}(f) \equiv \bar{P}_{n_1}(f) + \Omega_{b,I} H(f), \qquad \bar{P}_{2,I}(f) \equiv \bar{P}_{n_2}(f) + \Omega_{b,I} H(f). \tag{3.46}$$

As previously mentioned in Section 3.4.1, for the estimation of the noise PSDs $\bar{P}_{n_i}(f)$ in each detector, we rely on the `pygwb` package. Note that switching to coloured noise PSDs therefore constitutes more of a conceptual change, rather than an involved coding alteration, although an important one nevertheless.

To illustrate the changes above, we simulate stochastic bursts for the LIGO Hanford and Livingston baseline, i.e., non co-located and non co-aligned detectors, and inject these in coloured noise that follows a LIGO-like[17] noise PSD. The parameters used for the simulation are provided in Table 3.2. The results are depicted in Figure 3.14, illustrating that the alterations to the SSI search were successful, still guaranteeing a recovery of the injected parameters.

Stochastic bursts, coloured noise, and non co-located detectors									
N_{seg}	N	T	r_{min}	r_{max}	f_{low}	f_{high}	m	$\langle\Omega_b\rangle$	ξ
10^5	2048	4 s	750 Mpc	1278 Mpc	20 Hz	256 Hz	30 $M_\odot$	10^{-5}	10^{-3}

Table 3.2. Parameters used for the analysis presented in Figure 3.14.

---

[16] Note that this does not include any non-stationarities and glitches that are present in real detector data. These are left for future investigation.

[17] By this, we mean it has the same spectral shape as the LIGO noise PSD, but is rescaled arbitrarily to obtain the desired SNR. In addition, we use a smooth version of the LIGO noise PSD to not have to deal with the noise lines in the spectrum, as presented in e.g., Figure 1.5. However, note that we could exclude these noise lines through a frequency notching procedure within `pygwb` [222, 223].

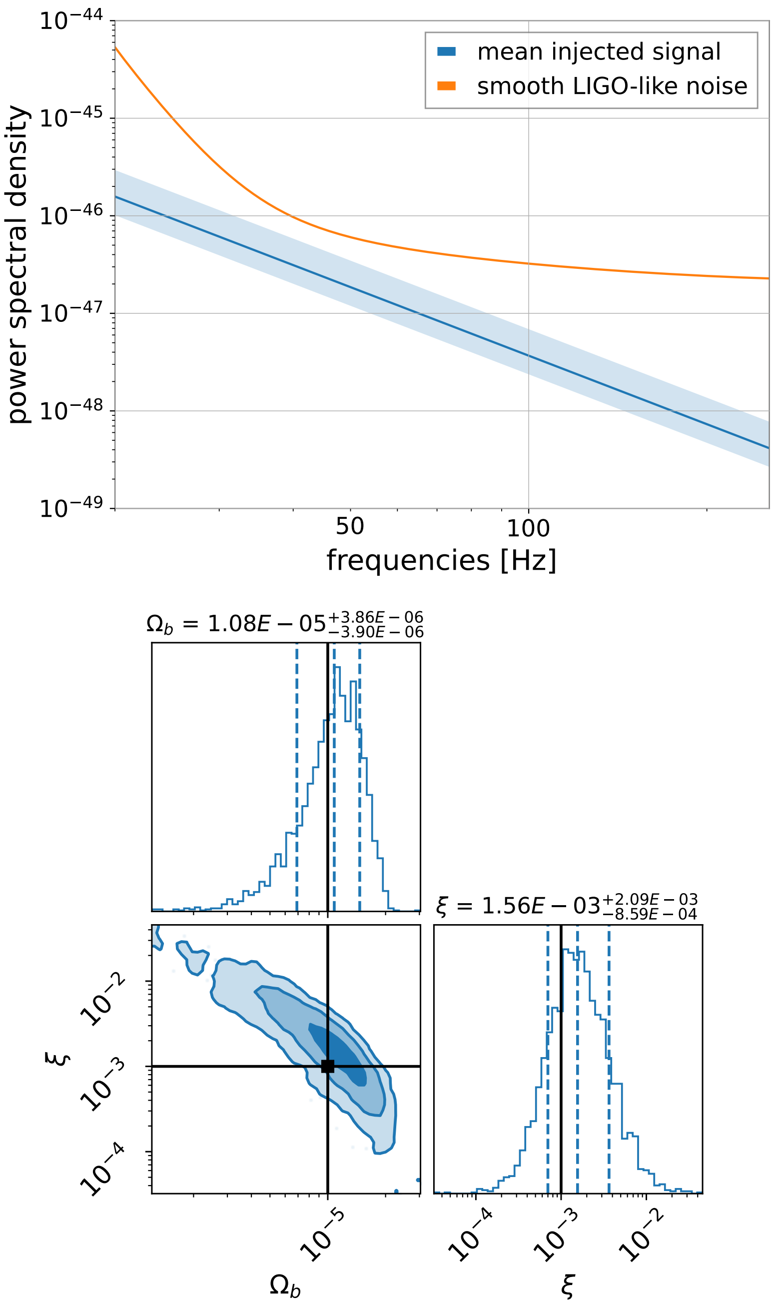

Figure 3.14. **Top**: Example of a coloured noise PSD (orange), introduced as one of the generalisations to our SSI method. The injected signal is made of stochastic bursts, with mean injected signal represented in blue. **Bottom**: Posterior corner plot for an individual data realisation to illustrate the generalisation to non co-located and non co-aligned detectors with coloured noise PSDs of the SSI method.

The above shows that we are able to generate signals for non co-located and non co-aligned detectors, with Gaussian coloured noise, bringing our SSI search a step closer to real detector data. To conclude this part on generalisations of the method, we now comment on updated detection prospects for SSI, given the above modifications to the code.

3.4.4 Updated Detection Prospects

The above alterations allow us to update predictions for the improvements of SSI compared to SSC, previously shown in Figure 3.13. In particular, we consider the time SSI would need to claim the detection of the predicted astrophysical BBH background. Concretely, we consider the LIGO Hanford and LIGO Livingston baseline at Advanced LIGO Design sensitivity, corresponding to the expected sensitivity at the end of the fourth observing run[18]. The injected signal is constituted of stochastic bursts such as the ones used in Section 3.3.2, whose resulting background is characterised by a power-law $\Omega_{\rm GW}(f)$ spectrum with spectral index $\alpha = 2/3$ and reference population-averaged amplitude $\langle \Omega_b(f_{\rm ref}) \rangle = 5 \times 10^{-7}$. This population-averaged amplitude, together with a duty cycle $\xi = 10^{-3}$ corresponds to the predicted $\Omega_{\rm GW}(f_{\rm ref} = 25\text{ Hz}) = 5 \times 10^{-10}$ for an astrophysical BBH background, given current individual BBH merger detections [17]. We vary the duty cycle and the length of data analysed, as represented by the observation time $T_{\rm obs}$, and compute the resulting Bayes factor averaged over fifty data realisations for each point in parameter space. As a detection threshold, we use $\ln \mathcal{B} = 8$, which corresponds to a SNR[19] of approximately 4, usually associated with the threshold required to claim the detection of a GWB [19]. The results are illustrated in Figure 3.15. As can be seen, the detection threshold is reached after two weeks of data at Advanced LIGO Design sensitivity for a duty cycle $\xi = 10^{-3}$, representing a tremendous improvement compared to traditional search methods such as SSC for which this background would only be detectable after ~ 40 months observing time at design sensitivity [4].

To end this section, however, we issue a word of caution with regards to this updated prediction for the detection prospects. Although providing an optimistic time-to-detection of the BBH background, several assumptions went into generating these prospects. For example, the injected signal is still stochastic in nature, i.e., composed of stochastic bursts, rather than chirp waveforms. Additionally, although current predictions for the Advanced LIGO Design sensitivity curve were used to generate the noise, discrepancies between actual detector noise and predicted noise curves can arise due to unforeseen circumstances. Nevertheless, these updated predictions form a strong case for the added value of a search like SSI in decreasing the time-to-detection of the BBH background, keeping in mind possible refinements given the points above.

---

[18] To mimic this, we simulate Gaussian noise according to the Advanced LIGO Design noise PSD, as obtained from `https://dcc.ligo.org/LIGO-T2000012-v1/public`.

[19] The $\ln \mathcal{B}$ can be translated into terms of SNR, as described in [230].

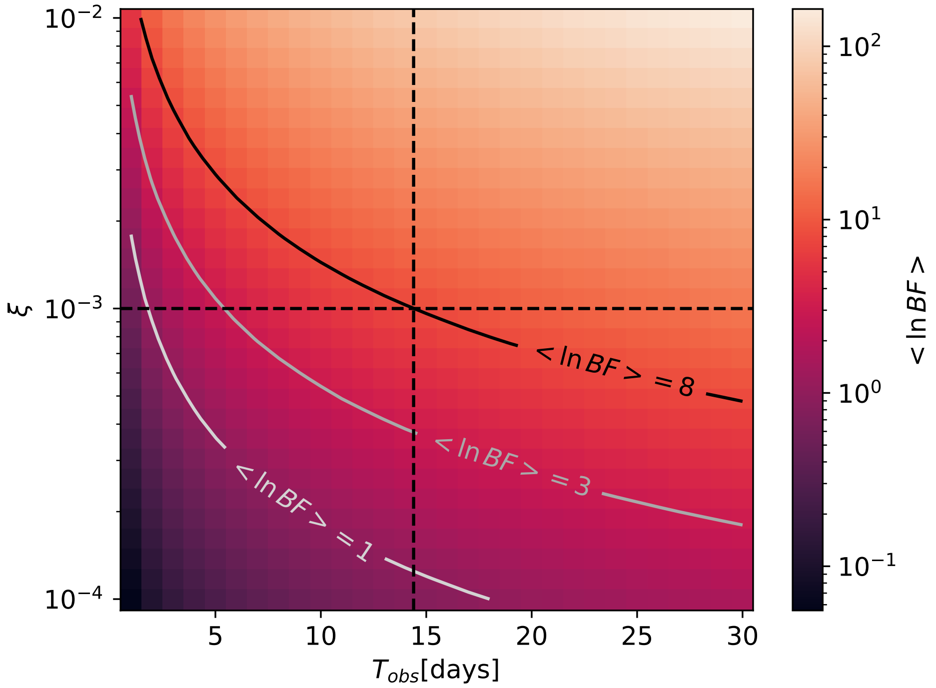

Figure 3.15. ln Bayes factor as observation time $T_{\rm obs}$ and duty cycle ξ are varied. Contours denote lines of constant ln Bayes factor, with $\ln \mathcal{B} = 8$ used as a detection threshold. The dashed lines show the intersection of the detection threshold contour with the $\xi = 10^{-3}$ line, as expected for the BBH background. This illustrates that the detection threshold could be reached within two weeks for such a BBH background with duty cycle $\xi = 10^{-3}$.

3.4.5 Further Ongoing Generalisations

The previous subsections highlighted some of the modifications made to the code since the publication of [176]. Additionally, several other new features are currently being tested, which we briefly mention below without too many details as these are still in the development stage.

- **Segment boundary** – For all of our data in this chapter, we only simulated signals which lie completely within the analysis segment boundaries[20]. A crucial next step is investigating how a signal which extends past a segment boundary will impact our results. Preliminary results seem to suggest that since the typical fraction-of-a-second duration that chirps are in the frequency band of the LVK detectors, signals being spread across boundaries happen only a small fraction of the time. This seems to have a negligible impact on the SSI results. However, this needs to be investigated further to fully understand the effects on our method.

- **Realistic waveforms** – With the synergy between SSI and `pygwb`, the simulation of real-

---

[20] We remind the reader that SSI divides the data stream in short segments of 4 seconds each, potentially cutting signals at segment boundaries.

istic waveforms is almost child's play. As mentioned earlier, these waveforms include the inspiral, merger and ringdown, offering a more complete picture of the BBH constituting the background, compared to the simpler case considered in our previous work where we only considered the inspiral $f^{-7/3}$ phase. Additionally, these waveforms are drawn from a population of BBHs, as specified by the user. This puts us in a position to slowly increase the complexity of the population we consider, and explore how this affects the SSI method. Examples include random sky-localisation of the mergers, as well as more realistic BBH mass distributions. This is currently being investigated.

All the generalisations above bring us a step closer to being able to run the SSI method on real detector data. However, an additional challenge which is not addressed above will be the detector noise. Although generalised to allow for coloured noise PSDs, our method does not account for the possible features in the detector noise, such as glitches and non-stationarities. However, in the first instance, we decide to focus the developments regarding SSI on the complexity of the population making up the GWB, and leave the assessment of the impact of these noise artefacts for future work.

3.5 Conclusions

Developing data-analysis techniques to reduce the time-to-detection of an astrophysical GWB with the LVK detectors is one of the current challenges that the GW community faces. Searches that include the intermittency of the BBH background to improve detection statistics have been proposed in the past [67, 111, 241, 264]. In this chapter, we proposed a new, stochastic search for intermittent GWBs and compared its efficiency with other searches. Our stochastic-based search looks for excess cross-correlated power in short stretches of data, ignoring the deterministic form of the GW signal waveforms and, hence the need to marginalise over all the associated signal parameters, as is done in the deterministic-signal-based approach of Smith and Thrane [241]. Not only is it beneficial to develop multiple searches in order to cross-check a potential detection, but there is an added benefit to running a search which does not look for a specific waveform in the data. The stochastic signal model allows our search to be flexible with respect to the type of signal it can detect.

For a series of analyses on data of increasing complexity, we showed that for data with low duty cycles our search performs better than the SSC, which does not take the intermittent nature of the BBH background into account. Furthermore, we showed that SSI is more flexible to the source of the intermittent GWB than our implementation of the Smith and Thrane approach [241] and should be more computationally efficient in detecting a signal.

Before being able to apply this search method on real GW data, further generalisations need to be made. Several examples of such generalisations were given, both in the implementation process and left for future work. For example, the generalisation to non co-located and non co-aligned detectors was made, as well as allowing for coloured noise PSDs. Furthermore, ongoing investigations regarding the impact of signals lying across segment boundaries and using more realistic waveforms are performed.

Note also that various assumptions were made about the individual BBH chirps we considered. For example, the two component masses were chosen to be equal, and the resulting chirp mass chosen to be identical for all the chirps (with only the distance to the source varying from one data segment to another). In reality, the black hole masses will most likely follow a power-law + peak distribution as shown by the LVK results at the end of their third observing run [17]. Generalising our method to allow for such mass distributions, as well as assessing the performance of our search in that case, is currently being investigated.

In addition, challenges related to the correct noise estimation will likely present themselves, but will be addressed in future work. For example, the Gaussian noise assumption will probably be violated, due to the presence of noise transients: glitches. During the third observing run of the LVK collaborations, these glitches were omnipresent in the data [19, 100]. Although successfully mitigated through gating procedures during the third observing run, the sensitivity of our search to the presence of such glitches and the impact of such gating procedures will have to be investigated before analysing real detector data. Additional complications related to noise estimation arise from the presence of a continuous GWB of BNS mergers. At any time, several BNS mergers are expected to be emitting GWs in the LVK frequency band. Not only does this violate the assumption that a segment contains either one signal or noise only, but it will also affect the noise PSD estimation. Analysing real detector data will introduce many challenges, which we plan to address incrementally, considering more and more realistic detectors and signals.

4 THE METALLICITY DEPENDENCE AND EVOLUTIONARY TIMES OF MERGING BINARY BLACK HOLES

> Why are black holes so different from all other objects in the macroscopic Universe? Why are they, and they alone, so elegantly simple? If I knew the answer, it would probably tell me something very deep about the nature of physical laws. But I don't know.
>
> Kip S. Thorne

Since the first detection of GWs by the LIGO-Virgo collaborations in 2015 [2, 6, 22, 44], the number of detected CBCs has been steadily increasing, amounting to around ninety detections in the third observing run [17]. These individual detections offer new insights into the demographics of compact binary mergers, including their mass and spin distributions. At the same time, growing GW catalogues offer an opportunity to study the evolution of the binary merger rate over cosmic time. The redshift-dependent merger rate is dictated by a confluence of environmental conditions governing compact binary formation and evolutionary processes describing their subsequent evolution. It therefore offers a window through which we can learn about the births of compact binaries and the lives of their progenitors.

Compact binaries are expected to preferentially arise from massive stars in low metallicity environments [59, 82, 135, 184, 194, 236]. Both the underlying metallicity-specific star formation rate (SFR) and the metallicity dependence of compact object formation, however, remain poorly understood [81, 83, 85, 244]. Therefore, GW observations might provide one of the best observational routes to constraining or measuring the metallicity specific SFR and compact object formation efficiency. Furthermore, the time-delay distribution between progenitor formation and eventual binary merger is not known and, if measured, it could provide hints as to what are the dominant formation channels and environments of BBHs. Binaries in the field, i.e., that are not part of a stellar cluster, for example, exhibit longer/shorter evolutionary time delays if they undergo stable/unstable (e.g., common envelope) mass transfer, respectively [244]. Binaries assembled dynamically in clusters might experience a different range of time delays altogether, with further distinctions depending on whether these dynamical systems merge inside the cluster or are jettisoned and merge outside the cluster [235].

Current GW detectors, however, are limited in their ability to probe high-redshift BBH merger events. For example, current catalogues provide meaningful constraints on the merger rate only to $z \lesssim 1$ [17, 69], although the formation rate can be probed out to $z \sim 4$ for population synthesis-motivated assumptions about the time-delay distribution [128]. Even with the future Advanced LIGO A+ sensitivity [57], the redshifts that will be probed by individual compact binary detections will likely remain below $z \sim 3$, thus suggesting that the high-redshift investigation of the BBH merger rate will remain challenging, at least until the era of next-generation instruments like the ET and CE [62, 124, 257].

Direct compact binary detections are not our only source of information, however. In addition to those individual binaries detected by the LVK collaborations, a GWB from unresolvable CBCs is expected, as introduced in Chapter 2 [80, 221, 230]. Even though a GWB remains to be detected by the LVK collaborations, current upper limits on the GWB can already allow us to constrain the merger rate at higher redshifts than individual BBH merger detections alone [18, 19].

Many studies have previously used catalogues of GW detections to study the formation history of compact binaries [126, 127, 203, 227, 257]. In this chapter, we will study the evolutionary history of compact binaries by combining direct detections with constraints on the GWB. The approach of combining individual BBH merger events with upper limits on the GWB was first explored in [71], where a phenomenological broken power-law model was adopted for the BBH merger rate. In this study, however, we will seek to go a step further, moving past the merger rate itself and constraining the metallicity dependence and evolutionary time delays associated with compact binary formation and evolution.

This chapter is structured as follows. In Section 4.1, we introduce our model for the BBH merger rate, starting from a metallicity-dependent SFR and an evolutionary time-delay distribution. In parallel, we demonstrate how differing assumptions regarding BBH formation impact the expected amplitude of the GWB. The methodology for our joint individual BBH and GWB analysis method is outlined in Section 4.2. Our results using data from the first three LVK observing runs are discussed in Section 4.3.1. Finally, we explore the potential of the analysis method with future constraints by considering the Advanced LIGO A+ sensitivity in Section 4.3.2.

This chapter is based on work in collaboration with Thomas Callister, Max Lalleman, and Nick van Remortel, as published in [253].

4.1 Binary Black Hole Merger Rate

Whereas past work, as discussed in [71], focussed on characterising the resulting merger rate of black holes, in this chapter we will seek to work further backwards, studying the underlying formation efficiency and time-delay distribution of BBHs. Standard models for the merger history of compact binaries rely on three ingredients: a metallicity specific SFR, an efficiency with which stellar progenitors yield merging compact objects, and a distribution of evolutionary time delays.

Throughout this chapter, we will consider the SFR as given in [188]. They obtain a fit to the global SFR per unit volume of the form:

$$R_*(z) \propto \frac{(1+z)^{2.7}}{1+((1+z)/2.9)^{5.6}}. \tag{4.1}$$

Note, however, that in Appendix B.2, we provide results for an alternative SFR proposed in [255] to illustrate that the main conclusions of this chapter can still be drawn if one assumes a different SFR.

It is expected that merging BBHs preferentially form in low metallicity environments, with efficiencies falling steeply at metallicities $Z \gtrsim 0.1\ Z_\odot$ [59, 82, 135, 194, 236]. Motivated by this, we will assume that the birth rate of BBHs is proportional to the product $R_*(z)F(Z^{\max}, z)$, where $F(Z^{\max}, z)$ is the fraction of star formation occurring at redshift z below metallicity $Z^{\max}$. An analytic prescription for the fraction of star formation is given by [174] as

$$F(Z^{\max}, z) \sim \hat{\Gamma}\left(0.84, \left(\frac{Z^{\max}}{Z_\odot}\right)^2 10^{0.3z}\right), \tag{4.2}$$

where $\hat{\Gamma}$ is the incomplete gamma function and $Z_\odot$ is the solar metallicity. The merger rate as a function of redshift is then obtained by performing a convolution of the metallicity-dependent SFR and a distribution of time delays $p(t_d)$ between binary formation and merger. We model this time-delay distribution as a power law:

$$p\left(t_d|\kappa, t_d^{\min}\right) \propto \begin{cases} (t_d)^\kappa & \left(t_d^{\min} \leq t_d \leq t_d^{\max}\right) \\ 0 & (\text{else}) \end{cases}, \tag{4.3}$$

where $t_d^{\max}$ is fixed to the age of the Universe, i.e., 13.5 Gyrs, and $t_d^{\min}$ is a parameter that can be inferred from the data. The merger rate as a function of redshift is now given by the convolution of the time-delay distribution with the metallicity-dependent SFR:

$$\mathcal{R}(z) = \int dt_d \; p(t_d) R_* \left(z_f(z, t_d) \right) F \left(Z \leq Z^{\max}, z_f(z, t_d) \right), \tag{4.4}$$

where the binary formation redshifts $z_f = z_f(z, t_d)$ are regarded as a function of merger redshift and time delay.

Our prescription for the BBH merger rate left three parameters undefined – the slope κ of the time-delay distribution, the minimum time delay $t_d^{\min}$, and the maximum metallicity $Z^{\max}$ amenable to compact binary formation. Our goal in this chapter will be to *infer* these parameters from GW observations. The measurement of these parameters could shed light on the different binary formation channels, as each of these predicts different values of the spectral index κ. For example, the value of κ is expected to be -1 in the classical field formation scenario [108, 109].

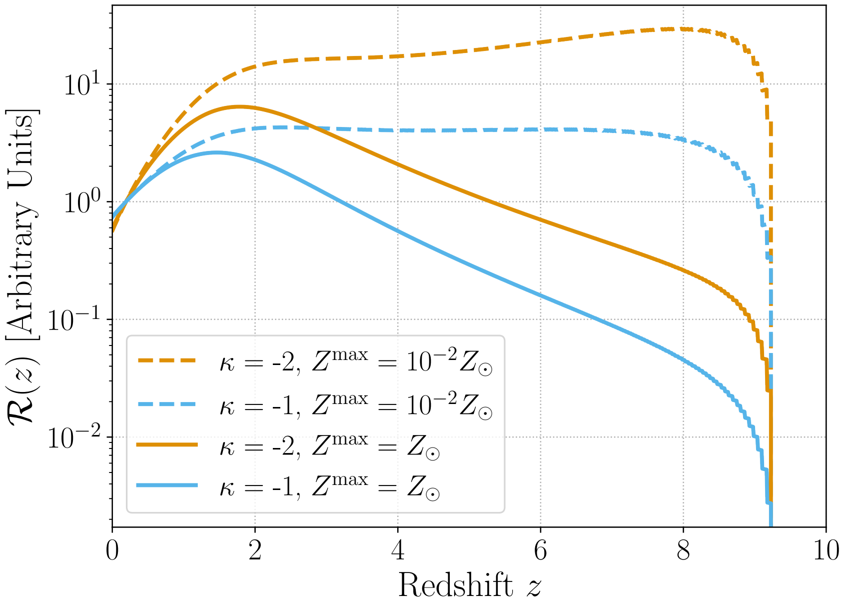

Figure 4.1. Examples of the BBH merger rate $\mathcal{R}(z)$ for different values of the slope of the time-delay distribution, κ, and different values of the maximum metallicity below which black holes are formed, $Z^{\max}$. All curves are arbitrarily normalised to $\mathcal{R}(z = 0.2) = 1$. The value of the minimum time-delay parameter, $t_d^{\min}$, is set to 0.05 Gyrs. Steeper time-delay distributions result in a larger merger rate at large redshifts, whereas larger metallicity thresholds result in a lower merger rate at large redshifts.

An example of the merger rate $\mathcal{R}(z)$ is given in Figure 4.1. We vary the slope of the time-delay distribution κ, as well as the maximum metallicity below which black hole formation occurs $Z^{\max}$, but fix the value of the minimum time-delay parameter $t_d^{\min}$ to an arbitrary value of 0.05 Gyrs. Each curve is arbitrarily normalised to $\mathcal{R}(z = 0.2) = 1$. A more negative slope

κ corresponds to more events that merged at early evolutionary times. Given a fixed *observed* merger rate in the local Universe, more negative κ correspondingly boosts the merger rate at large redshifts, as illustrated in Figure 4.1. Similarly, lower metallicity thresholds allow for a larger merger rate at earlier times, i.e., at large redshifts, when the metallicity of the environment in which the binaries formed was still low. Note that, although the effect of varying the minimum time-delay parameter is not displayed, decreasing its value would result in an increased merger rate at high redshifts, as mergers now occur at earlier times, and therefore, larger redshifts.

As we vary parameters, the behaviour of the black hole merger history in the local Universe, where BBH mergers are currently observed, remains practically unaltered [17]. In contrast, the most dramatic differences occur at large redshifts. Although these redshifts are too distant to directly observe, these different models yield very different predictions regarding the GWB.

One recalls that the GWB can be expressed in terms of the dimensionless energy density fraction $\Omega(f)$, as previously introduced in Eq. (2.13) in Chapter 2 [230]. More specifically, for the GWB coming from unresolved compact binaries throughout the Universe, the dimensionless energy density takes the form [71, 211]:

$$\Omega(f) = \frac{f}{\rho_c} \int_0^{z_{\max}} dz \, \frac{\mathcal{R}(z) \left\langle \frac{dE_s}{df_s} \right\rangle \Big|_{f(1+z)}}{(1+z)H(z)}, \tag{4.5}$$

where the Hubble rate at redshift z is given by $H(z) = H_0\sqrt{\Omega_M(1+z)^3 + \Omega_\Lambda}$, neglecting the contribution from the radiation density, and $\mathcal{R}(z)$ denotes the BBH merger rate. The matter and dark energy densities are taken to be $\Omega_M = 0.3$ and $\Omega_\Lambda = 0.7$, respectively [212]. We impose a redshift cut-off $z_{\max} = 10$, as few BBHs are expected beyond this redshift, provided the BBHs are stellar progenitors. The quantity $\langle dE_s/df_s \rangle$ is the GW energy spectrum of a single binary, averaged across the BBH population [34]. If λ denotes the intrinsic properties of a given binary (masses, spins, etc.) and $p(\lambda)$ is the distribution of these parameters across the BBH population, then

$$\left\langle \frac{dE_s}{df_s} \right\rangle = \int d\lambda p(\lambda) \frac{dE_s}{df_s}(\lambda), \tag{4.6}$$

where this quantity is evaluated at the source-frame frequency $f_s = f(1+z)$ in Eq. (4.5). More details about the assumed mass and spin distributions will be given below.

In Figure 4.2, we show an example of the computed $\Omega(f)$ spectrum for different values of the time-delay distribution parameters, as introduced in Eqs. (4.3) and (4.4). The variation in the $\Omega(f)$ spectrum when varying the time-delay distribution and metallicity parameters can be directly linked to the behaviour of the merger rate $\mathcal{R}(z)$ in Figure 4.1. Indeed, increasing the integrated merger rate correspondingly increases the $\Omega(f)$ spectrum. Note that the largest background comes from a steep time-delay distribution and a very low maximum metallicity, while the smallest background comes from allowing long time delays and a high maximum metallicity. For a more detailed explanation of the computation of $\Omega(f)$, we refer the reader to Appendix B.4. Furthermore, we note that the example given here is largely illustrative. For example, more detailed investigations have recently been performed in [178].

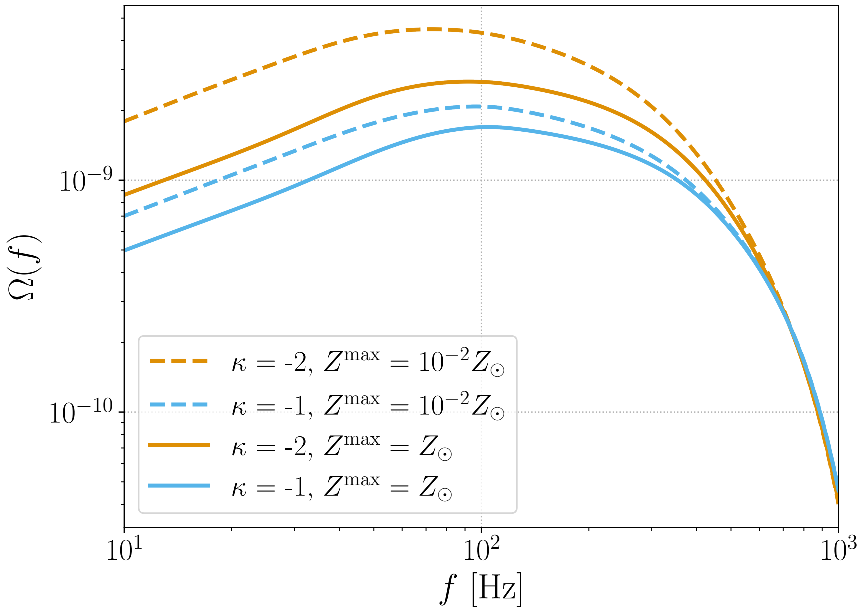

Figure 4.2. Example of the $\Omega(f)$ spectrum for different values of the same parameters κ and $Z^{\max}$ as in Figure 4.1. The value of all other parameters that enter in the mass distribution as given by Eqs. (4.13) - (4.15) is fixed to arbitrary values: $m_{\text{low}} = 10M_\odot$, $m_{\text{high}} = 80M_\odot$, $\alpha = -2$, $\mu_m = 20M_\odot$, $\sigma_m = 3M_\odot$, $f_p = 0.01$, $\beta_q = 2$, $\mathcal{R}_{\text{ref}} = 1\, M_\odot^{-1}\,\text{Gpc}^{-3}\,\text{yr}^{-1}$, $\delta m_{\text{low}} = 1M_\odot$, $\delta m_{\text{high}} = 3M_\odot$, and $t_d^{\min} = 0.05$ Gyrs. For more details on the time-delay parameter $t_d^{\min}$ and $\mathcal{R}_{\text{ref}}$, we refer the reader to Eqs. (4.3) and (4.11), respectively. The behaviour of the $\Omega(f)$ spectrum as the time-delay parameters are varied can directly be related to the behaviour of the merger rate in Figure 4.1, as a larger integrated merger rate results in a larger net $\Omega(f)$ spectrum.

4.2 Analysis Method

Our goal is to learn about the evolutionary history of BBHs by synthesising all available GW information, combining both direct detections of BBH mergers with upper limits on the integrated GWB, based on a framework first proposed in [71]. The inputs to our analysis are a set of N_{obs} direct BBH detections, with data $\{d\}_{i=1}^{N_{\text{obs}}}$, along with cross-correlation measurements $\hat{C}(f)$ of the GWB, as first introduced in Eq. (2.26). Let Λ signify the set of hyperparameters describing the BBH population, e.g., the slope of the time-delay distribution, κ, introduced in

Eq. (4.3). We assume that the joint likelihood of these measurements can be factorised as

$$\mathcal{L}\big(\{d_i\},\hat{C}|\Lambda\big)=\mathcal{L}_{\rm BBH}\left(\{d_i\}\,|\Lambda\right)\mathcal{L}_{\rm GWB}(\hat{C}|\Lambda), \tag{4.7}$$

where $\mathcal{L}_{\rm BBH}$ and $\mathcal{L}_{\rm GWB}$ denote the likelihoods for the individual BBH detections and the GWB, respectively.[1]

Individual binary black hole contribution

The individual BBH likelihood takes the form [186, 193, 249]:

$$\mathcal{L}_{\rm BBH}\left(\{d_i\}\,|\Lambda\right)\propto e^{-N_{\rm exp}(\Lambda)}\prod_{i=1}^{N_{\rm obs}}\int p\left(d_i|\lambda\right)\frac{dN}{d\lambda}(\Lambda)d\lambda, \tag{4.8}$$

where, as in Section 4.1, λ denotes the parameters (redshift, masses, spins, etc.), and $p(d_i|\lambda)$ denotes the likelihood of a GW event d_i given parameters λ. In the expression above, we also note the presence of the differential mass-redshift distribution for BBHs, which is given by:

$$\frac{dN}{dzdm_1dm_2}=Np(z,m_1,m_2), \tag{4.9}$$

where N denotes the total number of BBH mergers integrated across all redshifts and masses.

Assuming that the component mass distributions do not vary with redshift[2], this allows us to decompose the mass-redshift distribution, and adopt the following parameterization:

$$\frac{dR}{dm_1dm_2}=\mathcal{R}_{\rm ref}\frac{\mathcal{R}(z)}{\mathcal{R}(0.2)}\frac{\phi(m_1)}{\phi(20M_\odot)}p(m_2), \tag{4.10}$$

where

$$\mathcal{R}_{\rm ref}=\left.\frac{dR}{dzdm_1}\right|_{z=0.2,\ m_1=20M_\odot} \tag{4.11}$$

is the merger rate at redshift $z=0.2$ and primary component mass $m_1=20M_\odot$. As a reminder, the merger rate $\mathcal{R}(z)$ was previously introduced in Eq. (4.4), whereas $\phi(m_1)$ and $p(m_2)$ denote the mass distributions and will be given below.

The rate in Eq. (4.10) can be related to the differential mass-redshift distribution in Eq. (4.9) by

$$\frac{dN}{dzdm_1dm_2}=\frac{dV_c}{dz}\frac{1}{1+z}\frac{dR}{dm_1dm_2}, \tag{4.12}$$

---

[1] This factorisation does not strictly hold, as the same stretches of data contribute to both the direct compact binary detections and the GWB measurements. However, the contributions of direct detections to GWB measurements are negligible, making the factorisation a good approximation at current detector sensitivity.

[2] Although intrinsic evolution of the compact binary mass distribution with redshift is a generic prediction [244, 265], no such evolution is detected with current data [17, 129, 244].

where the factor $(1+z)^{-1}$ transforms from detector-frame to source-frame time, and $\frac{dV_c}{dz}$ denotes the co-moving volume per unit redshift.

In addition, the differential mass-redshift distribution, given in Eq. (4.9), contains a mass distribution for each of the masses. According to the most recent results of LVK's GWTC-3 catalogue [17], we model the primary mass distribution as a mixture between a power law and an additional Gaussian excess[3]:

$$p(m_1) = \frac{f_p}{\sqrt{2\pi\sigma_m^2}} \exp\left(-\frac{(m_1-\mu_m)^2}{2\sigma_m^2}\right) + (1-f_p)\left(\frac{1+\alpha}{(100M_\odot)^{1+\alpha}-(2M_\odot)^{1+\alpha}}\right) m_1^\alpha, \tag{4.13}$$

where α is the spectral index of the power law, the mean μ_m and variance σ_m^2 characterise the Gaussian peak, and f_p denotes the relative contribution of the Gaussian peak and the power law [14, 247]. A smoothing function is applied, such that the mass distribution is suppressed for $m_1 < m_{\text{low}}$ and $m_1 > m_{\text{high}}$:

$$\phi\left(m_1\right) = \begin{cases} p\left(m_1\right)\exp\left(\frac{-(m_1-m_{\text{low}})^2}{2\delta m_{\text{low}}^2}\right) & \left(m_1 < m_{\text{low}}\right) \\ p\left(m_1\right)\exp\left(\frac{-(m_1-m_{\text{high}})^2}{2\delta m_{\text{high}}^2}\right) & \left(m_1 > m_{\text{high}}\right) \\ p\left(m_1\right) & (\text{else}) \end{cases} \tag{4.14}$$

where δm_{low} and δm_{high} denote the scale of smoothing. The secondary mass m_2 is assumed to follow a power-law distribution, while ensuring $m_2 < m_1$:

$$p(m_2|m_1) = \left(\frac{1+\beta_q}{m_1^{1+\beta_q} - (2M_\odot)^{1+\beta_q}}\right) m_2^{\beta_q}, \tag{4.15}$$

where β_q denotes the spectral index of the distribution, and $p(m_2|m_1)$ is set to zero below $2M_\odot$. Although not explicitly mentioned throughout this section, the spin magnitudes and spin-orbit tilt angles are included in the analysis as well, for which the distributions are provided in Appendix B.3.

In Eq. (4.8), the total number of GW events, i.e., detected and undetected, is denoted by $N(\Lambda)$, whereas the number of observed events is represented by N_{obs}. The expected number of observations N_{exp} is given by

$$N_{\text{exp}}(\Lambda) = \int d\lambda P_{\text{det}}(\lambda)\frac{dN}{d\lambda}(\lambda|\Lambda), \tag{4.16}$$

where $P_{\text{det}}(\lambda)$ is the probability of successfully detecting a BBH merger described by parameters λ. In practice, $N_{\text{exp}}(\Lambda)$ can be approximated through a Monte Carlo average over artificial

---

[3] This is often referred to as power-law+peak in the community.

signals injected into detector data:

$$N_{\rm exp}(\Lambda) = \frac{1}{N_{\rm inj}} \sum_{i}^{N_{\rm found}} \frac{dN/d\lambda_i}{p_{\rm inj}(\lambda_i)}, \tag{4.17}$$

where the sum runs over the number of above detection threshold injections, $N_{\rm found}$, drawn from a reference distribution $p_{\rm inj}(\lambda_i)$ [70]. More details about the set of injections used in this analysis can be found in Appendix B.1.

The remaining necessary element in Eq. (4.8) is the individual BBH likelihood $p(d_i|\lambda)$, which can be estimated using Monte Carlo integration over posterior samples drawn from a reference prior $p_{\rm pe}$ [186, 193, 249]:

$$\mathcal{L}_{\rm BBH}\left(\{d_i\}\,|\Lambda\right) \propto e^{-N_{\rm exp}(\Lambda)} \prod_{i=1}^{N_{\rm obs}} \left\langle \frac{dN/d\lambda_i}{p_{\rm pe}\left(\lambda_i\right)} \right\rangle_{\rm samples}, \tag{4.18}$$

where $p_{\rm pe}(\lambda_i)$ denotes the prior used during the parameter estimation to infer the distribution of the parameters describing the GW event, and the average is taken over the posterior samples of each event.

Gravitational-wave background contribution

Our joint analysis also incorporates the contribution from the GWB. Remember that GWB searches, such as the one performed by the LVK collaborations [19] and described in Section 2.1.4, aim to measure the dimensionless energy density $\Omega(f)$. To this end, an optimal cross-correlation estimator $\hat{C}(f)$ is introduced, as was defined in Eq. (2.26) [35]. Recall that the normalisation of this estimator is such that $\langle \hat{C}(f)\rangle = \Omega(f)$. An estimator of the variance is given by $\left\langle \hat{C}(f)\hat{C}(f')\right\rangle = \delta(f-f')\sigma^2(f)$, where $\sigma^2(f)$ was previously defined in Eq. (2.27).

This cross-correlation estimator then enters in the likelihood $\mathcal{L}_{\rm GWB}$ in Eq. (4.7), which is well-approximated by a Gaussian distribution [19], as was seen in Eq. (2.38) in Chapter 2. The model $\Omega_M(f)$ in Eq. (2.38) is then given by the $\Omega(f)$ introduced previously in this chapter in Eq. (4.5), given some hyperparameters Λ. For additional information, we refer the reader to [19].

All together, we infer 16 hyperparameters: the nine parameters governing the primary and secondary mass distributions in Eqs. (4.14) and (4.15), the three spin parameters detailed in Appendix B.3, the three parameters $\{Z^{\rm max},\ \kappa,\ t_d^{\rm min}\}$ characterising the formation and evolution of BBH systems, as well as the reference merger rate amplitude $\mathcal{R}_{\rm ref}$ defined in Eq. (4.11). The priors used for the parameter estimation are summarised in Table B.1 in Appendix B.3.

4.3 Results

In this section, we discuss the results of our analyses. Section 4.3.1 presents the results using currently available LVK data, while Section 4.3.2 shows results that will be available in future observing runs with the improved A+ sensitivity of the Advanced LIGO detectors.

4.3.1 Constraints from LVK O1, O2, and O3 Data

We now apply the methodology outlined in the previous sections to place constraints on the time-delay parameters giving rise to the BBH population, using data from LVK's first three observing runs. More details about the exact data used are given in Appendix B.1.

In Figure 4.3, we show the obtained posteriors on the time-delay parameters $\{\kappa,\ Z^{\max}, t_d^{\min}\}$ from Eqs. (4.3) and (4.4), as well as the merger rate amplitude $\mathcal{R}_{\rm ref}$ at $z = 0.2$ and $m_1 = 20M_\odot$, as defined by Eq. (4.11). We simultaneously infer all the hyperparameters, e.g., also appearing in the mass distributions, but these are omitted from the plot for the sake of visual clarity. Since the merger rate amplitude $\mathcal{R}_{\rm ref}$ parameterizes the merger rate at $z = 0.2$ and $m_1 = 20M_\odot$, it will be almost solely determined by LVK's individual BBH detections, which happen at low to moderate redshifts. This is indeed the case, as illustrated by the recovery of the $\mathcal{R}_{\rm ref}$ parameter in Figure 4.3, which is dominated by individual BBH events. In addition, the slope of the time-delay distribution κ is constrained to negative values. A positive value of κ would give rise to a merger rate $\mathcal{R}(z)$ that decreases with z at low redshifts, contradicting the currently observed merger rate dependence on the redshift. Current individual BBH detections together with the GWB estimator are not able to constrain the metallicity threshold $Z^{\max}$, nor the minimum time-delay parameter $t_d^{\min}$.

The authors of [127] similarly constrained the conditions of compact binaries using direct detections of binary mergers from the first two LIGO observing runs (but without additional constraints from the GWB). We do note, however, that they assume an alternate SFR given by [189], and that only two parameters are varied at a time, contrarily to our case where the slope, the minimum time delay, and the metallicity threshold are varied simultaneously. Keeping these differences in mind, our results are consistent with the ones obtained in [127]. They constrained the slope of the time delay distribution to negative values at the 90% confidence level, and are unable to constrain the value of the metallicity threshold for the values of the minimum time delay considered in this chapter.

In principle, measurements or upper limits on the GWB are dominated by binaries at higher redshifts, and could thus offer a complementary constraint on the slope of the time-delay distribution κ, the metallicity threshold $Z^{\max}$, and the minimum time delay $t_d^{\min}$. However, we find that current constraints on the GWB are not sufficiently sensitive to appreciably change

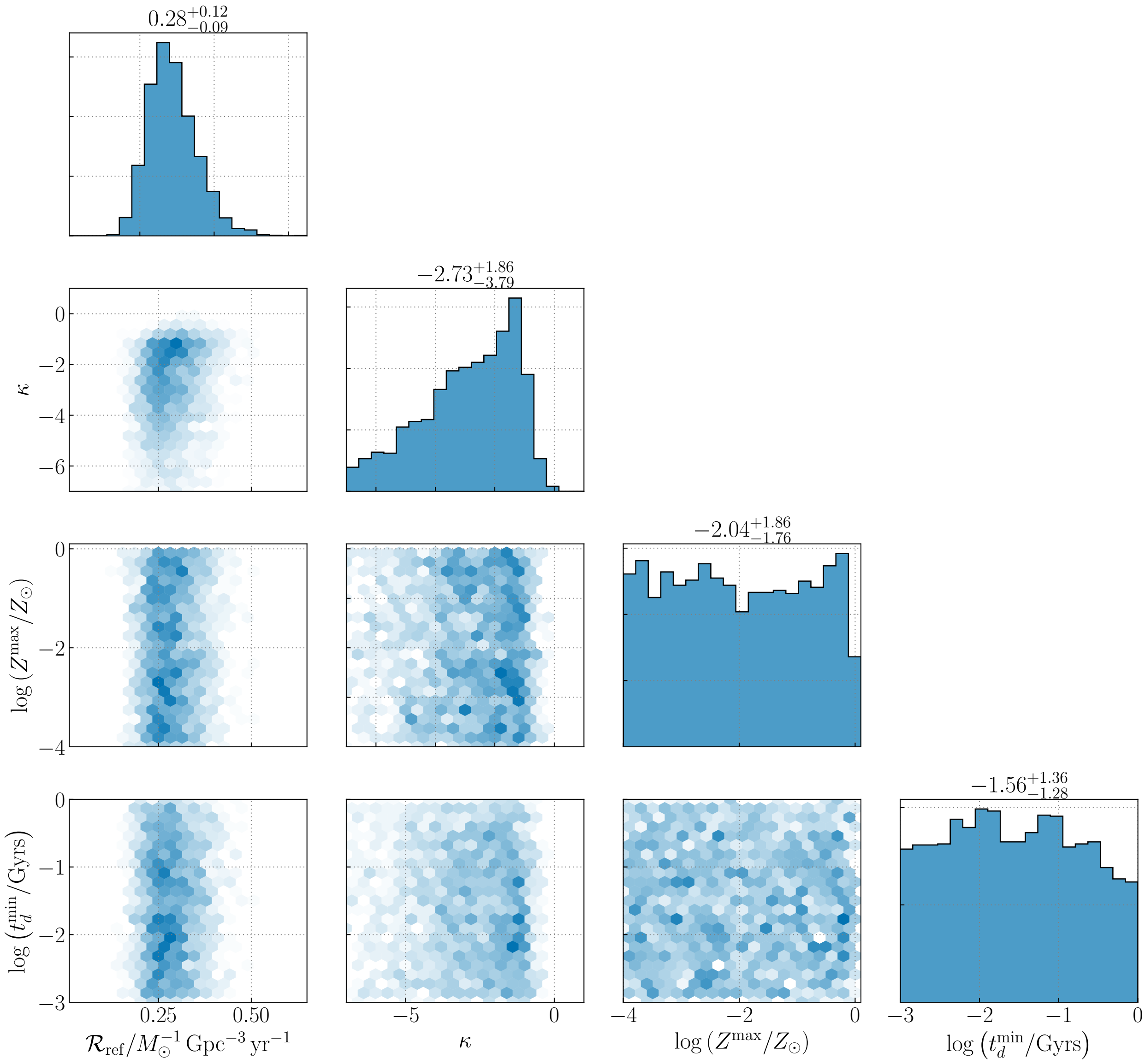

Figure 4.3. Posteriors on the parameters governing BBH birth and evolution using both direct detections and GWB constraints on the first three LVK observing runs. For clarity, the only posteriors that are shown are for the reference merger rate amplitude $\mathcal{R}_{\mathrm{ref}}$, the slope of the time-delay distribution κ, the metallicity threshold $Z^{\max}$, and the minimum time delay $t_d^{\min}$, although we simultaneously inferred the BBH mass distribution as introduced in Section 4.2. The reference merger rate amplitude $\mathcal{R}_{\mathrm{ref}}$ is well constrained due to the currently observed individual BBH merger events happening at low redshifts. Although the metallicity threshold $Z^{\max}$ and the minimum time-delay parameter $t_d^{\min}$ cannot be constrained with data from the first three observing runs, the slope of the time-delay distribution κ is constrained to negative values. Positive values of this parameter would give rise to a different merger rate that decreases with redshift, contradicting current observations.

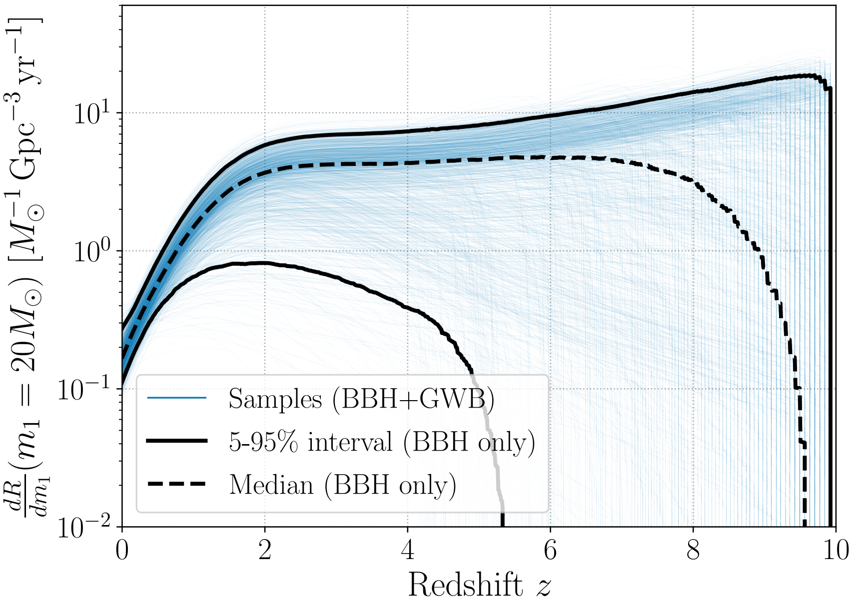

Figure 4.4. Posterior samples on the merger rate $\frac{dR}{dm_1}(m_1 = 20M_\odot)$ for the joint analysis using both direct detections and GWB constraints. For reference, the 5% and 95% credible limits are shown in full black lines for the individual BBH run, and the dashed black line shows the median value for the BBH only run. The results of the individual BBH run and the joint analysis using both direct detections and GWB constraints are comparable, illustrating that the GWB upper limits are not informative at current detector sensitivity. Furthermore, we note that the merger rate is well-constrained at low redshifts because of the individual BBH mergers detected at those redshifts.

the measurements using solely individual BBHs. To illustrate this point further, we compare the resulting posterior samples on the merger rate $\frac{dR}{dm_1}(m_1 = 20M_\odot)$ in Figure 4.4. The individual blue traces correspond to individual posterior samples drawn from Figure 4.3, while solid black curves show the bounds obtained from analysing BBHs only. This shows that, at current sensitivity, results are entirely dominated by individual BBH mergers.

To illustrate why current upper limits on the GWB are not yet informative, we show the expected $\Omega(f)$ from the posterior samples of the joint analysis using both direct detections and GWB constraints in Figure 4.5. We compare these samples with the 2σ O3 PI sensitivity curve, which illustrates the sensitivity to an isotropic GWB, as introduced in Section 2.2.1 [250]. Recall that, approximately, spectra lying above the PI curve typically have a SNR large enough to be detected, while spectra lying below have a SNR that is not sufficiently large for detection. As can be seen, none of the posterior samples for $\Omega(f)$ are within reach of the PI curve, illustrating that we do not expect additional information from the GWB contribution to the likelihood at current sensitivities.

Note that our results rely on our fairly strong systematic choice of a fixed SFR. As a check on the corresponding systematic uncertainty inherent in our results, we repeat this analysis

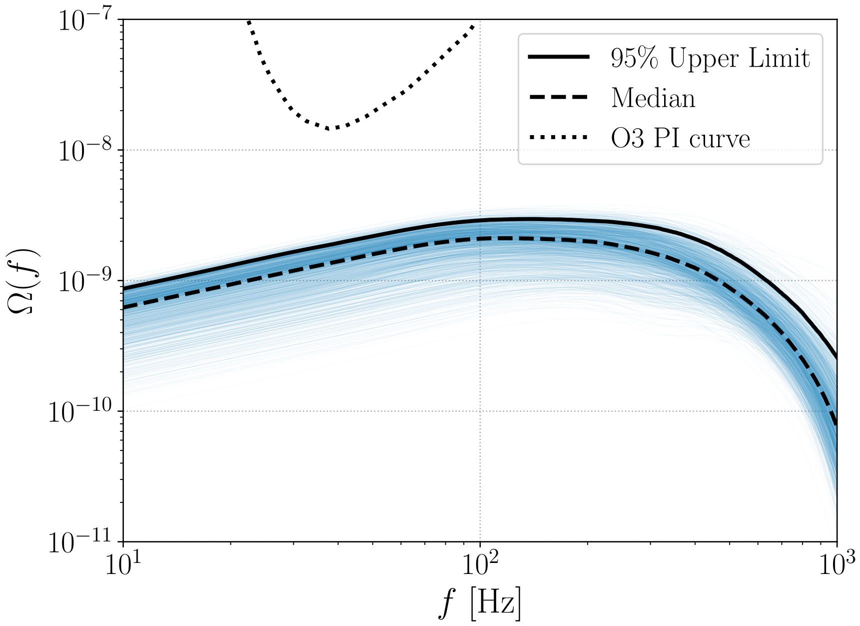

Figure 4.5. Posterior on $\Omega(f)$ using the posterior samples from the joint analysis using both direct detections and GWB constraints on the first three LVK observing runs. The median is denoted by the dashed black line, and the 95% credible upper limit by the full black line. The 2σ O3 PI curve from [19] is shown (dotted black) as an indication of the GWB detection threshold after the first three LVK observing runs. All posterior samples fall below the O3 PI curve, illustrating that we do not expect the GWB contribution to be informative at current detector sensitivity.

in Appendix B.2 for an alternative SFR given by [255], illustrating that our main conclusions remain unaltered when assuming a different SFR. The stellar metallicity distribution in Eq. (4.2) represents an additional systematic uncertainty in our analysis. Although we use a fit provided by [174] in this work, more modern fits have recently been proposed, e.g., [84, 243]. Future work will assess the impact of the choice of metallicity distribution on our results.

4.3.2 Constraints Using Advanced LIGO A+ Sensitivity

Although current GWB limits are not yet informative, increased integration time will give increasingly sensitive GWB measurements, even in cases where detector horizons do not appreciably change. This improved sensitivity will be increasingly informative regarding the evolutionary history of BBHs. We therefore consider GWB measurements obtainable with the Advanced LIGO detectors at their future A+ sensitivities [57], assessing the potential of our joint analysis method in constraining the time-delay parameters.

Following a future observing run with LIGO A+ instruments, there are two possibilities: a detection of the GWB could be made, or the background could go undetected still. We will consider both cases, exploring the resulting constraints on the time-delay parameter space in each case. In both cases, we simulate a GWB signal consistent with the results obtained in Section 4.3.1 using data from the first three observing runs. To accomplish this, we choose two samples from the posterior distribution presented in Figure 4.3: one posterior sample predicting a GWB that should be detectable with LIGO A+, and a second predicting a background that should remain undetected[4]. For both cases, we consider the LIGO Hanford and LIGO Livingston baseline, and assume an observation time of one year at the Advanced LIGO A+ sensitivity [57]. Future observing runs with more sensitive instruments will certainly also yield additional direct detections of BBH mergers. Our goal in this section, however, is primarily to understand the astrophysical information contained in a detection (or non-detection) of the GWB. We therefore do not simulate additional compact binary mergers, but use the same GWTC-3 catalogue of direct detections as in Section 4.3.1.

Case 1: A Detection

We first consider the detectable GWB case, for which the simulated $\Omega(f)$ spectrum is shown in Figure 4.8, together with the 2σ A+ PI curve assuming a one-year observation time, for reference. Note that as the injected GWB lies above the PI curve, we indeed expect a detection. We infer the slope of the time-delay distribution κ, the metallicity threshold $Z^{\max}$, and minimum time delay $t_d^{\min}$ using both the individual BBH events from the GWTC-3 catalogue, and the simulated detectable GWB at A+ sensitivity. The posteriors for these parameters are shown in Figure 4.6, where the black dashed histograms represent the results of the analysis with current data reported in Figure 4.3 to facilitate comparison. We omit the $\mathcal{R}_{\text{ref}}$ posterior from the plot, and note that since the merger rate amplitude $\mathcal{R}_{\text{ref}}$ is currently entirely determined by individual BBH events, the addition of GWB measurement at A+ sensitivity does not alter the posterior on $\mathcal{R}_{\text{ref}}$ compared to the runs at current sensitivity in the previous section. Contrarily, the posteriors on the time-delay parameters are much more constrained than in the runs using data from the first three observing runs of the previous section. Larger negative values are favoured for the slope of the time-delay distribution κ, whereas smaller values are supported for both the metallicity parameter $Z^{\max}$, and the minimum time delay $t_d^{\min}$. In Figure 4.2, it was illustrated that smaller values of $Z^{\max}$, κ and $t_d^{\min}$ corresponded to larger GWB signals. A detection of a GWB by definition requires a reasonably large signal, pushing our posteriors on all three parameters to smaller values in Figure 4.6.

---

[4] This is done by comparing the predicted $\Omega(f)$ spectrum of the posterior sample with the Advanced LIGO A+ PI curve [19]. A sample lying above the PI curve is labelled as detectable, whereas the opposite is true for samples lying below the PI curve [250]. More information regarding PI curves can be found in Section 2.2.1.

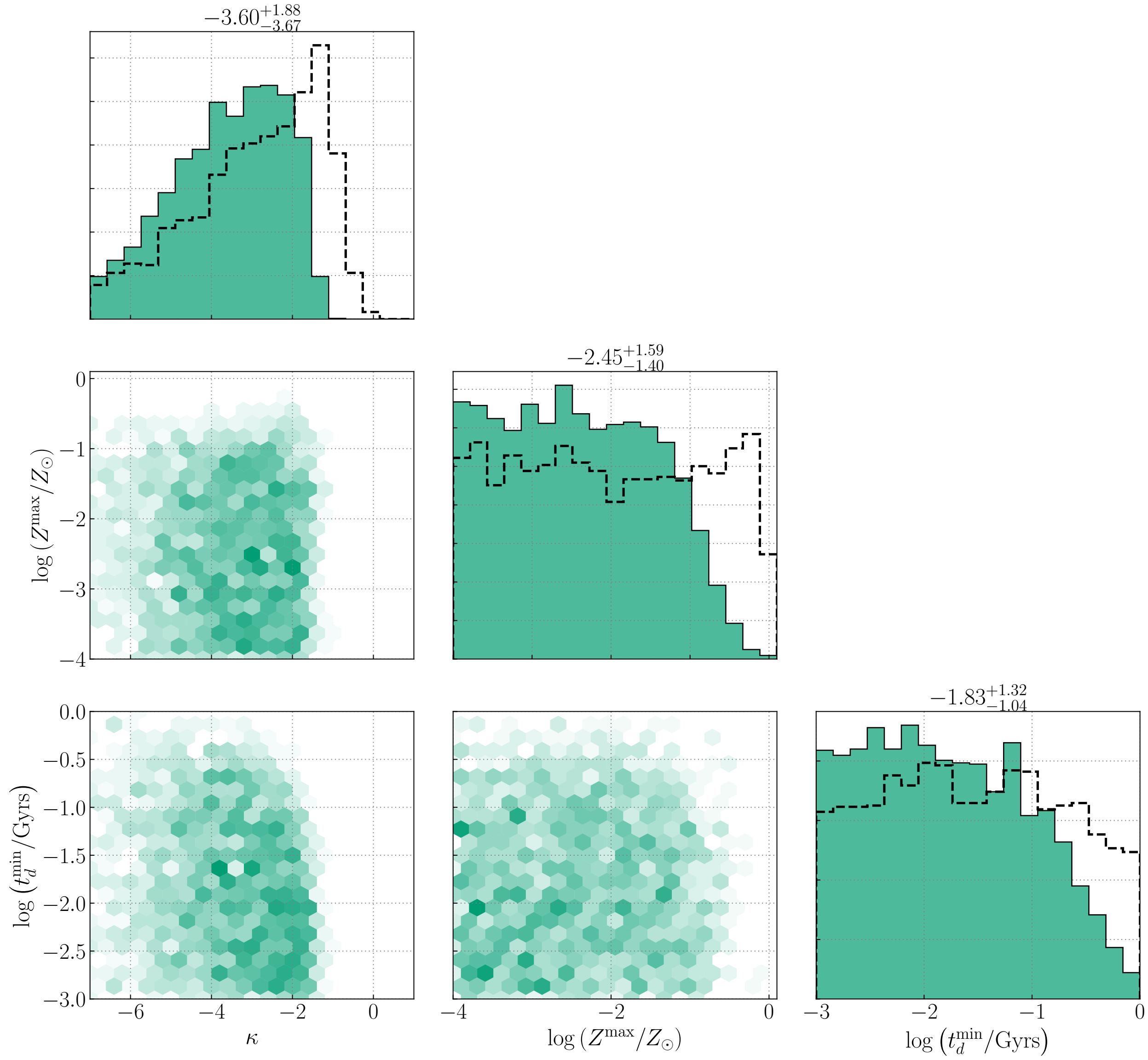

Figure 4.6. Posterior on the slope of the time-delay distribution κ, the metallicity threshold $Z^{\max}$, and the minimum time-delay parameter $t_d^{\min}$ for the joint analysis using both direct detections and GWB constraints at Advanced LIGO A+ sensitivity, in the presence of a *detectable* GWB. The dashed black lines represent the 1D histograms for the joint analysis on data from the first three observing runs from Figure 4.3, for reference. We note that there is more support for larger negative values of the slope of the time-delay distribution κ, and that smaller values of the metallicity parameter $Z^{\max}$ and the minimum time delay $t_d^{\min}$ are favoured. In addition, we point out the complementarity of these constraints with the case of an undetectable GWB at A+ sensitivity, as reported in Figure 4.9.

In addition to the posteriors, we show the merger rate $\frac{dR}{dm_1}(m_1 = 20M_\odot)$ constructed from the posterior samples in Figure 4.7, as well as the posterior samples on $\Omega(f)$ in Figure 4.8. The posterior samples of both quantities show agreement with the injected quantities, which are denoted by the red dash-dotted line in both figures.

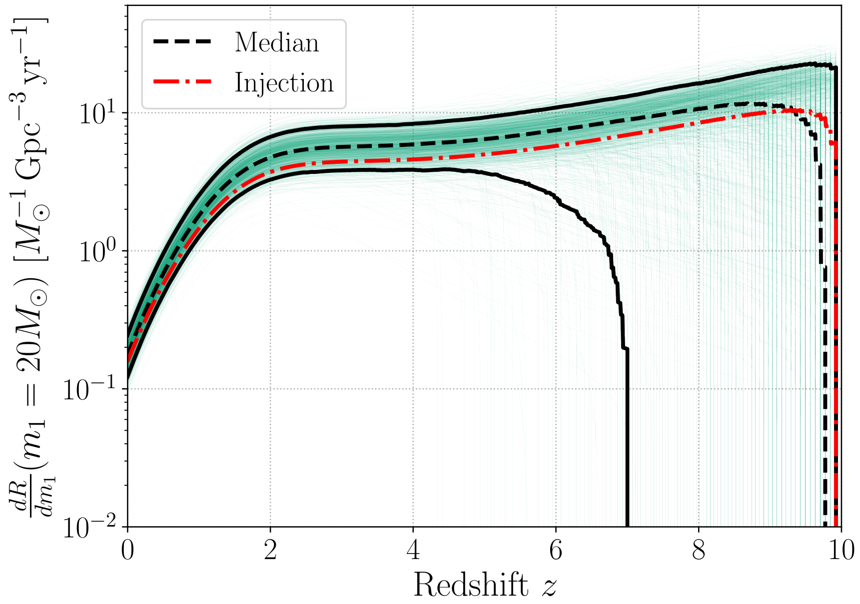

Figure 4.7. Posterior samples for $\frac{dR}{dm_1}(m_1 = 20M_\odot)$ with the injected rate corresponding to a detectable GWB at A+ sensitivity indicated by the red dash-dotted line. The full black lines denote the 5-95% confidence interval, and the dashed black line denotes the median.

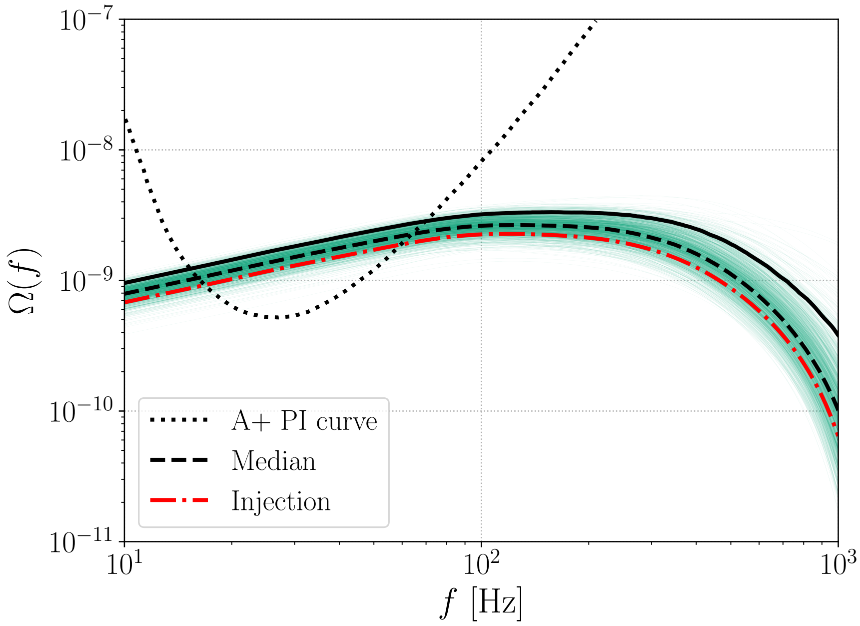

Figure 4.8. Posterior samples for $\Omega(f)$ with the injected detectable background denoted by the red dash-dotted line. The 95% upper limit is denoted by the full black line, and the dashed black line represents the median. The dotted black line represents the 2σ A+ PI curve.

Case 2: A Non-Detection

We now repeat the above analysis, but with a GWB measurement at A+ sensitivity that falls below the expected sensitivity of a GWB search, as displayed in Figure 4.11. This is illustrated by the fact that the injected GWB falls below the A+ PI curve. Similarly to the detectable case, the simulated GWB measurement is constructed from a posterior sample of the run with current data to ensure consistency with observed GWTC-3 BBH events. In Figure 4.9, we show that the improved A+ sensitivity, even in the absence of a GWB detection, allows for better constraints on the time-delay parameters. In particular, we note that the slope κ of the time-delay distribution and the metallicity threshold $Z^{\max}$ are now required to lie along a preferred two-dimensional contour. The same is true of κ and the minimum time delay $t_d^{\min}$. The result is that very large and negative values of κ, and small values of $Z^{\max}$ and $t_d^{\min}$ are excluded, since these values would all have yielded a detectable GWB. Larger values of the metallicity parameter $Z^{\max}$ and the minimum time delay $t_d^{\min}$ are favoured to be consistent with a non-detection of a GWB. Furthermore, we note that $\frac{dR}{dm_1}(m_1 = 20M_\odot)$ is poorly constrained in the case a GWB detection cannot be claimed, as illustrated in Figure 4.10. In particular, we point out the similarity of this posterior with the result with current data presented in Figure 4.4, but note the somewhat lower 95% upper limit due to the improved A+ sensitivity. Furthermore, the $\Omega(f)$ posterior in Figure 4.11 is consistent with the results using current data shown in Figure 4.5, although with a slightly lower 95% upper limit, again as a result of the improved A+ sensitivity.

It is particularly interesting to stress that distinct regions of parameter space can be constrained depending on whether the GWB is detected or not. The non-detection of a GWB at A+ sensitivity would allow us to heavily constrain the slope of the time-delay distribution κ, as other values of that parameter would have given rise to a detectable GWB, which was not observed. However, the $Z^{\max}$-$t_d^{\min}$ parameter space remains mostly unconstrained, although slightly favouring larger values of both parameters. In contrast, the detection of a GWB instead allows us to place stronger bounds on $Z^{\max}$ and $t_d^{\min}$, but yields less stringent constraints on the κ parameter, favouring larger negative values.

To illustrate why distinct regions of parameter space can be constrained with the detection or non-detection of a GWB, we consider the SNR, which we remind the reader is given by

$$\rho = \sqrt{2T}\frac{3H_0^2}{10\pi^2}\left(\int_{f_{\min}}^{f_{\max}} df \, \frac{\gamma_{12}^2(f)\Omega^2(f)}{f^6 P_1(f)P_2(f)}\right)^{1/2}, \tag{4.19}$$

where T denotes the observation time, $\gamma_{12}(f)$ the ORF as introduced in Section 2.1.3, and $P_i(f)$ the noise PSD of detector $i = \{1,\ 2\}$ [230]. In Figure 4.12, we show contours of the stochastic SNR in the $\kappa - Z^{\max}$ parameter space, using the Advanced LIGO A+ sensitivity. When computing the expected GWB spectrum $\Omega(f)$, the minimum time delay was set to $t_d^{\min} = 0.05$ Gyrs and the values of other hyperparameters were set to the median values of the posteriors in Figure 4.3. Additionally, we show 1D histograms of regions of parameter space where the

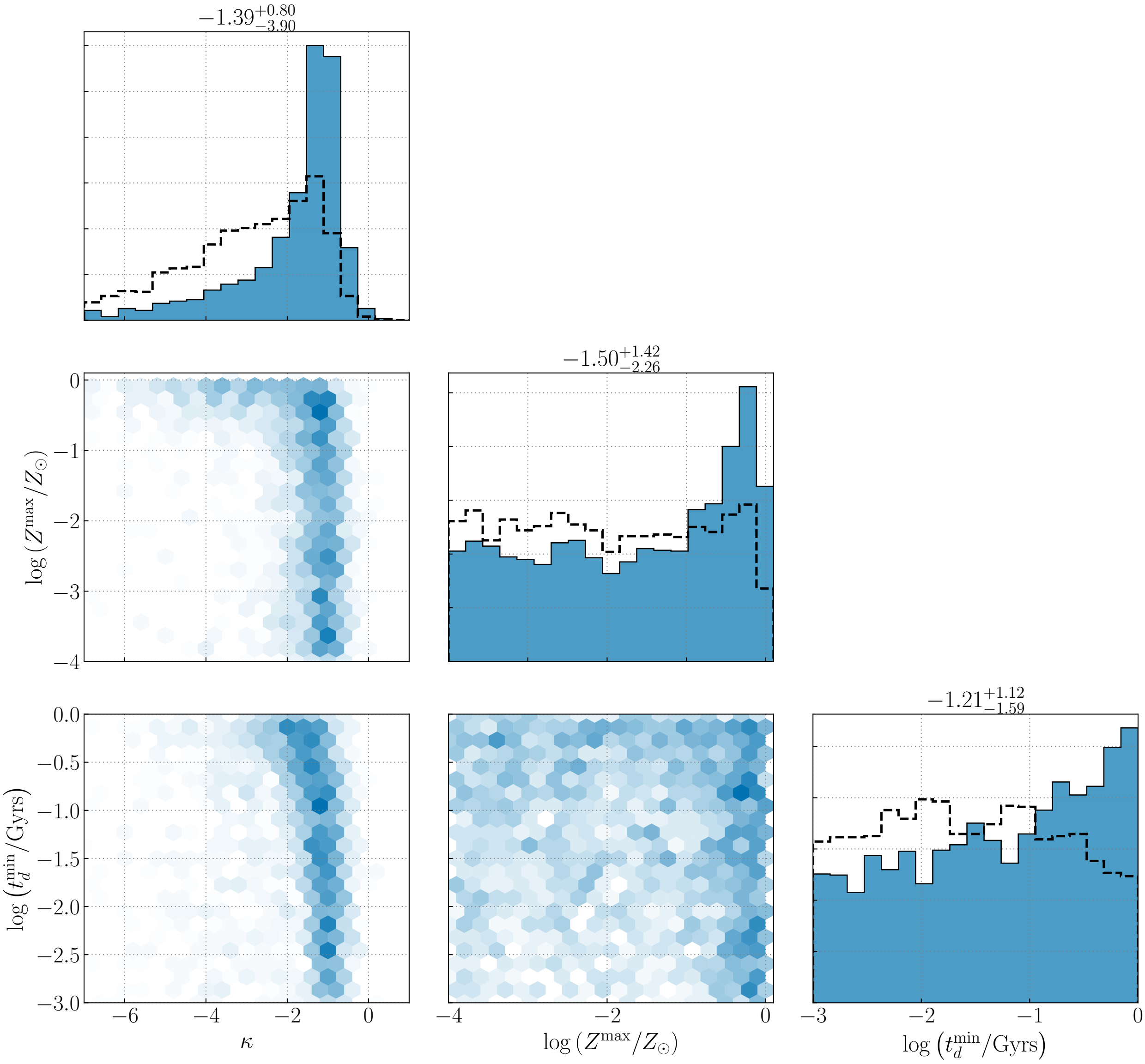

Figure 4.9. Posterior on the slope of the time-delay distribution κ, the metallicity threshold Z^{max}, and the minimum time-delay parameter t_d^{min} for the joint analysis using both direct detections and GWB constraints at Advanced LIGO A+ sensitivity, in the presence of an *undetectable* GWB. The dashed black lines represent the 1D histograms for the joint analysis on data from the first three observing runs from Figure 4.3, for reference. We note that large negative values for the slope of the time-delay distribution κ are disfavoured, and that there is an enhanced support for larger values of the metallicity parameter Z^{max} and the minimum time delay t_d^{min}. In addition, we point out the complementarity of these constraints with the case of a detectable GWB at A+ sensitivity, as reported in Figure 4.6.

expected SNR is smaller (larger) than 3 in blue (green). In particular, we want to highlight that the regions of parameter space where the SNR is larger (smaller) than 3 corresponds to the region of parameter space where most posterior samples lie for a detectable (undetectable) GWB in Figure 4.6 (Figure 4.9). The detection (non-detection) effectively forces the posterior sam-

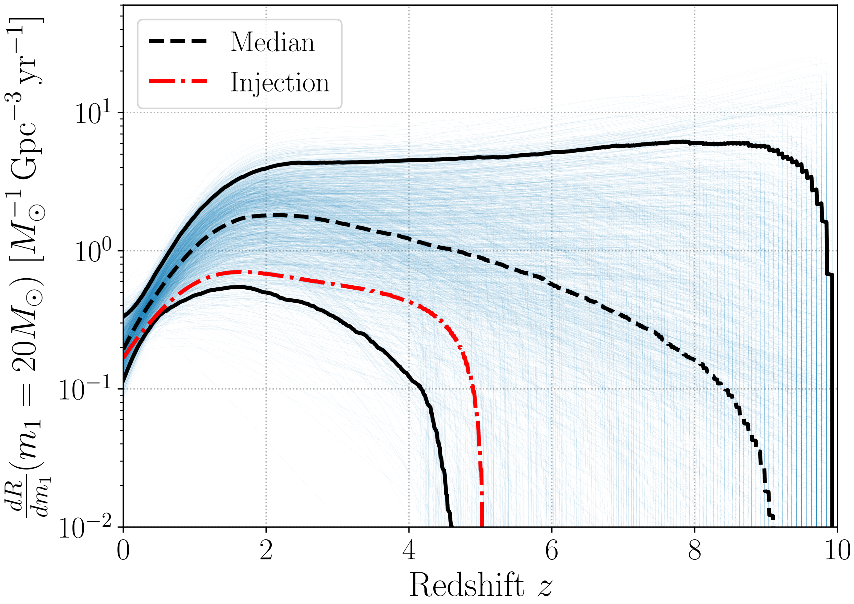

Figure 4.10. As in Figure 4.7, but now for the case of an *undetectable* GWB.

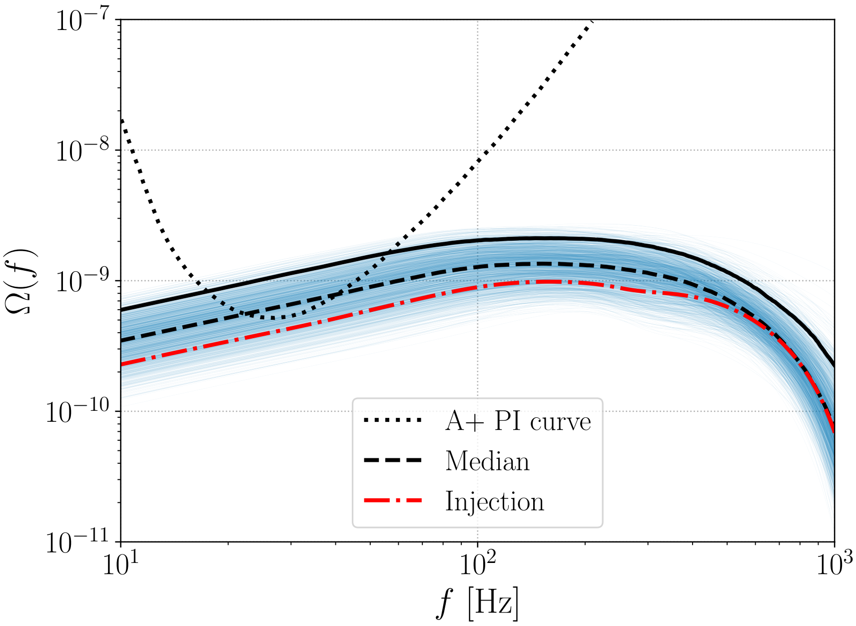

Figure 4.11. As in Figure 4.8, but now for the case of an *undetectable* GWB.

ples to lie within a region of parameter space with a corresponding SNR that is above (below) the detection threshold of $\rho = 3$. Therefore, the two cases considered in this chapter, both a GWB detection and non-detection at the Advanced LIGO A+ sensitivity, provide complementary information about the time-delay distribution and metallicity-specific SFR.

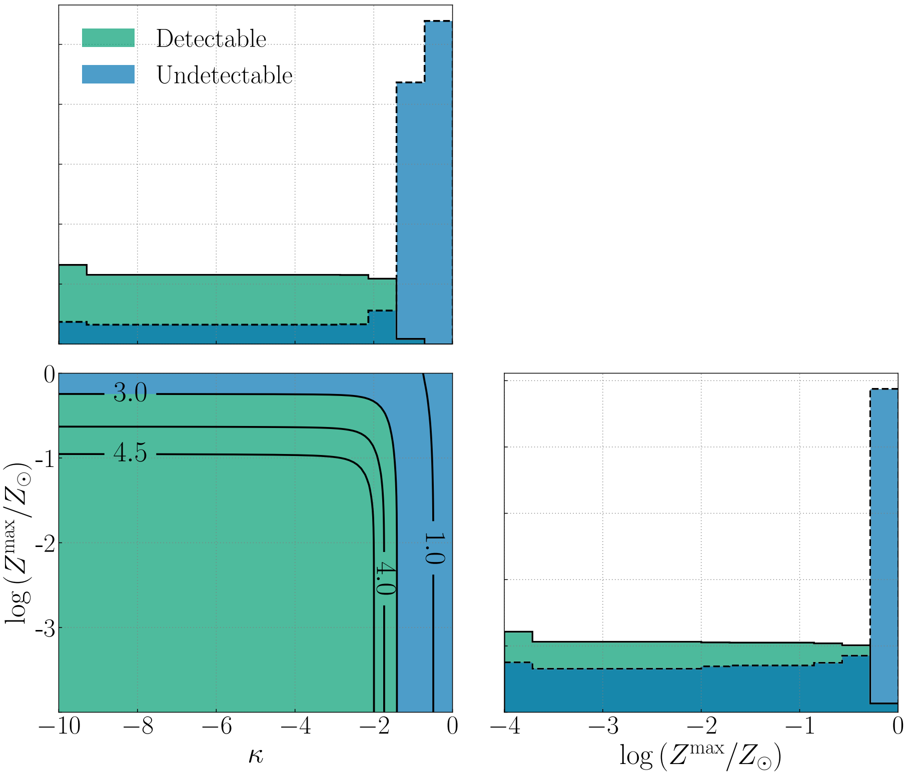

Figure 4.12. Contours of the expected stochastic SNR using the Advanced LIGO A+ sensitivity for the slope of the time-delay distribution κ and the maximum metallicity below which black holes are formed $Z^{\max}$. The 1D histograms denote the regions of parameter space where the SNR is smaller (larger) than 3 in blue (green). In constructing the stochastic SNR contours, the minimum time delay was set to $t_d^{\min} = 0.05$ Gyrs and all other hyperparameters were set to the median value of the posteriors in Figure 4.3. The regions of parameter space where the SNR lies above (below) 3 corresponds to the region of parameter space where most posterior samples lie for a detectable (undetectable) GWB in Figure 4.6 (Figure 4.9).

4.4 Conclusions

The target of this chapter was to shed light on the evolution of BBHs with GW data. We currently have two sources of information – the direct BBH detections comprised in GWTC-3, and the upper limits on the GWB. Each of these observational inputs provides us information about the binary merger rate at different redshifts. Our goal was to synthesise both together to constrain the parameters that govern the metallicity-specific formation rate of BBH progenitors and their subsequent evolutionary time delays.

We considered LVK data from the first three observing runs, including both individual BBH mergers from the GWTC-3 catalogue, as well as current upper limits on the GWB. Current individual BBH mergers allowed to constrain the slope of the time-delay distribution to negative values, but left the other parameters of interest unconstrained. The addition of information from the GWB in our joint analysis using individual BBH mergers and the upper limits on a GWB did not provide more stringent constraints at current sensitivity.

Nevertheless, we considered the future Advanced LIGO A+ sensitivity and considered both the case of a GWB detection and non-detection at that sensitivity. We showed that both cases offer unique and complementary constraints on the parameter space of interest. Indeed, the non-detection of a GWB at Advanced LIGO A+ sensitivity results in tight constraints on the slope of the time-delay distribution. On the other hand, the detection of a GWB would allow to constrain larger parameter space regions of the metallicity threshold and minimum time-delay parameter.

Although considering current GWB upper limits did not improve the constraints on the metallicity-specific SFR and time-delay parameters at current sensitivity, this chapter showed that the additional information contained in a GWB measurement will be essential to learn more about the environment in which compact binaries formed and their evolution.

Data and code

Data produced in this paper are available at `https://zenodo.org/doi/10.5281/zenodo.10016289`. The code used to produce the results in this paper can be found on `https://github.com/kevinturbang/bbh_gwb_time_delay_inference/tree/main`.

Part III

Cosmological Gravitational-Wave Backgrounds

In addition to the vast amount of astrophysical sources contributing to the GWB, an abundance of cosmological processes could have generated GWs throughout the history of the Universe. Potential sources include inflation, cosmic strings, first order phase transitions, domain walls, and many more [68, 75]. The resulting background from these phenomena offers a unique probe of the early times of the Universe, or equivalently, the high energies involved in those processes, unattainable by particle detectors on Earth. In this thesis, however, we focus on one of these scenarios: first order phase transitions.

Chapter 5 - First Order Phase Transitions

First order phase transitions are predicted in many Beyond the Standard Model theories. Their unique GWB signature within current and future GW experiments would offer smoking gun evidence for new physics. This chapter reviews the theory behind first order phase transitions and the resulting background, while commenting on the special case of supercooled phase transitions. We then proceed by placing constraints on supercooled phase transitions using LVK data from the first three observing runs. We then consider two well-motivated particle physics models and constrain their relevant parameter space through the non-observation of a first order phase transition signal in LVK data.

5 FIRST ORDER PHASE TRANSITIONS

Bubbles! Bubbles! My bubbles!

Finding Nemo (Pixar Animation Studios)

The richness of the GWB lies in its many contributions from various processes of completely different origins. Additionally to the contribution from astrophysical sources, a vast amount of cosmological processes that happened during the history of the Universe could have contributed to the overall GWB. In this chapter, however, we focus on the contribution from first order phase transitions (FOPTs) [173].

In the context of particle physics, FOPTs take place as the temperature of the Universe decreases, allowing the scalar field to tunnel from the so-called false vacuum to the lower-energy, true vacuum. Similarly to what happens when water boils, i.e., goes from a fluid phase to a gaseous one, this process is accompanied by the nucleation of bubbles, which then expand throughout the Universe, converting false vacuum into true vacuum as these sweep through the vast extent of our Universe. This results in the generation of GWs as bubbles collide and produce sound waves and turbulence in the plasma of the Universe. This mechanism provides a powerful way to probe the very high energy scales involved during these processes through the observation of a GWB. Furthermore, this interplay between particle physics and GWs provides a unique opportunity to explore regions of parameter space otherwise unreachable in typical particle physics experiments. Indeed, the new physics energy scales $\gtrsim 100$ TeV fall outside the range probed by Earth-based accelerators. However, precisely such large energy scales can give rise to a signal within the frequency range of the LVK detectors, since the peak of the GWB spectrum is expected to fall within the range $\sim 10 - 1000$ Hz for these scales.

This chapter starts by reviewing the theory of FOPTs by first introducing the concept of effective potential, and then taking a closer look at the generation of GWs from FOPTs. Section 5.2 is dedicated to deriving constraints using LVK data from their first three observing runs on a specific type of FOPTs: supercooled phase transitions. We then apply the same methodology to constrain the parameter space of two concrete particle physics models that exhibit supercooling in Section 5.3.

This chapter is partially based on work in collaboration with Charles Badger, Bartosz Fornal, Katarina Martinovic, Alba Romero, Huai-Ke Guo, Alberto Mariotti, Mairi Sakellariadou, Alexander Sevrin, Feng-Wei Yang, and Yue Zhao, as published in [50].

5.1 Theory of First Order Phase Transitions

In this section, we review the theory governing FOPTs. The concept of the effective potential is introduced, together with a toy model illustration of FOPTs and second order phase transitions (SOPTs), highlighting the main differences between the two. In addition, we review the mechanism behind the production of GWs from phase transitions and provide expressions for the predicted GWB signal. We end this section by commenting on a special class of FOPTs: supercooled phase transitions.

5.1.1 The Effective Potential and Phase Transitions

We now introduce the concept of effective potential, basing our review on [216]. When considering particle physics models that contain a scalar field, one usually thinks of the so-called Mexican hat potential:

$$V_0(\phi) = -\frac{\mu^2}{2}\phi^2 + \frac{\lambda}{4}\phi^4. \tag{5.1}$$

In reality, however, this tree-level potential receives contributions from quantum loop diagrams. Considering only one-loop contributions[1], these extra contributions take the form:

$$V_1^{\mathrm{CW}}(\phi) = \sum_i \frac{n_i}{64\pi^2}\left\{m_i^4(\phi)\left[\log\left(\frac{m_i^2(\phi)}{\mu^2}\right) - c_i\right]\right\}, \tag{5.2}$$

where the index i runs over the particle content of the model, n_i denotes the number of degrees of freedom for each of the particles (including a negative sign for fermions), and $m_i(\phi)$ are the masses of the i particles that couple to the scalar field ϕ. The parameter μ denotes the so-called renormalisation scale and $c_i = 5/6$ for gauge bosons, and $c_i = 3/2$ for other fields.

Additionally, the high energy scales, or equivalently high temperatures, make quantum field theory alone unsuitable to accurately describe the physics governing phase transitions. Instead of assuming these phase transitions take place in a vacuum, one relies on thermal field theory for a more precise description of the thermal bath in the Universe. This is captured by an

---

[1] Higher-order loops are assumed to be subdominant.

additional contribution to the potential:

$$V_T(\phi, T) = \sum_i n_i \frac{g_i T^4}{2\pi^2} J_i(\beta^2 m_i^2(\phi)), \tag{5.3}$$

where

$$J_i(\beta^2 m_i^2(\phi)) = \int dx\, x^2 \log\left(1 - (-1)^{F_i} \exp\left(-\sqrt{x^2 + \beta^2 m_i^2(\phi)}\right)\right). \tag{5.4}$$

The sum in the above expression runs over the particles i, with associated number of degrees of freedom n_i, $\beta = \frac{1}{T}$, and where $F_i = 1$ for fermions and $F_i = 0$ for bosons.

In the high-temperature limit, the integral in the above expression can be approximated [216]. For bosons, the integral can be expanded as:

$$J_B(m^2/T^2) = -\frac{\pi^4}{45} + \frac{\pi^2}{12}\frac{m^2}{T^2} - \frac{\pi}{6}\left(\frac{m^2}{T^2}\right)^{3/2} - \frac{1}{32}\frac{m^4}{T^4}\log\frac{m^2}{a_b T^2} + \ldots, \tag{5.5}$$

where $\log a_b = 5.4076$. For fermionic contributions, the high-temperature expansion of the integral takes the form:

$$J_F(m^2/T^2) = \frac{7\pi^4}{360} - \frac{\pi^2}{24}\frac{m^2}{T^2} - \frac{1}{32}\frac{m^4}{T^4}\log\frac{m^2}{a_f T^2} + \ldots, \tag{5.6}$$

where $\log a_f = 2.6351$. Both of the above expressions will be useful to build up some intuition when discussing two toy models later on in this section.

Furthermore, an additional term is sometimes added to the effective potential, the so-called Daisy contribution:

$$V_{\text{Daisy}}(\phi, T) = \sum_i n_i \frac{T}{12\pi}\left(\left(m_i^2(\phi)\right)^{3/2} - \left(m_i^2(\phi) + \Pi_i\right)^{3/2}\right), \tag{5.7}$$

where the sum again runs over the particles i and Π_i is the leading contribution in temperature to the one-loop thermal mass [95]. This contribution is introduced to deal with the re-summation of thermal loop diagrams, a topic that goes beyond the scope of this thesis. We refer the interested reader to [95] for additional information. Note, however, that these corrections to the potential are often small and do not have a large impact on the shape of the potential.

Taking all the above additions to the tree-level potential into account, one obtains the effective potential:

$$V_{\text{eff}}(\phi, T) = V_0(\phi) + V_1^{\text{CW}}(\phi) + V_T(\phi, T) + V_{\text{Daisy}}(\phi, T). \tag{5.8}$$

The above expressions dictate the temperature evolution of the potential, and therefore also the dynamics of the scalar field obeying this potential. Different model parameters and particle content of the theory will have a direct impact on the shape of the potential, influencing its evolution with temperature. As we will see below, the shape of the potential will determine whether a FOPT or a SOPT takes place as the temperature of the Universe decreases. Indeed, a potential barrier between the origin and the true vacuum will prove to be a characteristic and necessary feature for FOPTs. This is illustrated with two toy models below, based on [216].

Second or higher order phase transition

We start by discussing the case of SOPTs, by studying a concrete toy model realisation of the effective potential introduced above. In practice, it can be shown that SOPTs are approximately well-characterised by the following toy model:

$$V(\phi,T) = D\left(T^2 - T_0^2\right)\phi^2 + \frac{\lambda}{4}\phi^4, \tag{5.9}$$

where D, T_0, and λ are constants, determined by the underlying particle physics theory. Indeed, working in the high-temperature expansion introduced in Eqs. (5.5) and (5.6), it can easily be seen that the leading-order[2] contributions to the potential scale as $\sim \phi^2 T^2$. The temperature-dependent curvature, $m^2 = \partial^2 V/\partial\phi^2$, is given by

$$m^2(\phi,T) = 3\lambda\phi^2 + 2D\left(T^2 - T_0^2\right), \tag{5.10}$$

with two stationary points of the system being:

$$\phi(T) = 0, \qquad \phi(T) = \sqrt{\frac{2D\left(T_0^2 - T^2\right)}{\lambda}}. \tag{5.11}$$

Considering the evolution of the potential with the temperature T, one notices that for $T > T_0$, only the first solution in Eq. (5.11) exists, and $m^2(\phi,T) > 0$, rendering the origin the only stable minimum of the theory. When $T = T_0$, the potential only contains the quartic term, and both stationary points coincide. Once a regime where $T < T_0$ is entered, the origin becomes unstable due to the negative mass term in Eq. (5.10). The origin becomes a local maximum, with two new stationary points appearing away from the origin ($\phi \neq 0$). At $T = 0$, the mass term is negative, making the origin unstable. On the other hand, the other minimum at $\phi = \pm\sqrt{2D/\lambda}\,T_0$ is favoured due to its lower energy, spontaneously breaking the original $\phi \longleftrightarrow -\phi$ symmetry of the theory. The field configuration corresponding to $\phi = 0$ is called the symmetric

---

[2] Note that the next-to-leading order term for bosons scales as $\sim \phi^3 T$, leading to a FOPT as will be illustrated below.

phase or false vacuum, whereas $\phi \neq 0$ is said to be the broken phase or true vacuum. This is illustrated in Figure 5.1.

A key characteristic of SOPTs is that the transition happens smoothly as the temperature decreases. As will be seen below for FOPTs, it is the presence of a potential barrier between the true and false vacuum that enables the generation of GWs. Since this feature in the potential is not present for SOPTs, GWs cannot be generated during such transitions.

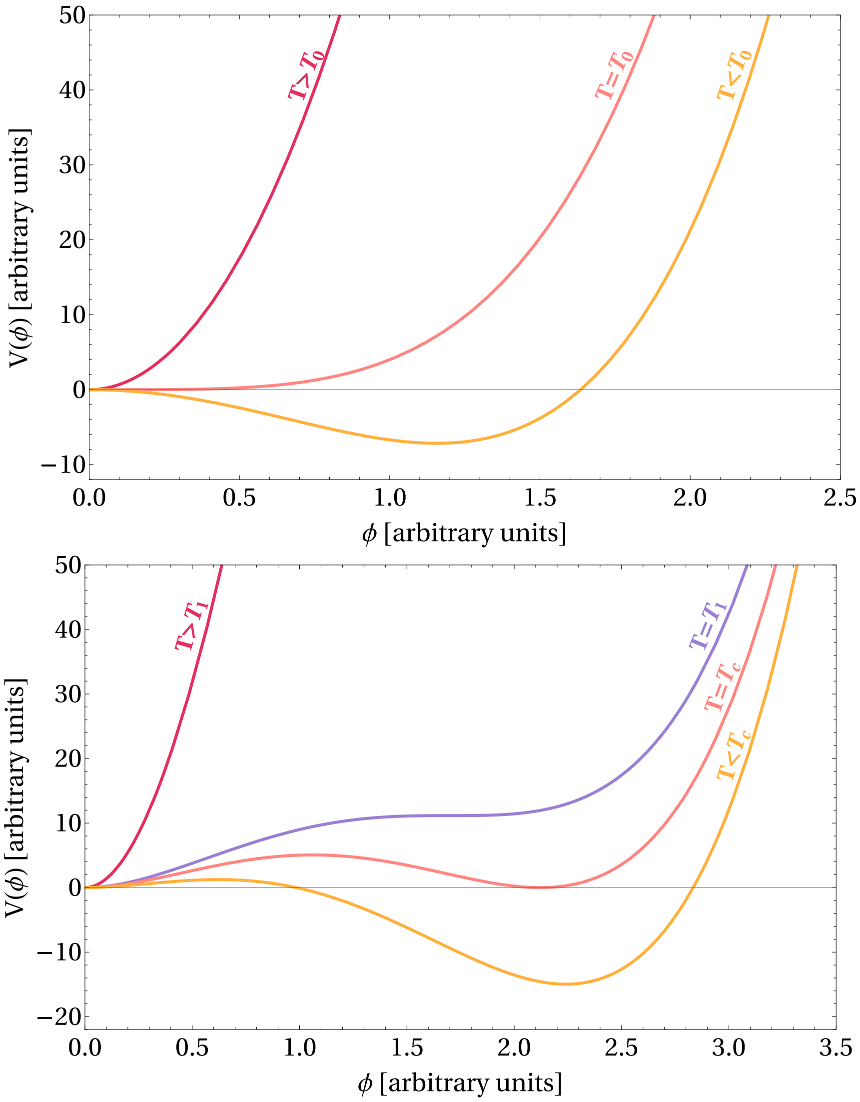

Figure 5.1. **Top**: A toy model representation of SOPTs. As the temperature of the Universe decreases, the origin becomes unstable, resulting in the true vacuum of the theory being away from the origin. For concreteness, the values of the parameters in Eq. (5.9) were chosen to be $D = 1$, $\lambda = 16$, and $T_0 = 10$. **Bottom**: A toy model representation of FOPTs. As the Universe cools down, an inflection point appears in the potential. Both minima (at the origin and away from it) are degenerate when the critical temperature T_c is reached, with a barrier between the two minima for even lower temperatures. For concreteness, the values of the parameters in Eq. (5.12) were chosen to be $D = 2$, $E = 4$, $\lambda = 16$, and $T_0 = 3$.

First order phase transition

We now move to the description of FOPTs through the same toy model approach as done above for SOPTs. However, FOPTs differ from second or higher order ones due to the presence of a barrier in the potential between the symmetric and broken phase. To illustrate this characteristic feature, the toy model potential now contains a cubic term in the potential:

$$V(\phi,T) = D\left(T^2 - T_0^2\right)\phi^2 - ET\phi^3 + \frac{\lambda}{4}\phi^4, \tag{5.12}$$

where D, T_0, E, and λ are constants, again determined by the underlying particle physics theory. As pointed out above, working in the high-temperature limit, the appearance of the cubic term can intuitively be understood from the next-to-leading order term in the bosonic contribution in Eq. (5.5), which scales as $\sim \phi^3 T$. As the Universe cools down, an inflection point is formed at a temperature $T = T_1$, given by

$$T_1^2 = \frac{8\lambda D T_0^2}{8\lambda D - 9E^2}, \tag{5.13}$$

with corresponding field value $\phi(T_1) = 3ET_1/2\lambda$. As the temperature decreases further, a barrier appears between this inflection point and the origin. The two points become degenerate at the critical temperature T_c:

$$T_c^2 = \frac{\lambda D T_0^2}{\lambda D - E^2}. \tag{5.14}$$

Once the critical temperature is reached, the origin becomes metastable, with the other minimum at $\phi \neq 0$ taking on the role of true vacuum of the theory with lower energy. Finally, the barrier completely disappears at some temperature T_0, making the origin a local maximum of the potential. This is illustrated in Figure 5.1. Although the barrier impedes the scalar to roll to the true vacuum, we will see that thermal tunnelling through the barrier will allow the scalar field to reach the true vacuum. This is an important part of the mechanism that will eventually lead to GWs, as will be illustrated below.

Before moving on to the discussion of GW generation from FOPTs, we want to point out that the particle content of the Standard Model (SM) alone does not give rise to FOPTs in the early Universe. Nevertheless, FOPTs are a generic feature in a number of theories beyond the Standard Model (BSM). As such, the observation of a FOPT GWB signal will provide smoking gun evidence for BSM physics, making it an exciting topic to investigate. Some examples include models with new physics at the electroweak scale [36, 77, 110, 140, 256], hidden sectors [66, 93, 144, 239], dark matter [49, 52, 53, 55, 145], unification [65, 92, 157, 207], confinement [94, 150, 158], baryon and/or lepton number violation [48, 54, 78, 133, 148, 168], neutrino mass models [64, 104, 206, 267], axions [101, 103, 258], supersymmetry breaking

[90, 102, 134], or theories explaining flavour anomalies [132, 139]. For a more complete list of references on models exhibiting FOPTs, we refer the reader to [68].

This first section established the basic concepts related to phase transitions, and stressed the key feature of FOPTs enabling the generation of GWs: the potential barrier. In the next section, we review how a potential barrier allows for the generation of GWs and provide the GW spectra of the resulting GWB.

5.1.2 Gravitational Waves from First Order Phase Transitions

In this section, we review the mechanism behind the generation of GWs during FOPTs happening in the early stages of the Universe. We start by introducing the concept of FOPT bubbles, naturally followed by the introduction of a set of key parameters characterising the phase transition. We then proceed with a review of the expected contributions to the GWB and detail how the introduced parameters enter in the predicted GWB spectra.

Bubble Dynamics

The toy model introduction of FOPTs given in Eq. (5.12) revealed a key feature that characterises the FOPT: the potential barrier. Although this barrier prevents the scalar field from "rolling" from the false vacuum at the origin to the lower-energy true vacuum away from the origin, thermal tunnelling presents itself as an alternative way to reach the true vacuum. After reaching the critical temperature T_c, such thermal tunnelling can occur through the generation of true vacuum bubbles in the Universe. These bubbles of true vacuum will expand in a sea of false vacuum, converting false vacuum into true vacuum [75, 191]. This is schematically represented in Figure 5.2.

To describe the above tunnelling process, one needs to find the field configuration that interpolates between the false and the true vacuum: the bounce solution. This is the solution to the following equation of motion:

$$\frac{d^2\phi}{dr^2} + \frac{2}{r}\frac{d\phi}{dr} - \frac{\partial V}{\partial \phi}(\phi, T) = 0, \tag{5.15}$$

with boundary conditions $\lim\limits_{r\to\infty} \phi(r) = 0$, and $\frac{d\phi}{dr}\Big|_{r=0} = 0$. The solution to this equation of motion can be computed numerically by using the so-called shooting method [112]. Several implementations of the method are publicly available, e.g., `FindBounce` [141] or `CosmoTransitions` [259]. An example of such a bounce profile solution is given in the top panel of Figure 5.3.

With the bounce solution at hand, the tunnelling process from false to true vacuum is then

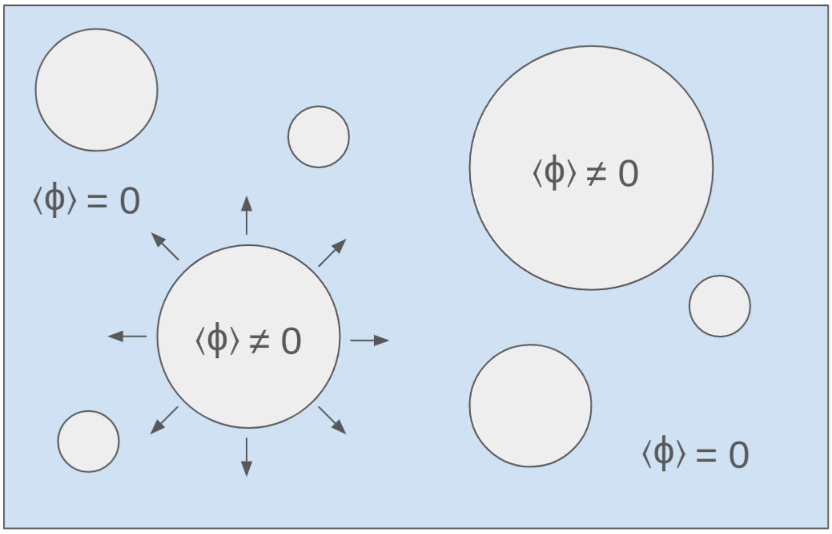

Figure 5.2. Schematic representation of true vacuum bubbles expanding in the false vacuum Universe. Inside the bubbles, the field ϕ sits in the true vacuum, i.e., $\phi \neq 0$, whereas in the remainder of the Universe, the field is still in the false vacuum, i.e., $\phi = 0$, waiting to be converted to the true vacuum.

characterised by a tunnelling probability per unit volume:

$$\Gamma(T) = A(T)\exp\left(-S(T)\right), \tag{5.16}$$

where $A(T)$ denotes some proportionality factor, and the quantity $S(T)$ stands for the Euclidean action, evaluated on the bounce solution from the equation of motion above [191]. We are interested in FOPTs taking place at finite temperatures, for which the tunnelling probability can be approximated as [183]:

$$\Gamma(T) \simeq T^4 \exp\left(-\frac{S_3(T)}{T}\right), \tag{5.17}$$

where

$$S_3(T) = \int d^3x \left(\frac{1}{2}(\partial_i \phi)^2 + V(\phi, T)\right). \tag{5.18}$$

In particular, one can consider spherical bubbles possessing an $O(3)$ symmetry, yielding [191]:

$$S_3(T) = 4\pi \int_0^\infty dr\, r^2 \left(\frac{1}{2}\left(\frac{d\phi}{dr}\right)^2 + V(\phi, T)\right), \tag{5.19}$$

where again, this quantity is evaluated on the bounce solution by substituting the solution of Eq. (5.15) for $\phi(r)$. An example of the bounce action is given in the bottom panel of Figure 5.3.

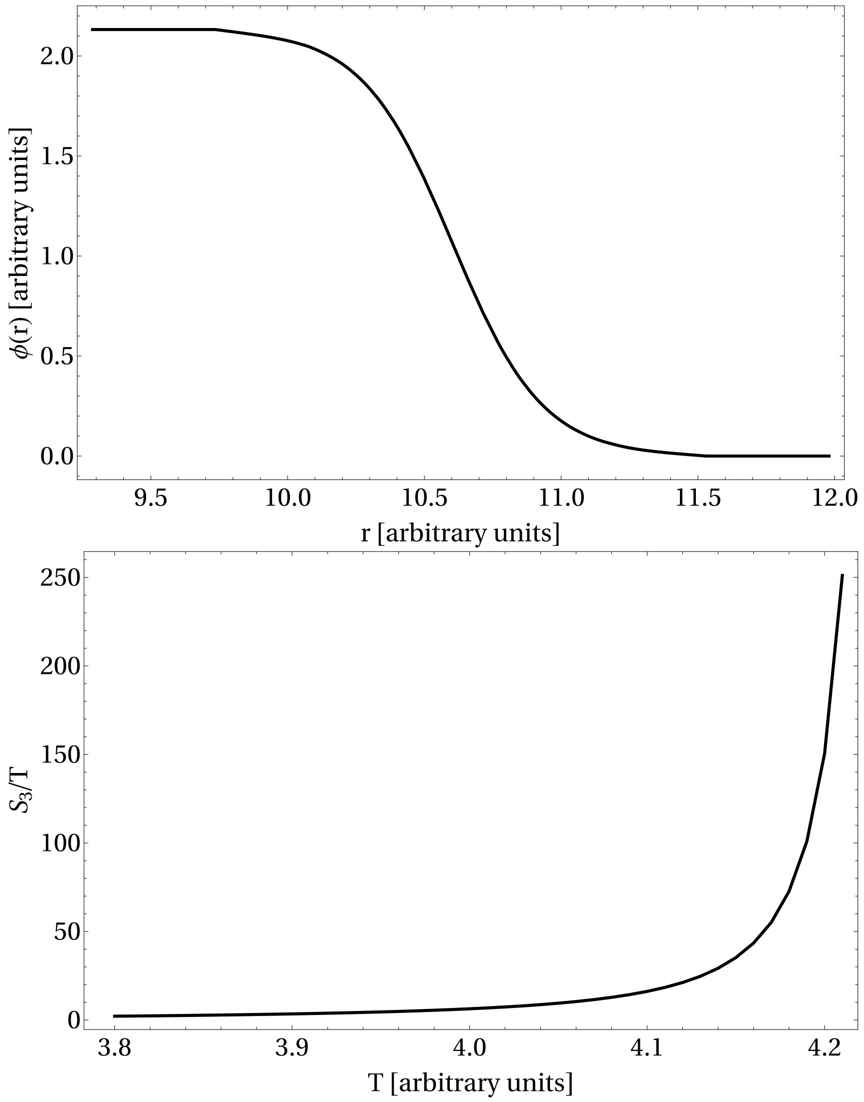

Figure 5.3. **Top**: Bounce profile as a solution to the equation of motion in Eq. (5.15), with potential parameters in Eq. (5.12) set to $D = 2$, $E = 4$, $\lambda = 16$, $T_0 = 3$, and $T = 4.22$. **Bottom**: Bounce action S_3/T as a function of temperature for the potential in Eq. (5.12) with parameters $D = 2$, $E = 4$, $\lambda = 16$, and $T_0 = 3$.

Properties of First Order Phase Transitions

A natural question that arises is how long the conversion of false to true vacuum takes, and more importantly, whether the bubble expansion is fast enough compared to the expansion rate of the Universe for the FOPT to complete. The latter is characterised by the Hubble parameter $H(t) = \dot{a}(t)/a(t)$, where $a(t)$ is the scale factor parameterizing the expansion of the Universe [76]. The Friedmann equation then relates the evolution of the Hubble parameter with the energy content of the Universe, which for radiation and vacuum domination reads:

$$H^2(T) = \frac{1}{3M_p^2}\left(\frac{\pi^2 g_*}{30}T^2 + \Delta V\right), \tag{5.20}$$

where $M_p = 2.435 \times 10^{18}$ GeV denotes the Planck mass, ΔV denotes the difference between the zero-temperature potential evaluated at the false vacuum and the true vacuum, and g_* denotes the effective number of relativistic degrees of freedom[3] [119]. To compare the expansion rate of the Universe to the tunnelling rate of the bubble, one can consider the tunnelling rate inside a Hubble volume $1/H^3(T)$. Requiring the number of bubbles that nucleated between $t = 0$ and $t = t_*$ to be of $\mathcal{O}(1)$ gives an estimate of the time t_* at which the phase transition happened:

$$\int_0^{t_*} dt\, \frac{\Gamma}{H^3(t)} = \mathcal{O}(1). \tag{5.21}$$

The above condition can easily be translated in terms of temperature, rather than time, as $dT/T = -Hdt$:

$$\int_{T_*}^{T_c} \frac{dT}{T}\frac{\Gamma}{H^4(T)} = \mathcal{O}(1), \tag{5.22}$$

which once solved, yields an expression for the nucleation temperature T_* of the FOPT. Since the above integral is dominated by its value at T_*, the condition can be approximated as:

$$\frac{S_3(T_*)}{T_*} \approx 4\log\left(\frac{T_*}{H}\right), \tag{5.23}$$

which can be solved numerically for arbitrary bounce actions. However, as an example, one can consider a phase transition around the electroweak scale, for which $T_* \simeq 100$ GeV. Assuming radiation domination, i.e., where ΔV is negligible in Eq. (5.20), the nucleation condition then reduces to finding the intersection $S_3(T_*)/T_* \simeq 145$ [191].

In addition to the nucleation temperature, several other quantities describe the FOPT. For example, a measure of the strength of the phase transition is given by the following parameter, normalised to the radiation energy density of the Universe:

$$\alpha = \frac{\rho_{\text{vac}}(T_*)}{\rho_{\text{rad}}(T_*)}, \tag{5.24}$$

which is proportional to the vacuum energy density of the transition, ρ_{vac}, evaluated at the

---

[3] Typical values for energy scales around the electroweak scale are around $g_* \sim \mathcal{O}(100)$ [119].

temperature at which the phase transition takes place:

$$\rho_{\text{vac}}(T_*) = \left(-V(\eta(T),T) + T\frac{d}{dT}V(\eta(T),T)\right)\Bigg|_{T=T_*}. \tag{5.25}$$

Here, $\eta(T)$ denotes the vacuum expectation value (VEV) in the true vacuum of the effective potential at temperature T.

Additionally, the inverse duration of the phase transition in Hubble units is characterised by:

$$\frac{\beta}{H_*} = T_*\frac{d}{dT}\left(\frac{S_3(T)}{T}\right)\Bigg|_{T=T_*}, \tag{5.26}$$

where $H_* = H(T_*)$ is the Hubble parameter evaluated at the temperature of the phase transition.

Although the nucleation condition, given in Eq. (5.22), was introduced as a way to verify that the phase transition actually takes place, this requirement might not be enough to guarantee that the whole Universe is converted from false to true vacuum. This is especially true in vacuum-dominated universes, where the second term of Eq. (5.20) dominates [121]. In that case, one can consider the so-called percolation temperature at which the probability of being in the true vacuum is large enough to ensure the completion of the FOPT relative to the expansion of the Universe. This is defined through the probability of a point still being in the false vacuum:

$$P(T) = e^{-I(T)}, \tag{5.27}$$

where

$$I(T) = \frac{4\pi}{3}\int_T^{T_c}\frac{dT'}{T'}\frac{\Gamma(T')}{T'^4H(T')}\left(\int_T^{T'}d\tilde{T}\frac{v_w}{H(\tilde{T})}\right)^3, \tag{5.28}$$

with v_w the bubble wall velocity [121, 143]. The temperature at which $P(T_p) = 1/e$, or equivalently $I(T_p) = 1$, is defined as the percolation temperature. In addition, one needs to verify that this probability decreases faster than the increase of the expanding Universe volume being considered:

$$\frac{1}{\mathcal{V}_{\text{false}}}\frac{d\mathcal{V}_{\text{false}}}{dt}\Bigg|_{t=t_p} = H(T)\left(3 + T\frac{dI(T)}{dT}\right)\Bigg|_{T=T_p} < 0, \tag{5.29}$$

where $\mathcal{V}_{\text{false}}$ is the physical volume of false vacuum. In other words, the bubble has to expand faster than the expansion rate of the volume it resides in. For weak FOPTs, with generally large values of β/H_*, the value of the nucleation and percolation temperatures typically coincide. However, for stronger phase transitions, the percolation temperature should be computed to ensure the phase transition completes.

With the above parameters and concepts at hand, we now proceed with the discussion of the various contributions from FOPTs to the GWB. The previously introduced bubbles and their expansion throughout the plasma in the early stages of the Universe will be at the center of the GW generation mechanism. In addition, we will see below how the parameters introduced above enter in the different contributions to the GW spectra.

Gravitational-Wave Background

The previous section laid out the necessary concepts and parameters that describe FOPTs. Below, we illustrate how these parameters enter in the predictions for the GWB signal from FOPTs and review the generation mechanisms of GWs from FOPTs.

Recall that the dimensionless energy density $\Omega_{\rm GW}(f)$, previously introduced in Eq. (2.13) in Chapter 2, characterises the GWB. For FOPTs, the total GWB spectrum is given by the sum of several contributions:

$$\Omega_{\rm GW}(f) = \Omega_{\rm bc}(f) + \Omega_{\rm sw}(f) + \Omega_{\rm turb}(f), \tag{5.30}$$

where $\Omega_{\rm bc}$ represents the contribution from bubble collisions, $\Omega_{\rm sw}$ that of sound waves, and finally, $\Omega_{\rm turb}$ the contribution from magneto-hydrodynamic turbulence. The prediction for each of these contributions forms the results of a plethora of numerical simulations[4].

The relative strength of these contributions is controlled by the total energy budget of the FOPT and can be parameterized by additional parameters κ_i which denote the efficiency of each contribution i to the total GWB spectrum. The value of these factors capture the intricacies of the processes involved in the FOPT and form the result of involved computations which go beyond the scope of this thesis. Nevertheless, we point out that many factors have an impact on these quantities, such as the particle content of the plasma and its resulting friction on the bubble walls. More information can be found in [121].

Below, we provide additional information about the different generation mechanisms and give the predicted GWB spectra for each of the contributions to the total GWB from FOPTs.

Bubble collisions

A first contribution arises from the collision of expanding bubbles throughout the Universe. Working under the assumption that the energy is stored in the walls of the bubble, and that

---

[4] New simulation results appear regularly, often with different GW spectra predictions, see e.g., [96, 97, 138, 164, 181, 200, 262]. In this thesis, we stick to one expression throughout, although being aware that more recent or different versions of the spectra are available. Nevertheless, the work presented below still illustrates the methodology as a proof of concept, easily applicable to other GWB spectra available in the literature.

these are thin[5], one finds [74]:

$$h^2\Omega_{\rm bc} = 1.67 \times 10^{-5} \left(\frac{H_*}{\beta}\right)^2 \left(\frac{\kappa_{\rm bc}\alpha}{1+\alpha}\right)^2 \left(\frac{100}{g_*}\right)^{1/3} \left(\frac{0.11 v_w^3}{0.42+v_w^2}\right) S_{\rm bc}(f), \tag{5.31}$$

where the spectral shape of the GWB is captured by $S_{\rm bc}(f)$. The bubble wall velocity is denoted by v_w, and the efficiency parameter mentioned above, or more precisely, the fraction of latent heat converted into kinetic energy of the walls, is denoted by $\kappa_{\rm bc}$ [121, 122, 137]. One also notes the appearance of the α and β/H_* parameters, as previously introduced in Eqs. (5.24) and (5.26), respectively. From simulations [159], the spectral shape is found to be:

$$S_{\rm bc}(f) = \frac{3.8(f/f_{\rm bc})^{2.8}}{1+2.8(f/f_{\rm bc})^{3.8}}, \tag{5.32}$$

where the peak frequency redshifted to today is given by:

$$f_{\rm bc} = 16.5 \left(\frac{0.62}{1.8-0.1v_w+v_w^2}\right)\left(\frac{\beta}{H_*}\right)\left(\frac{T_*}{100{\rm GeV}}\right)\left(\frac{g_*}{100}\right)^{1/6} \mu{\rm Hz}. \tag{5.33}$$

In this expression, T_* stands for the temperature at which the phase transition took place, and g_* denotes the number of relativistic degrees of freedom. A few examples of such spectra are shown in the top panel of Figure 5.4.

Sound waves

We now proceed with the contribution from sound waves. Indeed, following the collision of bubbles, sound waves are generated throughout the plasma of the Universe, which in turn can generate GWs. Numerical simulations predict the GW spectrum to take the form [74, 142, 153]:

$$h^2\Omega_{\rm sw}(f) = 2.65 \times 10^{-6} \left(\frac{H_*}{\beta}\right) \left(\frac{\kappa_{\rm sw}\alpha}{1+\alpha}\right)^2 \left(\frac{100}{g_*}\right)^{1/3} v_w \Upsilon(\tau_{\rm sw}) S_{\rm sw}(f) \tag{5.34}$$

where $S_{\rm sw}(f)$ denotes the spectral shape of the spectrum:

$$S_{\rm sw}(f) = \left(\frac{f}{f_{\rm sw}}\right)^3 \left(\frac{7}{4+3(f/f_{\rm sw})^2}\right)^{7/2}. \tag{5.35}$$

The redshifted peak frequency $f_{\rm sw}$ is given by

$$f_{\rm sw} = 19 \frac{1}{v_w}\left(\frac{\beta}{H_*}\right)\left(\frac{T_*}{100{\rm GeV}}\right)\left(\frac{g_*}{100}\right)^{1/6} \mu{\rm Hz}. \tag{5.36}$$

---

[5] This defines the so-called envelope approximation. In recent years, it has been shown that more accurate predictions can be found if one moves away from this approximation [164, 181, 200, 262].

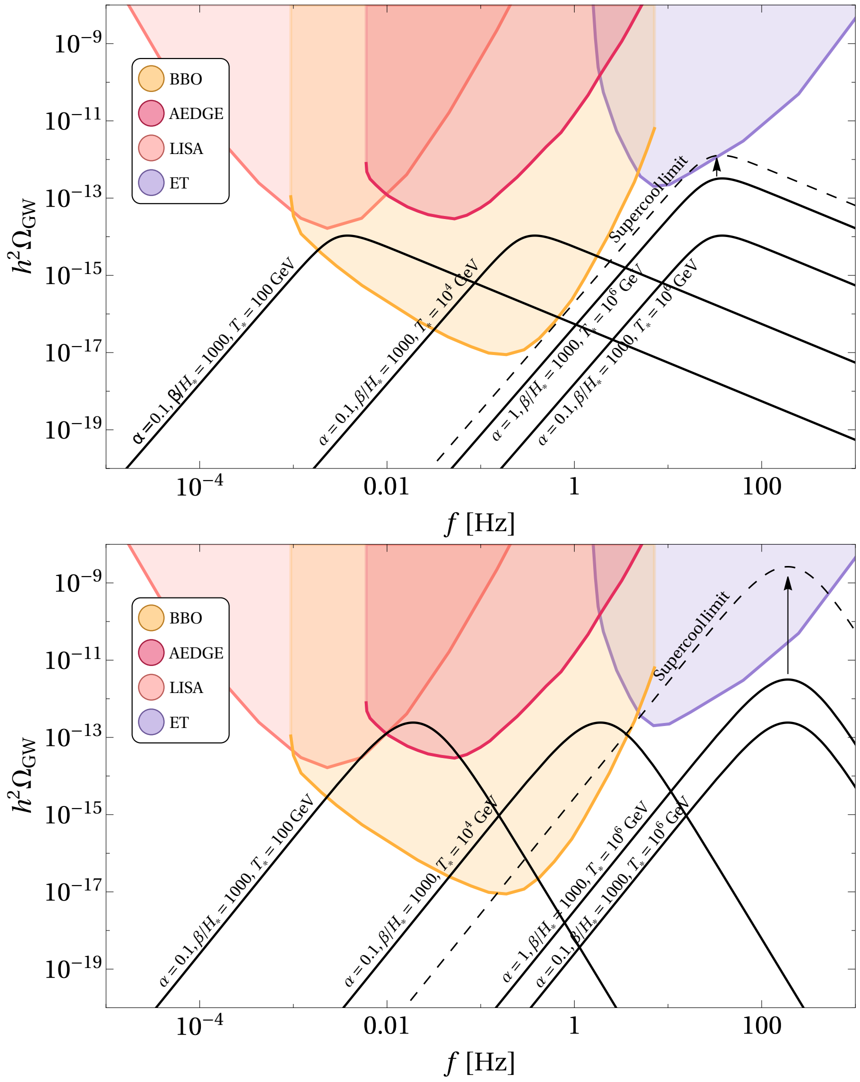

Figure 5.4. Examples of spectra for the bubble collision contribution (top), as given by Eq. (5.31), and the sound waves contribution (bottom), as given by Eq. (5.34). Different values of the α, β/H_*, and T_* parameters are used to illustrate the dependence of the GWB spectra on these quantities. The dashed lines denote the supercooling limit, in which $\alpha \gg 1$, as given in Eq. (5.39) (Eq. (5.41)) for bubble collisions (sound waves). The coloured lines denote the PI curves for several experiments: BBO[263], AEDGE[205], LISA[58], and ET [215].

An additional suppression due to the finite lifetime of the sound waves contribution[6], $\tau_{\rm sw}$, is captured by [118, 142]:

$$\Upsilon(\tau_{\rm sw}) = 1 - (1 + 2\tau_{\rm sw} H_*)^{-1/2}, \tag{5.37}$$

where $\tau_{\rm sw} \approx R_*/\bar{U}_f$, with $R_* = (8\pi)^{1/3} v_w/\beta$ [142, 152], and $\bar{U}_f^2 = 3\kappa_{\rm sw}\alpha/(4(1+\alpha))$ [261]. The parameter $\kappa_{\rm sw}$ denotes the fraction of vacuum energy transferred into the kinetic energy of the

---

[6] The finite sound wave lifetime, $\tau_{\rm sw}$, results in a multiplicative factor that is a function of $\tau_{\rm sw}$ and the expansion rate of the Universe when the sound waves were active [118, 142]. Currently, the value of $\tau_{\rm sw}$ remains highly uncertain, though an analytical estimate is usually adopted in the literature.

bulk flow [122, 137]. A few examples of such spectra are given in the bottom panel of Figure 5.4.

Turbulence

An additional contribution from subsequent magneto-hydrodynamic turbulence in the plasma usually also forms a source of GWs. However, due to the large uncertainty in the predicted spectrum, and the usually smaller amplitude of the spectrum compared to the other contributions, we refrain from including this contribution in this work [74, 167].

Detectability of Gravitational-Wave Background Signals

Although below we will focus on the LVK interferometers and provide constraints from real detector data from the first three LVK observing runs, we briefly discuss the detectability of FOPT signals at future sensitivities. To this end, we consider the ET, LISA, and the Advanced LIGO A+ detector configurations. To assess the detectability of the FOPT GWB signals, we use the PI curve formalism introduced in Section 2.2.1 and check whether a given predicted spectrum lies above this curve. Note that this exercise is mostly for illustrative purposes, as many uncertainties are involved in this example. Indeed, the PI curves are designed to assess the detectability of signals that follow a power law across the detector's frequency range, rather than the broken power law (BPL) shape of FOPT spectra. Additionally, both the predicted FOPT GWB spectra and the sensitivities of future interferometers are still subject to change. Nevertheless, this analysis provides a ballpark estimate of the FOPT parameter space that can be probed by future detector configurations.

In Figures 5.5, 5.6, and 5.7 we illustrate the detection prospects for FOPT signals from bubble collisions and sound waves for the Advanced LIGO A+, the ET, and the LISA detector configurations, respectively. Coloured regions denote regions of the FOPT parameter space where the predicted signal intersects the PI curve, where the colour denotes the minimum value of the α parameter for the signal to be detectable. As can be seen from Eqs. (5.31) and (5.34), as α increases, so does the signal, eventually reaching an asymptotic value. Therefore, any value of the α parameter above the minimum value required for detection will also be detectable.

These examples illustrate the different parts of parameter space that will be probed by future detector sensitivities. In particular, one notes the difference in energy scales, as given by the temperature T_* at which phase transitions happened. Indeed, as can be seen from Eqs. (5.33) and (5.36), the peak frequency of the FOPT spectrum is proportional to the energy scale at which the phase transition happened. Therefore, each experiment in a different frequency range opens a window to the physics happening at the corresponding, different energy scales.

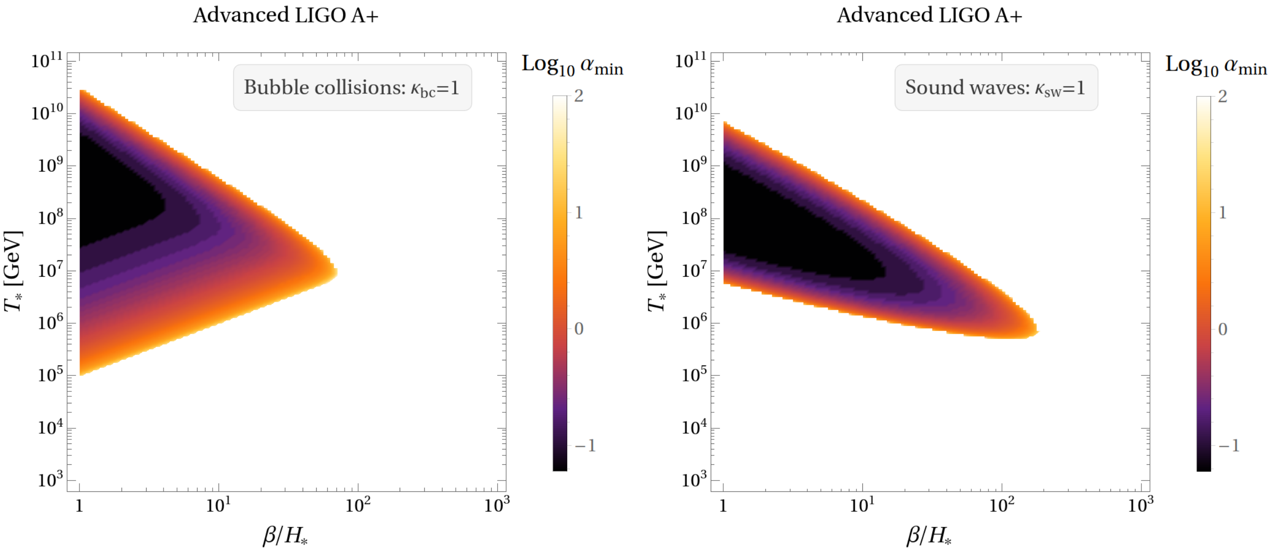

Figure 5.5. Detectability region of FOPT GWB signals using the Advanced LIGO A+ sensitivity [19] assuming a dominant bubble collisions contribution (left) and a dominant sound waves contribution (right). The colour denotes the minimum value of the α parameter for the signal to be within reach of the detector sensitivity.

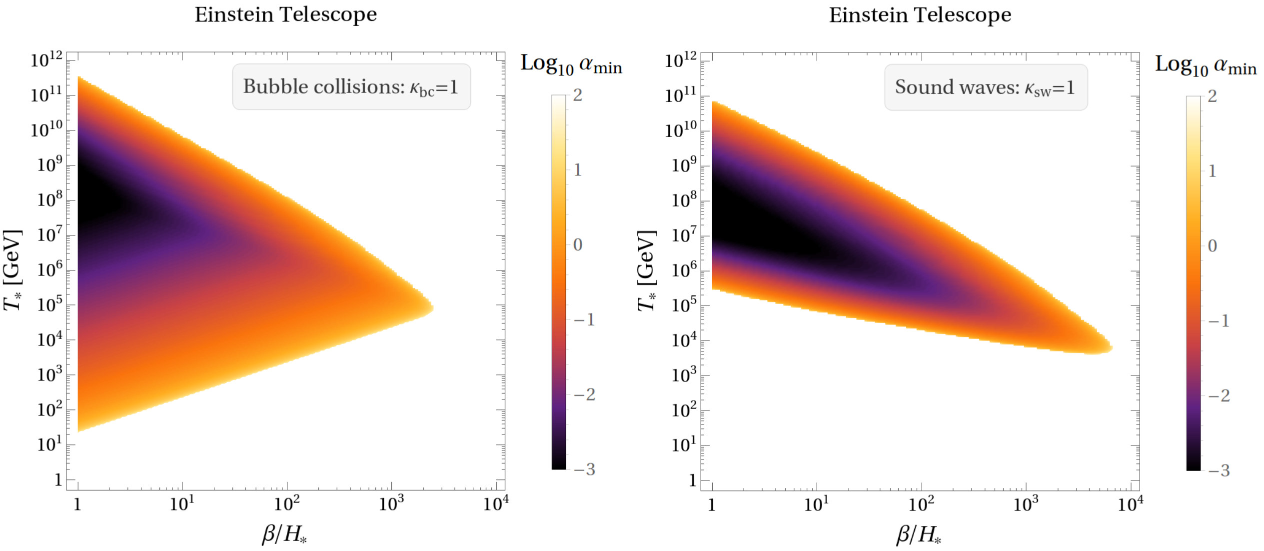

Figure 5.6. Detectability region of FOPT GWB signals using the ET sensitivity [215] assuming a dominant bubble collisions contribution (left) and a dominant sound waves contribution (right). The colour denotes the minimum value of the α parameter for the signal to be within reach of the detector sensitivity. Note the different axes scaling and colour scaling with respect to Figure 5.5, illustrating the improved reach and sensitivity of the ET.

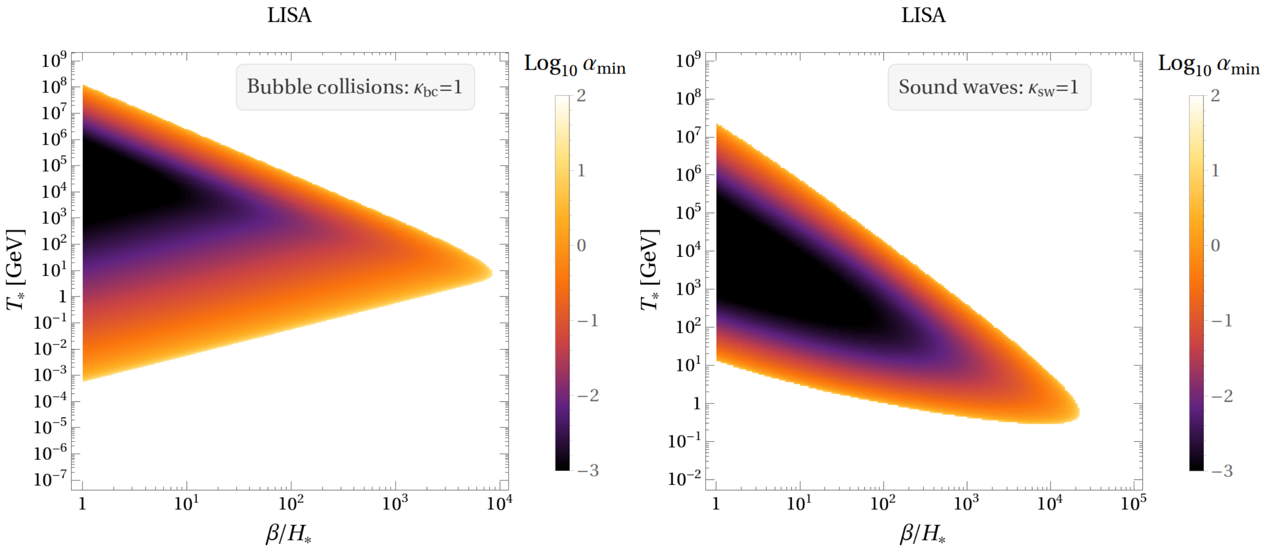

Figure 5.7. Detectability region of FOPT GWB signals using the LISA sensitivity [58] assuming a dominant bubble collisions contribution (left) and a dominant sound waves contribution (right). The colour denotes the minimum value of the α parameter for the signal to be within reach of the detector sensitivity. Note the different axes scaling and colour scaling with respect to Figure 5.5, illustrating the improved reach and sensitivity of the LISA, as well as the different energy scales it can reach.

5.1.3 Supercooled Phase Transitions

A particularly interesting scenario is when the FOPT is supercooled, which often increases the duration of the FOPT, leading to an enhancement of the GWB signal. The phenomenon of supercooling occurs when the nucleation temperature is much lower than the scale of the symmetry breaking triggering the FOPT, leading to a large FOPT strength, i.e., $\alpha \gg 1$. Given the current sensitivity of the LVK detectors, one may expect that FOPT GWB signals in reach of the experiment would most probably come from a supercooled FOPT. Such prolonged periods of supercooling can arise in theories with Coleman-Weinberg-type symmetry breaking [86] or in strongly-coupled scenarios. Some models of this type are discussed in [26, 27, 56, 91, 101, 118, 120, 121, 146, 165, 166, 172, 180, 181, 196, 204, 214, 217, 258].

Although the theory behind FOPTs remains the same as the one discussed in the previous sections, a few differences should be noted compared to the case of FOPTs without supercooling. For example, the temperature of the thermal bath at the time when the GWs are produced is not the nucleation temperature, but rather the reheating temperature $T_{\rm RH}$[7]. Indeed, after the collision of bubbles, the scalar field oscillates around the minimum of the potential, eventually decaying and reheating the plasma [121]. The reheating temperature is approximately given

---

[7] Note that, in the case of supercooled FOPTs, special care needs to be taken to make sure that bubble percolation is possible despite the exponential expansion of the false vacuum [120]. More information regarding percolation can be found around Eq. (5.27) and in [120, 121].

by:

$$T_{\rm RH}^4 \simeq \frac{30}{\pi^2 g_*}\Delta V, \tag{5.38}$$

where ΔV is the potential difference between the true and false vacuum, and g_* is the number of relativistic degrees of freedom. It is often the case that $T_{\rm RH} \gg T_*$, especially for supercooled phase transitions. However, for sufficiently fast reheating one has $H(T_*) \simeq H(T_{\rm RH})$, which implies that $\beta/H_* \simeq \beta/H_{\rm RH}$ [74]. In addition, it has been argued that in such a supercooled case, the bubble wall velocity is close to the speed of light [120]. We therefore set $v_w = c$ in the subsequent analyses.

Keeping the above in mind, we recall that several processes contributed to the GW signal from FOPTs. Those included bubble collisions, sound waves, and turbulence (the last of which we would not consider here, as it is generally subdominant [74, 167]). For the case of supercooling, we assume $\alpha \gg 1$ and modify the spectra in Eqs. (5.31) and (5.34) accordingly[8]. When calculating the contribution of bubble collisions to the GWB signal, we assume that, in the limit of large α, the fraction of the latent heat deposited into the bubble front is $\kappa_{\rm bc} \sim 1$, leading to [74, 159, 173]:

$$h^2\Omega_{\rm bc}(f) \approx 4.88\times 10^{-6} \frac{(f/f_{\rm bc})^{2.8}}{1+2.8\,(f/f_{\rm bc})^{3.8}}\left(\frac{H_{\rm RH}}{\beta}\right)^2\left(\frac{100}{g_*}\right)^{\frac{1}{3}}. \tag{5.39}$$

The peak frequency $f_{\rm bc}$ is given by:

$$f_{\rm bc} \approx 37\left(\frac{g_*}{100}\right)^{\frac{1}{6}}\left(\frac{\beta}{H_{\rm RH}}\right)\left(\frac{T_{\rm RH}}{1\ \text{TeV}}\right)\mu\text{Hz}. \tag{5.40}$$

When considering cases in which the released energy is efficiently transferred to the plasma in the form of sound waves, we assume $\kappa_{\rm sw} \sim 1$, and the resulting spectrum is [74, 151]

$$h^2\Omega_{\rm sw}(f) \approx 1.86\times 10^{-5} \frac{(f/f_{\rm sw})^{3}}{\left[1+0.75\,(f/f_{\rm sw})^{2}\right]^{7/2}}\left(\frac{H_{\rm RH}}{\beta}\right)\left(\frac{100}{g_*}\right)^{\frac{1}{3}}, \tag{5.41}$$

where the peak frequency $f_{\rm sw}$ takes the form:

$$f_{\rm sw} \approx 190\left(\frac{g_*}{100}\right)^{\frac{1}{6}}\left(\frac{\beta}{H_{\rm RH}}\right)\left(\frac{T_{\rm RH}}{1\ \text{TeV}}\right)\mu\text{Hz}. \tag{5.42}$$

Implicit in this spectrum is an infinite sound wave lifetime $\tau_{\rm sw}$. Note that this is a good approximation only if turbulence and other damping processes are ignored, which is what we assume

---

[8] The GW spectra in [74, 151, 159, 167, 173] are simulated for FOPTs not exhibiting large supercooling. In our analyses we assume that those results can be extrapolated to the region of large α.

in the subsequent analyses. Note that, as we assumed a supercooled FOPT and considered the limit of $\alpha \gg 1$, the dependence on the α parameter completely vanishes from the spectra above. These spectra are illustrated by the dashed lines in Figure 5.4 for some benchmark values of the parameters entering the GWB spectrum.

This concludes the first section on the theory governing the GWB emission during FOPTs. We seek to apply this formalism to search for signatures of such GWB signals in LVK data. We will start by remaining agnostic about the model in which the FOPT arises, and simply constrain the spectra above and the relevant FOPT parameters, without assuming a specific particle physics model in which the FOPT arises. This will be done by constraining a general BPL spectrum and using the spectra in Eqs. (5.39) and (5.41), which will be referred to as the phenomenological approach below in Section 5.2. Then, in Section 5.3, we will consider two specific particle physics models in which such FOPTs arise, and provide constraints on the parameter space of the models under consideration.

5.2 Constraints on Supercooled Phase Transitions Using LVK Data

To place constraints on model parameters using public GWB data from the first three observing runs of the LVK collaborations [19], we apply a Bayesian inference search following the methodology of [231]. Although a search for FOPT signals was already performed in [231], we now apply this search under the assumption that the signal comes from a supercooled phase transition, which, as mentioned in the previous section, is highly probable given the current sensitivity of the LVK detectors. As shown in Eqs. (5.39) and (5.41), the supercooling assumption gets rid of some parameter dependence and simplifies the GWB spectra, e.g., the α parameter, and therefore results in less parameters in the Bayesian inference search. The remainder of this chapter is based on original results [50].

For the Bayesian inference, we use the likelihood previously defined in Eq. (2.38), but now modify the model assumption for $\Omega_{\rm M}(f)$ to denote the GWB spectrum from FOPTs. The optimal estimators $\hat{C}_{IJ}(f)$ and $\sigma_{IJ}(f)$ in Eq. (2.38), are the ones defined by Eqs. (2.26) and (2.27), as produced by the LVK collaborations[9] [19, 230].

In the remainder of this section, two approaches will be explored. One of these is based on approximating the GWB signal as a BPL and another using the spectra provided in the previous section, as given by Eqs. (5.39) and (5.41). In both cases, the contribution from the astrophysical background, i.e., from unresolved CBCs, will be taken into account as well. Indeed, whereas a GWB from cosmological origin is purely speculative, the background from

---

[9] The data products are available to the public here.

unresolved CBCs results from the current (limited) sensitivity of the detectors and will likely present itself as a foreground for cosmological GWBs. For the frequency range of the LVK instruments, the CBC background is expected to follow a power law:

$$\Omega_{\rm CBC}(f) = \Omega_{\rm ref}\left(\frac{f}{f_{\rm ref}}\right)^{2/3}, \tag{5.43}$$

where $f_{\rm ref}$ is a reference frequency set to $f_{\rm ref} = 25$ Hz, in line with LVK GWB searches [19]. It is worth noting that the constraints obtained in this section are general and can be applied to any model exhibiting supercooled FOPTs to constrain the underlying physical parameters. This will be done in Section 5.3 for two concrete particle physics models.

5.2.1 General Broken Power Law Search

We first start by considering the BPL approach. It can be observed that the spectra in Eqs. (5.39) and (5.41) can be approximately modelled as BPLs. Motivated by this observation, we model the FOPT contribution to the GW spectrum with a BPL as

$$\Omega_{\rm BPL}(f) = \Omega_* \left(\frac{f}{f_*}\right)^{n_1} \left[1+\left(\frac{f}{f_*}\right)^{\Delta}\right]^{(n_2-n_1)/\Delta}, \tag{5.44}$$

where n_1 and n_2 denote the spectral indices before and after the peak, respectively, Δ is a peak smoothing parameter, and Ω_* and f_* can be related to the peak amplitude and peak frequency of the spectrum. Given the above BPL parameterization, one can see that the spectra introduced in Eqs. (5.39) and (5.41) approximately follow a BPL with parameters $n_1 = 3$, $n_2 = -1$, $\Delta = 4$ and $n_1 = 3$, $n_2 = -4$, $\Delta = 2$ for bubble collisions and sound waves, respectively. We perform a parameter estimation search for both contributions separately, corresponding to the case where one of the contributions dominates the GWB spectrum. In each case, the values of n_1, n_2, and Δ are set to the relevant values of that contribution, as given above[10].

The likelihood to perform this search is given by Eq. (2.38), where $\Omega_M(f) = \Omega_{\rm CBC}(f) + \Omega_{\rm BPL}(f)$, with $\Omega_{\rm CBC}(f)$ defined in Eq. (5.43) and $\Omega_{\rm BPL}(f)$ in Eq. (5.44). The GW parameters to be constrained are $\boldsymbol{\Theta} = (\Omega_{\rm ref},\ \Omega_*,\ f_*)$. The priors used during the analysis are summarised in Table 5.1. We report the results in Figure 5.8 for bubble collisions (top panel) and sound waves (bottom panel). From the posteriors on the amplitude of the CBC background, $\Omega_{\rm ref}$, upper limits[11] at 95% confidence level are obtained: 5.60×10^{-9} when bubble collisions are the dominant production mechanism and 5.70×10^{-9} when sound waves dominate, both

---

[10] Note that in [231], n_2 was allowed to vary, meaning no assumption was made about whether bubble collisions or sound waves dominate.

[11] For additional information about Bayesian upper limits, we refer the reader to Section 2.2.2.

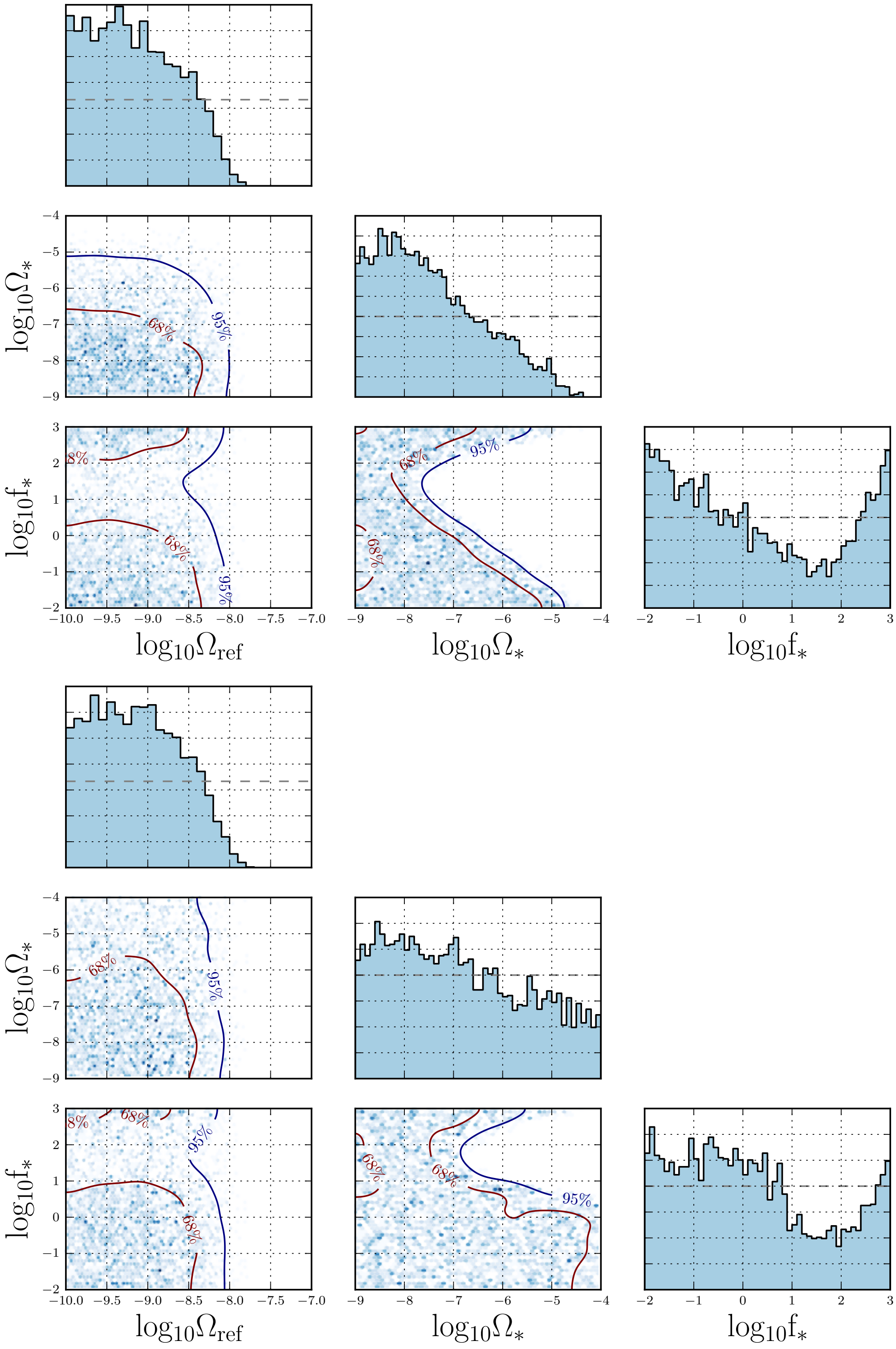

Figure 5.8. Constraints from LVK's first three observing runs on the BPL parameters of a FOPT signal, together with the contribution from the CBC background as represented by Ω_{ref}, assuming dominant bubble collision spectrum (top) and a dominant sound waves spectrum (bottom). The 68% and 95% confidence regions are denoted by the red and blue line, respectively. The priors are given by the dashed gray lines in the 1D posterior plots.

consistent with the upper limits obtained in [19, 231]. Similarly, 95% confidence level contours are obtained on the amplitude and peak frequency of the contribution from FOPTs, Ω_* and f_*, as depicted in Figure 5.8. The values of the Bayes factor, as previously introduced in Eq. (2.43), are $\log \mathcal{B}^{\mathrm{CBC+BC}}_{\mathrm{noise}} = -1.26$ and $\log \mathcal{B}^{\mathrm{CBC+SW}}_{\mathrm{noise}} = -0.80$, showing no evidence for a FOPT GWB signal in the data.

Broken power law			
Parameter	Prior	Minimum	Maximum
Ω_{ref}	Log-Uniform	10^{-10}	10^{-7}
Ω_*	Log-Uniform	10^{-9}	10^{-4}
f_*	Log-Uniform	10^{-2}	10^{3}
Phenomenological			
Ω_{ref}	Log-Uniform	10^{-10}	10^{-7}
β/H_{RH}	Log-Uniform	1	10^{3}
T_{RH}	Log-Uniform	10^{5}	10^{10}

Table 5.1. Summary of the priors used for parameter estimation for the BPL model search and the phenomenological model search. The narrow prior on Ω_{ref} stems from estimates of the CBC background [4]. The prior on the peak frequency is chosen such that it lies in the region where the LVK instruments are most sensitive. Values lower than 1 for $\beta/\mathrm{H}_{\mathrm{RH}}$ are not considered, since otherwise the phase transition would not take place.

5.2.2 Phenomenological Search

We now proceed with a different model assumption. Instead of the general BPL model used above, we consider the GW spectra introduced in Section 5.1.3, more specifically Eqs. (5.39) and (5.41), corresponding to bubble collisions and sound waves. The likelihood used to perform this search is then given by Eq. (2.38), with $\Omega_M(f) = \Omega_{\mathrm{CBC}}(f) + \Omega_{\mathrm{bc}}(f)$ and $\Omega_M(f) = \Omega_{\mathrm{CBC}}(f) + \Omega_{\mathrm{sw}}(f)$ for bubble collisions and sounds waves, respectively. Therefore, the GW parameters to be constrained in this search are $\boldsymbol{\Theta} = (\Omega_{\mathrm{ref}}, \; \beta/H_{\mathrm{RH}}, \; T_{\mathrm{RH}})$. We again highlight the difference with the search conducted in [231], where the α parameter was included. As discussed earlier, for supercooled FOPTs with $\alpha \gg 1$, neglecting this parameter is a valid assumption. The priors on the parameters used for parameter estimation are given in Table 5.1, and the resulting posterior distributions are presented in Figure 5.9. From the posteriors on the amplitude of the CBC background, Ω_{ref}, upper limits at 95% confidence level are obtained. The value for the case in which bubble collisions dominate is 5.89×10^{-9}, and 5.93×10^{-9} for when sound waves dominate. These are consistent with the upper limits obtained in [19, 231]. Furthermore, exclusions at 95% CL for temperatures T_{RH} and inverse duration of the FOPT β/H_{RH} are also depicted in Figure 5.9.

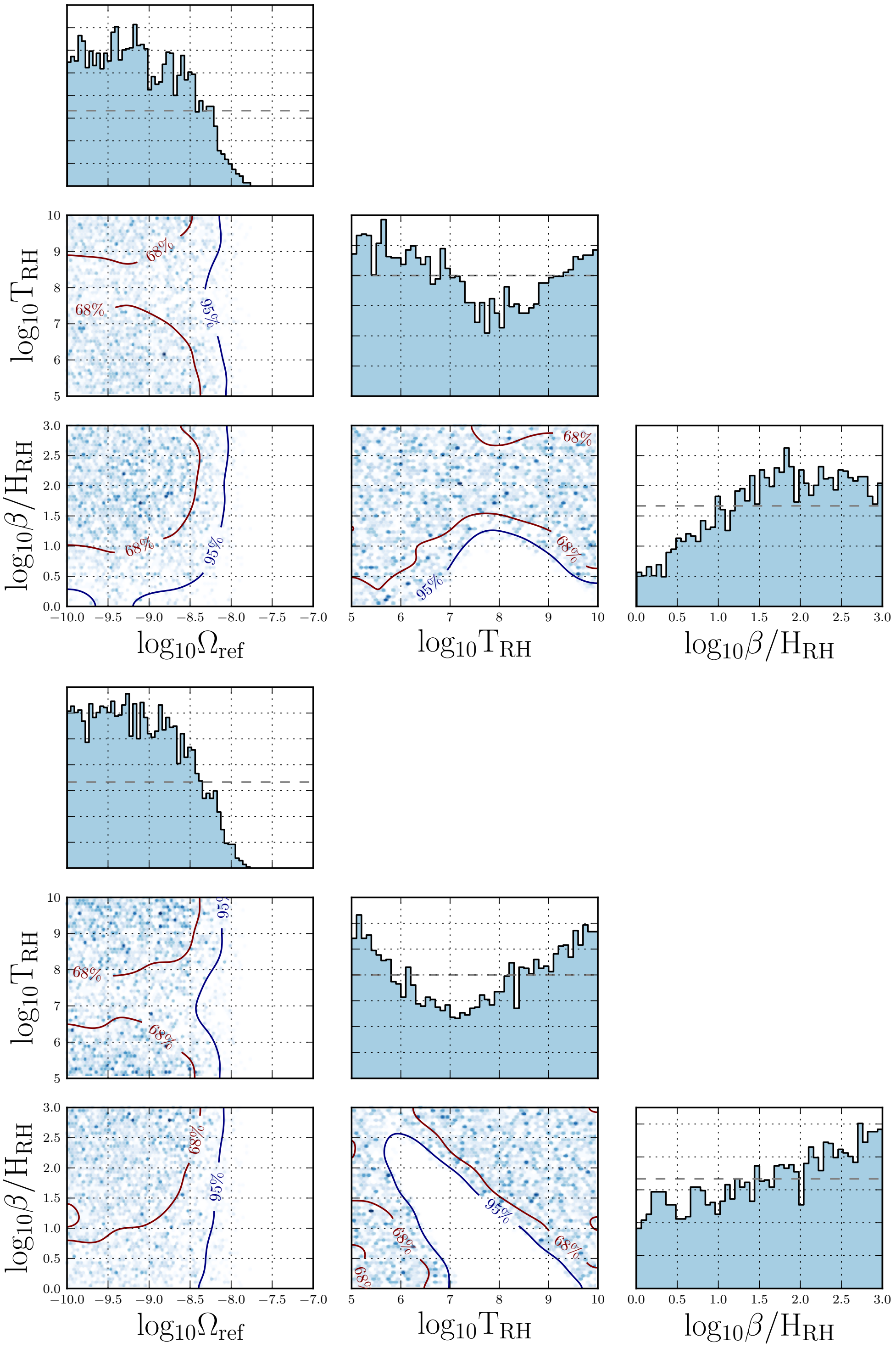

Figure 5.9. Constraints from LVK's first three observing runs on the phenomenological parameters β/H_{RH} and T_{RH} of a supercooled FOPT signal, together with the contribution from the CBC background as represented by Ω_{ref}, assuming a dominant bubble collision spectrum (top) and a dominant sound waves spectrum (bottom). The 68% and 95% confidence regions are denoted by the red and blue line, respectively. The priors are given by the dashed gray lines in the 1D posterior plots.

By using Bayesian inference and the GWB estimators from the first three observing runs of the LVK collaborations, we set constraints on general GWB spectra coming from supercooled FOPTs. It should be emphasised that the constraints derived above can be used in any model exhibiting supercooling. More precisely, once a model and its parameters are specified, one can compute the expected FOPT parameters $\beta/H_{\rm RH}$ and $T_{\rm RH}$ (or equivalently Ω_* and f_*) and compare them with the 95% confidence upper limits provided here. In this way, one can use GW data to exclude regions of the parameter space in concrete particle physics models. We illustrate this in the next section for two concrete particle physics models.

5.3 Two Well-Motivated Particle Physics Models

We now apply the same methodology as in the previous section to concrete particle physics models. In this study, we focus on Model I [121] and Model II [101], which exhibit supercooling. They are both well-motivated from a particle physics point of view and require few additional particles beyond the SM particle content. We note, however, that our analysis can be applied to any other model with supercooling. The general goal is to assess the detectability of signals from supercooled FOPTs with the LVK detectors, and determine the regions of parameter space that can be excluded with current GW data in concrete particle physics models.

This is the first time that LVK data from the first three observing runs are being used to set limits on the parameters of particle physics models through a FOPT search. So far, only general constraints on the GWB from FOPTs had been derived [231]. In particular, in the current analysis, we derive constraints directly at the level of the particle physics parameters, e.g., particle masses and couplings, using the predicted FOPT GWB signal in our Bayesian inference analysis. This presents a novel way of bridging the gap between data analysis and theoretical particle physics model building.

Below, each model is introduced by sketching the general context of the theory and its relevance within the current particle physics landscape. After a brief theoretical introduction of the model outlining the particle content and effective potential governing the theory, the GWB spectrum is determined and Bayesian inference is performed to set constraints on the parameter space of each model. This section is based on original work [50].

5.3.1 Model I: a Minimal U(1)$_{B-L}$ Extension of the Standard Model

Introduction

The first model we consider is based on a theoretically attractive minimal U(1)$_{B-L}$ extension of the SM gauge group [120, 121, 196]. Upon introducing three right-handed neutrinos, the theory is anomaly-free, realises the see-saw mechanism providing an explanation for the observed neutrino masses, and can be incorporated into SO(10) grand unification. The model includes only two new bosonic fields: a real scalar ϕ and a gauge boson Z'. Below, we summarise the theory governing this simple model, and proceed to discuss the constraints on the resulting FOPT GWB signals.

Theoretical Framework

This model extends the SM particle content with the addition of the following particles: three right-handed neutrinos[12], a $U(1)_{B-L}$ gauge boson Z', and a complex scalar field φ with charge +2 under $U(1)_{B-L}$ (containing a real scalar field ϕ). The latter will be responsible for the symmetry breaking. The full scalar potential will include terms for the Higgs scalar, as well as the newly introduced $U(1)_{B-L}$ scalar. However, due to collider constraints on the mass of the gauge boson Z', the FOPT is forced to happen along the new scalar direction first [121]. Indeed, since the mass of the Z' is at least of the order of ∼TeV, i.e., above the electroweak scale, the phase transition will first happen along the new scalar direction, and then along the Higgs direction. The zero-temperature scalar potential, according to Eqs. (5.1) and (5.2), is therefore given by

$$V_0(\phi)+V_1^{CW}(\phi)=\frac{1}{4}\lambda_\phi\phi^4+\sum_{i=\phi,G,Z'}\frac{n_i}{64\pi^2}\left\{m_i^4(\phi)\left[\log\left(\frac{m_i^2(\phi)}{\mu^2}\right)-c_i\right]\right\}, \tag{5.45}$$

where n_i is the number of degrees of freedom, $c_{\phi,G}=3/2$, $c_{Z'}=5/6$, μ is the renormalisation scale which we set at the VEV v of the scalar ϕ, and G denotes the Goldstone boson [121]. The field-dependent masses are:

$$m_{Z'}^2(\phi)=4g^2\phi^2\,,\quad m_\phi^2(\phi)=3\lambda_\phi\phi^2\,,\quad m_G^2(\phi)=\lambda_\phi\phi^2\,, \tag{5.46}$$

---

[12] These cancel the $U(1)_{B-L}$ anomaly, see [121].

where g is the gauge coupling under the new $U(1)_{B-L}$ symmetry. The finite temperature part of the effective potential is

$$V_T(\phi,T) = \frac{T^4}{2\pi^2}\sum_{i=\phi,G,Z'} n_i \int_0^\infty dy\, y^2 \log\left(1-e^{-\sqrt{m_i^2(\phi)/T^2+y^2}}\right) + \frac{T}{12\pi}\sum_{j=\phi,G,Z'_L} n'_j \left\{m_j^3(\phi) - [m_j^2(\phi)+\Pi_j(T)]^{\frac{3}{2}}\right\}, \tag{5.47}$$

with the thermal masses given by

$$\Pi_\phi(T) = \Pi_G(T) = \left(g^2+\tfrac{1}{3}\lambda_\phi\right)T^2\,,\Pi_{Z'_L}(T) = 4g^2T^2\,, \tag{5.48}$$

where the subscript L denotes longitudinal components. The second term in this thermal potential comes from the Daisy contribution, previously introduced in Eq. (5.7). Note that the interactions with the right-handed neutrinos do not appear in the expressions above, as [120, 121] assume the Yukawa couplings to be negligible, i.e., $Y_i \ll g$.

To summarise, the behaviour of the potential in this simple extension of the SM, and therefore also the FOPT itself, is entirely governed by two parameters: the VEV v, and the $\mathrm{U}(1)_{B-L}$ gauge coupling g. This means that also the GWB is completely specified through these two parameters. Trading the VEV v for the the gauge boson mass $m_{Z'}$, related via

$$m_{Z'} = 2gv\,, \tag{5.49}$$

the two parameters describing Model I are $(m_{Z'}, g)$. For additional information on this model, we refer the interested reader to [120, 121, 196].

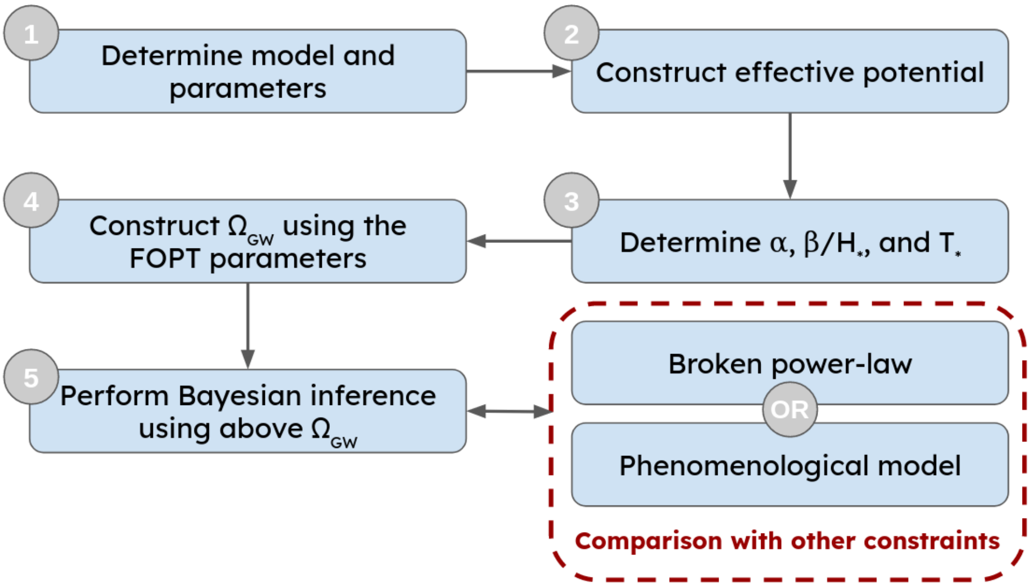

Figure 5.10. Schematic representation of the steps taken to obtain constraints on the model parameters of Model I and Model II.

Constraints from LVK Data

For each point $(m_{Z'}, g)$ of the parameter space, one can compute the parameters describing the phase transition, i.e., $T_{\rm RH}$ and $\beta/H_{\rm RH}$, and the resulting GWB spectrum. This is schematically represented in Figure 5.10. We restrict ourselves to $m_{Z'} \in [10^4,\ 10^{11}]$ GeV and $g \in [0.3,\ 0.4]$, which corresponds to FOPTs where the GWB signal is dominated by sound waves as given by Eq. (5.41) [120]. If the gauge coupling g is chosen to be larger than 0.4, the FOPT is not supercooled and $\alpha \sim 1$. Furthermore, we are not exploring values of g below 0.3, as these correspond to a regime where both bubble collisions and sound waves contribute considerably to the GW spectrum, as discussed in [120].

We perform a Bayesian inference search over the $(m_{Z'}, g)$ parameter space, and include the contribution of the CBC background. The likelihood is given by Eq. (2.38), with $\Omega_M(f) = \Omega_{\rm CBC}(f) + \Omega_{\rm sw}(f)$, where $\Omega_{\rm sw}(f)$ is calculated from Eq. (5.41) using the model parameters $(m_{Z'}, g)$. Thus, the parameters of the search are $\boldsymbol{\Theta} = (\Omega_{\rm ref},\ m_{Z'},\ g)$. The priors are summarised in Table 5.2 and the resulting posteriors are shown in Figure 5.11. The upper limits on the amplitude of the astrophysical CBC background are consistent with [19, 231]. Furthermore, a region of parameter space around $m_{Z'} \sim \mathcal{O}(10^8$ GeV) is excluded, and corresponds to FOPT GWB signals peaked within the frequency range of the LVK detectors.

Model I			
Parameter	Prior	Minimum	Maximum
$\Omega_{\rm ref}$	Log-Uniform	10^{-10}	10^{-7}
$m_{Z'}$	Log-Uniform	10^4 GeV	10^{11} GeV
g	Uniform	0.3	0.4
Model II			
$\Omega_{\rm ref}$	Log-Uniform	10^{-10}	10^{-7}
F	Log-Uniform	1.4×10^9 GeV	10^{11} GeV
λ	Uniform	0.325	0.6

Table 5.2. Summary of the priors used for parameter estimation for Model I and Model II. The narrow prior on $\Omega_{\rm ref}$ stems from estimates of the CBC background [4].

Additionally, in Figure 5.12, we show the GWB spectrum for two benchmark points to illustrate the constraints obtained in Figure 5.11. As can be seen, a GWB spectrum that was within reach of the LVK 2σ PI curve [19] in Figure 5.12 is excluded in Figure 5.11. This is because no evidence for a GWB is found in the data, therefore excluding any sets of parameters that would have given rise to a detectable signal. Contrarily, the benchmark corresponding to the undetectable spectrum is not excluded, as the LVK detectors are not sensitive enough to access that part of parameter space.

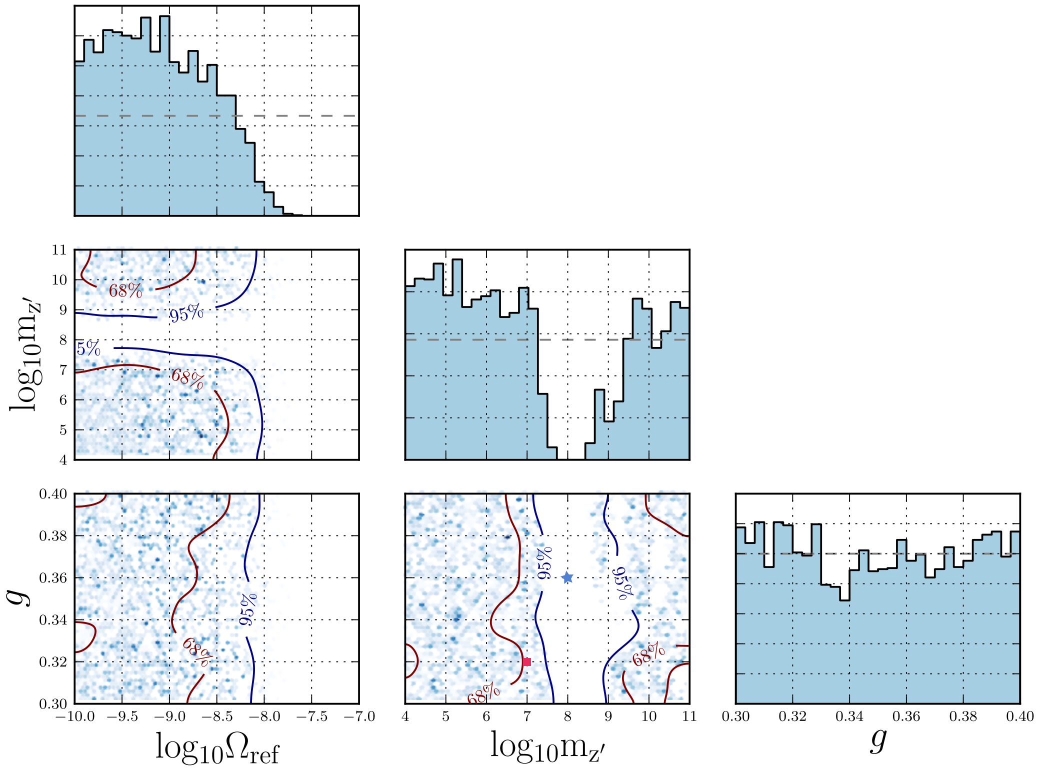

Figure 5.11. Constraints from LVK's first three observing runs on the parameter space $(m_{Z'}, g)$ for Model I, together with constraints on the astrophysical CBC background amplitude $\Omega_{\rm ref}$. The 68% and 95% confidence regions are denoted by the red and blue line, respectively. The priors are given by the dashed gray lines in the 1D posterior plots. Two benchmark points are indicated, for which the GWB spectra are reported in Figure 5.12 for illustrative purposes.

We now compare the exclusion regions obtained directly on the parameters of the model with the ones deduced from the analysis in Section 5.2[13]. Given a choice of the parameters $(m_{Z'}, g)$, one can verify whether the corresponding values of $(\beta/H_{\rm RH}, T_{\rm RH})$ or (f_*, Ω_*) are excluded using the analysis in Section 5.2. As Figure 5.13 demonstrates, a good agreement is found between the various exclusion regions, regardless of the search performed. Therefore, the results obtained in Section 5.2 are easily reinterpreted in any specific model with supercooling. This is also supported by the analysis we perform below for another well-motivated particle physics model.

---

[13] The particle physics masses and couplings can be mapped into the parameters of the BPL and the phenomenological search by computing the expected GWB from FOPTs.

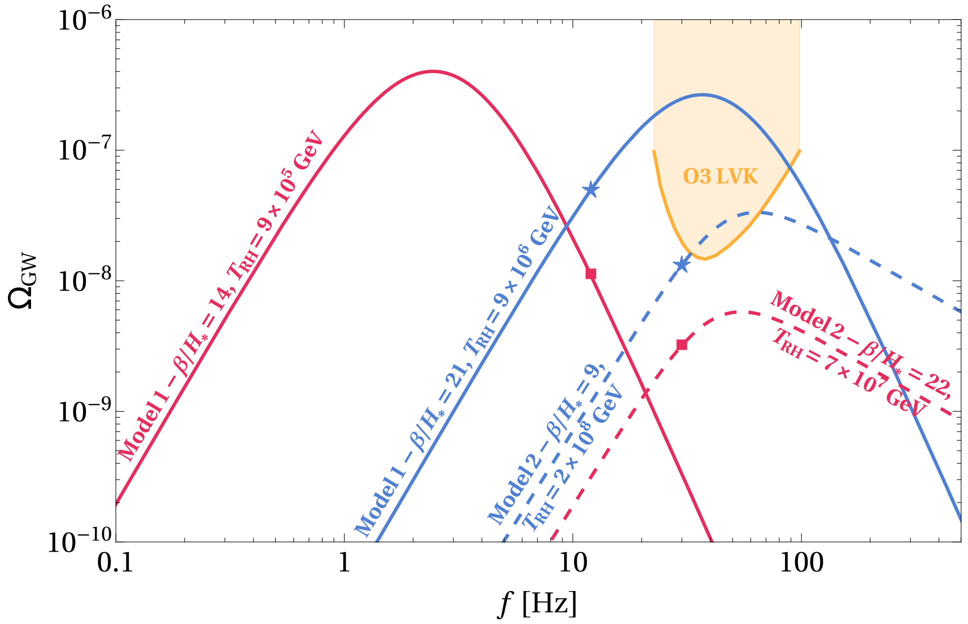

Figure 5.12. Gravitational-wave spectra $\Omega_{\rm GW}(f)$ for two benchmark points in Model I and Model II in full and dashed lines, respectively. Detectable benchmark points are given in blue, whereas undetectable benchmark points are represented in red. These benchmark points are indicated in the corresponding parameter space in Figure 5.11 for Model I and in Figure 5.14 for Model II.

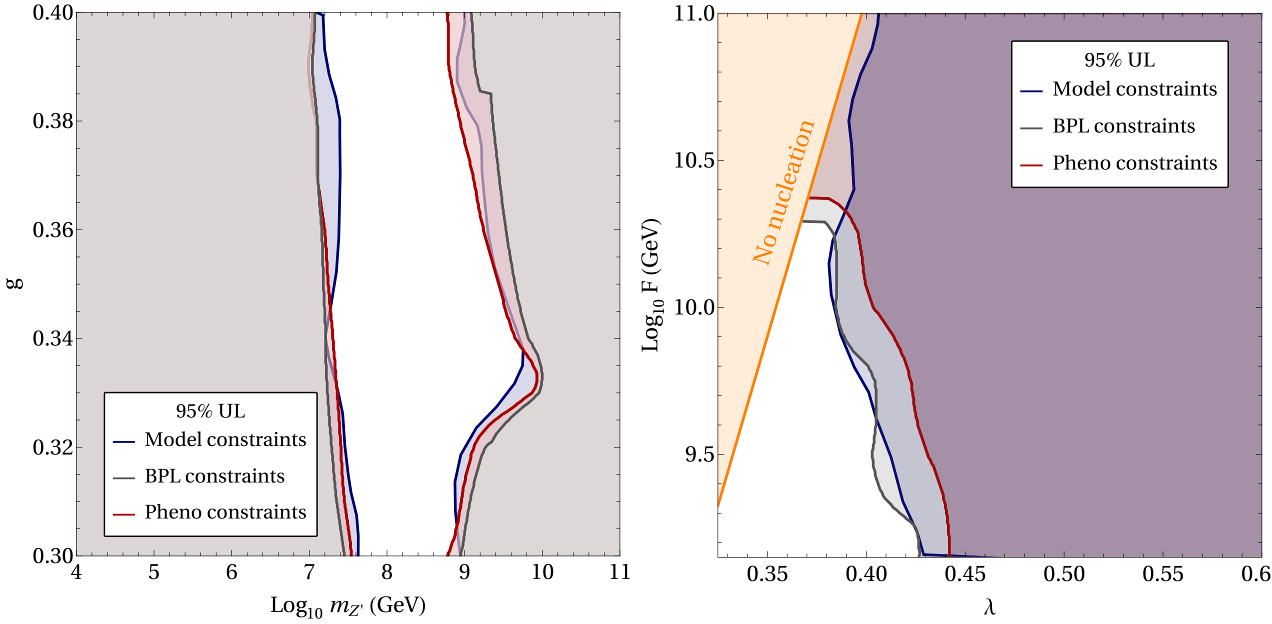

Figure 5.13. Comparison of the constraints on the parameter space $(m_{Z'}, g)$ for Model I (left panel) and on (λ, F) for Model II (right panel) obtained by constraining the model parameters directly as in Figures 5.11 and 5.14 (blue line), with those obtained by adopting the BPL model as given in Figure 5.8 (gray line), and those adopting the phenomenological model in Figure 5.9 (red line).

5.3.2 Model II: a Radiatively Broken U(1) Peccei-Quinn Symmetry

Introduction

The model described in [101] is based on the symmetry breaking of the U(1) Peccei-Quinn symmetry. This symmetry is often invoked as a solution to the strong CP problem, which pertains to the $\theta G\tilde{G}$ term in the quantum chromodynamics (QCD) Lagrangian, where G denotes the field strength and $\tilde{G}$ its dual. The SM is unable to explain the smallness of the value of the θ parameter, as constrained by neutron electric dipole experiments [156]. However, by introducing the Peccei-Quinn symmetry, a similar term containing the field strength and its dual appear, but now contains the axion field because of the anomaly between the Peccei-Quinn symmetry and QCD. The smallness of this term is then naturally explained by the axion potential forcing the axion to take on a zero VEV, thus solving the strong CP problem [156]. Not only does the axion provide a solution to the strong CP problem, but it has also been considered as a possible dark matter candidate, therefore solving two open problems in the SM. The model considered in [101] accommodates this new symmetry and extends the SM by including just two new complex scalar fields, S and X, which are SM singlets, and both carry Peccei-Quinn charges. More details on the theory describing this model is given below.

Theoretical Framework

After adding the two new scalars S and X, the tree-level scalar potential is given by

$$V_0(S,X) = \lambda_S|S|^4 + \lambda_X|X|^4 + \lambda_{SX}|S|^2|X|^2 \ . \tag{5.50}$$

It exhibits a flat direction for $\lambda_{SX} = -2\sqrt{\lambda_S\lambda_X}$, which can be parameterized by

$$(S,X) = (\sin\alpha, \cos\alpha)\frac{\phi}{\sqrt{2}} \ , \quad \sin^2\alpha = \frac{\sqrt{\lambda_X}}{\sqrt{\lambda_S}+\sqrt{\lambda_X}} \ . \tag{5.51}$$

The mass of the field along the direction orthogonal to ϕ is

$$m_\tau = (4\lambda_S\lambda_X)^{1/4}\phi \ . \tag{5.52}$$

Assuming that the condition for the flat direction holds at the renormalisation scale Λ, and substituting the parameter Λ for the field value at the minimum of the potential, F, the zero-temperature scalar potential is given by

$$V_0(\phi) + V_1^{CW}(\phi) = \frac{2\lambda_S \lambda_X}{16\pi^2} \phi^4 \left(\log \frac{\phi}{F} - \frac{1}{4} \right) . \tag{5.53}$$

At the minimum, ϕ has a loop-suppressed mass, whereas the phase of X is massless up to QCD anomalies, and becomes the axion with a decay constant $F_a = F \cos \alpha$. The finite temperature part of the effective potential is given by a formula analogous to Eq. (5.47), but with just a single term involving m_τ. To prevent the finite temperature effects from moving the true vacuum away from the flat direction, we set

$$\lambda_X = \lambda_S \equiv \lambda , \tag{5.54}$$

which is equivalent to imposing a $\mathbb{Z}_2$ symmetry at the level of the Lagrangian. Additional details about this model can be found in [101].

To summarise, just as in the previous model, this model is governed by two parameters: (λ, F). Both of these determine the shape of the potential, and therefore also the FOPT and the resulting GWB signal. We now proceed with the derivation of constraints on the parameter space of this model using GWB data from the first three LVK observing runs.

Constraints from LVK Data

Similarly to Model I, one can compute the FOPT parameters $\beta/H_{\rm RH}$ and $T_{\rm RH}$, and determine the GW spectrum, as represented schematically in Figure 5.10. We again conduct a Bayesian inference search directly on the parameters of the model. In the case of Model II, the dominant GW contribution comes from bubble collisions [101]. In the likelihood given by Eq. (2.38), $\Omega_M(f) = \Omega_{\rm CBC}(f) + \Omega_{\rm bc}(f)$, where $\Omega_{\rm bc}(f)$ is given by Eq. (5.39) and can be obtained from the underlying model parameters (λ, F). The parameters used for the search are therefore $\boldsymbol{\Theta} = (\Omega_{\rm ref},\ F,\ \lambda)$ and the priors on $\Omega_{\rm ref}$, F and λ are summarised in Table 5.2. The ranges of parameters we consider are: $F \in [1.4 \times 10^9,\ 10^{11}]$ GeV and $\lambda \in [0.325, 0.6]$. A value of F smaller than 1.4×10^9 GeV (corresponding to an axion decay constant of 10^9 GeV) is experimentally excluded [105], whereas values of λ lower than 0.325 correspond to cases when the phase transition does not complete, i.e., no nucleation occurs. The prior upper bounds on F and λ are not constrained and were set arbitrarily. Figure 5.14 displays the exclusion regions implied by the data from the first three LVK observing runs. The gray region represents part of the parameter space where no nucleation occurs and the phase transition does not complete. As shown in Figure 5.14, part of the parameter space can be excluded at a 95% confidence level. This mostly puts constraints on the values of λ, excluding smaller values, as these are the ones that give rise to the strongest GW signals. Furthermore, one notes consistency with the usual CBC upper limits found in this work, and in [19, 231].

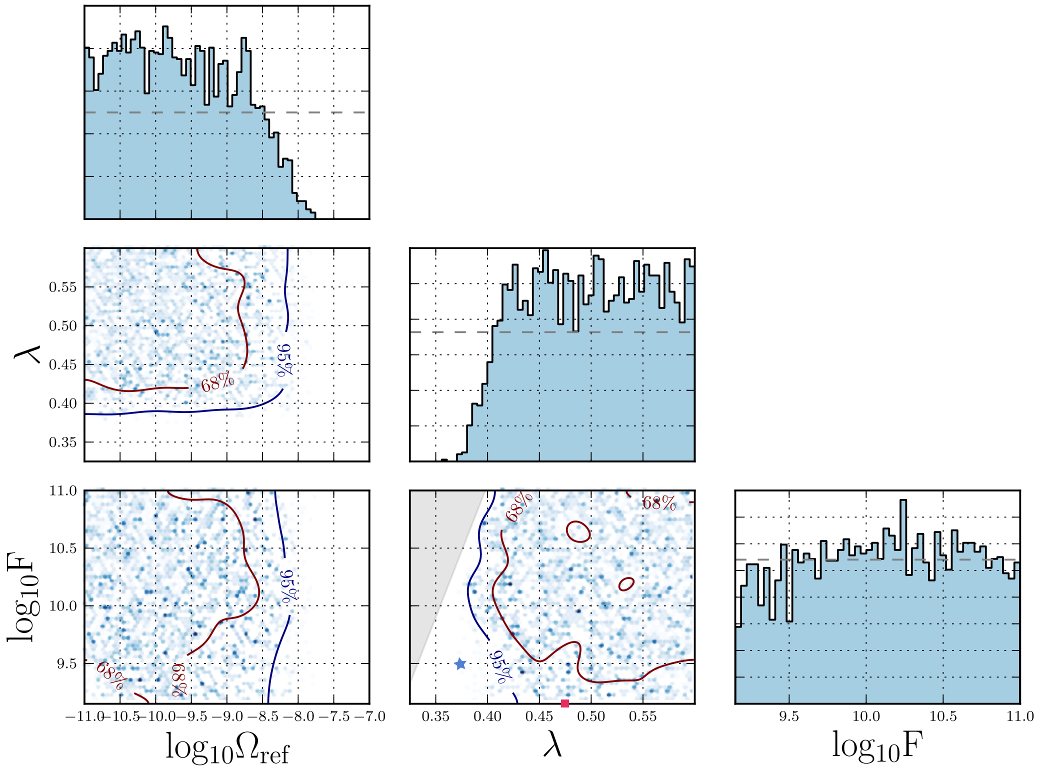

Figure 5.14. Constraints from LVK's first three observing runs on the parameters λ and F for Model II, together with constraints on the astrophysical CBC background amplitude $\Omega_{\rm ref}$. The 68% and 95% confidence regions are denoted by the red and blue line, respectively. The priors are given by the dashed gray lines in the 1D posterior plots. The gray region in the bottom plot corresponds to a region where nucleation does not occur and the phase transition does not complete. Two benchmark points are indicated, for which the GWB spectra are reported in Figure 5.12 for illustrative purposes.

As done above for Model I, in Figure 5.12, we again provide the GWB spectrum for two benchmark points to illustrate the constraints obtained in Figure 5.14. Both a detectable and undetectable benchmark point are shown, illustrating the same reasoning as given above for Model I.

One can now compare the exclusion regions obtained directly on the model parameters, with those derived following the analysis in Section 5.2. The results are shown in the right-hand side of Figure 5.13, where we note a decent agreement between the exclusion regions arising from the different searches, similar to the agreement obtained in the case of Model I. Once again, this illustrates how the exclusion regions in Section 5.2 can be used to constrain any supercooled FOPT at a particle physics model level.

5.4 Conclusions

Standard high energy physics experiments are approaching the limits of their discovery potential. In many cases, the most natural regions of model parameter space relevant for addressing questions in particle physics are not even within their target sensitivity. New discovery tools are needed to probe physics at the PeV energy scale and beyond. Such a novel and powerful discovery tool has recently been provided by GW detectors, with their relevance destined only to increase in future years, given the upcoming upgrades to existing GW experiments and the construction of new GW detectors sensitive to a wider range of frequencies.

We started by reviewing the theory that governs FOPTs and discussed the resulting GWB signal in detail. Subsequently, to demonstrate the huge opportunity for particle physics arising from GW searches, we carried out the pioneering study in which we used the data from the first three LVK observing runs to perform a Bayesian inference analysis and set direct limits on the parameter space of particle physics models. This is a natural extension of [231], in which only general constraints on FOPT parameters were derived. In our analysis, we focussed on supercooled FOPTs, since they are naturally characterised by an enhanced signal strength, potentially already within the reach of current LVK detectors.

To illustrate our methodology, we applied our analysis to two well-motivated particle physics models, which address some of the most intriguing open questions about the Universe: the dark matter puzzle, the strong CP problem, and the origin of the neutrino masses. We place Bayesian 95% upper limits on the parameter space of those models, providing valuable insights into the available room for new physics. The same strategy can be used to impose limits on other models exhibiting supercooled FOPTs and is left for future work.

It is worth emphasising that our work bridges a gap between data analysis and phenomenological studies, making the constraints from GW searches easier to reinterpret, and applicable to any particle physics model with a supercooled phase transition. Furthermore, even though predictions for the GWB from FOPTs might change in the future, our work established a framework that is easily applicable to alternative GWB spectra.

Part IV

Epilogue

6 CONCLUSIONS AND OUTLOOK

> Before I came here, I was confused about this subject. Having listened to your lecture I am still confused. But on a higher level.
>
> Enrico Fermi

This work explored various aspects related to the gravitational-wave background (GWB). In particular, the development of a novel detection method to decrease the time until the detection of such a background formed an important part of this thesis. Additionally, special attention was devoted to several models, both astrophysical and cosmological, in which those GWBs arise, and the implications for each of these models were investigated.

In this thesis, we started with a review of gravitational waves (GWs) arising in Einstein's theory of general relativity (GR) in Chapter 1. The essential concepts of GR were reviewed, GWs were introduced as solutions to the Einstein equations and several detection methods were discussed. For the latter, we focussed on the current state-of-the-art GW interferometers of the LIGO-Virgo-KAGRA (LVK) collaborations, although next-generation interferometers and other detection methods were also briefly touched upon. To conclude the chapter, several examples of GW sources were provided, with an emphasis on the ones expected in the LVK detectors: compact binary coalescences, continuous waves, GW bursts and the GWB.

The idea of a GWB coming from the superposition of weak, unresolved GWs was then formalised in Chapter 2. We started by reviewing general concepts related to the GWB, and introduced the standard method used to search for such a background, which relies on the cross-correlation of data from multiple detectors. The explanation of a few helpful tools used in GWB searches constituted the end of the chapter. This toolkit included concepts related to Bayesian inference, power-law integrated sensitivity curves, and the `pygwb` package used to perform GWB searches based on the cross-correlation of data.

The chapter above concluded the review of theoretical background knowledge needed for the rest of this thesis. The remainder of this work was then dedicated to two main goals:

the development of a new data analysis method, and the investigation of implications derived from information contained in a GWB measurement, both for astrophysical and cosmological models.

In this spirit, Chapter 3 was devoted to the development of a new data analysis method: the stochastic search for intermittent backgrounds (SSI). This new data analysis method is particularly relevant in the context of the detection of the astrophysical binary black hole (BBH) background. Indeed, as the BBH signals are only visible in the LVK frequency band for a fraction of a second, but happen every few minutes, this background is intermittent or popcorn-like. Whereas standard GWB search methods assume the signal is continuously present, SSI relaxed this assumption by introducing the duty cycle, which represents the probability of an analysis segment to contain a signal. Although generalised to capture the intermittency of the signal, this new method retains the core methodology of standard searches by looking for bursts of cross-correlated power across the detectors in short analysis segments. Through a series of toy models, we showed that our search performs better than the standard cross-correlation search which assumes the background is present all the time. In addition, we provided several examples of ongoing generalisations to the method. Although still in its development stages, the method already shows promising results awaiting to be applied to real detector data and potentially discover the background sooner than expected with traditional methods.

The next two chapters were dedicated to deriving constraints and discussing implications for the astrophysical and the cosmological background. We started by considering the former in Chapter 4. More concretely, we investigated the metallicity dependence and evolutionary times of merging BBHs. Due to the limited sensitivity of current-generation detectors, our ability to probe the evolution of these quantities at large redshifts remains minimal. However, as the GWB comes from the superposition of events throughout the Universe, its detection could provide additional information, even at larger redshifts. Our investigation was therefore performed by considering both the individual BBH detections, as well as the current upper limits on the GWB from the first three LVK observing runs. This allowed us to constrain some of the parameters that govern the metallicity dependence and the evolutionary times of BBH formation, although these results were entirely dominated by individual BBH detections. Nevertheless, even though current detector sensitivities do not illustrate the added value of the GWB contribution yet, our analysis showed that the (non-)detection of a GWB at Advanced LIGO A+ sensitivity will provide additional information compared to using individual BBHs alone. In addition, our work provides the methodology needed for this type of analyses, and allows for the generalisation to more complex models with e.g., a different metallicity-dependent star formation history.

In the last chapter of this manuscript, Chapter 5, we slightly switched gears and considered a cosmological source of the GWB: first order phase transitions (FOPTs). As the temperature of the Universe decreases, a scalar field can tunnel through a potential barrier to reach the true vacuum of the theory. In doing so, bubbles of true vacuum are created, whose evolution and collisions through the plasma of the Universe can generate a GWB of cosmological origin. This chapter reviewed the main concepts related to FOPTs and their resulting GWB signal. We then focussed on a specific type of phase transitions which typically enhances the GWB signal: supercooled FOPTs. By using data from the first three observing runs of the LVK collaborations, we were able to set constraints on the parameter space of supercooled phase transitions. In addition to constraining general spectra describing supercooled FOPTs, we also considered two concrete beyond the Standard Model particle physics models and studied the supercooled FOPT GWB signal therein. By applying the same methodology, we were able to set limits on the parameter space of these particle physics models. This was the first time LVK data were used to constrain the parameter space of particle physics models directly.

Not only did the first few chapters of this work provide a complete review of the necessary ingredients to perform GWB searches, but the subsequent chapters illustrated what was at the core of the work during this PhD: modelling and observations. Both the data analysis chapters as well as the chapters related to deriving implications for different astrophysical and cosmological models reflect one of the main goals of this thesis which was to bridge the gap between data analysis and modelling. Furthermore, those three chapters not only showcase the quantity of potential science applications within the context of the GWB, but also the variety of them, which makes the GWB an extremely exciting topic of investigation.

Future work

Contrarily to this PhD coming to an end, the list of things to investigate still seems never-ending. Below, we list a few items that could be addressed in the future for each of the topics discussed above.

As already discussed at the end of Chapter 3, several aspects need to be generalised before the SSI method can be applied to real detector data. Some of these have been addressed since the publication of [176], while others remain to be investigated. Before considering real detector data, our first step is complexifying the injected signals and assessing the impact on our method. One of the biggest challenges, however, will be related to real detector noise. Whereas our simulated noise is Gaussian and well-behaved, real detector noise can come with many features that could impact our search, e.g., glitches and non-stationarities. This should be investigated, after which the method could be applied to data from the first three observing runs of the LVK collaborations to assess the performance of our search on real data.

Additionally, the more complex modelling of our source population will allow us to make increasingly realistic statements about the astrophysical objects that generated the astrophysical background. In particular, the duty cycle can be related to the BBH merger rate. Studying the merger rate within the context of SSI illustrates one of the possible synergies with the work done in Chapter 4 and should be explored.

In addition to the interesting results provided in Chapter 4, some further generalisations to the method described in that chapter could be looked into. The derived constraints on the parameters describing the metallicity dependence and evolutionary times of BBH formation were obtained assuming a specific metallicity-dependent star formation rate. However, it has been shown in recent years that the model used in our work is oversimplified, see e.g., [243] for a more accurate description of the metallicity-dependent star formation history. Assessing the impact of generalising our work to other metallicity-dependent star formation rates forms an interesting path to dedicate future work to. Nevertheless, it is important to stress that our work provides the initial methodology that can then be applied to different metallicity-dependent star formation rates. Furthermore, with the ongoing fourth observing run of the LVK collaborations, updated constraints should be derived to assess how the improvements in detector sensitivity affect our constraints.

Whether with traditional search methods as already in place within the LVK collaborations or proposed methods such as SSI, the detection of the astrophysical BBH background will provide a wealth of information about the population of binaries that generated it. As we await the better sensitivity of upgraded or future detectors, the methodology of combining individual detections with the detection of or upper limits on the GWB possibly forms our best hope of capturing a glimpse of the high-redshift evolution of astrophysical quantities through GW observations. Beyond probing the merger rate, this could also be used to probe the redshift dependence of other distributions, e.g., the mass distribution, in an attempt to shine light on the different properties of the binary population.

Regarding FOPTs, an abundance of options seems to be available. As pointed out in the dedicated chapter, the number of particle physics models exhibiting supercooled FOPTs appears to be almost endless. It would be interesting to apply our methodology to other existing models and investigate what part of other particle physics models' parameter space can be excluded using the (non-)detection of a GWB from FOPTs. Although we focussed on the resulting GWB signal at the LVK detectors, studying FOPTs in the context of next-generation detectors such as the Einstein Telescope and the Laser Interferometer Space Antenna are equally useful investigations. This is especially true when future GW experiments probe different frequency ranges, as these correspond to completely different energy scales at which the FOPT took place. Furthermore, as mentioned in Chapter 5, the predictions for GWB spectra are evolving as more simulation results are published. Applying our methodology to these more recent spectra and assessing the impact on the bounds we derived for various models should be considered. In addition, although only FOPTs were discussed in this thesis, various other cosmological sources could have generated a GWB during the history of the Universe. Some time during this PhD was dedicated to the study of domain walls [61], but other sources could be investigated as well. Studying each of these sources and the models in which these arise offers a unique and complementary probe of the particle physics happening at the very early stages of our Universe, unlocking the secrets of the Universe step by step.

Part V

Appendices

A APPENDIX A - SSI LIKELIHOODS

Throughout Chapter 3, various searches for GWBs were compared. In this appendix, we provide the likelihoods corresponding to those searches. We start by giving an overview of the likelihoods used in Section 3.3.1, i.e., applicable to white signals, and conclude with the likelihoods for coloured signals used in Sections 3.3.2 and 3.3.3. We also remind the reader that all likelihoods considered in this work are for stationary, white-Gaussian noise (see Eq. (3.11)).

A.1 Likelihoods for White Signals

A.1.1 SSC-full

For white signals, we define the likelihood functions for a continuous stochastic search (SSC-full) as [197]:

$$\begin{aligned}&\mathcal{L}(d|\sigma^2_{\rm gw},\sigma^2_{n_1},\sigma^2_{n_2})\\&=\prod_{I=1}^{N_{\rm seg}}\frac{1}{(2\pi)^N\left(\sigma_1^2\sigma_2^2-(\sigma^2_{\rm gw})^2\right)^{N/2}}\exp\left\{-\frac{1}{2}\frac{N}{\left(\sigma_1^2\sigma_2^2-(\sigma^2_{\rm gw})^2\right)}\left[\hat{\sigma}^2_{1,I}\sigma_2^2+\hat{\sigma}^2_{2,I}\sigma_1^2-2\hat{\sigma}^2_{{\rm gw},I}\sigma^2_{\rm gw}\right]\right\},\end{aligned} \tag{A.1}$$

where

$$\sigma_1^2\equiv\sigma^2_{n_1}+\sigma^2_{\rm gw}\,,\qquad \sigma_2^2\equiv\sigma^2_{n_2}+\sigma^2_{\rm gw}\,, \tag{A.2}$$

are parameters describing the total auto-correlated power in detectors 1 and 2, and

$$\hat{\sigma}^2_{1,I}\equiv\frac{1}{N}\sum_i d^2_{1,Ii}\,,\qquad \hat{\sigma}^2_{2,I}\equiv\frac{1}{N}\sum_i d^2_{2,Ii}\,,\qquad \hat{\sigma}^2_{{\rm gw},I}\equiv\frac{1}{N}\sum_i d_{1,Ii}d_{2,Ii}\,, \tag{A.3}$$

are the quadratic combinations of the data from segment I that enter the likelihood function, and i labels the time sample in data segment I. The noise variances in each detector are $\sigma^2_{n_1}$

and $\sigma^2_{n_2}$. It turns out that $\hat{\sigma}^2_{1,I}$, $\hat{\sigma}^2_{2,I}$, $\hat{\sigma}^2_{\mathrm{gw},I}$ are the maximum-likelihood estimates of σ^2_1, σ^2_2, σ^2_{gw} for segment I.

A.1.2 SSC-reduced

For a large number of samples per segment ($N \gg 1$), one can define a *reduced* version of the likelihood function, which is given by [197]:

$$\mathcal{L}(d|\sigma^2_{\mathrm{gw}}, \bar{\sigma}^2_{n_1}, \bar{\sigma}^2_{n_2}) = \prod_{I=1}^{N_{\mathrm{seg}}} \frac{1}{\sqrt{2\pi\,\mathrm{var}(\bar{\sigma}^2_{\mathrm{gw}})}} \exp\left[-\frac{(\hat{\sigma}^2_{\mathrm{gw},I} - \sigma^2_{\mathrm{gw}})^2}{2\,\mathrm{var}(\bar{\sigma}^2_{\mathrm{gw}})}\right], \tag{A.4}$$

where

$$\mathrm{var}(\bar{\sigma}^2_{\mathrm{gw}}) \equiv \frac{1}{N}\bar{\sigma}^2_1\bar{\sigma}^2_2, \tag{A.5}$$

with

$$\bar{\sigma}^2_1 \equiv \frac{1}{N_{\mathrm{tot}}}\sum_{I,i} d^2_{1,Ii}, \qquad \bar{\sigma}^2_2 \equiv \frac{1}{N_{\mathrm{tot}}}\sum_{I,i} d^2_{2,Ii} \tag{A.6}$$

being estimates of the total auto-correlated power in the two detectors constructed from all the data. We expect SSC-reduced and SSC-full to perform equally well, assuming $N \gg 1$, which is needed for the cross-correlation data to be approximately Gaussian.

A.1.3 SSI-full

For our proposed stochastic search for intermittent GWBs, we build upon the framework of Drasco and Flanagan [111] and extend their proposed formalism to a larger number of samples per segment ($N \gg 1$) and allow for the amplitudes to be drawn from a UIV distribution. The likelihood takes the same form as Eq. (3.1), where the segment-dependent signal and noise likelihoods are now respectively given by:

$$\begin{aligned}\mathcal{L}_s(d_I|\langle\sigma^2_b\rangle, \sigma^2_{n_1}, \sigma^2_{n_2}) = &\int_{\sigma^2_{b,\min}(\langle\sigma^2_b\rangle)}^{\sigma^2_{b,\max}} \mathrm{d}\sigma^2_{b,I}\; \pi(\sigma^2_{b,I}|\langle\sigma^2_b\rangle) \frac{1}{(2\pi)^N\left(\sigma^2_{1,I}\sigma^2_{2,I} - (\sigma^2_{b,I})^2\right)^{N/2}} \\ &\times \exp\left\{-\frac{1}{2}\frac{N}{\left(\sigma^2_{1,I}\sigma^2_{2,I} - (\sigma^2_{b,I})^2\right)}\left[\hat{\sigma}^2_{1,I}\sigma^2_{2,I} + \hat{\sigma}^2_{2,I}\sigma^2_{1,I} - 2\hat{\sigma}^2_{b,I}\sigma^2_{b,I}\right]\right\},\end{aligned} \tag{A.7}$$

$$\mathcal{L}_n(d_I|\sigma^2_{n_1}, \sigma^2_{n_2}) = \frac{1}{(2\pi)^N\left(\sigma^2_{n_1}\sigma^2_{n_2}\right)^{N/2}} \exp\left\{-\frac{N}{2}\left[\frac{\hat{\sigma}^2_{1,I}}{\sigma^2_{n_1}} + \frac{\hat{\sigma}^2_{2,I}}{\sigma^2_{n_2}}\right]\right\}, \tag{A.8}$$

where

$$\hat{\sigma}^2_{b,I} \equiv \frac{1}{N}\sum_i d_{1,Ii}d_{2,Ii}\,, \qquad \hat{\sigma}^2_{1,I} \equiv \frac{1}{N}\sum_i d^2_{1,Ii}\,, \qquad \hat{\sigma}^2_{2,I} \equiv \frac{1}{N}\sum_i d^2_{2,Ii}\,. \tag{A.9}$$

In the above expression for the signal likelihood, we used

$$\sigma^2_{1,I} \equiv \sigma^2_{n_1} + \sigma^2_{b,I}\,, \qquad \sigma^2_{2,I} \equiv \sigma^2_{n_2} + \sigma^2_{b,I}\,, \tag{A.10}$$

which are parameters describing the *segment-dependent* total auto-correlated power, with the segment dependence coming from the burst variance $\sigma^2_{b,I}$.

Note that the segment-dependent signal likelihood requires a marginalisation over the segment-dependent burst variances $\sigma^2_{b,I}$, which is taken into account by the appropriate use of prior distribution, as introduced in Eq. (3.28):

$$\pi(\sigma^2_{b,I}|\langle\sigma^2_b\rangle) = \frac{\langle\sigma^2_b\rangle(\sigma^2_{b,\max})^{1/2}}{\sqrt{-3+12\sigma^2_{b,\max}/\langle\sigma^2_b\rangle}-3}(\sigma^2_{b,I})^{-5/2}\,, \tag{A.11}$$

where

$$\sigma^2_{b,\min}(\langle\sigma^2_b\rangle) = \frac{2\sigma^2_{b,\max}}{6\sigma^2_{b,\max}/\langle\sigma^2_b\rangle - 1 - \sqrt{-3+12\sigma^2_{b,\max}/\langle\sigma^2_b\rangle}}\,, \qquad \sigma^2_{b,\max} = \sigma^2_{\mathrm{ref}}\frac{r^2_{\mathrm{ref}}}{r^2_{\min}} \tag{A.12}$$

are the limits of integration, which depend on the fixed (known) parameter $r_{\min}$ and the (unknown) population-averaged variance $\langle\sigma^2_b\rangle$.

A.1.4 SSI-reduced

Similarly to the case of SSC, one can define a *reduced* version of the SSI likelihood, provided the number of samples per segment N is large. The segment-dependent signal likelihood still requires a marginalisation over the segment-dependent burst variances $\sigma^2_{b,I}$:

$$\mathcal{L}_s(d_I|\langle\sigma^2_b\rangle, \bar{\sigma}^2_{n_1}, \bar{\sigma}^2_{n_2}) = \int_{\sigma^2_{b,\min}(\langle\sigma^2_b\rangle)}^{\sigma^2_{b,\max}} \mathrm{d}\sigma^2_{b,I}\; \pi(\sigma^2_{b,I}|\langle\sigma^2_b\rangle)\frac{1}{\sqrt{2\pi\,\mathrm{var}(\bar{\sigma}^2_{b,I})}}\exp\left[-\frac{(\hat{\sigma}^2_{b,I}-\sigma^2_{b,I})^2}{2\,\mathrm{var}(\bar{\sigma}^2_{b,I})}\right], \tag{A.13}$$

where the prior and limits of integration are the same as those used for SSI-full. In addition,

$$\mathrm{var}(\bar{\sigma}^2_{b,I}) \equiv \frac{1}{N}\bar{\sigma}^2_{1,I}\bar{\sigma}^2_{2,I} \tag{A.14}$$

with

$$\bar{\sigma}^2_{1,I} \equiv \bar{\sigma}^2_{n_1} + \sigma^2_{b,I}\,, \qquad \bar{\sigma}^2_{1,I} \equiv \bar{\sigma}^2_{n_2} + \sigma^2_{b,I}\,. \tag{A.15}$$

We estimate the white noise variances from the auto-correlated and cross-correlated power in the two detector outputs using the full set of data:

$$\bar{\sigma}^2_{\rm gw} \equiv \hat{\sigma}^2_{\rm gw}\theta(\hat{\sigma}^2_{\rm gw}), \qquad \bar{\sigma}^2_{n_1} \equiv (\hat{\sigma}^2_1 - \bar{\sigma}^2_{\rm gw})\theta(\hat{\sigma}^2_1 - \bar{\sigma}^2_{\rm gw}), \qquad \bar{\sigma}^2_{n_2} \equiv (\hat{\sigma}^2_2 - \bar{\sigma}^2_{\rm gw})\theta(\hat{\sigma}^2_2 - \bar{\sigma}^2_{\rm gw}), \tag{A.16}$$

where

$$\hat{\sigma}^2_{\rm gw} \equiv \frac{1}{N_{\rm tot}}\sum_{I,i} d_{1,Ii}d_{2,Ii}, \qquad \hat{\sigma}^2_1 \equiv \frac{1}{N_{\rm tot}}\sum_{I,i} d^2_{1,Ii}, \qquad \hat{\sigma}^2_2 \equiv \frac{1}{N_{\rm tot}}\sum_{I,i} d^2_{2,Ii}. \tag{A.17}$$

In the above expressions, $\theta(x)$ is the usual Heaviside step function, which is defined as $\theta(x) = 0$ or 1 depending on whether $x < 0$ or $x > 0$, and the hatted quantities $\hat{\sigma}^2_{\rm gw}$, $\hat{\sigma}^2_1$, $\hat{\sigma}^2_2$ are the quadratic combinations of the data in the two detectors. This simplification is possible since the simulated noise is stationary.

As before, the segment-dependent noise likelihood $\mathcal{L}_n(d_I|\bar{\sigma}^2_{n_1}, \bar{\sigma}^2_{n_2})$ is given by:

$$\mathcal{L}_n(d_I|\bar{\sigma}^2_{n_1}, \bar{\sigma}^2_{n_2}) = \sqrt{\frac{N}{2\pi\,\bar{\sigma}^2_{n_1}\bar{\sigma}^2_{n_2}}}\exp\left[-\frac{N}{2}\frac{(\hat{\sigma}^2_{b,I})^2}{\bar{\sigma}^2_{n_1}\bar{\sigma}^2_{n_2}}\right]. \tag{A.18}$$

A.2 Likelihoods for Coloured Signals

The signal and noise-dependent likelihoods for SSI are specified in Section 3.2 for both the full (infer noise parameters) and reduced (use estimated noise parameters) analyses. When analysing stochastic bursts (Section 3.3.2) and deterministic chirps (Section 3.3.3), the segment prior and integration bounds are specified in Eq. (3.35) and the subsequent paragraph.

A.2.1 SSC-full

For the continuous search, SSC, the full likelihood is specified by

$$\begin{aligned}\mathcal{L}(d|\Omega_{\rm gw}, \sigma^2_{n_1}, \sigma^2_{n_2}) = &\prod_{I=1}^{N_{\rm seg}}\prod_k \frac{1}{(\pi T/2)^{2M}(P_1(f_k)P_2(f_k) - P^2_{\rm gw}(f_k))^M} \\ &\times \exp\left\{-\frac{M}{(P_1(f_k)P_2(f_k) - P^2_{\rm gw}(f_k))}\left[\hat{P}_{1,Ik}P_2(f_k) + \hat{P}_{2,Ik}P_1(f_k) - 2\hat{P}_{{\rm gw},Ik}P_{\rm gw}(f_k)\right]\right\},\end{aligned} \tag{A.19}$$

where

$$P_1(f) \equiv P_{n_1}(f) + P_{\rm gw}(f), \qquad P_2(f) \equiv P_{n_2}(f) + P_{\rm gw}(f), \tag{A.20}$$

with

$$P_{n_1}(f) \equiv \frac{\sigma^2_{n_1}}{(f_{\rm high} - f_{\rm low})}\,, \qquad P_{n_2}(f) \equiv \frac{\sigma^2_{n_2}}{(f_{\rm high} - f_{\rm low})}\,, \qquad P_{\rm gw}(f) \equiv \Omega_{\rm gw} H(f)\,, \tag{A.21}$$

and $H(f)$ is given by Eq. (3.14) and encompasses the spectral shape. Note that the population parameter for SSC is $\Omega_{\rm gw}$, the time and population-averaged energy density amplitude. In addition, the data enter the signal evidence via the same quadratic combinations as for SSI-full (see Eq. (3.15)), but with the cross-correlation combination now defining $\hat{P}_{{\rm gw},Ik}$ as opposed to $\hat{P}_{b,Ik}$.

A.2.2 SSC-reduced

For SSC-reduced, we have [197]:

$$\mathcal{L}(d|\Omega_{\rm gw}, \bar{\sigma}^2_{n_1}, \bar{\sigma}^2_{n_2}) = \prod_{I=1}^{N_{\rm seg}} \frac{1}{\sqrt{2\pi\,{\rm var}(\bar{\Omega}_{\rm gw})}} \exp\left[-\frac{(\hat{\Omega}_{{\rm gw},I} - \Omega_{\rm gw})^2}{2\,{\rm var}(\bar{\Omega}_{\rm gw})}\right], \tag{A.22}$$

where

$$\hat{\Omega}_{{\rm gw},I} \equiv \frac{\sum_k Q(f_k)\hat{P}_{{\rm gw},Ik}}{\sum_{k'} Q(f_{k'})H(f_{k'})}\,, \qquad {\rm var}(\bar{\Omega}_{\rm gw}) \equiv \left(2M\sum_k Q(f_k)H(f_k)\right)^{-1} \tag{A.23}$$

are the optimally-filtered cross-correlation estimators and corresponding variances, which are constructed from coarse-grained estimates of the cross-correlated power $\hat{P}_{{\rm gw},Ik}$, and the optimal filter function

$$Q(f) \equiv \frac{H(f)}{\bar{P}_1(f)\bar{P}_2(f)}\,. \tag{A.24}$$

In the above expression,

$$\bar{P}_1(f) \equiv \frac{\bar{\sigma}^2_{n_1}}{(f_{\rm high} - f_{\rm low})} + \bar{\Omega}_{\rm gw} H(f)\,, \qquad \bar{P}_2(f) \equiv \frac{\bar{\sigma}^2_{n_2}}{(f_{\rm high} - f_{\rm low})} + \bar{\Omega}_{\rm gw} H(f)\,, \tag{A.25}$$

where $\bar{\sigma}^2_{n_1}$, $\bar{\sigma}^2_{n_2}$ are measured estimates of the detector noise power as defined in Eq. (A.16), and $\bar{\Omega}_{\rm gw}$ is related to $\bar{\sigma}^2_{\rm gw}$ (also defined in Eq. (A.16)) via

$$\bar{\Omega}_{\rm gw} = \frac{4}{3}\frac{\bar{\sigma}^2_{\rm gw}}{f_{\rm ref}}\left(\frac{3H_0^2}{10\pi^2}\frac{1}{f_{\rm ref}^3}\right)^{-1}\left[\left(\frac{f_{\rm ref}}{f_{\rm low}}\right)^{4/3} - \left(\frac{f_{\rm ref}}{f_{\rm high}}\right)^{4/3}\right]^{-1}. \tag{A.26}$$

This last equation follows from the general relation between variance and power spectrum:

$$\sigma_{\rm gw}^2 \equiv \int_{f_{\rm low}}^{f_{\rm high}} {\rm d}f \, P_{\rm gw}(f) = \Omega_{\rm gw} \int_{f_{\rm low}}^{f_{\rm high}} {\rm d}f \, H(f) = \Omega_{\rm gw} \left(\frac{3H_0^2}{10\pi^2} \frac{1}{f_{\rm ref}^3} \right) \int_{f_{\rm low}}^{f_{\rm high}} {\rm d}f \, \left(\frac{f}{f_{\rm ref}} \right)^{-7/3} . \tag{A.27}$$

A.2.3 DSI-full

We also analyse the coloured data with DSI, our much simpler implementation of the deterministic-signal-based search. Following [241] for two detectors, we define the DSI segment-dependent signal likelihood to be

$$\mathcal{L}_s(d_I | r_{\rm max}, \sigma_{n_1}^2, \sigma_{n_2}^2) \sim \int_{r_{\rm min}}^{r_{\rm max}} {\rm d}r_I \; \pi(r_I | r_{\rm max}) \exp \left\{ -\frac{1}{2} (4\Delta f) \sum_k \sum_{\mu=1,2} \frac{|(\tilde{d}_{\mu,Ik} - \tilde{h}_{\rm chirp}(r_I; f_k))|^2}{P_{n_\mu}} \right\} , \tag{A.28}$$

where $\tilde{d}_{\mu,Ik}$ and $\tilde{h}_{\rm chirp}(r_I; f_k)$ are the Fourier transform of the data and chirp waveform, respectively, with all of the other chirp parameters assumed to be known a priori. In the above signal evidence, we are marginalising over the segment-dependent source distance r_I, which is drawn from a UIV distribution $\pi(r_I | r_{\rm max})$ as given by Eq. (3.24).

By taking $\tilde{h}_{\rm chirp}(r_I; f_k) = 0$, i.e., corresponding to no signal in the data, the corresponding segment-dependent noise likelihood is

$$\mathcal{L}_n(d_I | \sigma_{n_1}^2, \sigma_{n_2}^2) \sim \exp \left\{ -\frac{1}{2} (4\Delta f) \sum_k \sum_{\mu=1,2} \frac{|\tilde{d}_{\mu,Ik}|^2}{P_{n_\mu}} \right\} . \tag{A.29}$$

A.2.4 DSI-reduced

For the reduced implementation, we substitute the noise parameters with the auto-correlated power estimates which gives,

$$\mathcal{L}_s(d_I | r_{\rm max}, \bar{\sigma}_{n_1}^2, \bar{\sigma}_{n_2}^2) \propto \int_{r_{\rm min}}^{r_{\rm max}} {\rm d}r_I \; \pi(r_I | r_{\rm max}) \exp \left\{ -\frac{1}{2} (4\Delta f) \sum_k \sum_{\mu=1,2} \frac{|(\tilde{d}_{\mu,Ik} - \tilde{h}_{\rm chirp}(r_I; f_k))|^2}{\bar{P}_{n_\mu}} \right\} \tag{A.30}$$

and

$$\mathcal{L}_n(d_I | \bar{\sigma}_{n_1}^2, \bar{\sigma}_{n_2}^2) \propto \exp \left\{ -\frac{1}{2} (4\Delta f) \sum_k \sum_{\mu=1,2} \frac{|\tilde{d}_{\mu,Ik}|^2}{\bar{P}_{n_\mu}} \right\} \tag{A.31}$$

for the segment-dependent signal and noise likelihoods, respectively.

B Appendix B - BBH Time Delay

B.1 Data

In this appendix, we provide more detailed information regarding the exact inputs to our analysis in Chapter 4. In our analyses, we include the BBHs of the GWTC-3 catalogue [17] detected with a false-alarm rate (FAR) below 1 yr^{-1}. In the GWTC-3 catalog, there are two events, GW190814 [13] and GW190917, that are possibly BBHs but which are known to be outliers with respect to the bulk binary population [17]. We do not consider these two events, leaving 69 BBHs to be included in our analysis. Publicly-available parameter estimation samples are used, which are provided by the GWOSC[1] [10, 225, 254] and/or Zenodo. We use the "Overall posterior" samples[2] for GWTC-1 events [5], use the "PrecessingSpinIMRHM" samples for events from GWTC-2 [14][3], and use use the "C01:Mixed" samples[4] for new events in GWTC-3 [17]. These contain the combination of parameter estimation samples from several waveform families, each of which include the physical effects of spin precession. We note that the GWTC-2 and GWTC-3 samples additionally include higher-order mode content, whereas GWTC-1 samples, in contrast, do not.

In our analysis, injected signals are used to characterise selection effects, as given by Eq. (4.17). We use the injection set[5] detailed in [17], labeling injections as "found" when they are recovered with FARs below 1 yr^{-1} in at least one search pipeline. However, the injections for the O1 and O2 observing runs do not have associated FARs, only network SNRs ρ. We therefore consider them "found" if $\rho \geq 10$.

In addition, for the joint analysis using both direct detections and GWB constraints at current O3 sensitivity, we use the results of the search for an isotropic GWB following the LVK O3 observing run[6] [19]. Note that we only consider the LIGO Hanford – LIGO Livingston baseline, since the LIGO-Virgo baselines have negligible sensitivity to CBC signals.

---

[1] https://www.gw-openscience.org/

[2] https://dcc.ligo.org/LIGO-P1800370/public

[3] https://dcc.ligo.org/LIGO-P2000223/public

[4] https://zenodo.org/record/5546663

[5] https://zenodo.org/record/5636816

[6] https://dcc.ligo.org/LIGO-G2001287/public

B.2 Results with an Alternative Star Formation History

In order to turn GW observations into constraints on evolutionary conditions (their metallicity dependence and time delays) of BBHs, it was necessary to *assume* an underlying global SFR. In the main text, we used the [188] model, but the global SFR remains highly uncertain, and thus represents a source of systematic uncertainty in our analysis. In this section, we explore this systematic uncertainty by repeating our analyses under a different model for the global SFR. We find that our conclusions in the main text remain robust under such alternative assumptions.

We consider a global SFR as given by [255]:

$$R_*(z) \propto \frac{\exp(b(z-z_0))}{a-b+b\exp(a(z-z_0))}, \tag{B.1}$$

where $a = 2.8$, $b = 2.46$, and $z_0 = 1.72$. We show an example of the corresponding merger rate $\mathcal{R}(z)$ and the expected $\Omega(f)$ spectrum in Figures B.1 and B.2, in analogy to Figures 4.1 and 4.2 in the main text. As the parameters of the underlying distributions are varied, both the merger rate $\mathcal{R}(z)$ and the $\Omega(f)$ spectrum vary similarly to the ones discussed in the main text. We therefore refrain from providing a detailed discussion here about the various parameters, and refer to the main text for more details.

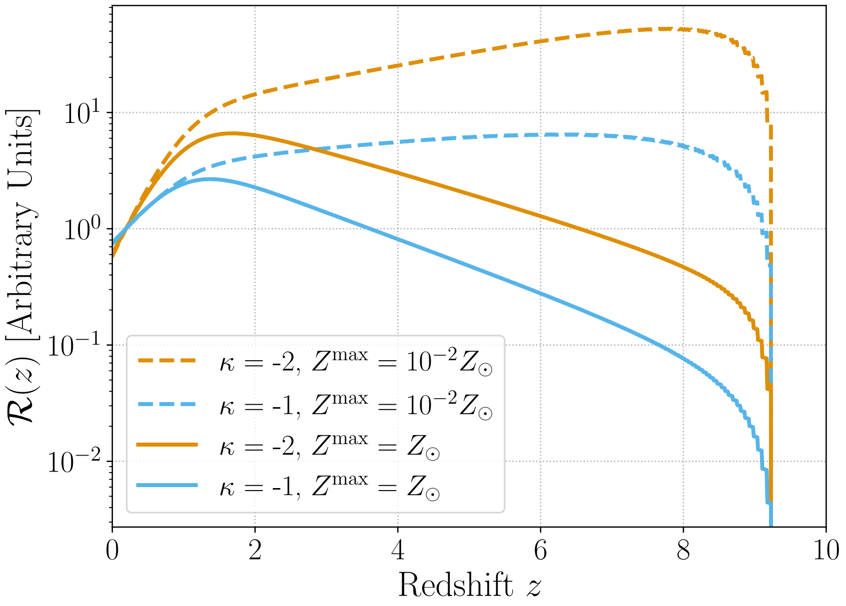

Figure B.1. As in Figure 4.1, but using an alternative global SFR given by [255].

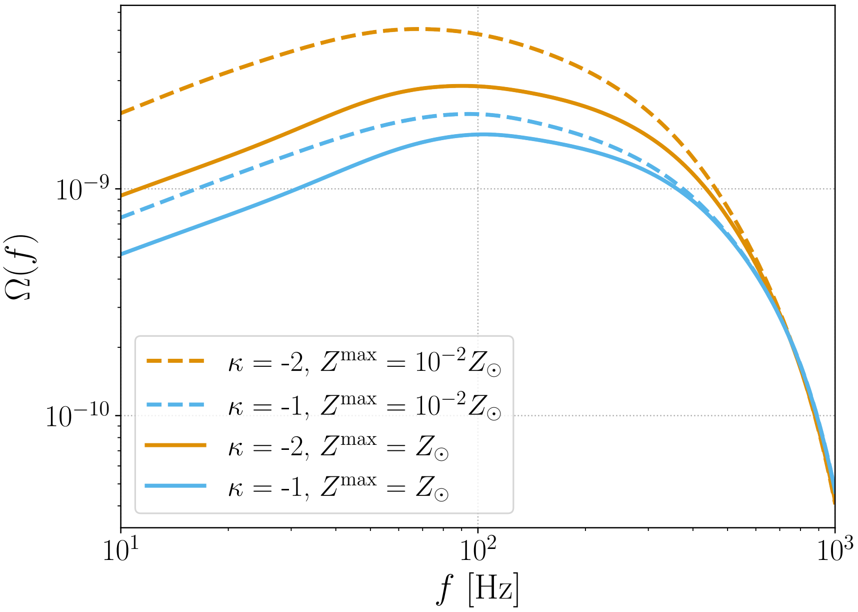

Figure B.2. As in Figure 4.2, but using an alternative global SFR given by [255].

Using this alternate SFR, we repeat our inference of the BBH metallicity dependence and time-delay distribution, using both black hole detections in GWTC-3 and the latest constraints on the GWB. The results are effectively identical to those shown previously in Figure 4.3 using the [188] SFR model. We therefore do not show them here. Instead, we will look ahead to constraints possible with future A+ LIGO instruments, as in Section 4.3.2.

Similarly to the analysis in the main text, we report the posteriors for the joint analysis using both direct detections and GWB constraints using the [255] SFR for a simulated GWB at A+ sensitivity, both detectable and undetectable. The analogue of Figures 4.6 and 4.9 in the main text are reported in Figures B.3 and B.4. Comparing these sets of figures, we see that our qualitative results show little dependence on the exact model used for global star formation. Once more, we see that an undetectable GWB at A+ sensitivity results in strong constraints on the slope of the time-delay distribution, but leaves the metallicity and the minimum time-delay parameters unconstrained. Conversely, a detectable GWB at A+ sensitivity still results in larger regions of the metallicity and minimum time-delay parameter space being excluded, and shows support for larger negative values of the slope of the time-delay distribution. Therefore, also with the SFR given in [255], both cases at future Advanced LIGO A+ sensitivity would yield distinct and complementary information about the environment in which binaries formed and their evolution throughout time.

In addition, our choice of model for the cumulative metallicity of star formation, as given by Eq. (4.2), represents a similar systematic source of uncertainty. Future work will explore how variations in metallicity models similarly impact our conclusions.

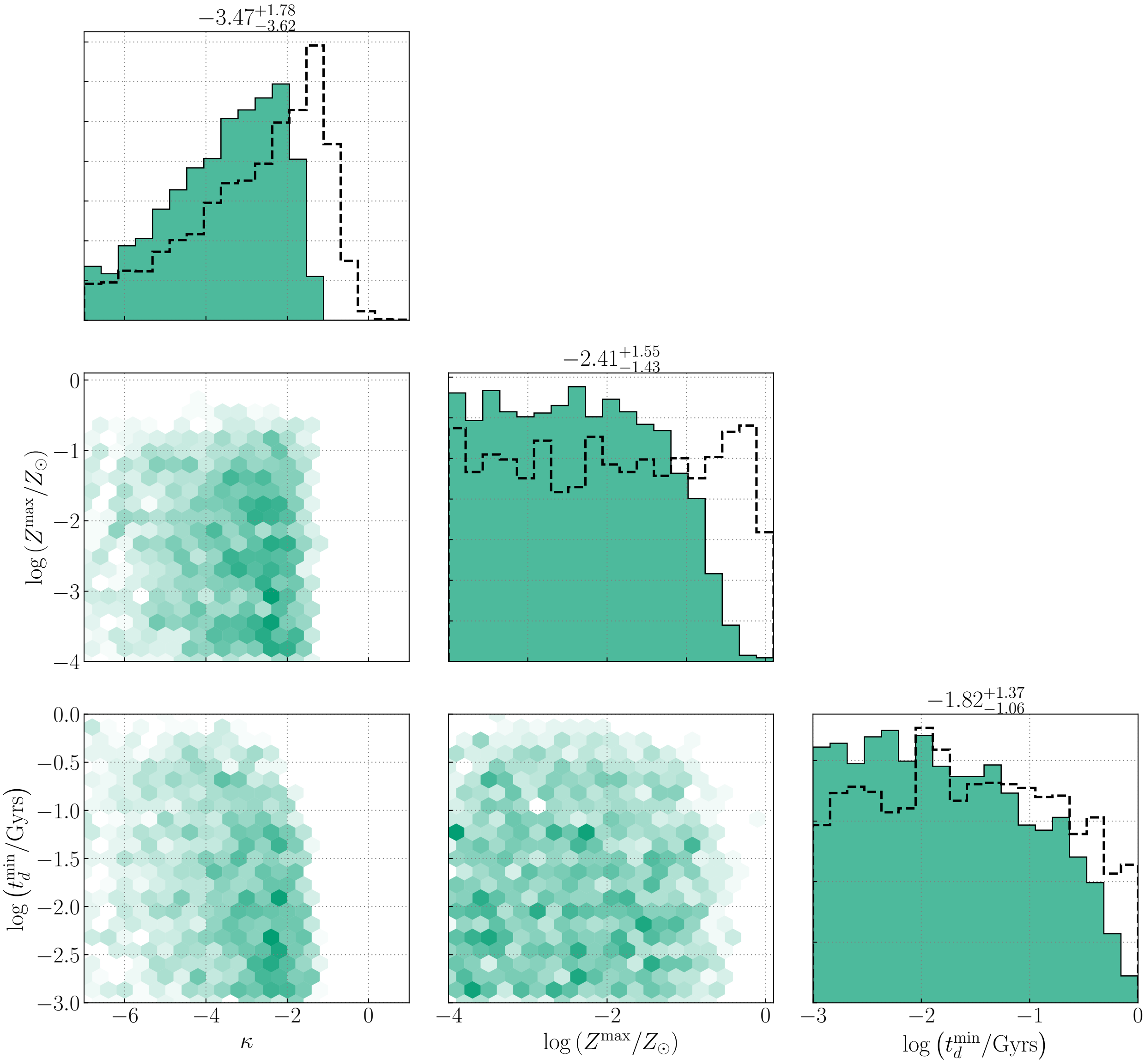

Figure B.3. Posterior on the slope of the time-delay distribution κ, the metallicity threshold $Z^{\max}$, and the minimum time-delay parameter $t_d^{\min}$ for the joint analysis using both direct detections and GWB constraints at Advanced LIGO A+ sensitivity, in the presence of a detectable GWB. The dashed black lines represent the 1D histograms for the joint analysis on data from the first three observing runs, for reference. We note that there is more support for larger negative values of the slope of the time-delay distribution κ, and note that smaller values of the metallicity parameter $Z^{\max}$ and the minimum time delay $t_d^{\min}$ are favoured. In addition, we point out the complementarity of these constraints with the case of an undetectable GWB at A+ sensitivity, as reported in Figure B.4.

B.3 Additional Distributions and Priors

In addition to the mass and redshift distribution described in the main text, we provide the assumed distributions for the spin magnitudes and spin-orbit tilt angles. These are modelled

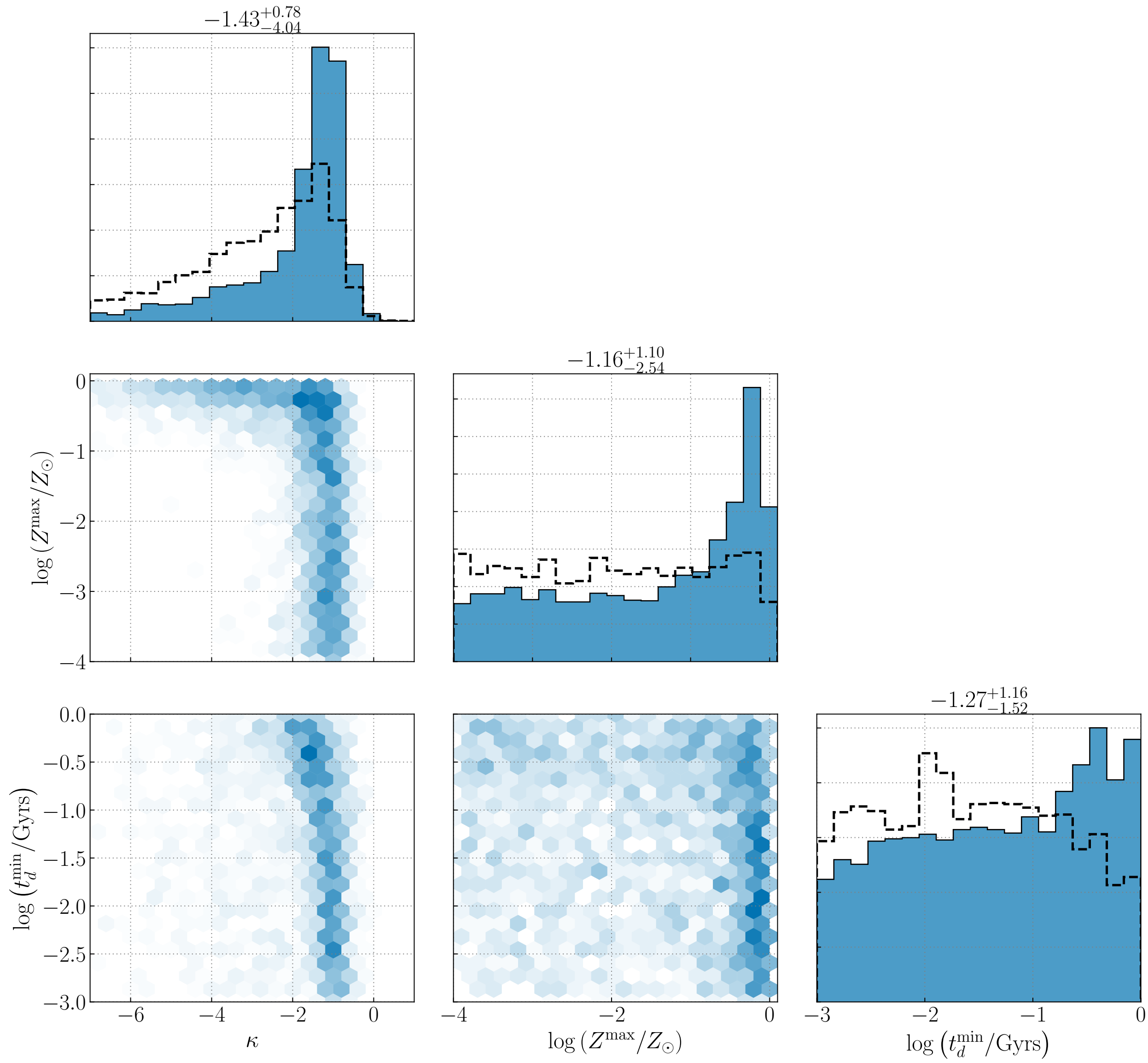

Figure B.4. Posterior on the slope of the time-delay distribution κ, the metallicity threshold $Z^{\max}$, and the minimum time-delay parameter $t_d^{\min}$ for the joint analysis using both direct detections and GWB constraints at Advanced LIGO A+ sensitivity, in the presence of an undetectable GWB. The dashed black lines represent the 1D histograms for the joint analysis on data from the first three observing runs, for reference. We note that large negative values for the slope of the time-delay distribution κ are disfavoured, and the support at larger values of the metallicity parameter $Z^{\max}$ and the minimum time delay $t_d^{\min}$. In addition, we point out the complementarity of these constraints with the case of an detectable GWB at A+ sensitivity, as reported in Figure B.3.

as truncated Gaussian distributions [69]:

$$\pi(\chi_i) = \sqrt{\frac{2}{\pi\sigma_\chi^2}} \frac{e^{-(\chi_i-\mu_\chi)^2/2\sigma_\chi^2}}{\mathrm{Erf}\left(\frac{1-\mu_\chi}{\sqrt{2\sigma_\chi^2}}\right) + \mathrm{Erf}\left(\frac{\mu_\chi}{\sqrt{2\sigma_\chi^2}}\right)}, \tag{B.2}$$

where μ_χ stands for the mean of the distribution, σ_χ^2 for the variance, and

$$\pi(\cos\theta_i) = \sqrt{\frac{2}{\pi\sigma_u^2}}\frac{e^{-(\cos\theta_i-1)^2/2\sigma_u^2}}{\mathrm{Erf}\left(\frac{-2}{\sqrt{2\sigma_u^2}}\right)}, \tag{B.3}$$

where the mean is assumed to be 1, and the variance σ_u^2 is inferred from the data.

Furthermore, we provide a list of priors used for the parameter estimation performed in the context of Chapter 4 in Table B.1.

Mass distribution			
Parameter	Prior	Minimum	Maximum
$m_{\mathrm{low}}/M_\odot$	Uniform	5	15
$m_{\mathrm{high}}/M_\odot$	Uniform	50	100
$\mu_m/M_\odot$	Uniform	20	50
$\sigma_m/M_\odot$	Uniform	1.5	15
f_{peak}	Log-Uniform	10^{-3}	1
$\delta m_{\mathrm{low}}/M_\odot$	Log-Uniform	10^{-1}	$10^{0.5}$
$\delta m_{\mathrm{high}}/M_\odot$	Log-Uniform	$10^{0.5}$	$10^{1.5}$
Parameter	Prior	Mean	Standard deviation
α	Gaussian	-2	3
β_q	Gaussian	0	3
Time-delay distribution			
Parameter	Prior	Minimum	Maximum
$\mathcal{R}_{\mathrm{ref}}/M_\odot^{-1}\mathrm{Gpc}^{-3}\mathrm{yr}^{-1}$	Log-Uniform	10^{-2}	10
$Z^{\mathrm{max}}/Z_\odot$	Log-Uniform	10^{-4}	1
$t_d^{\mathrm{min}}/\mathrm{Gyrs}$	Log-Uniform	10^{-3}	1
Parameter	Prior	Mean	Standard deviation
κ	Gaussian	-1	3
Spin distribution			
Parameter	Prior	Minimum	Maximum
μ_χ	Uniform	0	1
σ_χ	Log-Uniform	10^{-1}	1
σ_u	Uniform	0.3	2

Table B.1. Prior choice for the hyperparameters describing the mass distributions, the time-delay distribution and the spin distribution.

B.4 Computation of $\Omega(f)$

The computation of the expected $\Omega(f)$, given a set of hyperparameters Λ, can be written as in Eq. (4.5) in the main text. We recall that this depends on the average energy $\left\langle \frac{dE_s}{df_s} \right\rangle$ radiated by each binary, given by Eq. (4.6), where the integration is performed over the masses m_1 and m_2. Therefore, including the integration over redshift, the computation of the expected $\Omega(f)$ requires the evaluation of a three-dimensional integral. Numerically, the integral can be evaluated on a grid, resulting in a fairly inefficient and slow implementation of the computation. Alternatively, one can rely on a Monte Carlo integration technique to evaluate the integral, where one relies on averaging many individual draws of the population.

In our implementation of this approach, N samples are drawn from a uniform distribution at the start of the computation for each of the parameters z, m_1, and m_2. We denote the i-th parameter draw as $\phi^i = \{z^i, m_1^i, m_2^i\}$. We proceed by computing the energy spectra dE_s/df_s for each of these parameter draws and label these dE_s^i/df_s. However, we want to compute the $\Omega(f)$ for the population corresponding to the distributions described in the main text, with hyperparameters Λ. We therefore rely on reweighting dE_s^i/df_s given some hyperparameters Λ. Schematically, the computation takes the following form:

$$\Omega(f) \sim \frac{1}{N} \sum_i^N w_i \frac{dE_s^i}{df_s}, \tag{B.4}$$

where the average is taken over the number of sample draws N, and the weights w_i are defined as

$$w_i = \frac{\mathcal{R}(z^i)(1+z^i)^{-1} H(z^i)^{-1}}{p_{\text{draw}}(z^i)} \frac{\phi(m_1^i)}{p_{\text{draw}}(m_1^i)} \frac{p(m_2^i)}{p_{\text{draw}}(m_2^i)}. \tag{B.5}$$

The p_{draw} distributions represent the uniform distributions used to make the initial draws of the parameters ϕ^i, whereas the numerators denote the distributions we are reweighting to, characterising the population corresponding to a set of hyperparameters Λ for which we want to compute the $\Omega(f)$ spectrum.

In order to show the convergence of the Monte Carlo average, we show the $\Omega(f)$ spectrum computed by performing the integral explicitly and compare it to our implementation for several values of the number of initial draws. The results are displayed in Figure B.5. Note that although the results are only shown for one set of hyperparameters, i.e., one specific distribution, and therefore, one $\Omega(f)$ spectrum in the plot, tests were performed on various other distributions to verify convergence. In general, a value $N = 20000$ approximates the full integral computation well in the frequency range of interest for GWB searches with the LVK detectors, with relative errors of $\mathcal{O}(10^{-1} - 10^{-2})$. Therefore, throughout our work, we use $N = 20000$

when computing the $\Omega(f)$ spectrum with the Monte Carlo averaging procedure.

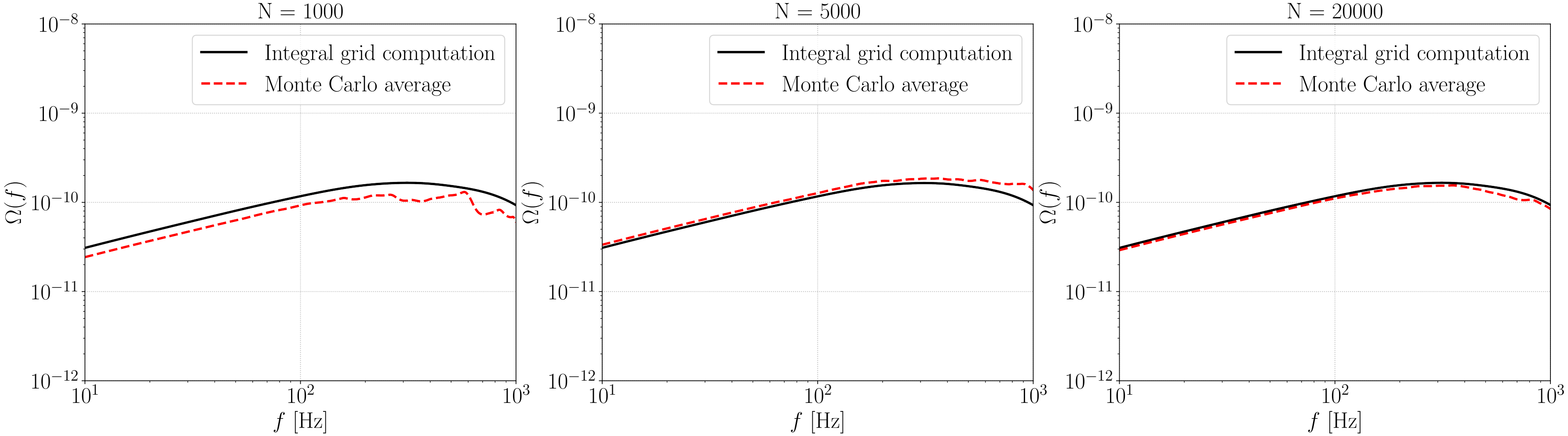

Figure B.5. Convergence of the $\Omega(f)$ spectrum using the Monte Carlo average approach, compared to the computation evaluating the integrals in Eq. (4.5) directly. The black line denotes the $\Omega(f)$ spectrum computed using by evaluating the integrals numerically on a grid, whereas the red dashed lines show the result of the Monte Carlo approach for different numbers of sample draws. For illustrative purposes, several numbers of sample draws N are used in the Monte Carlo average, namely 1000, 5000, and 20000. It was found that $N = 20000$ approximates the $\Omega(f)$ spectrum well enough.

LIST OF TABLES

LIST OF FIGURES

BIBLIOGRAPHY

[1] J Aasi *et al.* "The characterization of Virgo data and its impact on gravitational-wave searches". In: *Classical and Quantum Gravity* 29.15 (June 2012), p. 155002. DOI: 10.1088/0264-9381/29/15/155002. URL: https://doi.org/10.1088/0264-9381/29/15/155002.

[2] J. Aasi *et al.* "Advanced LIGO". In: *Class. Quant. Grav.* 32 (2015), p. 074001. DOI: 10.1088/0264-9381/32/7/074001. arXiv: 1411.4547 [gr-qc].

[3] B. P. Abbott *et al.* "Binary Black Hole Population Properties Inferred from the First and Second Observing Runs of Advanced LIGO and Advanced Virgo". In: *Astrophys. J. Lett.* 882.2, L24 (Sept. 2019), p. L24. DOI: 10.3847/2041-8213/ab3800. arXiv: 1811.12940 [astro-ph.HE].

[4] B. P. Abbott *et al.* "GW170817: Implications for the Stochastic Gravitational-Wave Background from Compact Binary Coalescences". In: *Phys. Rev. Lett.* 120 (9 Feb. 2018), p. 091101. DOI: 10.1103/PhysRevLett.120.091101. URL: https://link.aps.org/doi/10.1103/PhysRevLett.120.091101.

[5] B. P. Abbott *et al.* "GWTC-1: A Gravitational-Wave Transient Catalog of Compact Binary Mergers Observed by LIGO and Virgo during the First and Second Observing Runs". In: *Phys. Rev. X* 9 (3 Sept. 2019), p. 031040. DOI: 10.1103/PhysRevX.9.031040. URL: https://link.aps.org/doi/10.1103/PhysRevX.9.031040.

[6] B. P. Abbott *et al.* "Observation of Gravitational Waves from a Binary Black Hole Merger". In: *Phys. Rev. Lett.* 116 (6 Feb. 2016), p. 061102. DOI: 10.1103/PhysRevLett.116.061102. URL: https://link.aps.org/doi/10.1103/PhysRevLett.116.061102.

[7] B. P. Abbott *et al.* "Optically targeted search for gravitational waves emitted by core-collapse supernovae during the first and second observing runs of advanced LIGO and advanced Virgo". In: *Phys. Rev. D* 101 (8 Apr. 2020), p. 084002. DOI: 10.1103/PhysRevD.101.084002. URL: https://link.aps.org/doi/10.1103/PhysRevD.101.084002.

[8] B. P. Abbott *et al.* "Search for gravitational-wave bursts associated with gamma-ray bursts using data from LIGO science run 5 and Virgo science run 1". In: *The Astrophysical Journal* 715.2 (May 2010), p. 1438. DOI: 10.1088/0004-637X/715/2/1438. URL: https://dx.doi.org/10.1088/0004-637X/715/2/1438.

[9] B. P. Abbott *et al.* "Search for gravitational-wave bursts in the first year of the fifth LIGO science run". In: *Phys. Rev. D* 80 (10 Nov. 2009), p. 102001. DOI: 10.1103/PhysRevD.80.102001. URL: https://link.aps.org/doi/10.1103/PhysRevD.80.102001.

[10] R. Abbott *et al.* “Open Data from the Third Observing Run of LIGO, Virgo, KAGRA, and GEO”. In: *Astrophys. J. Suppl.* 267.2 (2023), p. 29. DOI: 10.3847/1538-4365/acdc9f. arXiv: 2302.03676 [gr-qc].

[11] R. Abbott *et al.* “All-sky search for short gravitational-wave bursts in the third Advanced LIGO and Advanced Virgo run”. In: *Phys. Rev. D* 104 (12 Dec. 2021), p. 122004. DOI: 10.1103/PhysRevD.104.122004. URL: https://link.aps.org/doi/10.1103/PhysRevD.104.122004.

[12] R. Abbott *et al.* “Constraints on Cosmic Strings Using Data from the Third Advanced LIGO–Virgo Observing Run”. In: *Phys. Rev. Lett.* 126 (24 June 2021), p. 241102. DOI: 10.1103/PhysRevLett.126.241102. URL: https://link.aps.org/doi/10.1103/PhysRevLett.126.241102.

[13] R. Abbott *et al.* “GW190814: Gravitational Waves from the Coalescence of a 23 Solar Mass Black Hole with a 2.6 Solar Mass Compact Object”. In: *The Astrophysical Journal Letters* 896.2 (June 2020), p. L44. DOI: 10.3847/2041-8213/ab960f. URL: https://dx.doi.org/10.3847/2041-8213/ab960f.

[14] R. Abbott *et al.* “GWTC-2: Compact Binary Coalescences Observed by LIGO and Virgo during the First Half of the Third Observing Run”. In: *Phys. Rev. X* 11 (2 June 2021), p. 021053. DOI: 10.1103/PhysRevX.11.021053. URL: https://link.aps.org/doi/10.1103/PhysRevX.11.021053.

[15] R. Abbott *et al.* “GWTC-3: Compact Binary Coalescences Observed by LIGO and Virgo during the Second Part of the Third Observing Run”. In: *Physical Review X* 13.4 (Dec. 2023). ISSN: 2160-3308. DOI: 10.1103/physrevx.13.041039. URL: http://dx.doi.org/10.1103/PhysRevX.13.041039.

[16] R. Abbott *et al.* “Open Data from the Third Observing Run of LIGO, Virgo, KAGRA, and GEO”. In: *The Astrophysical Journal Supplement Series* 267.2 (July 2023), p. 29. DOI: 10.3847/1538-4365/acdc9f. URL: https://dx.doi.org/10.3847/1538-4365/acdc9f.

[17] R. Abbott *et al.* “Population of Merging Compact Binaries Inferred Using Gravitational Waves through GWTC-3”. In: *Phys. Rev. X* 13 (1 Mar. 2023), p. 011048. DOI: 10.1103/PhysRevX.13.011048. URL: https://link.aps.org/doi/10.1103/PhysRevX.13.011048.

[18] R. Abbott *et al.* “Search for anisotropic gravitational-wave backgrounds using data from Advanced LIGO and Advanced Virgo’s first three observing runs”. In: *Physical Review D* 104.2 (July 2021). DOI: 10.1103/physrevd.104.022005. URL: https://doi.org/10.1103%2Fphysrevd.104.022005.

[19] R. Abbott *et al.* “Upper limits on the isotropic gravitational-wave background from Advanced LIGO and Advanced Virgos third observing run”. In: *Physical Review D* 104.2 (July 2021). ISSN: 2470-0029. DOI: 10.1103/physrevd.104.022004. URL: http://dx.doi.org/10.1103/PhysRevD.104.022004.

[20] Mahiro Abe *et al.* “Matter-wave Atomic Gradiometer Interferometric Sensor (MAGIS-100)”. In: *Quantum Science and Technology* 6.4 (July 2021), p. 044003. DOI: 10.1088/2058-9565/abf719. URL: https://dx.doi.org/10.1088/2058-9565/abf719.

[21] F Acernese *et al.* “Advanced Virgo: a second-generation interferometric gravitational wave detector”. In: *Classical and Quantum Gravity* 32.2 (Dec. 2014), p. 024001. ISSN: 1361-6382. DOI: 10.1088/0264-9381/32/2/024001. URL: http://dx.doi.org/10.1088/0264-9381/32/2/024001.

[22] F. Acernese *et al.* “Advanced Virgo: a second-generation interferometric gravitational wave detector”. In: *Class. Quant. Grav.* 32.2 (2015), p. 024001. DOI: 10.1088/0264-9381/32/2/024001. arXiv: 1408.3978 [gr-qc].

[23] F. Acernese *et al. Virgo Detector Characterization and Data Quality: results from the O3 run*. 2022. DOI: 10.48550/ARXIV.2210.15633. URL: https://arxiv.org/abs/2210.15633.

[24] R. Adam *et al.* “Planck2015 results: I. Overview of products and scientific results”. In: *Astronomy and Astrophysics* 594 (Sept. 2016), A1. ISSN: 1432-0746. DOI: 10.1051/0004-6361/201527101. URL: http://dx.doi.org/10.1051/0004-6361/201527101.

[25] Adeela Afzal *et al.* “The NANOGrav 15 yr Data Set: Search for Signals from New Physics”. In: *The Astrophysical Journal Letters* 951.1 (June 2023), p. L11. DOI: 10.3847/2041-8213/acdc91. URL: https://dx.doi.org/10.3847/2041-8213/acdc91.

[26] Kaustubh Agashe *et al.* “Cosmological Phase Transition of Spontaneous Confinement”. In: *JHEP* 05 (2020), p. 086. DOI: 10.1007/JHEP05(2020)086. arXiv: 1910.06238 [hep-ph].

[27] Kaustubh Agashe *et al.* “Phase Transitions from the Fifth Dimension”. In: *JHEP* 02 (2021), p. 051. DOI: 10.1007/JHEP02(2021)051. arXiv: 2010.04083 [hep-th].

[28] Gabriella Agazie *et al.* “The NANOGrav 15 yr Data Set: Bayesian Limits on Gravitational Waves from Individual Supermassive Black Hole Binaries”. In: *The Astrophysical Journal Letters* 951.2 (July 2023), p. L50. DOI: 10.3847/2041-8213/ace18a. URL: https://dx.doi.org/10.3847/2041-8213/ace18a.

[29] Gabriella Agazie *et al.* “The NANOGrav 15 yr Data Set: Constraints on Supermassive Black Hole Binaries from the Gravitational-wave Background”. In: *The Astrophysical Journal Letters* 952.2 (Aug. 2023), p. L37. DOI: 10.3847/2041-8213/ace18b. URL: https://dx.doi.org/10.3847/2041-8213/ace18b.

[30] Gabriella Agazie *et al.* “The NANOGrav 15 yr Data Set: Detector Characterization and Noise Budget”. In: *The Astrophysical Journal Letters* 951.1 (June 2023), p. L10. DOI: 10.3847/2041-8213/acda88. URL: https://dx.doi.org/10.3847/2041-8213/acda88.

[31] Gabriella Agazie *et al.* “The NANOGrav 15 yr Data Set: Evidence for a Gravitational-wave Background”. In: *The Astrophysical Journal Letters* 951.1 (June 2023), p. L8. DOI: 10.3847/2041-8213/acdac6. URL: https://dx.doi.org/10.3847/2041-8213/acdac6.

[32] Gabriella Agazie *et al.* “The NANOGrav 15 yr Data Set: Observations and Timing of 68 Millisecond Pulsars”. In: *The Astrophysical Journal Letters* 951.1 (June 2023), p. L9. DOI: 10.3847/2041-8213/acda9a. URL: https://dx.doi.org/10.3847/2041-8213/acda9a.

[33] Gabriella Agazie *et al.* “The NANOGrav 15 yr Data Set: Search for Anisotropy in the Gravitational-wave Background”. In: *The Astrophysical Journal Letters* 956.1 (Oct. 2023), p. L3. DOI: 10.3847/2041-8213/acf4fd. URL: https://dx.doi.org/10.3847/2041-8213/acf4fd.

[34] P. Ajith *et al.* “Template bank for gravitational waveforms from coalescing binary black holes: Nonspinning binaries”. In: *Phys. Rev. D* 77 (10 May 2008), p. 104017. DOI: 10.1103/PhysRevD.77.104017. URL: https://link.aps.org/doi/10.1103/PhysRevD.77.104017.

[35] B. Allen and J.D. Romano. “Detecting a stochastic background of gravitational radiation: Signal processing strategies and sensitivities”. In: *Phys. Rev. D* 59 (1999), p. 102001.

[36] Alexandre Alves *et al.* “Collider and Gravitational Wave Complementarity in Exploring the Singlet Extension of the Standard Model”. In: *JHEP* 04 (2019), p. 052. DOI: 10.1007/JHEP04(2019)052. arXiv: 1812.09333 [hep-ph].

[37] Pau Amaro-Seoane *et al.* *Laser Interferometer Space Antenna*. 2017. arXiv: 1702.00786 [astro-ph.IM].

[38] J. Antoniadis *et al.* *The second data release from the European Pulsar Timing Array IV. Search for continuous gravitational wave signals*. 2023. arXiv: 2306.16226 [astro-ph.HE].

[39] J. Antoniadis *et al.* “The second data release from the European Pulsar Timing Array: I. The dataset and timing analysis”. In: *Astronomy and Astrophysics* 678 (Oct. 2023), A48. ISSN: 1432-0746. DOI: 10.1051/0004-6361/202346841. URL: http://dx.doi.org/10.1051/0004-6361/202346841.

[40] J. Antoniadis *et al.* “The second data release from the European Pulsar Timing Array: II. Customised pulsar noise models for spatially correlated gravitational waves”. In: *Astronomy and Astrophysics* 678 (Oct. 2023), A49. ISSN: 1432-0746. DOI: 10.1051/0004-6361/202346842. URL: http://dx.doi.org/10.1051/0004-6361/202346842.

[41] J. Antoniadis *et al.* “The second data release from the European Pulsar Timing Array: III. Search for gravitational wave signals”. In: *Astronomy & Astrophysics* 678 (Oct. 2023), A50. ISSN: 1432-0746. DOI: 10.1051/0004-6361/202346844. URL: http://dx.doi.org/10.1051/0004-6361/202346844.

[42] J. Antoniadis *et al.* *The second data release from the European Pulsar Timing Array: V. Implications for massive black holes, dark matter and the early Universe*. 2023. arXiv: 2306.16227 [astro-ph.CO].

[43] Gregory Ashton *et al.* “Bilby: A User-friendly Bayesian Inference Library for Gravitational-wave Astronomy”. In: *The Astrophysical Journal Supplement Series* 241.2 (Apr. 2019), p. 27. ISSN: 1538-4365. DOI: 10.3847/1538-4365/ab06fc. URL: http://dx.doi.org/10.3847/1538-4365/ab06fc.

[44] Yoichi Aso *et al.* “Interferometer design of the KAGRA gravitational wave detector”. In: *Phys. Rev. D* 88 (4 Aug. 2013), p. 043007. DOI: 10.1103/PhysRevD.88.043007. URL: https://link.aps.org/doi/10.1103/PhysRevD.88.043007.

[45] P Astone *et al.* “The 2003 run of the EXPLORERNAUTILUS gravitational wave experiment”. In: *Classical and Quantum Gravity* 23.8 (Mar. 2006), S169. DOI: `10.1088/0264-9381/23/8/S22`. URL: `https://dx.doi.org/10.1088/0264-9381/23/8/S22`.

[46] P Astone *et al.* “The gravitational wave detector NAUTILUS operating at T = 0.1 K”. In: *Astroparticle Physics* 7.3 (1997), pp. 231–243. ISSN: 0927-6505. DOI: `https://doi.org/10.1016/S0927-6505(97)00023-6`. URL: `https://www.sciencedirect.com/science/article/pii/S0927650597000236`.

[47] P. Astone *et al.* “Search for coincident excitation of the widely spaced resonant gravitational wave detectors EXPLORER, NAUTILUS and NIOBE”. In: *Astroparticle Physics* 10.1 (1999), pp. 83–92. ISSN: 0927-6505. DOI: `https://doi.org/10.1016/S0927-6505(98)00033-4`. URL: `https://www.sciencedirect.com/science/article/pii/S0927650598000334`.

[48] Aleksandr Azatov, Miguel Vanvlasselaer, and Wen Yin. “Baryogenesis via relativistic bubble walls”. In: *JHEP* 10 (2021), p. 043. DOI: `10.1007/JHEP10(2021)043`. arXiv: `2106.14913 [hep-ph]`.

[49] Aleksandr Azatov, Miguel Vanvlasselaer, and Wen Yin. “Dark Matter production from relativistic bubble walls”. In: *JHEP* 03 (2021), p. 288. DOI: `10.1007/JHEP03(2021)288`. arXiv: `2101.05721 [hep-ph]`.

[50] Charles Badger *et al.* “Probing early Universe supercooled phase transitions with gravitational wave data”. In: *Physical Review D* 107.2 (Jan. 2023). DOI: `10.1103/physrevd.107.023511`. URL: `https://doi.org/10.1103%2Fphysrevd.107.023511`.

[51] L. Badurina *et al.* “AION: an atom interferometer observatory and network”. In: *Journal of Cosmology and Astroparticle Physics* 2020.05 (May 2020), p. 011. DOI: `10.1088/1475-7516/2020/05/011`. URL: `https://dx.doi.org/10.1088/1475-7516/2020/05/011`.

[52] Iason Baldes and Camilo Garcia-Cely. “Strong gravitational radiation from a simple dark matter model”. In: *JHEP* 05 (2019), p. 190. DOI: `10.1007/JHEP05(2019)190`. arXiv: `1809.01198 [hep-ph]`.

[53] Iason Baldes, Yann Gouttenoire, and Filippo Sala. “Hot and Heavy Dark Matter from Supercooling”. In: (July 2022). arXiv: `2207.05096 [hep-ph]`.

[54] Iason Baldes *et al.* “Baryogenesis via relativistic bubble expansion”. In: *Physical Review D* 104.11 (Dec. 2021). DOI: `10.1103/physrevd.104.115029`. URL: `https://doi.org/10.1103%2Fphysrevd.104.115029`.

[55] Iason Baldes *et al.* “Supercool composite Dark Matter beyond 100 TeV”. In: *JHEP* 07 (2022), p. 084. DOI: `10.1007/JHEP07(2022)084`. arXiv: `2110.13926 [hep-ph]`.

[56] Pietro Baratella, Alex Pomarol, and Fabrizio Rompineve. “The Supercooled Universe”. In: *JHEP* 03 (2019), p. 100. DOI: `10.1007/JHEP03(2019)100`. arXiv: `1812.06996 [hep-ph]`.

[57] L. Barsotti *et al.* “The A+ design curve”. In: (2018). URL: `https://dcc.ligo.org/LIGO-T1800042/public`.

[58] Nicola Bartolo *et al.* “Science with the space-based interferometer LISA. IV: probing inflation with gravitational waves”. In: *Journal of Cosmology and Astroparticle Physics* 2016.12 (Dec. 2016), pp. 026–026. ISSN: 1475-7516. DOI: `10.1088/1475-7516/2016/12/026`. URL: `http://dx.doi.org/10.1088/1475-7516/2016/12/026`.

[59] Krzysztof Belczynski *et al.* “The first gravitational-wave source from the isolated evolution of two stars in the 40100 solar mass range”. In: *Nature* 534.7608 (June 2016), pp. 512–515. DOI: `10.1038/nature18322`. URL: `https://doi.org/10.1038%2Fnature18322`.

[60] C. L. Bennett *et al.* “First-Year Wilkinson Microwave Anisotropy Probe Observations: Preliminary Maps and Basic Results”. In: *The Astrophysical Journal Supplement Series* 148.1 (Sept. 2003), p. 1. DOI: `10.1086/377253`. URL: `https://dx.doi.org/10.1086/377253`.

[61] Simone Blasi *et al.* “Friction on ALP domain walls and gravitational waves”. In: *Journal of Cosmology and Astroparticle Physics* 2023.04 (Apr. 2023), p. 008. DOI: `10.1088/1475-7516/2023/04/008`. URL: `https://doi.org/10.1088%2F1475-7516%2F2023%2F04%2F008`.

[62] Ssohrab Borhanian and B. S. Sathyaprakash. *Listening to the Universe with Next Generation Ground-Based Gravitational-Wave Detectors*. 2022. arXiv: `2202.11048 [gr-qc]`.

[63] Marica Branchesi *et al.* “Science with the Einstein Telescope: a comparison of different designs”. In: *JCAP* 07 (2023), p. 068. DOI: `10.1088/1475-7516/2023/07/068`. arXiv: `2303.15923 [gr-qc]`.

[64] V. Brdar, A. J. Helmboldt, and J. Kubo. “*Gravitational Waves from First-Order Phase Transitions: LIGO as a Window to Unexplored Seesaw Scales*”. In: *JCAP* 02 (2019), p. 021. DOI: `10.1088/1475-7516/2019/02/021`. arXiv: `1810.12306 [hep-ph]`.

[65] V. Brdar *et al.* “*Gravitational Waves as a Probe of Left-Right Symmetry Breaking*”. In: *JCAP* 12 (2019), p. 027. DOI: `10.1088/1475-7516/2019/12/027`. arXiv: `1909.02018 [hep-ph]`.

[66] Moritz Breitbach *et al.* “Dark, Cold, and Noisy: Constraining Secluded Hidden Sectors with Gravitational Waves”. In: *JCAP* 07 (2019), p. 007. DOI: `10.1088/1475-7516/2019/07/007`. arXiv: `1811.11175 [hep-ph]`.

[67] Riccardo Buscicchio *et al.* *Detecting non-Gaussian gravitational wave backgrounds: a unified framework*. 2022. DOI: `10.48550/ARXIV.2209.01400`. URL: `https://arxiv.org/abs/2209.01400`.

[68] Robert Caldwell *et al.* “Detection of early-universe gravitational-wave signatures and fundamental physics”. In: *General Relativity and Gravitation* 54.12 (Nov. 2022). ISSN: 1572-9532. DOI: `10.1007/s10714-022-03027-x`. URL: `http://dx.doi.org/10.1007/s10714-022-03027-x`.

[69] Thomas A. Callister and Will M. Farr. *A Parameter-Free Tour of the Binary Black Hole Population*. 2023. arXiv: `2302.07289 [astro-ph.HE]`.

[70] Thomas A. Callister *et al.* “No Evidence that the Majority of Black Holes in Binaries Have Zero Spin”. In: *The Astrophysical Journal Letters* 937.1 (Sept. 2022), p. L13. DOI: 10.3847/2041-8213/ac847e. URL: https://doi.org/10.3847%2F2041-8213%2Fac847e.

[71] Tom Callister *et al.* “Shouts and Murmurs: Combining Individual Gravitational-wave Sources with the Stochastic Background to Measure the History of Binary Black Hole Mergers”. In: *The Astrophysical Journal* 896.2 (June 2020), p. L32. DOI: 10.3847/2041-8213/ab9743. URL: https://doi.org/10.3847%2F2041-8213%2Fab9743.

[72] B Canuel *et al.* “ELGARa European Laboratory for Gravitation and Atom-interferometric Research”. In: *Classical and Quantum Gravity* 37.22 (Oct. 2020), p. 225017. DOI: 10.1088/1361-6382/aba80e. URL: https://dx.doi.org/10.1088/1361-6382/aba80e.

[73] B. Canuel *et al.* “Exploring gravity with the MIGA large scale atom interferometer”. In: *Scientific Reports* 8.1 (Sept. 2018). ISSN: 2045-2322. DOI: 10.1038/s41598-018-32165-z. URL: http://dx.doi.org/10.1038/s41598-018-32165-z.

[74] C. Caprini *et al.* “*Science with the Space-Based Interferometer eLISA. II: Gravitational Waves from Cosmological Phase Transitions*”. In: *JCAP* 04 (2016), p. 001. DOI: 10.1088/1475-7516/2016/04/001. arXiv: 1512.06239 [astro-ph.CO].

[75] Chiara Caprini and Daniel G Figueroa. “Cosmological backgrounds of gravitational waves”. In: *Classical and Quantum Gravity* 35.16 (July 2018), p. 163001. DOI: 10.1088/1361-6382/aac608. URL: https://dx.doi.org/10.1088/1361-6382/aac608.

[76] Sean M. Carroll. *Lecture Notes on General Relativity*. 1997. arXiv: gr-qc/9712019 [gr-qc].

[77] Mikael Chala, Claudius Krause, and Germano Nardini. “Signals of the electroweak phase transition at colliders and gravitational wave observatories”. In: *JHEP* 07 (2018), p. 062. DOI: 10.1007/JHEP07(2018)062. arXiv: 1802.02168 [hep-ph].

[78] Clifford Cheung, Alex Dahlen, and Gilly Elor. “Bubble Baryogenesis”. In: *JHEP* 09 (2012), p. 073. DOI: 10.1007/JHEP09(2012)073. arXiv: 1205.3501 [hep-ph].

[79] Nelson Christensen. “Measuring the stochastic gravitational-radiation background with laser-interferometric antennas”. In: *Phys. Rev. D* 46 (12 Dec. 1992), pp. 5250–5266. DOI: 10.1103/PhysRevD.46.5250. URL: https://link.aps.org/doi/10.1103/PhysRevD.46.5250.

[80] Nelson Christensen. “Stochastic Gravitational Wave Backgrounds”. In: *Rept. Prog. Phys.* 82.1 (2019), p. 016903. DOI: 10.1088/1361-6633/aae6b5. arXiv: 1811.08797 [gr-qc].

[81] Martyna Chruslinska and Gijs Nelemans. “Metallicity of stars formed throughout the cosmic history based on the observational properties of star-forming galaxies”. In: *Monthly Notices of the Royal Astronomical Society* 488.4 (July 2019), pp. 5300–5326. ISSN: 0035-8711. DOI: 10.1093/mnras/stz2057. eprint: https://academic.oup.com/mnras/article-pdf/488/4/5300/32358846/stz2057.pdf. URL: https://doi.org/10.1093/mnras/stz2057.

[82] Martyna Chruslinska, Gijs Nelemans, and Krzysztof Belczynski. “The influence of the distribution of cosmic star formation at different metallicities on the properties of merging double compact objects”. In: *Monthly Notices of the Royal Astronomical Society* 482.4 (Nov. 2018), pp. 5012–5017. DOI: `10.1093/mnras/sty3087`. URL: `https://doi.org/10.1093%2Fmnras%2Fsty3087`.

[83] Martyna Chruliska. *Chemical evolution of the Universe and its consequences for gravitational-wave astrophysics*. 2022. arXiv: `2206.10622 [astro-ph.GA]`.

[84] Martyna Chruliska *et al.* “The impact of the FMR and starburst galaxies on the (low metallicity) cosmic star formation history”. In: *Monthly Notices of the Royal Astronomical Society* 508.4 (Dec. 2021), pp. 4994–5027. DOI: `10.1093/mnras/stab2690`. arXiv: `2109.06187 [astro-ph.GA]`.

[85] Martyna Chruliska *et al. Trading oxygen for iron I: the [O/Fe] – specific star formation rate relation of galaxies*. 2023. arXiv: `2308.00023 [astro-ph.GA]`.

[86] Sidney R. Coleman and Erick J. Weinberg. “Radiative Corrections as the Origin of Spontaneous Symmetry Breaking”. In: *Phys. Rev. D* 7 (1973), pp. 1888–1910. DOI: `10.1103/PhysRevD.7.1888`.

[87] The International Pulsar Timing Array Collaboration *et al. Comparing recent PTA results on the nanohertz stochastic gravitational wave background*. 2023. arXiv: `2309.00693 [astro-ph.HE]`.

[88] The LIGO Scientific Collaboration *et al.* “Advanced LIGO”. In: *Classical and Quantum Gravity* 32.7 (Mar. 2015), p. 074001. DOI: `10.1088/0264-9381/32/7/074001`. URL: `https://dx.doi.org/10.1088/0264-9381/32/7/074001`.

[89] Michael Coughlin and Jan Harms. “Constraining the gravitational wave energy density of the Universe using Earths ring”. In: *Physical Review D* 90.4 (Aug. 2014). ISSN: 1550-2368. DOI: `10.1103/physrevd.90.042005`. URL: `http://dx.doi.org/10.1103/PhysRevD.90.042005`.

[90] Nathaniel Craig *et al.* “Ripples in Spacetime from Broken Supersymmetry”. In: *JHEP* 21 (2020), p. 184. DOI: `10.1007/JHEP02(2021)184`. arXiv: `2011.13949 [hep-ph]`.

[91] Paolo Creminelli, Alberto Nicolis, and Riccardo Rattazzi. “Holography and the electroweak phase transition”. In: *JHEP* 03 (2002), p. 051. DOI: `10.1088/1126-6708/2002/03/051`. arXiv: `hep-th/0107141`.

[92] D. Croon, T. E. Gonzalo, and G. White. “*Gravitational Waves from a Pati-Salam Phase Transition*”. In: *JHEP* 02 (2019), p. 083. DOI: `10.1007/JHEP02(2019)083`. arXiv: `1812.02747 [hep-ph]`.

[93] Djuna Croon, Verónica Sanz, and Graham White. “Model Discrimination in Gravitational Wave spectra from Dark Phase Transitions”. In: *JHEP* 08 (2018), p. 203. DOI: `10.1007/JHEP08(2018)203`. arXiv: `1806.02332 [hep-ph]`.

[94] Djuna Croon *et al.* “QCD baryogenesis”. In: *Phys. Rev. D* 101.5 (2020), p. 055042. DOI: `10.1103/PhysRevD.101.055042`. arXiv: `1911.01432 [hep-ph]`.

[95] David Curtin, Patrick Meade, and Harikrishnan Ramani. *Thermal Resummation and Phase Transitions*. 2016. arXiv: `1612.00466 [hep-ph]`.

[96] Daniel Cutting, Mark Hindmarsh, and David J. Weir. "Gravitational waves from vacuum first-order phase transitions: from the envelope to the lattice". In: *Phys. Rev. D* 97.12 (2018), p. 123513. DOI: `10.1103/PhysRevD.97.123513`. arXiv: `1802.05712 [astro-ph.CO]`.

[97] Daniel Cutting *et al.* "Gravitational waves from vacuum first-order phase transitions. II. From thin to thick walls". In: *Physical Review D* 103.2 (Jan. 2021). ISSN: 2470-0029. DOI: `10.1103/physrevd.103.023531`. URL: `http://dx.doi.org/10.1103/PhysRevD.103.023531`.

[98] Thibault Damour and Alexander Vilenkin. "Gravitational wave bursts from cusps and kinks on cosmic strings". In: *Phys. Rev. D* 64 (6 Aug. 2001), p. 064008. DOI: `10.1103/PhysRevD.64.064008`. URL: `https://link.aps.org/doi/10.1103/PhysRevD.64.064008`.

[99] Karsten Danzmann and the LISA study team. "LISA: laser interferometer space antenna for gravitational wave measurements". In: *Classical and Quantum Gravity* 13.11A (Nov. 1996), A247. DOI: `10.1088/0264-9381/13/11A/033`. URL: `https://dx.doi.org/10.1088/0264-9381/13/11A/033`.

[100] D Davis *et al.* "LIGO detector characterization in the second and third observing runs". In: *Classical and Quantum Gravity* 38.13 (June 2021), p. 135014. DOI: `10.1088/1361-6382/abfd85`. URL: `https://doi.org/10.1088/1361-6382/abfd85`.

[101] Luigi Delle Rose *et al.* "Gravitational Waves from Supercool Axions". In: *JHEP* 04 (2020), p. 025. DOI: `10.1007/JHEP04(2020)025`. arXiv: `1912.06139 [hep-ph]`.

[102] S. V. Demidov, D. S. Gorbunov, and D. V. Kirpichnikov. "*Gravitational Waves from Phase Transition in Split NMSSM*". In: *Phys. Lett. B* 779 (2018), pp. 191–194. DOI: `10.1016/j.physletb.2018.02.007`. arXiv: `1712.00087 [hep-ph]`.

[103] P. S. B. Dev *et al.* "*Gravitational Waves from First-Order Phase Transition in a Simple Axion-Like Particle Model*". In: *JCAP* 11 (2019), p. 006. DOI: `10.1088/1475-7516/2019/11/006`. arXiv: `1905.00891 [hep-ph]`.

[104] Pasquale Di Bari, Danny Marfatia, and Ye-Ling Zhou. "Gravitational waves from first-order phase transitions in Majoron models of neutrino mass". In: *JHEP* 10 (2021), p. 193. DOI: `10.1007/JHEP10(2021)193`. arXiv: `2106.00025 [hep-ph]`.

[105] Luca Di Luzio *et al.* "The landscape of QCD axion models". In: *Phys. Rept.* 870 (2020), pp. 1–117. DOI: `10.1016/j.physrep.2020.06.002`. arXiv: `2003.01100 [hep-ph]`.

[106] Savas Dimopoulos *et al.* "Testing General Relativity with Atom Interferometry". In: *Phys. Rev. Lett.* 98 (11 Mar. 2007), p. 111102. DOI: `10.1103/PhysRevLett.98.111102`. URL: `https://link.aps.org/doi/10.1103/PhysRevLett.98.111102`.

[107] Y. Dodge. "Kolmogorov–Smirnov Test". In: *The Concise Encyclopedia of Statistics*. New York, NY: Springer New York, 2008, pp. 283–287. ISBN: 978-0-387-32833-1. DOI: `10.1007/978-0-387-32833-1_214`. URL: `https://doi.org/10.1007/978-0-387-32833-1_214`.

[108] Michal Dominik *et al.* "Double compact objects II: Cosmological merger rates". In: *The Astrophysical Journal* 779.1 (Nov. 2013), p. 72. DOI: `10.1088/0004-637x/779/1/72`. URL: `https://doi.org/10.1088%2F0004-637x%2F779%2F1%2F72`.

[109] Michal Dominik *et al.* “Double Compact Objects. I. The Significance of the Common Envelope on Merger Rates”. In: *Astrophys. J.* 759.1, 52 (Nov. 2012), p. 52. DOI: 10.1088/0004-637X/759/1/52. arXiv: 1202.4901 [astro-ph.HE].

[110] G. C. Dorsch *et al.* “A Second Higgs Doublet in the Early Universe: Baryogenesis and Gravitational Waves”. In: *JCAP* 05 (2017), p. 052. DOI: 10.1088/1475-7516/2017/05/052. arXiv: 1611.05874 [hep-ph].

[111] Steve Drasco and Éanna É. Flanagan. “Detection methods for non-Gaussian gravitational wave stochastic backgrounds”. In: *Phys. Rev. D* 67 (8 Apr. 2003), p. 082003. DOI: 10.1103/PhysRevD.67.082003. URL: https://link.aps.org/doi/10.1103/PhysRevD.67.082003.

[112] Gerald V. Dunne and Hyunsoo Min. “Beyond the thin-wall approximation: Precise numerical computation of prefactors in false vacuum decay”. In: *Phys. Rev. D* 72 (12 Dec. 2005), p. 125004. DOI: 10.1103/PhysRevD.72.125004. URL: https://link.aps.org/doi/10.1103/PhysRevD.72.125004.

[113] Ruth Durrer. “The cosmic microwave background: the history of its experimental investigation and its significance for cosmology”. In: *Classical and Quantum Gravity* 32.12 (June 2015), p. 124007. DOI: 10.1088/0264-9381/32/12/124007. URL: https://dx.doi.org/10.1088/0264-9381/32/12/124007.

[114] Albert Einstein. “Die Grundlage der allgemeinen Relativitätstheorie”. In: *Annalen der Physik* 354.7 (Jan. 1916), pp. 769–822. DOI: 10.1002/andp.19163540702.

[115] Albert Einstein. “Erklarung der Perihelionbewegung der Merkur aus der allgemeinen Relativitätstheorie”. In: *Sitzungsber. preuss.Akad. Wiss* 47 (Jan. 1915), pp. 831–839.

[116] Albert Einstein. “Naherungsweise Integration der Feldgleichungen der Gravitation”. In: *Sitzungsber. preuss.Akad. Wiss* (Jan. 1916), pp. 688–696.

[117] Albert Einstein. “Über Gravitationswellen”. In: *Sitzungsber. preuss.Akad. Wiss* (Jan. 1918), pp. 154–167.

[118] John Ellis, Marek Lewicki, and José Miguel No. “Gravitational waves from first-order cosmological phase transitions: lifetime of the sound wave source”. In: *JCAP* 07 (2020), p. 050. DOI: 10.1088/1475-7516/2020/07/050. arXiv: 2003.07360 [hep-ph].

[119] John Ellis, Marek Lewicki, and José Miguel No. “On the maximal strength of a first-order electroweak phase transition and its gravitational wave signal”. In: *Journal of Cosmology and Astroparticle Physics* 2019.04 (Apr. 2019), pp. 003–003. ISSN: 1475-7516. DOI: 10.1088/1475-7516/2019/04/003. URL: http://dx.doi.org/10.1088/1475-7516/2019/04/003.

[120] John Ellis, Marek Lewicki, and Ville Vaskonen. “Updated predictions for gravitational waves produced in a strongly supercooled phase transition”. In: *JCAP* 11 (2020), p. 020. DOI: 10.1088/1475-7516/2020/11/020. arXiv: 2007.15586 [astro-ph.CO].

[121] John Ellis *et al.* “Gravitational wave energy budget in strongly supercooled phase transitions”. In: *JCAP* 06 (2019), p. 024. DOI: 10.1088/1475-7516/2019/06/024. arXiv: 1903.09642 [hep-ph].

[122] José R Espinosa *et al.* “Energy budget of cosmological first-order phase transitions”. In: *Journal of Cosmology and Astroparticle Physics* 2010.06 (June 2010), pp. 028–028. ISSN: 1475-7516. DOI: `10.1088/1475-7516/2010/06/028`. URL: `http://dx.doi.org/10.1088/1475-7516/2010/06/028`.

[123] *ETPathfinder design report*. `https://www.etpathfinder.eu/wp-content/uploads/2020/03/ETpathfinder-Design-Report.pdf`. Accessed: 2024-01-24.

[124] Matthew Evans *et al. A Horizon Study for Cosmic Explorer: Science, Observatories, and Community*. 2021. arXiv: `2109.09882 [astro-ph.IM]`.

[125] Will M. Farr *et al.* “Distinguishing spin-aligned and isotropic black hole populations with gravitational waves”. In: *Nature* 548.7668 (Aug. 2017), pp. 426–429. ISSN: 1476-4687. DOI: `10.1038/nature23453`. URL: `http://dx.doi.org/10.1038/nature23453`.

[126] Maya Fishbach, Daniel E. Holz, and Will M. Farr. “Does the Black Hole Merger Rate Evolve with Redshift?” In: *The Astrophysical Journal* 863.2 (Aug. 2018), p. L41. DOI: `10.3847/2041-8213/aad800`. URL: `https://doi.org/10.3847%2F2041-8213%2Faad800`.

[127] Maya Fishbach and Vicky Kalogera. “The Time Delay Distribution and Formation Metallicity of LIGO-Virgo’s Binary Black Holes”. In: *The Astrophysical Journal Letters* 914.2 (June 2021), p. L30. DOI: `10.3847/2041-8213/ac05c4`. URL: `https://doi.org/10.3847%2F2041-8213%2Fac05c4`.

[128] Maya Fishbach and Lieke van Son. *LIGO-Virgo-KAGRA’s Oldest Black Holes: Probing star formation at cosmic noon with GWTC-3*. 2023. arXiv: `2307.15824 [astro-ph.GA]`.

[129] Maya Fishbach *et al.* “When Are LIGO/Virgo’s Big Black Hole Mergers?” In: *The Astrophysical Journal* 912.2, 98 (May 2021), p. 98. DOI: `10.3847/1538-4357/abee11`. arXiv: `2101.07699 [astro-ph.HE]`.

[130] Éanna É. Flanagan. “Sensitivity of the Laser Interferometer Gravitational Wave Observatory to a stochastic background, and its dependence on the detector orientations”. In: *Phys. Rev. D* 48 (1993), p. 2389.

[131] Stefano Foffa *et al.* “Sensitivity of a small matter-wave interferometer to gravitational waves”. In: *Phys. Rev. D* 73 (2 Jan. 2006), p. 022001. DOI: `10.1103/PhysRevD.73.022001`. URL: `https://link.aps.org/doi/10.1103/PhysRevD.73.022001`.

[132] Bartosz Fornal. “Gravitational Wave Signatures of Lepton Universality Violation”. In: *Phys. Rev. D* 103.1 (2021), p. 015018. DOI: `10.1103/PhysRevD.103.015018`. arXiv: `2006.08802 [hep-ph]`.

[133] Bartosz Fornal and Barmak Shams Es Haghi. “Baryon and Lepton Number Violation from Gravitational Waves”. In: *Phys. Rev. D* 102.11 (2020), p. 115037. DOI: `10.1103/PhysRevD.102.115037`. arXiv: `2008.05111 [hep-ph]`.

[134] Bartosz Fornal *et al.* “Gravitational Waves from Mini-Split SUSY”. In: *Phys. Rev. D* 104 (2021), p. 115005. DOI: `10.1103/PhysRevD.104.115005`. arXiv: `2104.00747 [hep-ph]`.

[135] Chris L. Fryer *et al.* “Compact remnant mass function: dependence on the explosion mechanism and metallicity”. In: *The Astrophysical Journal* 749.1 (Mar. 2012), p. 91. DOI: `10.1088/0004-637x/749/1/91`. URL: `https://doi.org/10.1088%2F0004-637x%2F749%2F1%2F91`.

[136] Davide Gerosa *et al.* “Spin orientations of merging black holes formed from the evolution of stellar binaries”. In: *Physical Review D* 98.8 (Oct. 2018). ISSN: 2470-0029. DOI: `10.1103/physrevd.98.084036`. URL: `http://dx.doi.org/10.1103/PhysRevD.98.084036`.

[137] Felix Giese, Thomas Konstandin, and Jorinde van de Vis. “Model-independent energy budget of cosmological first-order phase transitionsA sound argument to go beyond the bag model”. In: *Journal of Cosmology and Astroparticle Physics* 2020.07 (July 2020), pp. 057–057. ISSN: 1475-7516. DOI: `10.1088/1475-7516/2020/07/057`. URL: `http://dx.doi.org/10.1088/1475-7516/2020/07/057`.

[138] Oliver Gould, Satumaaria Sukuvaara, and David Weir. “Vacuum bubble collisions: From microphysics to gravitational waves”. In: *Phys. Rev. D* 104.7 (2021), p. 075039. DOI: `10.1103/PhysRevD.104.075039`. arXiv: `2107.05657 [astro-ph.CO]`.

[139] A. Greljo, T. Opferkuch, and B. A. Stefanek. “*Gravitational Imprints of Flavor Hierarchies*”. In: *Phys. Rev. Lett.* 124.17 (2020), p. 171802. DOI: `10.1103/PhysRevLett.124.171802`. arXiv: `1910.02014 [hep-ph]`.

[140] C. Grojean and G. Servant. “*Gravitational Waves from Phase Transitions at the Electroweak Scale and Beyond*”. In: *Phys. Rev. D* 75 (2007), p. 043507. DOI: `10.1103/PhysRevD.75.043507`. arXiv: `hep-ph/0607107`.

[141] Victor Guada, Miha Nemevek, and Matev Pintar. “FindBounce: Package for multi-field bounce actions”. In: *Computer Physics Communications* 256 (Nov. 2020), p. 107480. ISSN: 0010-4655. DOI: `10.1016/j.cpc.2020.107480`. URL: `http://dx.doi.org/10.1016/j.cpc.2020.107480`.

[142] Huai-Ke Guo *et al.* “Phase Transitions in an Expanding Universe: Stochastic Gravitational Waves in Standard and Non-Standard Histories”. In: *JCAP* 01 (2021), p. 001. DOI: `10.1088/1475-7516/2021/01/001`. arXiv: `2007.08537 [hep-ph]`.

[143] Alan H. Guth and Erick J. Weinberg. “Cosmological consequences of a first-order phase transition in the SU_5 grand unified model”. In: *Phys. Rev. D* 23 (4 Feb. 1981), pp. 876–885. DOI: `10.1103/PhysRevD.23.876`. URL: `https://link.aps.org/doi/10.1103/PhysRevD.23.876`.

[144] E. Hall *et al.* “*Baryogenesis From a Dark First-Order Phase Transition*”. In: *JHEP* 04 (2020), p. 042. DOI: `10.1007/JHEP04(2020)042`. arXiv: `1910.08068 [hep-ph]`.

[145] Thomas Hambye, Alessandro Strumia, and Daniele Teresi. “Super-cool Dark Matter”. In: *JHEP* 08 (2018), p. 188. DOI: `10.1007/JHEP08(2018)188`. arXiv: `1805.01473 [hep-ph]`.

[146] Benedict von Harling and Geraldine Servant. “QCD-induced Electroweak Phase Transition”. In: *JHEP* 01 (2018), p. 159. DOI: `10.1007/JHEP01(2018)159`. arXiv: `1711.11554 [hep-ph]`.

[147] Jan Harms *et al.* “Lunar Gravitational-wave Antenna”. In: *The Astrophysical Journal* 910.1 (Mar. 2021), p. 1. DOI: 10.3847/1538-4357/abe5a7. URL: https://doi.org/10.3847/1538-4357/abe5a7.

[148] T. Hasegawa, N. Okada, and O. Seto. “*Gravitational Waves from the Minimal Gauged* $U(1)_{B-L}$ *Model*”. In: *Phys. Rev. D* 99.9 (2019), p. 095039. DOI: 10.1103/PhysRevD.99.095039. arXiv: 1904.03020 [hep-ph].

[149] R W Hellings and G S Downs. “Upper limits on the isotropic gravitational radiation background from pulsar timing analysis”. In: *Astrophys. J., Lett. Ed.; (United States)* 265 (Feb. 1983). DOI: 10.1086/183954. URL: https://www.osti.gov/biblio/6268184.

[150] Alexander J. Helmboldt, Jisuke Kubo, and Susan van der Woude. “Observational prospects for gravitational waves from hidden or dark chiral phase transitions”. In: *Phys. Rev. D* 100.5 (2019), p. 055025. DOI: 10.1103/PhysRevD.100.055025. arXiv: 1904.07891 [hep-ph].

[151] M. Hindmarsh *et al.* “*Gravitational Waves from the Sound of a First Order Phase Transition*”. In: *Phys. Rev. Lett.* 112 (2014), p. 041301. DOI: 10.1103/PhysRevLett.112.041301. arXiv: 1304.2433 [hep-ph].

[152] Mark Hindmarsh and Mulham Hijazi. “Gravitational waves from first order cosmological phase transitions in the Sound Shell Model”. In: *Journal of Cosmology and Astroparticle Physics* 2019.12 (Dec. 2019), pp. 062–062. ISSN: 1475-7516. DOI: 10.1088/1475-7516/2019/12/062. URL: http://dx.doi.org/10.1088/1475-7516/2019/12/062.

[153] Mark Hindmarsh *et al.* “Numerical simulations of acoustically generated gravitational waves at a first order phase transition”. In: *Physical Review D* 92.12 (Dec. 2015). ISSN: 1550-2368. DOI: 10.1103/physrevd.92.123009. URL: http://dx.doi.org/10.1103/PhysRevD.92.123009.

[154] G Hobbs. “The Parkes Pulsar Timing Array”. In: *Classical and Quantum Gravity* 30.22 (Nov. 2013), p. 224007. ISSN: 1361-6382. DOI: 10.1088/0264-9381/30/22/224007. URL: http://dx.doi.org/10.1088/0264-9381/30/22/224007.

[155] G Hobbs *et al.* “The International Pulsar Timing Array project: using pulsars as a gravitational wave detector”. In: *Classical and Quantum Gravity* 27.8 (Apr. 2010), p. 084013. ISSN: 1361-6382. DOI: 10.1088/0264-9381/27/8/084013. URL: http://dx.doi.org/10.1088/0264-9381/27/8/084013.

[156] Anson Hook. *TASI Lectures on the Strong CP Problem and Axions*. 2023. arXiv: 1812.02669 [hep-ph].

[157] Wei-Chih Huang, Francesco Sannino, and Zhi-Wei Wang. “Gravitational Waves from Pati-Salam Dynamics”. In: *Phys. Rev. D* 102.9 (2020), p. 095025. DOI: 10.1103/PhysRevD.102.095025. arXiv: 2004.02332 [hep-ph].

[158] Wei-Chih Huang *et al.* “Testing the dark SU(N) Yang-Mills theory confined landscape: From the lattice to gravitational waves”. In: *Phys. Rev. D* 104.3 (2021), p. 035005. DOI: 10.1103/PhysRevD.104.035005. arXiv: 2012.11614 [hep-ph].

[159] S. J. Huber and T. Konstandin. “*Gravitational Wave Production by Collisions: More Bubbles*”. In: *JCAP* 09 (2008), p. 022. DOI: 10.1088/1475-7516/2008/09/022. arXiv: 0806.1828 [hep-ph].

[160] R A Hulse and J H Taylor. “Discovery of a pulsar in a binary system”. In: *Astrophys. J., Lett.* 195.2 (Jan. 1975), pp. 51–53. DOI: 10.1086/181708. URL: https://www.osti.gov/biblio/4215694.

[161] B. Iyer *et al.* “LIGO-India, proposal of the consortium for Indian initiative in gravitational-wave observations (IndIGO)”. In: (2011). URL: https://dcc.ligo.org/LIGO-M1100296/public.

[162] Kamiel Janssens. “Prospects for an isotropic gravitational wave background detection with Earth-based interferometric detectors and the threat of correlated noise”. In: *57th Rencontres de Moriond on Gravitation*. May 2023. arXiv: 2305.02694 [gr-qc].

[163] Kamiel Janssens *et al.* “Impact of correlated seismic and correlated Newtonian noise on the Einstein Telescope”. In: *Physical Review D* 106.4 (Aug. 2022). ISSN: 2470-0029. DOI: 10.1103/physrevd.106.042008. URL: http://dx.doi.org/10.1103/PhysRevD.106.042008.

[164] Ryusuke Jinno and Masahiro Takimoto. “Gravitational waves from bubble dynamics: beyond the envelope”. In: *Journal of Cosmology and Astroparticle Physics* 2019.01 (Jan. 2019), pp. 060–060. ISSN: 1475-7516. DOI: 10.1088/1475-7516/2019/01/060. URL: http://dx.doi.org/10.1088/1475-7516/2019/01/060.

[165] Ryusuke Jinno and Masahiro Takimoto. “Probing a classically conformal B-L model with gravitational waves”. In: *Phys. Rev. D* 95.1 (2017), p. 015020. DOI: 10.1103/PhysRevD.95.015020. arXiv: 1604.05035 [hep-ph].

[166] Ryusuke Jinno *et al.* “Gravitational waves from first-order phase transitions: Ultra-supercooled transitions and the fate of relativistic shocks”. In: *JCAP* 10 (2019), p. 033. DOI: 10.1088/1475-7516/2019/10/033. arXiv: 1905.00899 [astro-ph.CO].

[167] M. Kamionkowski, A. Kosowsky, and M. S. Turner. “*Gravitational Radiation from First Order Phase Transitions*”. In: *Phys. Rev. D* 49 (1994), pp. 2837–2851. DOI: 10.1103/PhysRevD.49.2837. arXiv: astro-ph/9310044.

[168] Andrey Katz and Antonio Riotto. “Baryogenesis and Gravitational Waves from Runaway Bubble Collisions”. In: *JCAP* 11 (2016), p. 011. DOI: 10.1088/1475-7516/2016/11/011. arXiv: 1608.00583 [hep-ph].

[169] Seiji Kawamura *et al.* “Current status of space gravitational wave antenna DECIGO and B-DECIGO”. In: *Progress of Theoretical and Experimental Physics* 2021.5 (Feb. 2021), 05A105. ISSN: 2050-3911. DOI: 10.1093/ptep/ptab019. eprint: https://academic.oup.com/ptep/article-pdf/2021/5/05A105/38109685/ptab019.pdf. URL: https://doi.org/10.1093/ptep/ptab019.

[170] A. Khan *et al.* “The lunar moho and the internal structure of the Moon: A geophysical perspective”. In: *Tectonophysics* 609 (2013). Moho: 100 years after Andrija Mohorovicic, pp. 331–352. ISSN: 0040-1951. DOI: https://doi.org/10.1016/j.tecto.2013.02.024. URL: https://www.sciencedirect.com/science/article/pii/S0040195113001236.

[171] Edward W. Kolb and Michael S. Turner. *The Early Universe*. Vol. 69. 1990. ISBN: 978-0-201-62674-2. DOI: 10.1201/9780429492860.

[172] Thomas Konstandin and Geraldine Servant. "Cosmological Consequences of Nearly Conformal Dynamics at the TeV scale". In: *JCAP* 12 (2011), p. 009. DOI: 10.1088/1475-7516/2011/12/009. arXiv: 1104.4791 [hep-ph].

[173] A. Kosowsky, M. S. Turner, and R. Watkins. "*Gravitational Radiation from Colliding Vacuum Bubbles*". In: *Phys. Rev. D* 45 (1992), pp. 4514–4535. DOI: 10.1103/PhysRevD.45.4514.

[174] N. Langer and C. A. Norman. "On the Collapsar Model of Long Gamma-Ray Bursts:Constraints from Cosmic Metallicity Evolution". In: *Astrophys. J. Lett.* 638.2 (Feb. 2006), pp. L63–L66. DOI: 10.1086/500363. arXiv: astro-ph/0512271 [astro-ph].

[175] Paul D. Lasky *et al.* "Gravitational-Wave Cosmology across 29 Decades in Frequency". In: *Phys. Rev. X* 6 (1 Mar. 2016), p. 011035. DOI: 10.1103/PhysRevX.6.011035. URL: https://link.aps.org/doi/10.1103/PhysRevX.6.011035.

[176] Jessica Lawrence *et al.* "A stochastic search for intermittent gravitational-wave backgrounds". In: *Physical Review D* 107.10 (May 2023). DOI: 10.1103/physrevd.107.103026. URL: https://doi.org/10.1103%2Fphysrevd.107.103026.

[177] K. J. Lee. "Prospects of Gravitational Wave Detection Using Pulsar Timing Array for Chinese Future Telescopes". In: *Frontiers in Radio Astronomy and FAST Early Sciences Symposium 2015*. Ed. by L. Qain and D. Li. Vol. 502. Astronomical Society of the Pacific Conference Series. Feb. 2016, p. 19.

[178] Leonard Lehoucq *et al.* *Astrophysical Uncertainties in the Gravitational-Wave Background from Stellar-Mass Compact Binary Mergers*. 2023. arXiv: 2306.09861 [astro-ph.HE].

[179] L. Lentati *et al.* "European Pulsar Timing Array limits on an isotropic stochastic gravitational-wave background". In: *Monthly Notices of the Royal Astronomical Society* 453.3 (Aug. 2015), pp. 2577–2599. ISSN: 1365-2966. DOI: 10.1093/mnras/stv1538. URL: http://dx.doi.org/10.1093/mnras/stv1538.

[180] Marek Lewicki, Oriol Pujolàs, and Ville Vaskonen. "Escape from supercooling with or without bubbles: gravitational wave signatures". In: *Eur. Phys. J. C* 81.9 (2021), p. 857. DOI: 10.1140/epjc/s10052-021-09669-6. arXiv: 2106.09706 [astro-ph.CO].

[181] Marek Lewicki and Ville Vaskonen. "Gravitational waves from colliding vacuum bubbles in gauge theories". In: *The European Physical Journal C* 81.5 (May 2021). ISSN: 1434-6052. DOI: 10.1140/epjc/s10052-021-09232-3. URL: http://dx.doi.org/10.1140/epjc/s10052-021-09232-3.

[182] LIGO Scientific Collaboration, Gregory M Harry, *et al.* "Advanced LIGO: the next generation of gravitational wave detectors". In: *Classical and Quantum Gravity* 27.8 (Apr. 2010), p. 084006. DOI: 10.1088/0264-9381/27/8/084006. URL: https://dx.doi.org/10.1088/0264-9381/27/8/084006.

[183] A. D. Linde. "*Decay of the False Vacuum at Finite Temperature*". In: *Nuclear Physics B* 216.2 (1983), pp. 421–445. ISSN: 0550-3213. DOI: https://doi.org/10.1016/0550-3213(83)90293-6. URL: http://www.sciencedirect.com/science/article/pii/0550321383902936.

[184] Camille Liotine *et al.* “The Missing Link between Black Holes in High-mass X-Ray Binaries and Gravitational-wave Sources: Observational Selection Effects”. In: *The Astrophysical Journal* 946.1 (Mar. 2023), p. 4. DOI: 10.3847/1538-4357/acb8b2. URL: https://doi.org/10.3847%2F1538-4357%2Facb8b2.

[185] Andrea N Lommen. “Pulsar timing arrays: the promise of gravitational wave detection”. In: *Reports on Progress in Physics* 78.12 (Nov. 2015), p. 124901. DOI: 10.1088/0034-4885/78/12/124901. URL: https://doi.org/10.1088/0034-4885/78/12/124901.

[186] Thomas J. Loredo. “Accounting for Source Uncertainties in Analyses of Astronomical Survey Data”. In: *AIP Conference Proceedings* 735.1 (Nov. 2004), pp. 195–206. ISSN: 0094-243X. DOI: 10.1063/1.1835214. eprint: https://pubs.aip.org/aip/acp/article-pdf/735/1/195/11702739/195_1_online.pdf. URL: https://doi.org/10.1063/1.1835214.

[187] Jun Luo *et al.* “TianQin: a space-borne gravitational wave detector”. In: *Classical and Quantum Gravity* 33.3 (Jan. 2016), p. 035010. DOI: 10.1088/0264-9381/33/3/035010. URL: https://dx.doi.org/10.1088/0264-9381/33/3/035010.

[188] Piero Madau and Mark Dickinson. “Cosmic Star-Formation History”. In: *Annual Review of Astronomy and Astrophysics* 52.1 (2014), pp. 415–486. DOI: 10.1146/annurev-astro-081811-125615. eprint: https://doi.org/10.1146/annurev-astro-081811-125615. URL: https://doi.org/10.1146/annurev-astro-081811-125615.

[189] Piero Madau and Tassos Fragos. “Radiation Backgrounds at Cosmic Dawn: X-Rays from Compact Binaries”. In: *The Astrophysical Journal* 840.1 (May 2017), p. 39. DOI: 10.3847/1538-4357/aa6af9. URL: https://doi.org/10.3847%2F1538-4357%2Faa6af9.

[190] M. Maggiore. *Gravitational Waves: Volume 1: Theory and Experiments*. Gravitational Waves. OUP Oxford, 2008. ISBN: 9780198570745. URL: https://books.google.be/books?id=AqVpQgAACAAJ.

[191] Michele Maggiore. *Gravitational Waves. Vol. 2: Astrophysics and Cosmology*. Oxford University Press, Mar. 2018. ISBN: 978-0-19-857089-9.

[192] Michele Maggiore *et al.* “Science case for the Einstein telescope”. In: *Journal of Cosmology and Astroparticle Physics* 2020.03 (Mar. 2020), pp. 050–050. ISSN: 1475-7516. DOI: 10.1088/1475-7516/2020/03/050. URL: http://dx.doi.org/10.1088/1475-7516/2020/03/050.

[193] Ilya Mandel, Will M Farr, and Jonathan R Gair. “Extracting distribution parameters from multiple uncertain observations with selection biases”. In: *Monthly Notices of the Royal Astronomical Society* 486.1 (Mar. 2019), pp. 1086–1093. ISSN: 0035-8711. DOI: 10.1093/mnras/stz896. eprint: https://academic.oup.com/mnras/article-pdf/486/1/1086/28390969/stz896.pdf. URL: https://doi.org/10.1093/mnras/stz896.

[194] Michela Mapelli *et al.* “The properties of merging black holes and neutron stars across cosmic time”. In: *Monthly Notices of the Royal Astronomical Society* 487.1 (Apr. 2019), pp. 2–13. DOI: 10.1093/mnras/stz1150. URL: https://doi.org/10.1093%2Fmnras%2Fstz1150.

[195] Katarina Martinovic *et al.* "Searching for parity violation with the LIGO-Virgo-KAGRA network". In: *Phys. Rev. D* 104.8 (2021), p. L081101. DOI: 10.1103/PhysRevD.104.L081101. arXiv: 2103.06718 [gr-qc].

[196] Carlo Marzo, Luca Marzola, and Ville Vaskonen. "Phase transition and vacuum stability in the classically conformal BL model". In: *Eur. Phys. J. C* 79.7 (2019), p. 601. DOI: 10.1140/epjc/s10052-019-7076-x. arXiv: 1811.11169 [hep-ph].

[197] Andrew Matas and Joseph D. Romano. "Frequentist versus Bayesian analyses: Cross-correlation as an approximate sufficient statistic for LIGO-Virgo stochastic background searches". In: *Phys. Rev. D* 103 (6 Mar. 2021), p. 062003. DOI: 10.1103/PhysRevD.103.062003. URL: https://link.aps.org/doi/10.1103/PhysRevD.103.062003.

[198] Maura A. McLaughlin. "The North American Nanohertz Observatory for Gravitational Waves". In: *Class. Quant. Grav.* 30 (2013), p. 224008. DOI: 10.1088/0264-9381/30/22/224008. arXiv: 1310.0758 [astro-ph.IM].

[199] Duncan Meacher *et al.* "Mock data and science challenge for detecting an astrophysical stochastic gravitational-wave background with Advanced LIGO and Advanced Virgo". In: *Phys. Rev. D* 92.6, 063002 (Sept. 2015), p. 063002. DOI: 10.1103/PhysRevD.92.063002. arXiv: 1506.06744 [astro-ph.HE].

[200] Ariel Megevand and Federico Agustin Membiela. "Gravitational waves from bubble walls". In: *Journal of Cosmology and Astroparticle Physics* 2021.10 (Oct. 2021), p. 073. DOI: 10.1088/1475-7516/2021/10/073. URL: https://dx.doi.org/10.1088/1475-7516/2021/10/073.

[201] Jianwei Mei *et al.* "The TianQin project: Current progress on science and technology". In: *Progress of Theoretical and Experimental Physics* 2021.5 (Aug. 2020), 05A107. ISSN: 2050-3911. DOI: 10.1093/ptep/ptaa114. eprint: https://academic.oup.com/ptep/article-pdf/2021/5/05A107/37953035/ptaa114.pdf. URL: https://doi.org/10.1093/ptep/ptaa114.

[202] Andrew L. Miller. *Recent results from continuous gravitational wave searches using data from LIGO/Virgo/KAGRA's third observing run*. 2023. arXiv: 2305.15185 [gr-qc].

[203] Suvodip Mukherjee and Azadeh Moradinezhad Dizgah. "Toward a Precision Measurement of Binary Black Holes Formation Channels Using Gravitational Waves and Emission Lines". In: *The Astrophysical Journal Letters* 937.2 (Sept. 2022), p. L27. DOI: 10.3847/2041-8213/ac903b. URL: https://doi.org/10.3847%2F2041-8213%2Fac903b.

[204] Germano Nardini, Mariano Quiros, and Andrea Wulzer. "A Confining Strong First-Order Electroweak Phase Transition". In: *JHEP* 09 (2007), p. 077. DOI: 10.1088/1126-6708/2007/09/077. arXiv: 0706.3388 [hep-ph].

[205] Yousef Abou El-Neaj *et al.* "AEDGE: Atomic Experiment for Dark Matter and Gravity Exploration in Space". In: *EPJ Quantum Technology* 7.1 (Mar. 2020). ISSN: 2196-0763. DOI: 10.1140/epjqt/s40507-020-0080-0. URL: http://dx.doi.org/10.1140/epjqt/s40507-020-0080-0.

[206] N. Okada and O. Seto. "*Probing the Seesaw Scale with Gravitational Waves*". In: *Phys. Rev. D* 98.6 (2018), p. 063532. DOI: 10.1103/PhysRevD.98.063532. arXiv: 1807.00336 [hep-ph].

[207] Nobuchika Okada, Osamu Seto, and Hikaru Uchida. “Gravitational waves from breaking of an extra $U(1)$ in $SO(10)$ grand unification”. In: *PTEP* 2021.3 (2021), 033B01. DOI: 10.1093/ptep/ptab003. arXiv: 2006.01406 [hep-ph].

[208] Luca Pagano, Laura Salvati, and Alessandro Melchiorri. “New constraints on primordial gravitational waves from Planck 2015”. In: *Physics Letters B* 760 (2016), pp. 823–825. ISSN: 0370-2693. DOI: https://doi.org/10.1016/j.physletb.2016.07.078. URL: https://www.sciencedirect.com/science/article/pii/S0370269316304191.

[209] Ashis Paul *et al.* “The Indian Pulsar Timing Array (InPTA)”. In: *2019 URSI Asia-Pacific Radio Science Conference (AP-RASC)*. 2019, pp. 1–1. DOI: 10.23919/URSIAP-RASC.2019.8738505.

[210] Du Phan, Neeraj Pradhan, and Martin Jankowiak. “Composable Effects for Flexible and Accelerated Probabilistic Programming in NumPyro”. In: *arXiv preprint arXiv:1912.11554* (2019).

[211] E. S. Phinney. *A Practical Theorem on Gravitational Wave Backgrounds*. 2001. arXiv: astro-ph/0108028 [astro-ph].

[212] Planck Collaboration *et al.* “Planck 2015 results - XIII. Cosmological parameters”. In: *A&A* 594 (2016), A13. DOI: 10.1051/0004-6361/201525830. URL: https://doi.org/10.1051/0004-6361/201525830.

[213] *Press release. NobelPrize.org. Nobel Prize Outreach AB 2024.* https://www.nobelprize.org/prizes/physics/1993/summary/. Accessed: 2024-01-31.

[214] Tomislav Prokopec, Jonas Rezacek, and Bogumia wieewska. “Gravitational waves from conformal symmetry breaking”. In: *JCAP* 02 (2019), p. 009. DOI: 10.1088/1475-7516/2019/02/009. arXiv: 1809.11129 [hep-ph].

[215] M Punturo *et al.* “The Einstein Telescope: a third-generation gravitational wave observatory”. In: *Classical and Quantum Gravity* 27.19 (Sept. 2010), p. 194002. DOI: 10.1088/0264-9381/27/19/194002. URL: https://dx.doi.org/10.1088/0264-9381/27/19/194002.

[216] Mariano Quiros. *Finite temperature field theory and phase transitions*. 1999. arXiv: hep-ph/9901312 [hep-ph].

[217] Lisa Randall and Geraldine Servant. “Gravitational waves from warped spacetime”. In: *JHEP* 05 (2007), p. 054. DOI: 10.1088/1126-6708/2007/05/054. arXiv: hep-ph/0607158.

[218] Daniel J. Reardon *et al.* “The Gravitational-wave Background Null Hypothesis: Characterizing Noise in Millisecond Pulsar Arrival Times with the Parkes Pulsar Timing Array”. In: *The Astrophysical Journal Letters* 951.1 (June 2023), p. L7. DOI: 10.3847/2041-8213/acdd03. URL: https://dx.doi.org/10.3847/2041-8213/acdd03.

[219] Tania Regimbau. “The astrophysical gravitational wave stochastic background”. In: *Research in Astronomy and Astrophysics* 11.4 (Apr. 2011), p. 369. DOI: 10.1088/1674-4527/11/4/001. URL: https://dx.doi.org/10.1088/1674-4527/11/4/001.

[220] David Reitze *et al.* “Cosmic Explorer: The U.S. Contribution to Gravitational-Wave Astronomy beyond LIGO”. In: *Bulletin of the AAS* 51.7 (Sept. 2019). https://baas.aas.org/pub/2020n7i035.

[221] Nick van Remortel, Kamiel Janssens, and Kevin Turbang. "Stochastic gravitational wave background: Methods and implications". In: *Progress in Particle and Nuclear Physics* 128 (Jan. 2023), p. 104003. DOI: `10.1016/j.ppnp.2022.104003`. URL: `https://doi.org/10.1016%2Fj.ppnp.2022.104003`.

[222] Arianna I. Renzini *et al.* "pygwb: A Python-based Library for Gravitational-wave Background Searches". In: *Astrophys. J.* 952.1 (2023), p. 25. DOI: `10.3847/1538-4357/acd775`. arXiv: `2303.15696 [gr-qc]`.

[223] Arianna I. Renzini *et al.* "pygwb: a Python-based library for gravitational-wave background searches". In: *Journal of Open Source Software* 9.94 (2024), p. 5454. DOI: `10.21105/joss.05454`. URL: `https://doi.org/10.21105/joss.05454`.

[224] Arianna I. Renzini *et al.* "Stochastic Gravitational-Wave Backgrounds: Current Detection Efforts and Future Prospects". In: *Galaxies* 10.1 (2022). ISSN: 2075-4434. DOI: `10.3390/galaxies10010034`. URL: `https://www.mdpi.com/2075-4434/10/1/34`.

[225] Rich Abbott *et al.* "Open data from the first and second observing runs of Advanced LIGO and Advanced Virgo". In: *SoftwareX* 13 (Jan. 2021), p. 100658. DOI: `10.1016/j.softx.2021.100658`. URL: `https://doi.org/10.10%162Fj.softx.2021.100658`.

[226] K. Riles. "Gravitational waves: Sources, detectors and searches". In: *Progress in Particle and Nuclear Physics* 68 (2013), pp. 1–54. ISSN: 0146-6410. DOI: `https://doi.org/10.1016/j.ppnp.2012.08.001`. URL: `https://www.sciencedirect.com/science/article/pii/S0146641012001093`.

[227] Jeff Riley and Ilya Mandel. "Surrogate Forward Models for Population Inference on Compact Binary Mergers". In: *The Astrophysical Journal* 950.2 (June 2023), p. 80. DOI: `10.3847/1538-4357/accf90`. URL: `https://doi.org/10.3847%2F1538-4357%2Faccf90`.

[228] Carl L. Rodriguez *et al.* "Illuminating black hole binary formation channels with spins in Advanced LIGO". In: *The Astrophysical Journal Letters* 832.1 (Nov. 2016), p. L2. ISSN: 2041-8213. DOI: `10.3847/2041-8205/832/1/l2`. URL: `http://dx.doi.org/10.3847/2041-8205/832/1/L2`.

[229] Jameson Graef Rollins *et al. pygwinc: Gravitational Wave Interferometer Noise Calculator*. Astrophysics Source Code Library, record ascl:2007.020. July 2020. URL: `https://ascl.net/2007.020`.

[230] Joseph D. Romano and Neil. J. Cornish. "Detection methods for stochastic gravitational-wave backgrounds: a unified treatment". In: *Living Reviews in Relativity* 20.1 (Apr. 2017), p. 2. ISSN: 1433-8351. DOI: `10.1007/s41114-017-0004-1`. URL: `https://doi.org/10.1007/s41114-017-0004-1`.

[231] Alba Romero *et al.* "Implications for First-Order Cosmological Phase Transitions from the Third LIGO-Virgo Observing Run". In: *Physical Review Letters* 126.15 (Apr. 2021). DOI: `10.1103/physrevlett.126.151301`. URL: `https://doi.org/10.1103%2Fphysrevlett.126.151301`.

[232] Alba Romero-Rodrguez *et al.* "Search for a Scalar Induced Stochastic Gravitational Wave Background in the Third LIGO-Virgo Observing Run". In: *Phys. Rev. Lett.* 128 (5 Feb. 2022), p. 051301. DOI: `10.1103/PhysRevLett.128.051301`. URL: `https://link.aps.org/doi/10.1103/PhysRevLett.128.051301`.

[233] G. Rosi *et al.* “Quantum test of the equivalence principle for atoms in coherent superposition of internal energy states”. In: *Nature Communications* 8.1 (June 2017). ISSN: 2041-1723. DOI: 10.1038/ncomms15529. URL: http://dx.doi.org/10.1038/ncomms15529.

[234] M Saleem *et al.* “The science case for LIGO-India”. In: *Classical and Quantum Gravity* 39.2 (Dec. 2021), p. 025004. ISSN: 1361-6382. DOI: 10.1088/1361-6382/ac3b99. URL: http://dx.doi.org/10.1088/1361-6382/ac3b99.

[235] Johan Samsing and Daniel J D’Orazio. “Black Hole Mergers From Globular Clusters Observable by LISA I: Eccentric Sources Originating From Relativistic N-body Dynamics”. In: *Monthly Notices of the Royal Astronomical Society* 481.4 (Aug. 2018), pp. 5445–5450. DOI: 10.1093/mnras/sty2334. URL: https://doi.org/10.1093%2Fmnras%2Fsty2334.

[236] Filippo Santoliquido *et al.* “The Cosmic Merger Rate Density Evolution of Compact Binaries Formed in Young Star Clusters and in Isolated Binaries”. In: *The Astrophysical Journal* 898.2 (Aug. 2020), p. 152. DOI: 10.3847/1538-4357/ab9b78. URL: https://doi.org/10.3847%2F1538-4357%2Fab9b78.

[237] B. S. Sathyaprakash and Bernard F. Schutz. “Physics, Astrophysics and Cosmology with Gravitational Waves”. In: *Living Reviews in Relativity* 12.1 (Mar. 2009). ISSN: 1433-8351. DOI: 10.12942/lrr-2009-2. URL: http://dx.doi.org/10.12942/lrr-2009-2.

[238] Peter R Saulson. *Fundamentals of interferometric gravitational wave detectors; 1st ed.* Singapore: World Scientific, 1994. URL: https://cds.cern.ch/record/262163.

[239] P. Schwaller. “*Gravitational Waves from a Dark Phase Transition*”. In: *Phys. Rev. Lett.* 115.18 (2015), p. 181101. DOI: 10.1103/PhysRevLett.115.181101. arXiv: 1504.07263 [hep-ph].

[240] Clemente Smarra *et al.* “Second Data Release from the European Pulsar Timing Array: Challenging the Ultralight Dark Matter Paradigm”. In: *Phys. Rev. Lett.* 131 (17 Oct. 2023), p. 171001. DOI: 10.1103/PhysRevLett.131.171001. URL: https://link.aps.org/doi/10.1103/PhysRevLett.131.171001.

[241] Rory Smith and Eric Thrane. “Optimal Search for an Astrophysical Gravitational-Wave Background”. In: *Phys. Rev. X* 8 (2 Apr. 2018), p. 021019. DOI: 10.1103/PhysRevX.8.021019. URL: https://link.aps.org/doi/10.1103/PhysRevX.8.021019.

[242] Tristan L. Smith, Elena Pierpaoli, and Marc Kamionkowski. “New Cosmic Microwave Background Constraint to Primordial Gravitational Waves”. In: *Phys. Rev. Lett.* 97 (2 July 2006), p. 021301. DOI: 10.1103/PhysRevLett.97.021301. URL: https://link.aps.org/doi/10.1103/PhysRevLett.97.021301.

[243] L. A. C. van Son *et al.* “The Locations of Features in the Mass Distribution of Merging Binary Black Holes Are Robust against Uncertainties in the Metallicity-dependent Cosmic Star Formation History”. In: *The Astrophysical Journal* 948.2 (May 2023), p. 105. ISSN: 1538-4357. DOI: 10.3847/1538-4357/acbf51. URL: http://dx.doi.org/10.3847/1538-4357/acbf51.

[244] L. A. C. van Son *et al.* “The Redshift Evolution of the Binary Black Hole Merger Rate: A Weighty Matter”. In: *The Astrophysical Journal* 931.1 (May 2022), p. 17. DOI: 10.3847/1538-4357/ac64a3. URL: https://doi.org/10.3847%2F1538-4357%2Fac64a3.

[245] Joshua S Speagle. “dynesty: a dynamic nested sampling package for estimating Bayesian posteriors and evidences”. In: *Monthly Notices of the Royal Astronomical Society* 493.3 (Feb. 2020), pp. 3132–3158. ISSN: 1365-2966. DOI: 10.1093/mnras/staa278. URL: http://dx.doi.org/10.1093/mnras/staa278.

[246] R. Spiewak *et al.* “The MeerTime Pulsar Timing Array: A census of emission properties and timing potential”. In: *Publications of the Astronomical Society of Australia* 39 (2022), e027. DOI: 10.1017/pasa.2022.19.

[247] Colm Talbot and Eric Thrane. “Measuring the Binary Black Hole Mass Spectrum with an Astrophysically Motivated Parameterization”. In: *The Astrophysical Journal* 856.2 (Apr. 2018), p. 173. DOI: 10.3847/1538-4357/aab34c. URL: https://doi.org/10.3847%2F1538-4357%2Faab34c.

[248] J. H. Taylor and J. M. Weisberg. “A new test of general relativity - Gravitational radiation and the binary pulsar PSR 1913+16”. In: *APJ* 253 (Feb. 1982), pp. 908–920. DOI: 10.1086/159690.

[249] Stephen R. Taylor and Davide Gerosa. “Mining gravitational-wave catalogs to understand binary stellar evolution: A new hierarchical Bayesian framework”. In: *Phys. Rev. D* 98 (8 Oct. 2018), p. 083017. DOI: 10.1103/PhysRevD.98.083017. URL: https://link.aps.org/doi/10.1103/PhysRevD.98.083017.

[250] Eric Thrane and Joseph D. Romano. “Sensitivity curves for searches for gravitational-wave backgrounds”. In: *Physical Review D* 88.12 (Dec. 2013). ISSN: 1550-2368. DOI: 10.1103/physrevd.88.124032. URL: http://dx.doi.org/10.1103/PhysRevD.88.124032.

[251] Eric Thrane and Colm Talbot. “An introduction to Bayesian inference in gravitational-wave astronomy: Parameter estimation, model selection, and hierarchical models”. In: *Publications of the Astronomical Society of Australia* 36 (2019). ISSN: 1448-6083. DOI: 10.1017/pasa.2019.2. URL: http://dx.doi.org/10.1017/pasa.2019.2.

[252] G M Tino and F Vetrano. “Is it possible to detect gravitational waves with atom interferometers?” In: *Classical and Quantum Gravity* 24.9 (Apr. 2007), p. 2167. DOI: 10.1088/0264-9381/24/9/001. URL: https://dx.doi.org/10.1088/0264-9381/24/9/001.

[253] Kevin Turbang *et al.* “The Metallicity Dependence and Evolutionary Times of Merging Binary Black Holes: Combined Constraints from Individual Gravitational-wave Detections and the Stochastic Background”. In: *Astrophys. J.* 967.2 (2024), p. 142. DOI: 10.3847/1538-4357/ad3d5c. arXiv: 2310.17625 [astro-ph.HE].

[254] Michele Vallisneri *et al.* “The LIGO Open Science Center”. In: *Journal of Physics: Conference Series* 610.1 (Apr. 2015), p. 012021. DOI: 10.1088/1742-6596/610/1/012021. URL: https://dx.doi.org/10.1088/1742-6596/610/1/012021.

[255] Elisabeth Vangioni *et al.* “The impact of star formation and gamma-ray burst rates at high redshift on cosmic chemical evolution and reionization”. In: *Monthly Notices of the Royal Astronomical Society* 447.3 (Jan. 2015), pp. 2575–2587. ISSN: 0035-8711. DOI: 10.1093/mnras/stu2600. eprint: https://academic.oup.com/mnras/article-pdf/447/3/2575/9385019/stu2600.pdf. URL: https://doi.org/10.1093/mnras/stu2600.

[256] Ville Vaskonen. “Electroweak baryogenesis and gravitational waves from a real scalar singlet”. In: *Phys. Rev. D* 95.12 (2017), p. 123515. DOI: 10.1103/PhysRevD.95.123515. arXiv: 1611.02073 [hep-ph].

[257] Salvatore Vitale *et al.* “Measuring the Star Formation Rate with Gravitational Waves from Binary Black Holes”. In: *The Astrophysical Journal* 886.1 (Nov. 2019), p. L1. DOI: 10.3847/2041-8213/ab50c0. URL: https://doi.org/10.3847%2F2041-8213%2Fab50c0.

[258] Benedict Von Harling *et al.* “Peccei-Quinn Phase Transition at LIGO”. In: *JHEP* 04 (2020), p. 195. DOI: 10.1007/JHEP04(2020)195. arXiv: 1912.07587 [hep-ph].

[259] Carroll L. Wainwright. “CosmoTransitions: Computing cosmological phase transition temperatures and bubble profiles with multiple fields”. In: *Computer Physics Communications* 183.9 (Sept. 2012), pp. 2006–2013. ISSN: 0010-4655. DOI: 10.1016/j.cpc.2012.04.004. URL: http://dx.doi.org/10.1016/j.cpc.2012.04.004.

[260] J. Weber. “Detection and Generation of Gravitational Waves”. In: *Phys. Rev.* 117 (1 Jan. 1960), pp. 306–313. DOI: 10.1103/PhysRev.117.306. URL: https://link.aps.org/doi/10.1103/PhysRev.117.306.

[261] David J. Weir. “Gravitational waves from a first-order electroweak phase transition: a brief review”. In: *Philosophical Transactions of the Royal Society A: Mathematical, Physical and Engineering Sciences* 376.2114 (Jan. 2018), p. 20170126. ISSN: 1471-2962. DOI: 10.1098/rsta.2017.0126. URL: http://dx.doi.org/10.1098/rsta.2017.0126.

[262] David J. Weir. “Revisiting the envelope approximation: Gravitational waves from bubble collisions”. In: *Phys. Rev. D* 93 (12 June 2016), p. 124037. DOI: 10.1103/PhysRevD.93.124037. URL: https://link.aps.org/doi/10.1103/PhysRevD.93.124037.

[263] Kent Yagi and Naoki Seto. “Detector configuration of DECIGO/BBO and identification of cosmological neutron-star binaries”. In: *Physical Review D* 83.4 (Feb. 2011). ISSN: 1550-2368. DOI: 10.1103/physrevd.83.044011. URL: http://dx.doi.org/10.1103/PhysRevD.83.044011.

[264] Takahiro S. Yamamoto, Sachiko Kuroyanagi, and Guo-Chin Liu. *Deep learning for intermittent gravitational wave signals*. 2022. DOI: 10.48550/ARXIV.2208.13156. URL: https://arxiv.org/abs/2208.13156.

[265] Claire S. Ye and Maya Fishbach. “The Redshift Evolution of the Binary Black Hole Mass Distribution from Dense Star Clusters”. In: *arXiv e-prints*, arXiv:2402.12444 (Feb. 2024), arXiv:2402.12444. DOI: 10.48550/arXiv.2402.12444. arXiv: 2402.12444 [astro-ph.HE].

[266] Ming-Sheng Zhan *et al.* “ZAIGA: Zhaoshan long-baseline atom interferometer gravitation antenna”. In: *International Journal of Modern Physics D* 29.04 (July 2019), p. 1940005. ISSN: 1793-6594. DOI: `10.1142/s0218271819400054`. URL: `http://dx.doi.org/10.1142/S0218271819400054`.

[267] Ruiyu Zhou, Ligong Bian, and Yong Du. “Electroweak Phase Transition and Gravitational Waves in the Type-II Seesaw Model”. In: (Mar. 2022). arXiv: `2203.01561 [hep-ph]`.

[268] Andrew Zic *et al. The Parkes Pulsar Timing Array Third Data Release*. 2023. arXiv: `2306.16230 [astro-ph.HE]`.